ABSTRACT

Title of dissertation: TEMPORAL AND SPECTRAL EVOLUTIONARY FEATURES OF GAMMA-RAY BURSTS DETECTED BY THE FERMI GAMMA-RAY SPACE TELESCOPE

Donggeun Tak
Doctor of Philosophy, 2019

Dissertation directed by: Dr. Julie McEnery
Department of Physics

Gamma-ray bursts (GRBs) are the most powerful electromagnetic events in universe. GRBs are powered by either core-collapse of massive stars or binary mergers of two compact objects. These progenitor systems are believed to launch relativistic, collimated jets, which produce short, bright γ-ray flashes (prompt emission) and long-lived, fading emission (afterglow) in the broad energy band from radio to γ-rays. Even though the characteristics of the prompt emission and the afterglow have been vigorously studied, many details of the physics of GRBs remain uncertain. The *Fermi Gamma-ray Space Telescope* (*Fermi*) provides invaluable data for studying GRBs with the help of a very wide field of view and broad energy coverage from the hard X-ray to γ-ray band. *Fermi* consists of two instruments, the Gamma-ray Burst Monitor (GBM; 8 keV–40 MeV) and the Large Area Telescope (LAT; 20 MeV–>300 GeV).

In this thesis, I present dedicated analysis results on three bright GRBs:

GRB 131108A, GRB 160709A, and GRB 190114C. Each of them shows its own evolution that includes the unusual and general features of GRBs. In addition, I performed two systematic studies using the full 10 year samples of LAT and GBM detected GRBs. For the first, I focused on the high-energy emission (> 100 MeV) and its origin by tracking its temporal and spectral evolution. In the second, focusing on the prompt emission phase, I found an observational signature that originates in the geometry of the relativistic jet, which had been predicted but was previously unobserved.

Temporal and spectral evolutionary features of gamma-ray bursts detected by the *Fermi* Gamma-Ray Space Telescope

by

Donggeun Tak

Dissertation submitted to the Faculty of the Graduate School of the
University of Maryland, College Park in partial fulfillment
of the requirements for the degree of
Doctor of Philosophy
2019

Advisory Committee:
Professor Peter Shawhan, chair
Professor Julie McEnery, co-chair / advisor
Professor Jordan Goodman
Professor Kara Hoffman
Professor Suvi Gezari, Dean's Representative

For my grandmother

Acknowledgments

First of all, I'd like to thank my advisor, Julie McEnery. I have learned a lot from her, including logical thinking and judging what is important and what is not. I especially thank her for giving me a lot of opportunities to attend many schools and to present my work at conferences. Also, she has introduced me to many professionals. Under her supportive supervision, I was able to work with my own plans without heavy stress, and I am pleased to have such a great advisor.

I'd also like to thank Sylvain Guiriec, who helped me to build the basis of the data analysis. Without his help, this thesis would not contain a rich result. I am grateful to Lucas Uhm, who taught me the GRB theory a lot. Although I could not be an expert on GRB theory, I was able to learn about the physics of GRBs as much as I needed to interpret the results.

Many Goddard people have helped me a lot. I want to thank Judy Racusin, who has organized the GRB lunch meeting from which I could learn about GRB a lot (though I did not vigorously join the discussion). I'd also like to thank many GRB people at the Goddard, Judy, Amy, and Eric, for their willingness to answer my basic questions. Thanks to Liz, Jeremy, and Regina, who make me feel comfortable and to encourage me a lot. Also, I'd particularly like to thank many graduate students. Sylvia Zhu, who gave valuable comments when I started to work here and continuously encouraged me whenever I met her in other places (even in Slack). I want to thank Jeff Magill, my English teacher and office mate, who was willing to correct my scribbles. Also, many people in Goddard (Amy, Sylvain, Judy, and

Alyson) gave valuable comments on this thesis, and I appreciate that.

Many people in the Fermi collaboration have inspired me and have given a lot of comments on my analyses. I could learn many analysis techniques from them. I especially thank Nicola and Dan for their help in my works.

I'd thank Korean friends that I met at Goddard, UMD, and University Church. Finally, I'd like to thank my parents and my sister for supporting me a lot. They are always on my side.

Above all, thank you, God. "*Your word is a lamp to my feet and a light for my path*" (Psalms 119:105).

Table of Contents

List of Tables

List of Figures

List of Abbreviations

ACD	Anti-coincidence Detector
Band	Band Function
BATSE	Burst and Transient Source Experiment
BAT	Burst Alert Telescope
BH	Black Hole
BIC	Bayesian Information Criterion
C_{Stat}	Cash statistic
CAL	Calorimeter
CGRO	*Compton Gamma Ray Observatory*
CPL	Cutoff Power Law
CR	Closure Relation
dof	Degree of Freedom
Fermi	*Fermi Gamma-ray Space Telescope*
FLGC	*Fermi*-LAT Gamma-ray Burst Catalog
FoV	Field of View
GBM	Gamma-ray Burst Monitor
GRB	Gamma-ray Burst
GW	Gravitational Wave
HLE	High-Latitude Emission
IC	Inverse Compton
ICMART	Internal-Collision-Induced MAgnetic Reconnection and Turbulence
ISM	Interstellar Medium
LAT	Large Area Telescope
LIGO	Laser Interferometer Gravitational-Wave Observatory
LLE	LAT Low Energy
LoS	Line of Sight
LoSE	Line-of-Sight Emission
NS	Neutron Star
PG_{Stat}	Poisson data with Gaussian background statistic
PL	Power Law

RoI	Region of Interest
SN	Supernova
Swift	*Neil Gehrels Swift Observatory*
SSC	Synchrotron Self-Compton
TKR	Tracker
TS	Test Statistic
UVOT	Ultra-Violet/Optical Telescope
VHE	Very High Energy (100 GeV to 100 TeV)
XRT	X-Ray Telescope

Chapter 1: Introduction

A gamma-ray burst (GRB) is a burst of γ-rays, typically lasting from milliseconds to thousands of seconds in the energy band from tens of keV to several MeV. This bright and highly variable emission is usually called the prompt GRB emission. This is followed by a longer-lasting emission in the broad energy band from radio to γ-rays, which decays as a function of time. This is known as the GRB afterglow.

Since the first discovery of a GRB in the late 1960s, our understanding of this mysterious phenomenon has progressed dramatically. In 1990s, the first GRB afterglow was observed, followed by a redshift measurement, showing that GRBs are cosmological. With the measured distance scale, the typical isotropic γ-ray luminosity of GRBs is $\sim 10^{51}$–10^{53} erg s^{-1} (sometimes higher than 10^{54} erg s^{-1}), which suggests GRBs as the most energetic electromagnetic events in universe. Such energetics released within very short time scales imply that GRBs must be attributed to catastrophic events: either the core collapses of massive stars or the binary mergers of two compact objects such as neutron stars and black holes. In both cases, a black hole or a rapidly rotating highly magnetized neutron star (millisecond magnetar) can be formed and serve as the central engine for launching two relativistic, collimated outflows (jets) in opposite directions. The sketch of the origin of GRBs is

well established, but many details are still veiled such as the jet composition, the energy dissipation process, and the origin of the high-energy emission.

The *Fermi Gamma-Ray Space Telescope* was launched in 2008 with two instruments, the Gamma-ray Burst Monitor (GBM; 8 keV–40 MeV) and the Large Area Telescope (LAT; 30 MeV– >300 GeV). Since then, *Fermi* has provided invaluable data to broaden our understanding of GRBs, especially the GRB prompt emission. During the last 11 years (2008–2019), the LAT has detected more than 180 GRBs, all also detected at lower energies. In the same period, the GBM has detected more than $\sim$ 2500 GRBs. Both LAT and GBM observations provide a large sample size enabling systematic studies of the γ-ray emission to reveal general properties of GRBs. In addition, combined GBM and LAT observations allow us to study the broadband properties of GRBs over seven decades in energy. By tracking the temporal and spectral evolutionary features of the broadband GRB spectrum, the physics of GRBs can be further explored.

In this work, I present dedicated studies on three bright GRBs detected by both GBM and LAT: GRB 131108A, GRB 160709A, and GRB 190114C. The detailed analysis on those GRBs addresses the question of the origin of the broadband emission and their mechanisms. In addition, two systematic studies on the large sample of GRBs are presented: i) I test the leading afterglow model (the external forward shock model) to the LAT GRB sample and constrain several physical parameters. ii) I search for evidence of the curvature effect of a relativistic jet in the large sample of the GBM GRBs. These studies shed light on the physical properties and the detailed emission mechanisms of GRBs.

Chapter 2: Gamma-Ray Bursts

Gamma ray bursts are the most energetic explosions in the universe. Over the last 50 years, we have observed many surprising events, each of which gives us a small piece of information to understand mysterious GRBs. Here, I would like to present an outline for the journey to explore the evolutionary characteristics of GRBs.

2.1 Brief History of Gamma-Ray Bursts

The discovery of the first GRB was made by *Vela* satellites, which were a series of United States military satellites used to monitor γ-ray emission possibly from nuclear weapons tested in space. On July 2, 1967, the very first GRB, GRB 670702[1] was detected, and it was later confirmed that it was not associated with terrestrial events or supernovae [1] (Figure 2.1).

A breakthrough in the understanding of the origin of GRBs could not be made until the launch of the Compton Gamma Ray Observatory (*CGRO*) in 1991 due to the lack of significant improvement in detectors or telescopes. Nevertheless,

[1]The name of a GRB is determined by its detected year, month, and day. If multiple GRBs are detected on the same day, the additional alphabet is added in the order in which it occurs; e.g., GRB080916C was the third burst detected on August 16, 2008

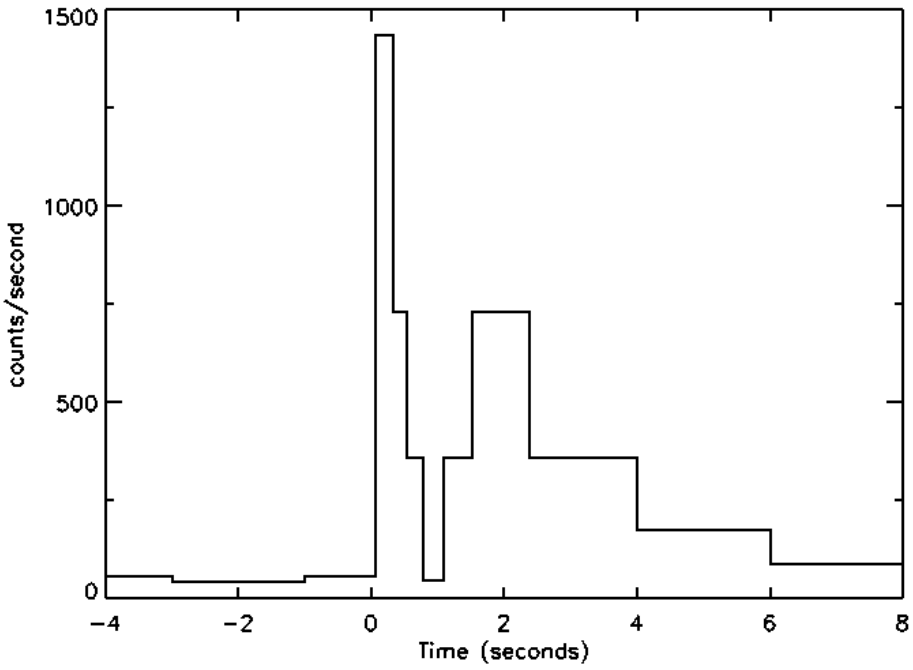

Figure 2.1: **The light curve of the very first GRB detected by *Vela* satellites on July 2, 1967.** [Credit: J.T. Bonnell 1995]

some tentative conclusions were derived. The first Konus GRB catalog [2] showed that the duration distribution of GRBs showed two categories (long and short) (left panel in Figure 2.2), and GRBs appeared to be isotropically distributed (left panel in Figure 2.3). In the meantime, over a hundred GRB models had been suggested [3], and the fireball model of GRBs, the standard GRB model, started to be established [4–6].

The Burst and Transient Source Experiment (BATSE; 25 keV–2 MeV), one of the four instruments on board *CGRO*, was dedicated to the study of GRBs. Over nine years of operation (1991–2000), the BATSE had detected 2704 GRBs and opened a new era in GRB research, especially for the prompt phase of GRBs. The GRB categories (long and short) were clearly confirmed, where the separation was made at $\sim$ 2 seconds (right panel in Figure 2.2) [10]: short bursts last less than 2

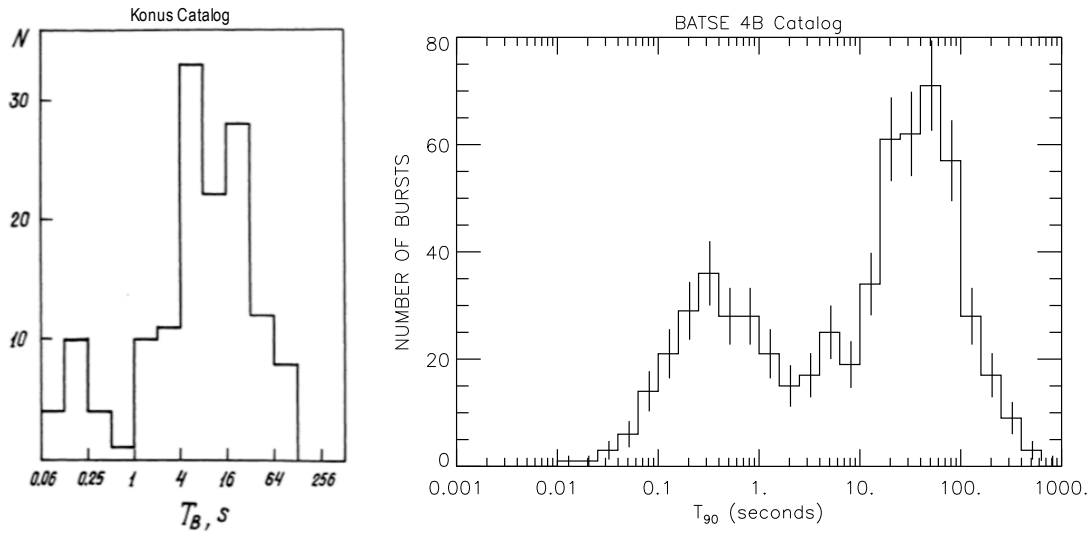

Figure 2.2: **The distribution of bursts in duration.** *Left*: from the first Konus GRB catalog [2]. *Right*: from the forth BATSE GRB catalog [7].

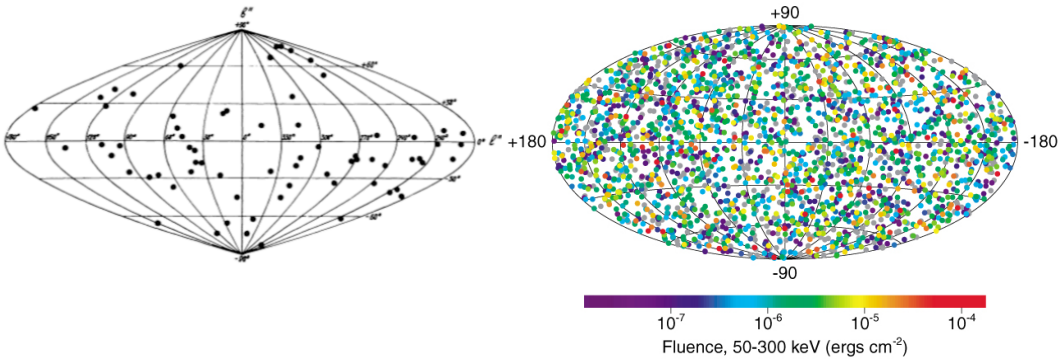

Figure 2.3: **The sky distribution (in galactic coordinates) of bursts.** *Left*: from the first Konus GRB catalog [2]. *Right*: 2704 bursts detected by BATSE during the nine-year mission (available at `http://gammaray.nsstc.nasa.gov/batse/grb/skymap/`).

seconds (T_{90}[2] ≤ 2), while long bursts continue longer ($T_{90} > 2$). A comparison of the spectral hardness between the two classes found that short GRBs tend to be described by harder spectra than those of long GRBs [10]. The BATSE observations supported the extragalactic origin of GRBs: the angular distribution of GRBs

[2]The time during which the cumulative background-subtracted counts increase from 5% to 95%.

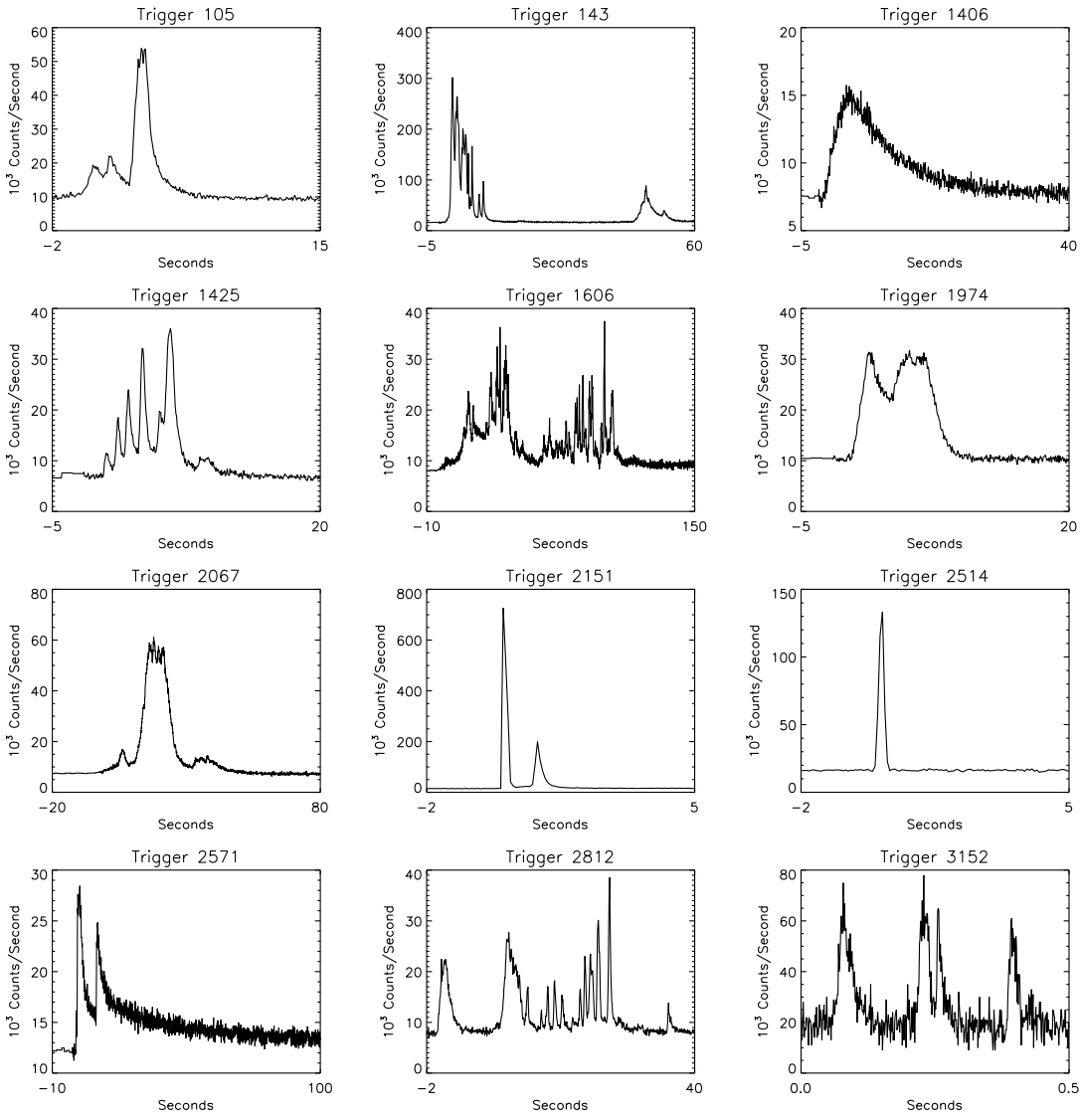

Figure 2.4: **GRB light curves observed by BATSE.** Twelve light curves show the variety of GRB light curves. [Credit: J.T. Bonnel]

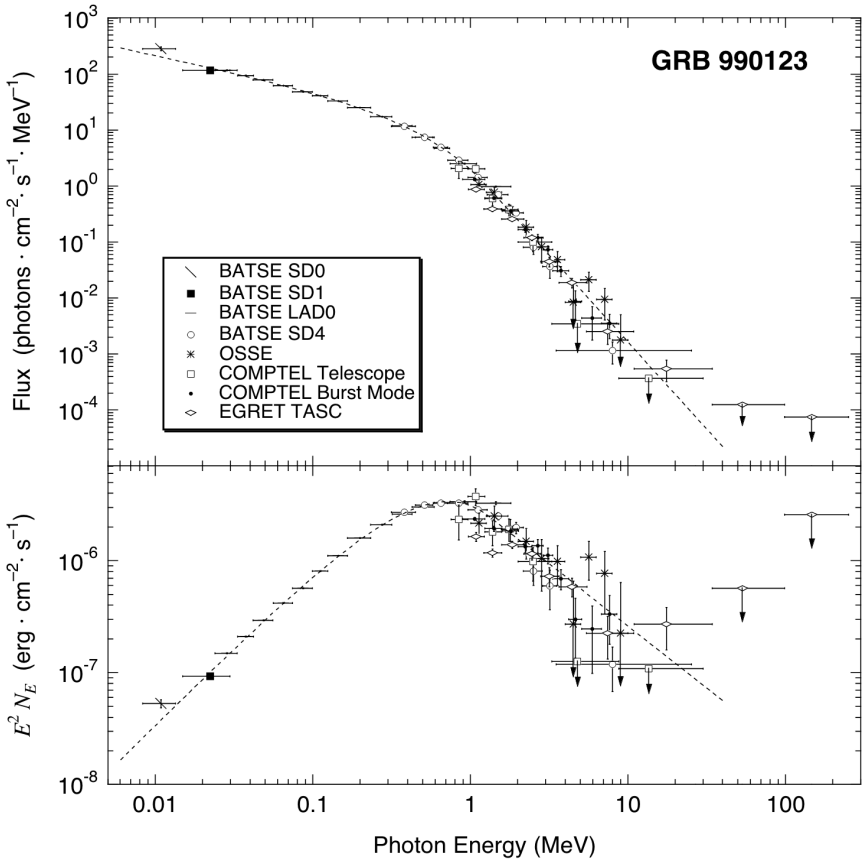

Figure 2.5: **The Band function [8] is one of GRB models widely used for explaining GRB spectra.** For example, the spectrum of GRB 990113 is well described by the Band function. Adopted from [9].

were highly isotropic (right panel in Figure 2.3) [11], and the intensity distribution deviated from the simple expectation of Euclidean geometry [12]. In addition to more elaborate systematic studies, BATSE allowed for the study of individual GRBs in great detail. The GRB light curves composed of a single pulse or multiple pulses were different from one another, and each pulse was rather asymmetric (Figure 2.4). The GRB energy spectra were non-thermal and usually well described by an empirical model, the "Band function", a smoothly joined broken power-law function [8] (Figure 2.5). As the cosmological origin with non-thermal emission of GRBs made the fireball model more attractive and elaborate, the standard fireball "shock" model was proposed: the external shock between a relativistic outflow and an external medium [13, 14] and internal shocks within an unsteady relativistic outflow [15]. During this period, the progenitors of GRBs were progressively studied: the binary merger model [16–18] and the collapsar model [19].

Due to the poor localization of the BATSE (the size of the error circle was at least a few degrees), a follow-up observation of the prompt emission of GRBs was unsuccessful until the *BeppoSAX* mission (1996–2002). *BeppoSAX* was able to quickly identify a possible X-ray counterpart of a GRB. In 1997, the first X-ray counterpart and afterglow of GRB 970228 was discovered [20], and the discovery of the first optical afterglow from the same burst followed [21] (Figure 2.6). Not long after, the first radio afterglow with a redshift measurement ($z = 0.835$) was made for GRB 970508 [22, 23], which confirmed the extragalactic origin of GRBs. Surprisingly, two weeks before the discovery of the first X-ray and optical afterglow of GRB 970228, the theoretical prediction of the multi-wavelength afterglows of GRBs

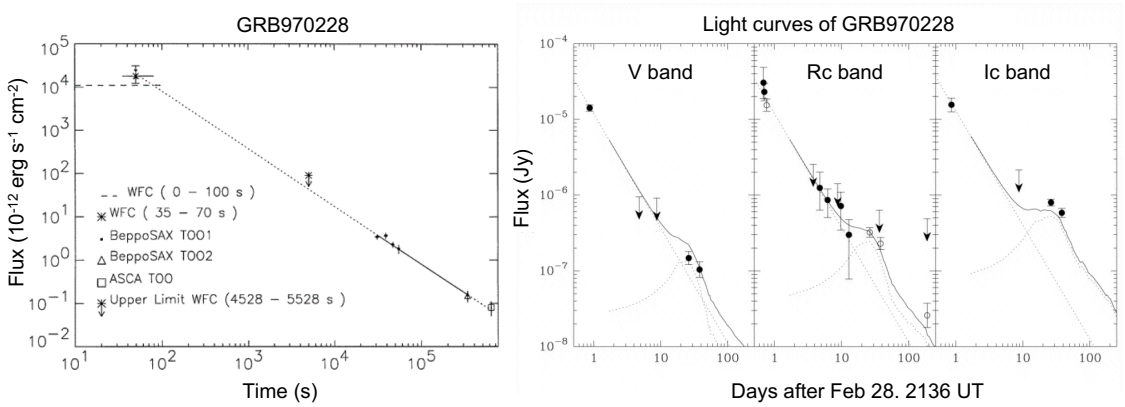

Figure 2.6: **The first observation of X-ray and optical afterglows of GRB 970228.** *Left*: the X-ray afterglow of GRB 970228 observed by *BeppoSAX* [20]. *Right*: the optical afterglow of GRB 970228. A later bump was interpreted as the contribution from an underlying supernova [29].

was published [24], which was found to be generally consistent with observations [25, 26]. In addition to these great achievements, a breakthrough in identifying the origin of long GRBs was made. The association between a Type Ic supernova (SN) and a long GRB was disclosed, which implies that long GRBs are attributed to the deaths of massive stars [27–29].

The next generation GRB mission was the *Neil Gehrels Swift Observatory* (*Swift*; 2004–present)[3] [30], which consists of three instruments: the Burst Alert Telescope (BAT; 15 to 150 keV), the X-Ray Telescope (XRT; 0.2 to 10 keV), and the Ultra-Violet/Optical Telescope (UVOT; 170 to 600 nm wavelengths). The unprecedented capability of *Swift* is to slew promptly to a GRB detected by the BAT, so that X-ray and UV/optical counterparts can easily be observed by the XRT and the UVOT, respectively. As a result, *Swift* has provided abundant afterglow

[3]The original name of the mission was the *Swift Gamma Ray Burst Explorer spacecraft*. In memory of the mission's original principal investigator, Neil Gehrels, the mission was renamed the *Neil Gehrels Swift Observatory* in 2018

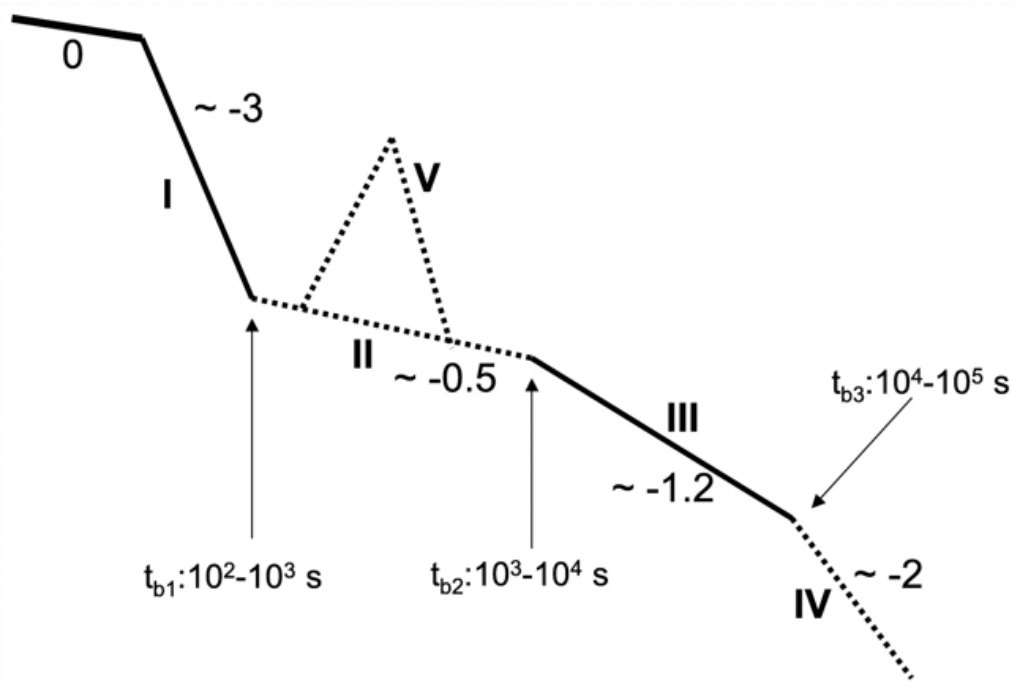

Figure 2.7: **The canonical GRB afterglow light curve.** The light curve is composed of five distinct components: an early steep decay (I), a shallower-than-normal decay or plateau (II), a normal decay (III), a late steeper decay (IV), and one or more X-ray flares (V). Adopted from [31].

data, and the canonical GRB X-ray afterglow light curve was identified [31, 32] (Figure 2.7). One surprise in X-ray afterglows was the observation of bright X-ray flares [33], suggesting that the GRB central engine can be reactivated after the end of the prompt emission phase [31].

BeppoSAX and *Swift* broadened our understanding of the GRB afterglow significantly, but the understanding of the prompt emission of GRBs was left behind; the broadband spectrum and its evolution, the jet composition, and the energy dissipation mechanism are not well understood. Furthermore, even though the Energetic Gamma Ray Experiment Telescope (EGRET; 20 MeV–30 GeV) on board *CGRO* provided some hints of the high-energy emission of GRBs such as the necessity of an additional spectral component and the evolution of the GeV emission, many

questions regarding the high-energy emission mechanism remain unsolved. *Fermi* (2007–present) with two scientific instruments, the GBM [34] and the LAT [35], is the mission to respond to the demand for in-depth exploration of the prompt emission with wider field of view and broader energy coverage. *Fermi* can monitor the whole sky for GRBs and cover more than 7 decades in energy. In particular, the LAT high-energy observations provide invaluable data for characterizing the high-energy emission ($>$ 100 MeV) of GRBs [36, 37]. By combining the GBM and the LAT data, time-integrated and time-resolved spectral analyses can be performed in unprecedented detail in a wide range of energy bands. Many *Fermi*-detected GRBs have shown one or more spectral components, implying one or more emission sources [38–41].

On August 17, 2017, a gravitational wave (GW), GW 170817, from the merging of binary neutron stars was detected by the *Laser Interferometer Gravitational-Wave Observatory* (*LIGO*) and the *Virgo* GW detectors, which was followed by a short GRB, GRB 170817A, about 1.7 seconds later detected by the GBM. This answered the long-standing question of the progenitor of short GRBs (at least low-luminosity short GRBs) [42, 43] (Figure 2.8). This event opened the multi-messenger era of GRB research.

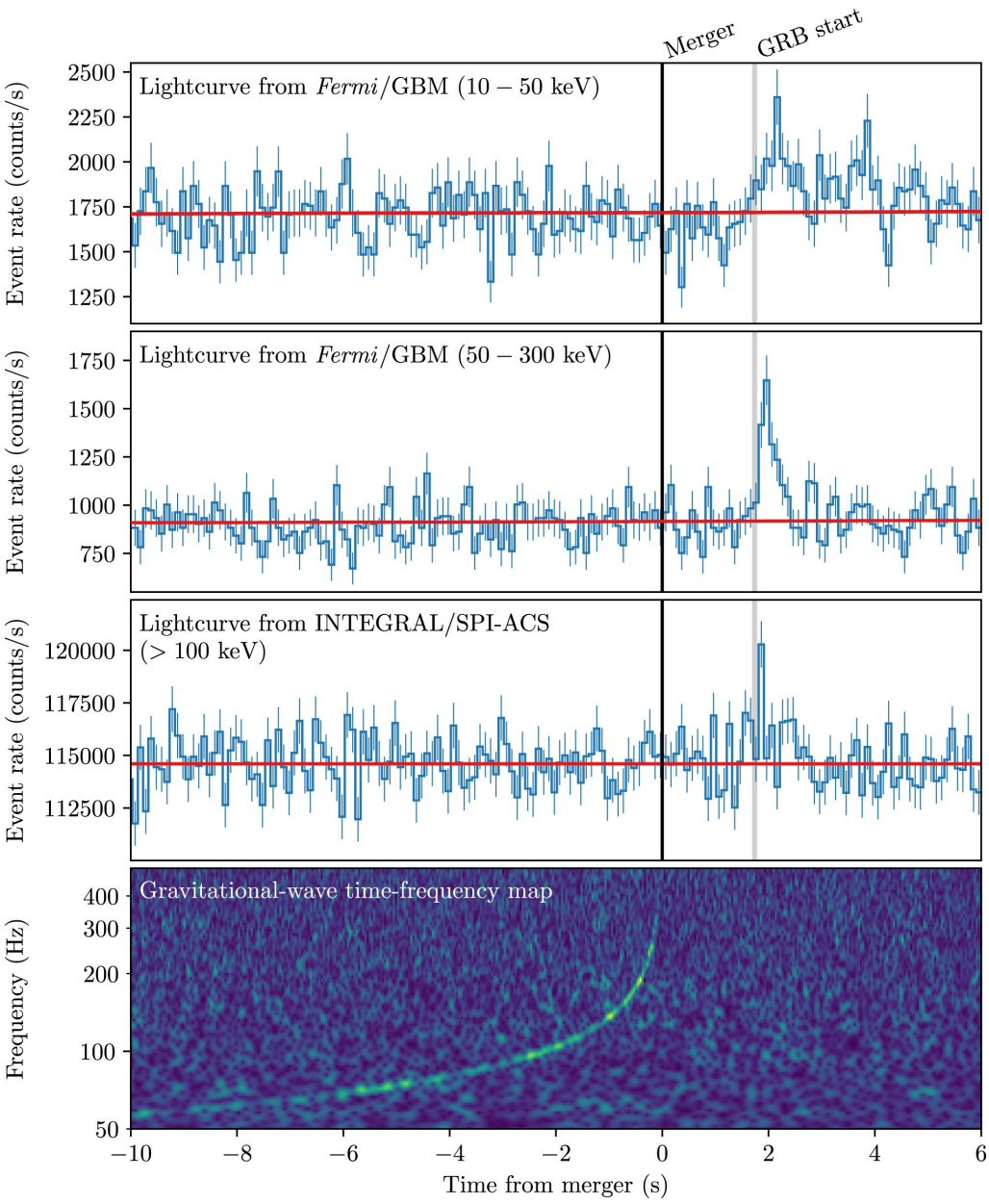

Figure 2.8: **Observation of GW 170817 and GRB 170817A.** The top three panels show GRB 170817A observed by two instruments (*Fermi*/GBM and *INTEGRAL*/SPI-ACS). The bottom panel shows GW 170817 about 1.7 seconds prior to GRB 170817A [43].

2.2 Gamma-ray Emission and Interaction Processes

The energy spectra of GRBs are in general observed to be non-thermal in that the nature of radiation cannot be described by a temperature of a source. The main radiation mechanism for GRBs is believed to be synchrotron radiation from relativistic electrons [44–46]. Inverse Compton scattering is usually suggested as a possible radiation mechanism for the high-energy emission [47]. In this chapter, I summarize non-thermal emission and interaction processes relevant to the physics of GRBs.

2.2.1 Particle Acceleration

In order to generate high-energy photons (in case of GRBs, keV–MeV photons), energetic charged particles (electrons, proton, or ions) are necessary. Energetic charged particles can be generated by the so-called Fermi acceleration processes. There are two types of the Fermi acceleration processes. Originally, Erico Fermi suggested a second-order Fermi acceleration mechanism [48], where charged particles are accelerated from collisions against magnetic field clouds. The efficiency for this process is proportional to $(V/c)^2$, where V ($\ll c$) is the the average random motion speed of the magnetic clouds, so that this process is inefficient to produce energetic particles required for high-energy emission. The more efficient first-order Fermi acceleration mechanism was later proposed [49–51], which is the acceleration process of charged particles in a shock environment. In a shock, there is a sharp jump in the physical conditions such as density, pressure, temperature, etc. Charged

particles can gyrate around magnetic field lines due to strong magnetic fields near the shock front. Each time charged particles cross the shock front moving a speed of V, the particles gain energy, $\Delta E/E \propto V/c$. At the same time, a small number of particles will escape the acceleration region. Considering the energy gain and retention rate of charged particles, the energy distribution can be derived as [49–51]

$$N(E) \propto E^{-p}, \quad \text{or} \quad N(\gamma) \propto \gamma^{-p}, \tag{2.1}$$

where p is the spectral index, γ is the Lorentz factor of charged particles,

$$\gamma = \frac{1}{\sqrt{1-\beta^2}}, \tag{2.2}$$

$\beta = v/c$, and v is the speed of particles. For electrons, this index is called the electron spectral index that determines the shape of the GRB light curve and spectrum.

2.2.2 Synchrotron Radiation

Synchrotron radiation is the electromagnetic radiation emitted when relativistic charged particles in a magnetic field are accelerated radially. The total synchrotron emission power per frequency by a charged particle in a magnetic field B, a synchrotron spectrum, can be described as

$$P(\nu) = \frac{\sqrt{3}q^3 B \sin\alpha}{mc^2} F\left(\frac{\nu}{\nu_{ch}}\right) \tag{2.3}$$

where q and m are charge and mass of the particle, and α is an incident angle with respect to the field line [52]. The characteristic (critical) frequency, ν_{ch}, is defined as

$$\nu_{ch}(\gamma) = \frac{3}{4\pi}\frac{\gamma^2 qB\sin\alpha}{mc}, \tag{2.4}$$

where γ is the Lorentz factor of the charged particle. The function $F\left(\frac{\nu}{\nu_{ch}}\right)$ for a single charged particle is

$$F\left(\frac{\nu}{\nu_{ch}}\right) \sim \begin{cases} \nu^{1/3}, & \text{for } \nu \ll \nu_{ch} \\ \nu^{1/2}e^{-(\nu/\nu_{ch})}, & \text{for } \nu \gg \nu_{ch}. \end{cases} \tag{2.5}$$

Top left panel of Figure 2.9 shows the synchrotron spectrum from a single relativistic particle. Integrated over ν, the total emission power of the charged particle via synchrotron radiation average over all angles is

$$P_{\rm syn} = \frac{4}{3}\sigma_{\rm T} c\beta^2\gamma^2 U_B, \tag{2.6}$$

where

$$\sigma_{\rm T} = \frac{8\pi}{3}\left(\frac{q^2}{mc^2}\right)^2 \tag{2.7}$$

is the Thompson cross section, and $U_B = B^2/(8\pi)$ is the magnetic energy density.

For a power-law distribution of charged particles (Equation 2.1), the total power per unit volume per unit frequency, the so-called specific flux, F_v, is described

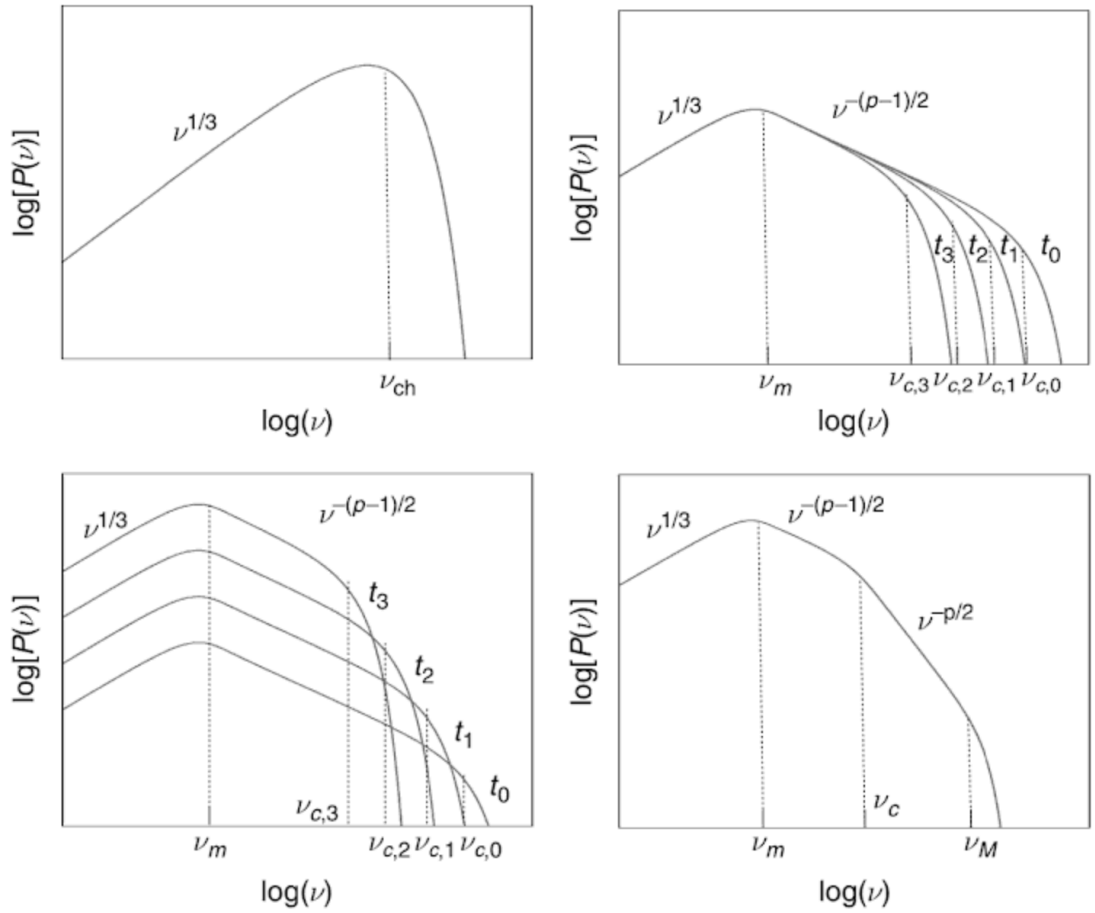

Figure 2.9: **Synchrotron spectra of electrons.** *Top left*: synchrotron spectrum for a single electron. *Top right*: synchrotron spectrum for a power-law distribution of electrons, $N(E) \propto E^{-p}$. The synchrotron cooling of electrons is also considered. *Bottom left*: Same condition as on the top right, but fresh electrons are injected continuously. *Bottom left*: putting all these effects together. The parameters, ν_m, ν_M, and ν_c are the minimum, maximum, and cooling frequencies, respectively. Adopted from [53].

as

$$F_\nu \propto \int P(\nu,\gamma)N(\gamma)d\gamma \propto \begin{cases} \nu^{1/3}, & \text{for } \nu < \nu_{\rm m} \equiv \nu_{\rm ch}(\gamma_m) \\ \nu^{-\frac{p-1}{2}}, & \text{for } \nu_{\rm m} < \nu < \nu_{\rm M} \equiv \nu_{\rm ch}(\gamma_{\rm M}), \\ \nu^{1/2}e^{-(\nu/\nu_{\rm M})}, & \text{for } \nu > \nu_{\rm M}, \end{cases} \tag{2.8}$$

where $\gamma_{\rm m}$ (ν_m) and $\gamma_{\rm M}$ (ν_M) are the minimum and maximum Lorentz factors (injection frequencies) of the charged particles (top right panel of Figure 2.9).

Relativistic charged particles lose their energy via synchrotron radiation (synchrotron cooling). In particular, particles with Lorentz factors above the so-called cooling Lorentz factor (γ_c) lose a significant fraction of their energy within time,

$$\tau_c \sim \frac{\gamma mc^2}{P_{\rm syn}} = \frac{6\pi mc}{\gamma\sigma_{\rm T}\beta^2 B^2} \propto \gamma^{-1}. \tag{2.9}$$

Rearranging this equation, the cooling Lorentz factor and corresponding frequency (ν_c) are given by

$$\gamma_c \simeq \frac{6\pi mc}{\sigma_{\rm T}B^2\tau_c} \quad \text{and} \quad \nu_c \equiv \nu_{\rm ch}(\gamma_c), \tag{2.10}$$

respectively. Depending on the relative position of the minimum injection frequency (ν_m) and the cooling frequency (ν_c), one can define two cooling regimes. When $\nu_c < \nu_m$, all particles cool down within the short time scale, the so-called fast cooling. Inversely, if $\nu_m < \nu_c$, only high-energy particles above ν_c cool down, the slow cooling.

The maximum synchrotron energy can be estimated from the assumption that

energy gain from the first-order Fermi acceleration is same as the energy loss by the synchrotron cooling. For each gyration in a relativistic shock taking $\tau_{gyr} \sim \gamma mc/qB$, a charged particle gains energy by a factor of about 2. If a particle loses more than a half of its energy, $\gamma mc^2/2$, it cannot recover its original energy from the acceleration process; i.e., the particle acceleration process is inefficient. This gives the condition for the maximum synchrotron energy [53, 54],

$$P_{syn}\,\tau_{gyr} = \frac{\sigma_{\rm T} mc^2 \beta^2 \gamma^3 B}{6\pi q} \lesssim \frac{\gamma mc^2}{2} \quad \rightarrow \quad \gamma_M \sim \left(\frac{3\pi q}{\sigma_{\rm T} B}\right)^{1/2} = \left(\frac{9m^2c^4}{8q^3 B}\right)^{1/2}, \quad (2.11)$$

assuming $\beta \sim 1$. Plugging in this Lorentz factor to Equation 2.4 gives the maximum synchrotron energy [54],

$$h\nu_M \sim h\frac{3}{4\pi}\frac{\gamma_M^2 qB\sin\alpha}{mc} \sim \frac{9mc^3 h}{16\pi q^2} \sim 50\,{\rm MeV}^4, \quad (2.12)$$

where the incident angle α has been averaged out by $\langle \sin\alpha \rangle = 2/3$. In GRB physics, shocks occur within a relativistic outflow moving with a Lorentz factor of $\Gamma_{\rm bulk}$, so that the maximum synchrotron limit in the observer frame is boosted,

$$E_{\gamma,\rm max} \simeq \frac{50\,\Gamma_{\rm bulk}}{1+z}\,{\rm MeV} \quad (2.13)$$

When fresh particles are continuously accelerated and injected to the emission region, $Q(\gamma > \gamma_m, t) = Q_0(t)\left[\frac{\gamma}{\gamma_m(t)}\right]^{-p}$, the continuity equation in energy space can

[4] This value may vary depending on the details of the acceleration, $h\nu_M \sim 30$–110 MeV [36, 55].

be described as [53]

$$\frac{\partial N(\gamma,t)}{\partial t} = -\frac{\partial}{\partial \gamma}[\dot{\gamma}\, N(\gamma,t)] + Q_0(t)\left(\frac{\gamma}{\gamma_m(t)}\right)^{-p}, \tag{2.14}$$

where $\dot{\gamma}$ is the energy loss rate via synchrotron, $\dot{\gamma} \propto -\gamma^2$ (Equation 2.6). By solving this continuity equation for three different regimes, one can derive the particle distributions and corresponding synchrotron spectra. For $\gamma_c < \gamma < \gamma_m$, particles in this regime are cooled in a very short time scale without injection ($t \gg \tau_c$ and $Q(\gamma,t) = 0$); i.e., $\dot{\gamma}\, N(\gamma,t) =$ constant. For $\gamma > \gamma_c$ and γ_m, all injected particles are again cooled within a very short time scale ($t \gg \tau_c$); i.e., the left hand side, $\partial N(\gamma,t)/\partial t$, is negligible. To sum up,

$$N(\gamma) \propto \begin{cases} \gamma^{-2}, \\ \gamma^{-p}, \\ \gamma^{-(p+1)}, \end{cases} \quad \text{and} \quad F_\nu \propto \begin{cases} \nu^{-\frac{1}{2}}, & \text{for } \gamma_c < \gamma < \gamma_m, \\ \nu^{-\frac{p-1}{2}}, & \text{for } \gamma_m < \gamma < \gamma_c, \\ \nu^{-\frac{p}{2}}, & \text{for } \gamma > \gamma_c \text{ and } \gamma_m. \end{cases} \tag{2.15}$$

See bottom panels in Figure 2.9.

2.2.3 Inverse Compton (IC) Scattering

Interaction (or scattering) between relativistic electrons and photons is another important radiation process ; low-energy photons are scattered by energetic electrons and gain energy in this process. Depending on the relative energies of an incident photon and an electron moving with a relativistic speed (with Lorentz factor γ),

there are two regimes in this scattering process: the Thompson regime ($h\nu' \ll m_e c^2$) and the Klein-Nishina regime ($h\nu' \lesssim m_e c^2$), where $h\nu'$ is the energy of the incident photon in the electron rest frame.

In the Thompson regime, this scattering is approximately elastic, so that the photon energy after the scattering is similar to the initial energy ($h\nu'_{\rm after} \sim h\nu'_{\rm before}$), but its direction of propagation is modified. As a result, the photon gains energy by a factor of order γ^2 by this scattering process,

$$h\nu_{\rm after} \sim \gamma^2 h\nu_{\rm before}. \tag{2.16}$$

In the Klein-Nishina (KN) regime, the electron receives a recoil force, so that the energy of the scattered photon is smaller than that of the incident photon ($h\nu'_{\rm after} < h\nu'_{\rm before}$). Thus, the photon energy after the scattering is limited to the electron energy in the rest frame,

$$h\nu_{\rm after} \sim \min(\gamma^2 h\nu_{\rm before}, \gamma m_e c^2). \tag{2.17}$$

Also, the scattering cross section is greatly suppressed compared to the Thompson regime [52],

$$\sigma_{\rm KN} \propto \sigma_{\rm T} \times \frac{m_e c^2}{h\nu}. \tag{2.18}$$

The IC emission power for a single scattering is given by [52]

$$P_{\rm IC} = \frac{4}{3}\sigma_{\rm T} c \beta^2 \gamma^2 U_{\rm ph}, \tag{2.19}$$

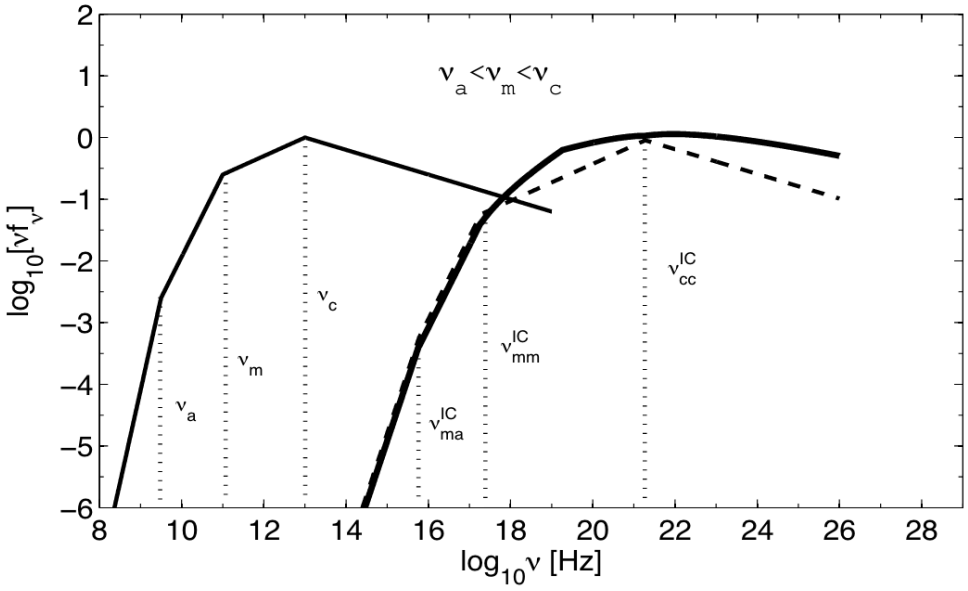

Figure 2.10: **Total synchrotron + SSC spectrum for $\nu_m < \nu_c$.** The thin and thick lines indicate the seed synchrotron component and the upscattered SSC component, respectively. The dotted line indicates the broken power-law approximation. The peaks for two components are normalized to unity. Adopted from [56].

where $U_{\rm ph}$ is the initial photon energy density.

2.2.3.1 Synchrotron Self-Compton

The most widely discussed case of IC radiation is synchrotron self-Compton (SSC), where the electron distribution, which produces seed photons via synchrotron, interacts with the seed photons up-scattered to higher energies via the IC process. In this case, the group of energetic electrons loses their energies by both synchrotron and IC processes.

The ratio of energy loss by synchrotron and IC, which is also known as a Y parameter in GRB physics[5], can be described as the ratio between the magnetic

[5]In some spectral regimes, this parameter is not exactly identical to the Compton-y parameter [52]. See discussion in [53].

field energy density and the photon energy. Assuming that the SSC occurs within an outflow moving with a Lorentz factor of $\Gamma_{\rm bulk}$,

$$Y \equiv \frac{P_{\rm SSC}}{P_{\rm syn}} \simeq \begin{cases} \frac{U_{\rm syn}}{U_B}, & \text{for the Thompson regime,} \\ \frac{U_{\rm syn}}{U_B} \min\left[1, \left(\frac{\Gamma_{\rm bulk} m_e c^2}{\gamma h\nu}\right)^2\right], & \text{for the KN regime,} \end{cases} \tag{2.20}$$

where $U_{\rm syn}$ is the energy density of the synchrotron photons. Therefore, the total emission power can be written as

$$P_{tot} = P_{\rm syn} + P_{\rm SSC} = P_{\rm syn}(1+Y). \tag{2.21}$$

The introduction of SSC enhances the electron cooling, reducing the electron cooling Lorentz factor and corresponding cooling frequency;

$$\tau_c \sim \frac{\gamma m_e c^2}{P_{\rm tot}} = \frac{\gamma m_e c^2}{P_{\rm syn}(1+Y)}, \quad \text{so that} \quad \gamma_c \to \frac{\gamma_c}{(1+Y)} \quad \text{and} \quad \nu_c \to \frac{\nu_c}{(1+Y)^2}. \tag{2.22}$$

Note that when the SSC component is negligible due to the KN effect ($Y \ll 1$), these equations are reduced to Equation 2.9 and Equation 2.10.

The spectrum of the SSC emission depends on both the synchrotron spectrum and the energy distribution of the electrons (Figure 2.10). For the details of the SSC spectrum, especially in GRB physics, see the references [56–58].

2.2.4 Pair Production and Annihilation

According to quantum electrodynamics (QED), when a photon has energy $\geq 2m_e c^2 \sim 1.022 MeV$, the photon can be converted to unstable electron-positron pairs (pair production), which instantly returns to a photon identical to the original photon. In order to produce stable electron-positron pairs, two photons should be involved to conserve both energy and momentum; $E_{\gamma,1} \cdot E_{\gamma,2} \geq (m_e c^2)^2$. Inversely, electron-positron pairs can annihilate and emit two photons (pair annihilation).

In an outflow with a Lorentz factor of $\Gamma_{\rm bulk}(\sim 100)$, each photon ($\sim$ MeV) can be considered to be de-boosted in the outflow comoving frame by a factor of $\Gamma_{\rm bulk}$, so that the photon energy becomes X-ray ($\sim$ few keV), lower than the pair production threshold; $E_{\gamma,1} \cdot E_{\gamma,2} \geq \Gamma_{\rm bulk}^2 (m_e c^2)^2$, and the inferred flux is lower. Therefore, this interaction is less likely to occur within the relativistic outflow.

Since the GRB prompt emission is mostly dominated in the keV–MeV energy band (sometimes with GeV photons), pair production and annihilation are the important effects [3, 59, 60].

2.2.5 Hadronic Process - $p\gamma$ Interaction

An interaction between photons and hadrons, which can be relevant to GRB physics, is a photo-meson ($p\gamma$) interaction[6]. The $p\gamma$ interaction in a relativistic outflow involves an accelerated proton and an energetic photon. This interaction

[6]Since the cross sections of synchrotron and SSC for protons are much smaller by a factor $(m_e/m_p)^2 \sim 10^{-7}$ than those of electrons, the synchrotron and IC contributions by protons can be generally ignored.

results in neutrinos, as well as hadrons and leptons:

$$p\gamma \rightarrow \begin{cases} n\pi^+ \rightarrow ne^+\nu_e\bar{\nu}_\mu\nu_\mu \\ \\ p\pi^0 \rightarrow p\gamma\gamma \end{cases} \tag{2.23}$$

Similar to the pair production, this interaction occurs only when involved particles have energy above a certain threshold [53],

$$E_p \cdot E_\gamma \geq 0.16(\mathrm{GeV})^2 \left(\frac{\Gamma_{\mathrm{bulk}}}{1+z}\right)^2. \tag{2.24}$$

The resultant neutrino energy would be [53]

$$E_\nu \sim 0.05 E_p, \quad \text{or} \quad E_\nu \gtrsim 8 \text{ GeV} \left(\frac{\Gamma_{\mathrm{bulk}}}{1+z}\right)^2 \left(\frac{E_\gamma}{\mathrm{MeV}}\right)^{-1}. \tag{2.25}$$

The observation of neutrinos from a source may indicate the existence of energetic protons in an emission site (§ 2.3.3).

2.3 Key Observational Results

Over more than 50 years of GRB observations, valuable data from various observatories or telescopes has been accumulated, which provides important clues to shed light on the physics of GRBs. In this section, I summarize the key observational results for two emission phases in a GRB: the prompt emission and the afterglow.

2.3.1 Prompt Emission

The prompt emission phase of a GRB can defined as the temporal phase during which short and spiky pulses are observed in the keV – MeV energy range (Figure 2.12)). GRBs are classified into two categories depending on the duration of their prompt emission, T_{90} (§ 4.1.1): short ($T_{90} \leq 2$) and long ($T_{90} > 2$). The recent distribution of T_{90} is shown in the left panel of Figure 2.11, which is well described with two Gaussian functions. Another well-known property, which shows a difference between long and short GRBs, is a hardness ratio (HR) that is defined as a ratio between the deconvolved counts in two energy bands (50–300 keV and 10–50 keV). It is known that long GRBs tend to be softer (or have smaller HR values) than short GRBs (the right panel of Figure 2.11). Several authors claim a third group in the T_{90} and HR distributions [63], but this has not been clearly identified [61]. Table 2.1 shows the detection rate, the energy band, and the field of

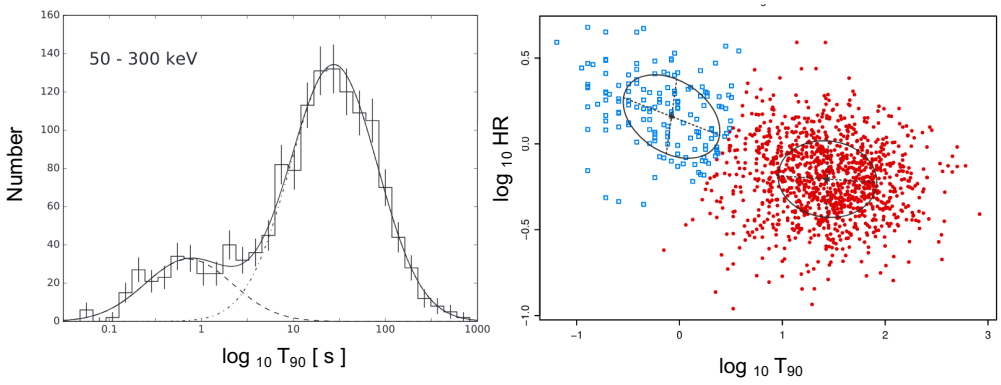

Figure 2.11: T_{90} **and hardness ratio (HR) distributions.** *Left*: T_{90} distribution measured in 50 keV–300 keV. The distribution is well described with two Gaussian functions. *Right*: duration versus hardness ratio distribution of GRBs. Ellipses show the best-fitting multivariate Gaussian model: one for short GRBs and the other for long GRBs. Adopted from [61]

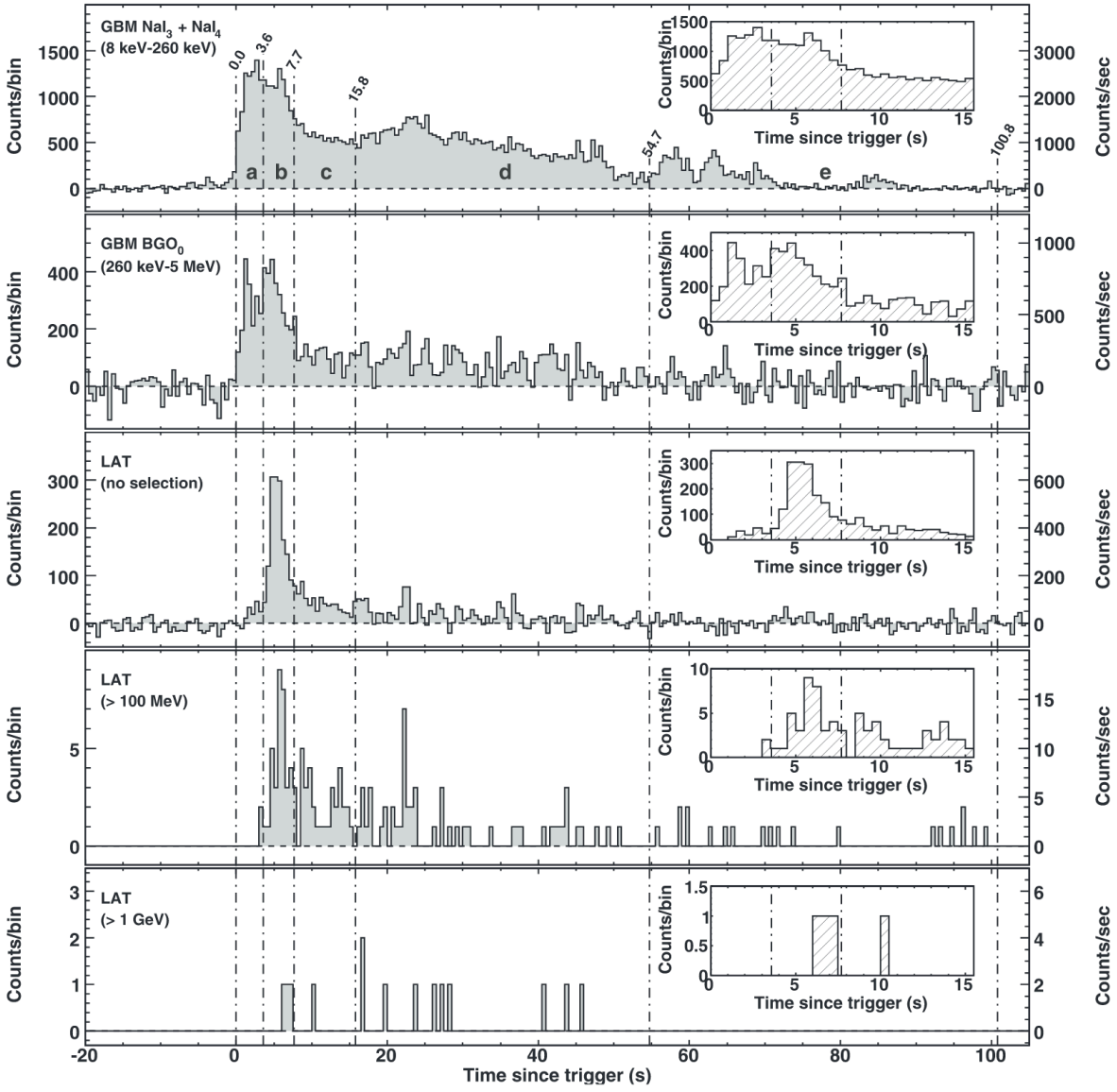

Figure 2.12: **Broadband light curve of GRB 080916C.** The five panels show the light curve in different energy bands from lowest to highest energies. Adopted from [62]

Table 2.1: **GRB detection rate of BAT, GBM, and LAT**

	Swift/BAT [64]	*Fermi*/GBM [61]	Fermi/LAT [37]
Long rate [per year]	~ 85	~ 200	$\sim$ 15–16
Short rate [per year]	~ 10	~ 40	$\sim$ 1–2
Total rate [per week]	$\sim$ 2–3	$\sim$ 4–5	< 1
Long : Short	9:1	5:1	10:1
Energy band	15–150 keV	8 keV–40 MeV	$>$ 100MeV
Field of view	2.2 sr ($\sim$ 1/6 all sky)	9.5 sr ($\sim$ 3/4 all sky)	2.4 sr ($\sim$ 1/5 all sky)

view of three detectors, *Swift*/BAT, *Fermi*/GBM, and *Fermi*/LAT.

The patterns of GRB light curves in the keV–MeV band are different from one another (Figure 2.4), which are irregular and consist of one or more pulses. However, there are several common features. Within the keV band, the spectrum tends to become softer with time [65,66]. This phenomenon is called the spectral lag. Several authors have suggested the curvature effect of the relativistic jet as a possible origin of such spectral lag [67], but this hypothesis was rejected by a simulation study [68]. Therefore, the origin of the spectral lag shown in the keV–MeV band is still in debate [69, 70]. A fraction of GRBs show the so-called precursor emission that is a weak and soft pulse well separated from the main burst [71–73]. The simplest interpretation for GRB precursors is that they are attributed to the erratic GRB central engine activities [74, 75]. Many pulses show a fast-rising exponential decay profile, which is well described by the so-called Norris function [65].

In general, the GRB spectrum is non-thermal and well described by either the Band function or a cutoff power law (CPL) (see § 4.2.2 for their functional forms). The distributions of model parameters observed in 487 GRBs detected by GBM

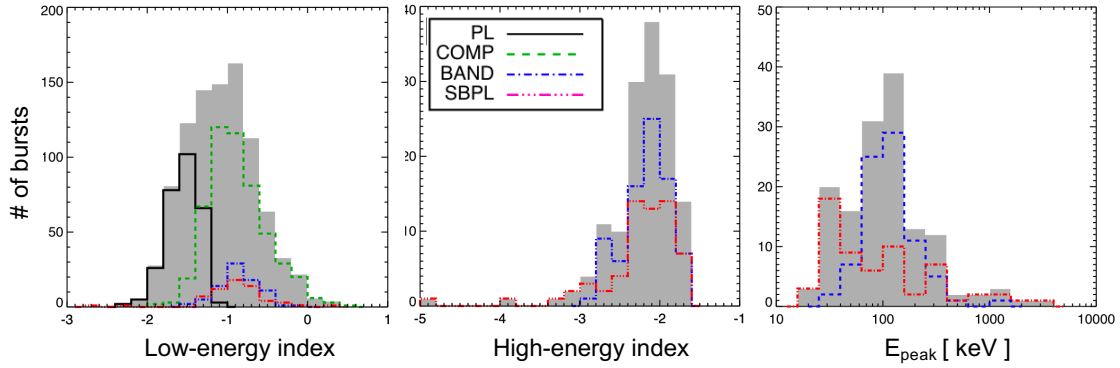

Figure 2.13: **Distribution of α, β, and E_{pk}.** PL is a power law, COMP is a power law with an exponential cutoff, BAND is the band function [8], and SBPL is a smoothly broken power law. *Left*: the distribution of the low-energy photon index α. *Middle*: the distribution of the high-energy photon index β. *Right*: the distribution of the peak energy E_{pk}. Adopted from [76]

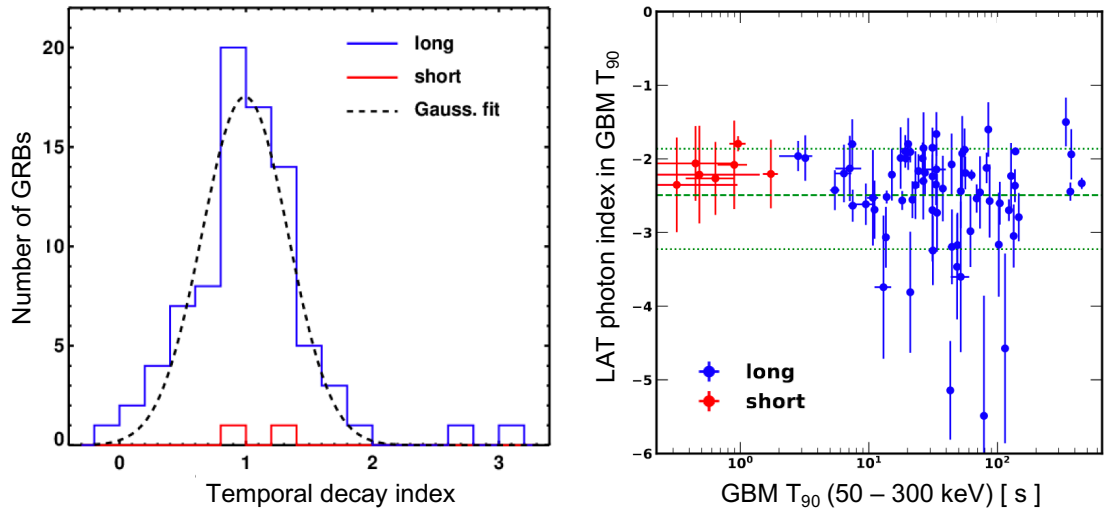

Figure 2.14: **Temporal decay index and spectral photon index of GRBs detected by LAT.** *Left*: the distribution of temporal indices ($\hat{\alpha}$) for 88 GRBs observed by LAT. *Right*: the spectral photon indices (Γ) versus GRB duration (T_{90}) for 169 GRBs. Adopted from [37]

are shown in Figure 2.13; the low-energy spectral photon index is $\alpha \sim -1$, the high energy spectral photon index is $\beta \sim -2.1$, and the peak energy is E_{pk} ∼150–200 keV [76]. Many GRBs show $\alpha > -2/3$ [76, 77], which challenge the standard GRB framework, because the energy spectrum of the synchrotron radiation resulted from the power-law electron distribution (§ 2.2.2) has an upper limit on its spectral steepness, $\alpha \leq -2/3$ [45][7]. In some GRBs, a thermal emission, which is well described by a Planck function (black body), was observed as either a dominant component as shown in GRB 090902B [38, 78] or a sub-dominant component accompanied by a dominant non-thermal component as shown in many GRBs [40, 41, 70, 79]. An extraordinary event, GW–GRB 170817A, showed a soft thermal emission with $kT \sim 10.3$ keV followed by the main non-thermal emission [80, 81]. Dedicated studies found 13 GRBs with characteristics similar to GW–GRB 170817A [82, 83].

One well-known phenomenon is the correlation between E_{pk} and flux in individual GRB pulses. There are, in general, two types of evolution patterns: a hard-to-soft evolution and an intensity tracking evolution [84]. The hard-to-soft evolution means that E_{pk} has its maximum at the beginning of the pulse and decreases throughout the pulse. The intensity tracking evolution is that E_{pk} tracks the intensity of the pulse. Both evolution patterns can be generated in the usual synchrotron emission and its evolution in time [85].

The high-energy emission above 100 MeV shows distinct features compared to the keV–MeV emission. The high-energy emission (> 100 MeV) shows a delayed

[7] This limit is derived from the synchrotron spectrum from a single electron (Equation 2.8). Note that α of -2/3 is equivalent to $\hat{\beta}$ of -1/3 in the convention of $F_\nu \propto \nu^{-\hat{\beta}}$.

onset compared to that of the keV–MeV emission (see Figure 2.12)[8]. Also, the high-energy emission (> 100 MeV) lasts longer than the keV–MeV emission, which is usually called the "GeV extended emission" [37]. In contrast to complicated keV–MeV light curves, light curves of the GeV extended emission are, in general, simple and well described by a power law with the temporal index $\hat{\alpha} \sim 1.0$ in the convention of $F_\nu \propto t^{-\hat{\alpha}}$ (left panel of Figure 2.14) [36, 37]. The spectral photon index for the high-energy energy band (> 100 MeV) is $\Gamma \sim -2.5$ (right panel in Figure 2.14), which is consistent with β fitted from keV–MeV emission (middle panel in Figure 2.13). However, the high-energy spectrum (> 100 MeV) is, sometimes, not explained by the extrapolation of the spectrum of the keV–MeV band, and an additional spectral component, usually shaped by a power law, is required to explain the observed high-energy emission successfully [39, 60, 62, 69].

Many empirical correlations among observational parameters have been established. Here, some of them are introduced. The Amati relation refers to a correlation between the GRB bolometric isotropic-equivalent energy, $E_{\rm iso}$, and the rest-frame peak energy, $E_{pk,z} = (1+z)E_{pk}$ [86] (Figure 2.15),

$$E_{pk,z} \propto {E_{\rm iso}}^{0.49^{+0.06}_{-0.05}}. \tag{2.26}$$

A similar relation is the Yonetoku relation, which is a correlation between the

[8] This high-energy delayed onset is thought to be irrelevant to the spectral lag of the keV–MeV emission [36, 37].

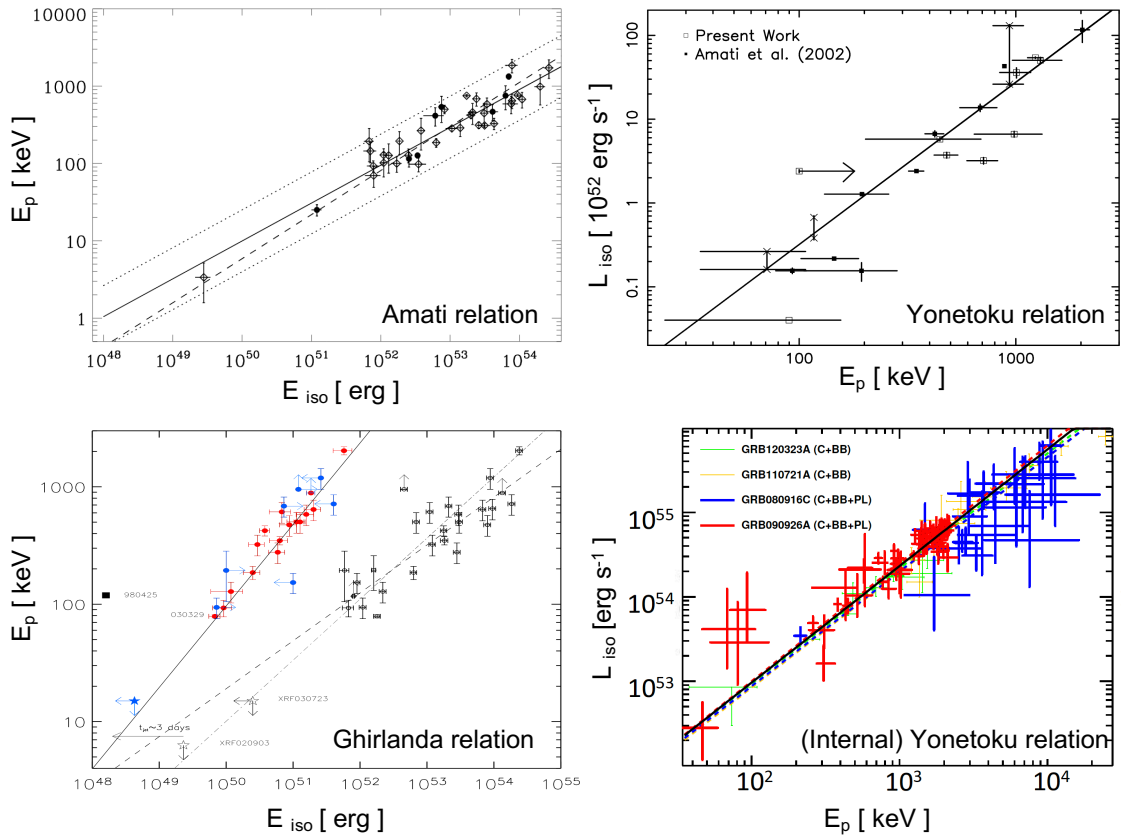

Figure 2.15: **GRB empirical correlations: Amati, Yonetoku, Ghirlanda relations.** *Top left*: Amati relation [86]. *Top right*: Yonetoku relation [87]. *Bottom left*: Ghirlanda relation [88]. *Bottom right*: Yonetoku relation within the same burst [89]

GRB isotropic peak luminosity, $L_{p,\mathrm{iso}}$, and $E_{pk,z}$ [87],

$$L_{\mathrm{iso}} \propto {E_{pk,z}}^{1.94\pm0.19}. \tag{2.27}$$

The Ghirlanda relation is a correlation between the "beaming-corrected" bolometric energy (Equation 2.36), and $E_{pk,z}$ [88],

$$E_{pk,z} \propto {E_{\gamma}}^{0.71\pm0.05}. \tag{2.28}$$

Since these relations are not physically motivated, the origins of them are under debate. Several groups argue that these relations results from an observational selection effect [90, 91]. Since current γ-ray detectors are less sensitive to E_{pk} lower than few keV and to low $E_{\rm iso}$ GRBs, it is possible that a large number of low $E_{pk,z}$–high $E_{\rm iso}$ GRBs or high $E_{pk,z}$–low $E_{\rm iso}$ GRBs may be undetected and omitted in these relations [90, 91]. Some groups found that these relations exist "internally" within the same burst [70, 84, 89, 92, 93]. For example, the Yonetoku relation within the same burst becomes [89]

$$L_{\rm iso}^{\rm NT} \propto {E_{pk,z}^{\rm NT}}^{1.38\pm0.04}, \tag{2.29}$$

where "NT" indicates that the parameters are estimated only from non-thermal spectral components.

2.3.2 Afterglow

The afterglow phase of a GRB is defined as the temporal phase after the end of the prompt keV–MeV emission. The afterglow is observed in the broad energy band from radio to X-ray (Figure 2.16 and Figure 2.17).

Through the use of numerous observations of GRB afterglows, a canonical X-ray afterglow picture has emerged [31, 32]. In general, the GRB afterglow light curve consists of five components: steep decay, shallow decay (or plateau), normal decay, post-jet-break decay, and flares (Figure 2.7):

- The steep decay phase is interpreted as the tail of the prompt emission, which is

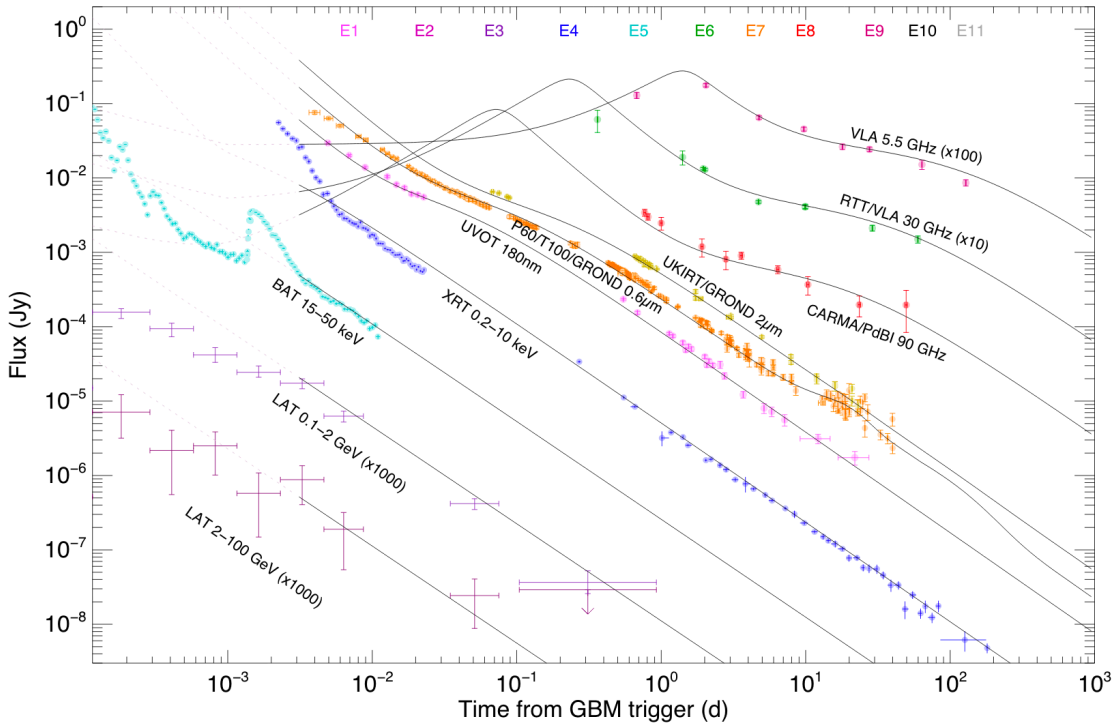

Figure 2.16: **Broadband afterglow light curves of GRB 130427A from radio to γ-ray.** Adopted from [94].

dominated by the high-latitude emission (HLE), emission from higher latitude relative to the observer's line of sight (§ 2.4.2.1).

- The shallow decay or plateau is usually observed in the X-ray energy band, and has a slope from 0 to ~ -0.7. This phase can be attributed to either internal or external dissipation [31].

- The normal decay phase is well explained by the external forward shock model (§ 2.4.7). The light curves and corresponding spectra during this phase are well described by a series of broken power laws or smoothly broken power laws [95, 96]; see Figure 2.16 and Figure 2.17 in the X-ray energy band or above[9]. The

[9]In early phase, observed emission below the X-ray energy band is dominated by the reverse shock emission

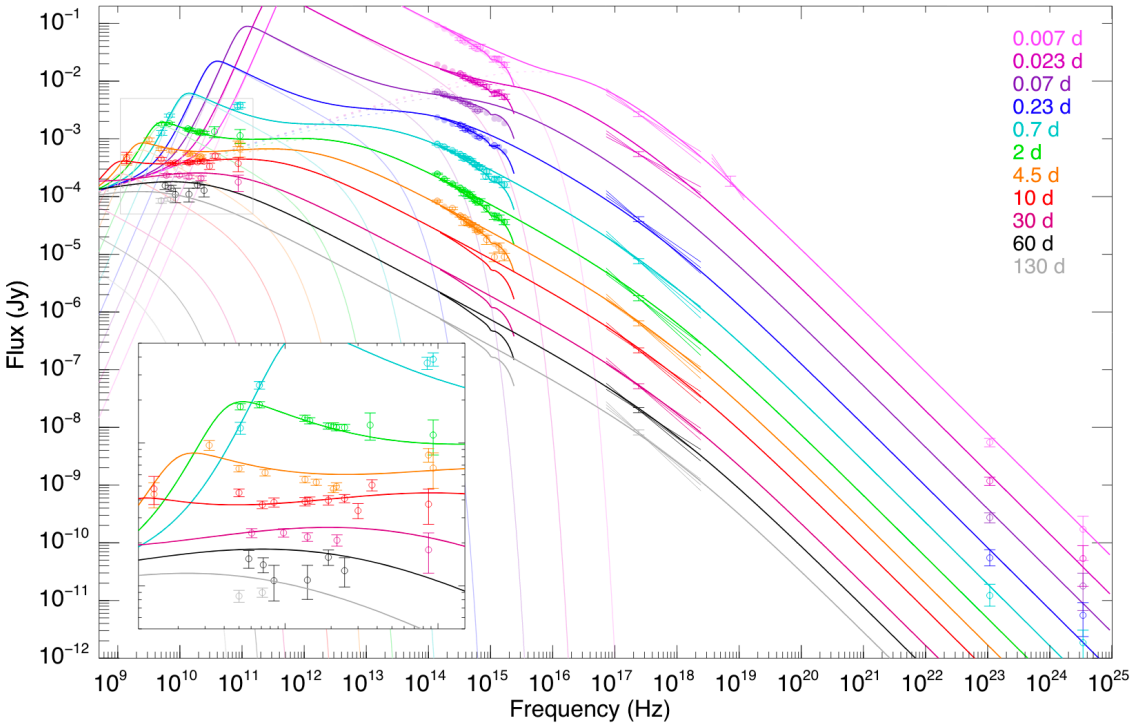

Figure 2.17: **Broadband afterglow spectra of GRB 130427A from radio to γ-ray.** The afterglow spectra for different epochs are overplotted, which are from 0.007 day (10 min) to 130 days after the trigger. Adopted from [94].

characteristics of the light curve and spectrum of the GeV extended emission are similar to those of the X-ray energy band during the normal phase (§ 2.3.1). The analogy between the GeV extended emission and the canonical X-ray afterglow leads to interpretation of the GeV extended emission as emission from the external forward shock [37, 97].

- During the afterglow phase, bright flares above an underlying emission have been observed. Nearly half of *Swift* GRBs show X-ray flares [98], and optical and radio flares have been rarely observed [99–101]. The X-ray flares have been explained as a result of the late-time activities of the central engine [31,98,102]. The steep decay of the X-ray flares is regarded as the HLE (§ 2.4.2.1) [98,103].

Several authors argue that X-ray flares, sometimes, decay faster than the HLE prediction, implying the need of the bulk acceleration[10] [104, 105].

2.3.3 Other phenomena associated with GRBs

Some long GRBs are associated with some broad-line Type Ic supernovae [27, 28, 106, 107]. This type of SNe does not show hydrogen, helium, and silicon absorption lines [108], and they are generated from core collapses of massive stars [109]. The first association was identified when SN 1998bw was observed shortly after the observation of GRB 980425 [27], and many SN–GRB observations have been followed [107, 110–112]. A SN light curve generally shows a peak at $\sim$ 1-2 weeks after a burst. Sometimes, the signature of a SN is observed as a bump in the optical afterglow light curve (Figure 2.6) [29, 106]. This clear association implies that the progenitor of long GRBs are core collapses of massive stars.

Another GRB associated phenomenon is a gravitational wave (GW) [42, 43]. GWs are "ripples" in space-time occurring when massive accelerating objects disturb space-time and generate time variations of the mass quadrupole moment. The first "direct" detection of a GW was made in 2015 by the LIGO team [113][11] [114]. Two years later, GW 170817 from the binary NS merger was observed, followed by GRB 170817A with a delay of 1.7 s (Figure 2.8) [42, 43]. This milestone confirmed that at least some of short GRBs are powered by NS–NS mergers. Interestingly, a bright kilonova, which is an optical transient event fainter than SNe, was also

[10] If an outflow is accelerated at the expense of internal energy, the HLE relation changes (Equation 2.41)

[11] GWs were "indirectly" detected from the observation of the change in the binary orbit

Table 2.2: **Comparison between short and long GRBs**

	Short GRBs	Long GRBs	Ref.
Duration	$T_{90} \lesssim 2$	$T_{90} \gtrsim 2$	[61]
Spectrum	On average hard	On average soft	[120]
E_{pk}	On average high	On average low	[120]
$E_{\rm iso}$	On average low	On average high	[37, 76]
Progenitor	Compact stars	Massive stars	[16, 19]
SN association	No	Yes	[27]
GW association	Yes	No	[42]
Density profile	Usually ISM	Wind or ISM	[121]
Host galaxy	Elliptical galaxies	Star forming galaxies	[122, 123]
Offset[a]	On average large	On average small	[124]
Redshift	On average low ($z \lesssim 1$)	On average high ($z \sim 2$)	[125]

[a] from the center of a host galaxy

observed at the position of GW–GRB 170817A [115]. The mechanism of a kilonova is attributed to rapid neutron-capture process and radioactive decay of the synthesized heavy elements [116, 117].

A possible phenomenon associated with GRBs is the high-energy neutrino, which has not been observed yet [118]. In a GRB outflow, it is possible that the protons are accelerated, and, then, interact with photons, resulting in the $p\gamma$ interaction (§ 2.2.5). From this interaction, three types of neutrinos can be produced, ν_e, ν_μ, and $\bar{\nu_\mu}$. Depending on the detail of the representative GRB models (§ 2.4.4, § 2.4.5, and § 2.4.6), each model yields different neutrino flux levels (Figure 2.18) [118, 119]. Non-detection of such high-energy neutrinos may constrain the GRB models and their parameters.

Table 2.2 summarizes the observational properties of GRBs. Some properties are not discussed in this chapter (and in this thesis). For them, see the references.

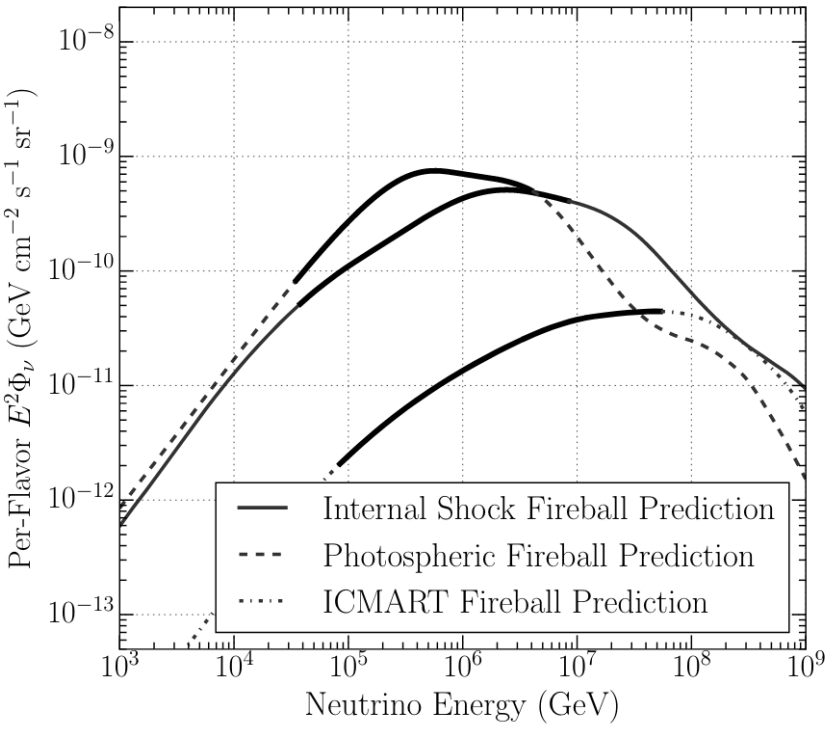

Figure 2.18: **Neutrino flux predictions for three GRB models.** The solid segments indicate the central 90% energies of neutrinos that could be detected by IceCube. Adopted from [118].

2.4 The Physics of Gamma-ray Bursts

A γ-ray burst is believed to be attributed to an outgoing relativistic, collimated jet, in which irregular activities of the central engine result in internal shocks (collisions between outflows), and the outflow later interacts with the circumburst medium invoking the external shock (the standard fireball model; Figure 2.19). In this section, I summarize the physics and leading models of GRBs by referring to excellent review articles [46, 126–128].

2.4.1 Compactness Problem

GRBs are the most powerful electromagnetic events that are extremely bright with high-energy photons, highly variable, and non-thermal emission. Observing these properties from a single source gives rise to an inevitable question: how observed high-energy photons above the electron rest mass energy can escape from

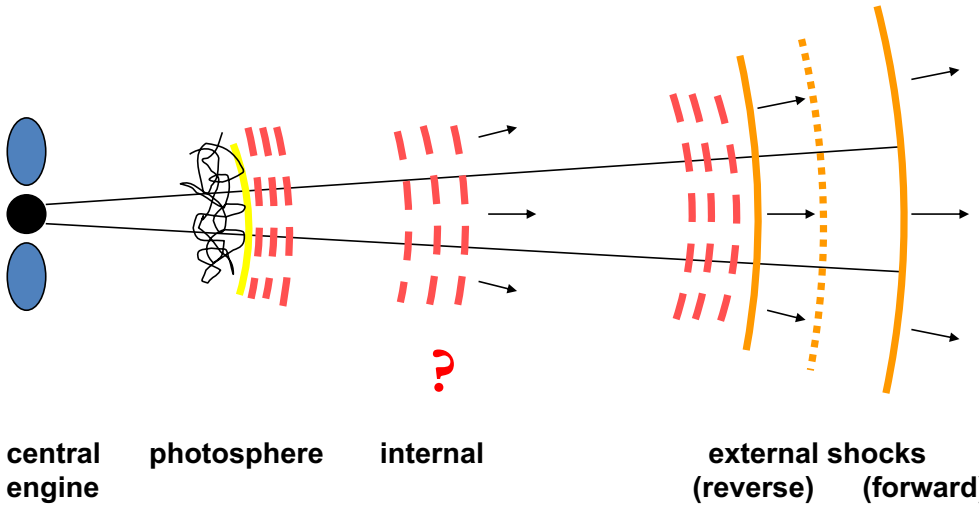

Figure 2.19: **A cartoon picture of the evolution of a GRB jet within the general theoretical framework of GRBs** [Credit: B. Zhang].

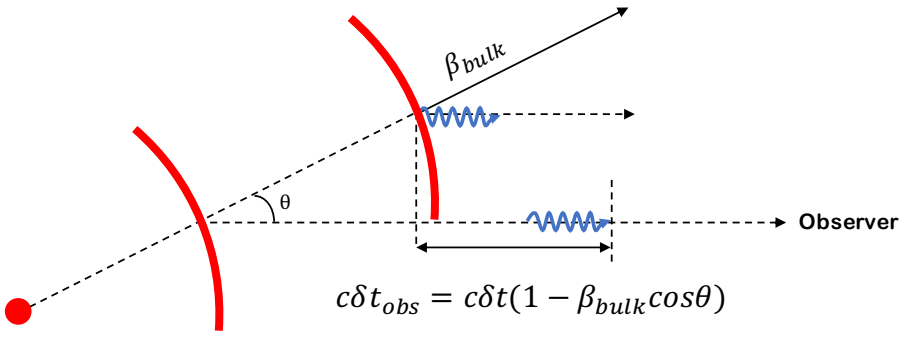

Figure 2.20: **The geometry sketch for explaining the observed temporal variability.** The source (outflow from the central engine) is moving with the Lorentz factor $\Gamma_{\rm bulk}$ at an angle θ with respect to the observer's line of sight.

the source. From the observed brightness, one can calculate the total energy release from a GRB ($E \sim 10^{51}$–10^{52} erg). Also, the highly variable light curve ($\delta \sim 10$ ms) implies that the emission region is very compact ($R \sim c\delta t \sim 3 \times 10^8$ cm). These facts imply a small and photon-dense region. In such photon-dense region, the high-energy photons can be converted into the electron-positron pair (§ 2.2.4). In order to escape from such region, it is required to have the opacity for the high-energy photons less than unity. With typical values of the energetics, the variability, and the luminosity distance, one can estimate the optical depth [126],

$$\tau_{\gamma\gamma} \sim \sigma_{\rm T} f_{\gamma\gamma} n R \sim \sigma_{\rm T} \left(\frac{f_{\gamma\gamma} 4\pi D^2 F}{E_\gamma c^3 \delta t^2} \right) (c\delta t) = \frac{f_{\gamma\gamma} \sigma_{\rm T} 4\pi D^2 F}{E_\gamma c^2 \delta t} \approx 10^{15} \gg 1, \qquad (2.30)$$

where $f_{\gamma\gamma}$ is the fraction of photon pairs above the pair production threshold, F is an observed flux, E_γ is a targeted photon energy, D is a distance to a source, and δt is a minimum variability time scale. This calculation implies that no MeV photons can escape from the source, which is contradictory to observations, the so-called compactness problems. This problem can be easily resolved by introducing a relativistic bulk motion.

2.4.2 Relativistic Jet

How can relativistic bulk motion alleviate the compactness problem? First of all, let's consider the size of the emission region R. In the non-relativistic case, the radius can be simply approximated as $R \sim c\,\delta t$. However, if a source moves with a Lorentz factor $\Gamma_{\rm bulk}$, the size of the emission region should be corrected by multiplying a factor $2\Gamma^2_{\rm bulk}$. Figure 2.20 shows the geometry of a moving source at speed $\beta_{\rm bulk}$. Since the source is moving, photons emitted at later time start to travel from the closer distance to an observer,

$$c\delta t_{\rm obs} = c\delta t(1-\beta_{\rm bulk}\cos\theta) \simeq \frac{c\delta t}{2\Gamma^2_{\rm bulk}}, \quad \rightarrow \quad R \sim 2\Gamma^2_{\rm bulk} c\delta t_{\rm obs}, \tag{2.31}$$

where the last equality is valid when $\Gamma_{\rm bulk} \gg 1$ and $\cos\theta \approx 1$.

Secondly, observed photons have been blue shifted by a factor $\Gamma_{\rm bulk}$; for $\Gamma_{\rm bulk} \sim 100$, the observed γ-ray photons can be the hard X-ray photons in the comoving frame,

$$h\nu_{\rm obs} = \Gamma_{\rm bulk} h\nu. \tag{2.32}$$

This implies that the threshold of the pair production in the observer frame should be shifted to $\Gamma_{\rm bulk} m_e c^2$, resulting in the decrease of the fraction of the photons above the pair production threshold. For a power-law energy spectrum of observed photons, $F_\nu \propto \nu^{-\hat{\beta}}$, the fraction of photons above the pair production threshold is decreased by a factor $\Gamma^{-2\hat{\beta}}_{\rm bulk}$, $f_{\gamma\gamma} \rightarrow f_{\gamma\gamma}\Gamma^{-2\hat{\beta}}$. Combining these two corrections, the

optical depth is greatly reduced,

$$\tau_{\mathrm{rel},\gamma\gamma} \propto f_{\gamma\gamma} R^{-2} \sim \frac{\tau_{\mathrm{non-rel},\gamma\gamma}}{\Gamma_{\mathrm{bulk}}^{2\hat{\beta}+4}}. \tag{2.33}$$

Assuming $\hat{\beta} \sim 1.2$, the required Lorentz factor is $\gtrsim 100$ to be optically thin ($\tau_{\gamma\gamma} \sim 1$).

Let's consider other relativistic effects. When an emission source with Γ_{bulk} emits isotropically in the comoving frame, the emission is beamed and seen within a small cone in the observer frame, the relativistic beaming (aberration of light; Figure 2.21). The size of the cone (the opening angle) can be described as a function of Γ_{bulk}. The half opening angle for an observer on Earth is written as

$$\tan\left(\frac{\theta}{2}\right) = \frac{\sin\theta}{1+\cos\theta} = \frac{\frac{\sin\theta'}{\Gamma_{\mathrm{bulk}}(1+\beta_{\mathrm{bulk}}\cos\theta')}}{1+\frac{\cos\theta'+\beta_{\mathrm{bulk}}}{1+\beta_{\mathrm{bulk}}\cos\theta'}} = \frac{1}{\Gamma_{\mathrm{bulk}}(1+\beta_{\mathrm{bulk}})}\tan\left(\frac{\theta'}{2}\right), \tag{2.34}$$

where θ and θ' are the opening angle in the observer frame and the comoving frame,

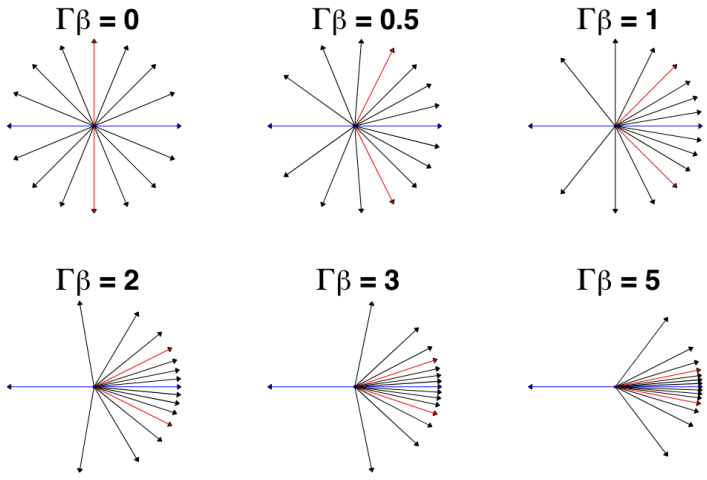

Figure 2.21: **Relativistic beaming.** Half of the photons is within an angle of $1/\Gamma_{\mathrm{bulk}}$ around the sources direction of motion. Adopted from [129]

respectively. Since the emission source emits isotropically in the comoving frame ($\theta' = \pi/2$) and moves relativistically with $\Gamma_{\rm bulk} \gg 1$ ($\beta_{\rm bulk} \approx 1$), Equation 2.34 reduces to

$$\theta \sim 1/\Gamma_{\rm bulk}. \tag{2.35}$$

Therefore, photons emitted at any direction or point on the relativistic jet are beamed and seen within a $1/\Gamma_{\rm bulk}$ cone by an observer on Earth.

It had been suggested that if the jet is not spherical but collimated within an angle θ_j, a sharp transition in the afterglow light curve can happen at a certain point [130, 131]. The argument follows. During the afterglow phase, as an outflow sweeps up the surrounding material, $\Gamma_{\rm bulk}$ is decreasing continuously (§ 2.4.7), and, thus, a $1/\Gamma_{\rm bulk}$ cone is getting wider. When the size of the cone starts to be wider than a certain cone (θ_j), the observer, from then on, sees the entire GRB jet, resulting in a sudden change in the decay rate in the flux. This feature, the so-called jet break, has been indeed observed in many afterglow light curves [132]. Now, a relativistic jet of GRBs is believed to be collimated with an opening angle $\theta_j \sim$ few degrees. This collimation reduces the total eneretics of GRBs by a factor of $f_b = (1 - \cos\theta_j)$ [133–135], which is called a beaming correction,

$$E_\gamma = f_b E_{\rm iso} = (1 - \cos\theta_j) E_{\rm iso} \tag{2.36}$$

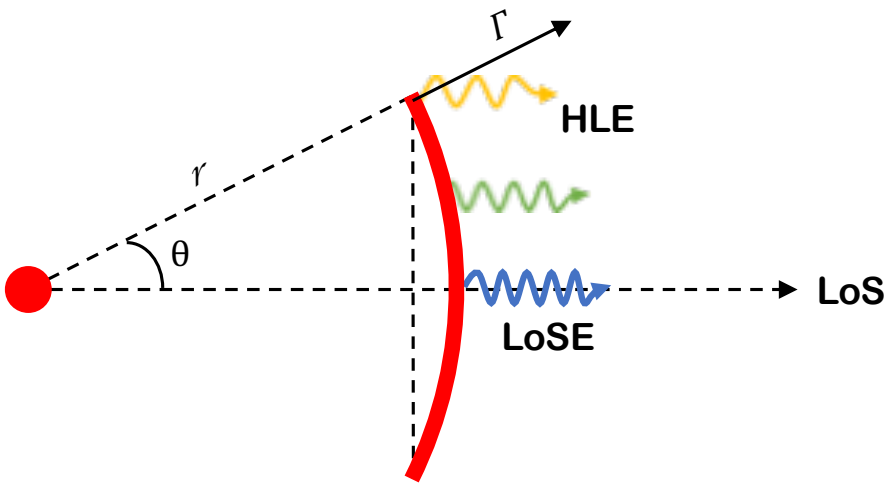

Figure 2.22: **The geometry sketch for explaining the curvature effect.** LoSE and HLE stand for the Line-of-Sight (LoS) Emission and High Latitude Emission, respectively. The shell expands with a Lorentz factor $\Gamma_{\rm bulk}$.

2.4.2.1 Curvature Effect - High-Latitude Emission

One interesting relativistic effect is the curvature effect. If an emission source turns off abruptly, a far away observer sees not only emission coming from the line of sight (LoS), but also emission from higher latitudes, the so-called high-latitude emission (HLE) (Figure 2.22). [136]. Equation 2.31 implies that a photon emitted from a relativistic shell ($\beta_{\rm bulk}$) at a certain position (r, θ) arrives at the observer with a time delay with respect to a photon emitted from $r = 0$ [136],

$$t_{\rm obs} = t(1 - \beta_{\rm bulk} \cos\theta). \tag{2.37}$$

For a fixed radius ($r = R$), a time delay of a high-latitude photon with respect to a photon emitted from the line of sight ($\theta = 0$) can be given by [136]

$$\Delta t_{\rm obs} = t_\theta - t_{\theta=0} = \frac{R}{c}(1 - \cos\theta), \quad \text{and} \quad R \simeq 2\Gamma^2_{\rm bulk} c \Delta t_{\rm obs}, \tag{2.38}$$

where $1 - \cos\theta \simeq 1/(2\Gamma^2_{\rm bulk})$ (Equation 2.35). This implies that photons from higher latitudes with respect to the LoS arrive at progressively later. Also, photons from an angle θ are boosted by the Doppler factor [136],

$$\nu = \mathcal{D}\nu' = \frac{\nu'}{\Gamma_{\rm bulk}(1 - \beta_{\rm bulk}\cos\theta)}. \tag{2.39}$$

Note that the LoSE ($\theta = 0$) is boosted by $2\Gamma_{\rm bulk}$.

The flux density is proportional to the integral of the specific intensity over the solid angle of the source [136],

$$F_\nu(\nu) \propto \int d\theta \sin(\theta) I'_{\nu'} \mathcal{D}^3, \tag{2.40}$$

where $I'_{\nu'}$ is the specific intensity in the comoving frame at radius r. Assuming a power-law spectrum for the intrinsic specific intensity, $I'_{\nu'} = I' {\nu'}^{-\hat{\beta}}$, the flux density becomes [128, 136]

$$F_\nu(\nu) \propto \int d\theta {\nu'}^{-\hat{\beta}} \mathcal{D}^3 \propto \nu^{-\hat{\beta}} \int d\theta \mathcal{D}^{(3+\hat{\beta})} \propto \nu^{-\hat{\beta}} \mathcal{D}^{(2+\hat{\beta})} \propto \nu^{-\hat{\beta}} t^{-(2+\hat{\beta})}{}^{12}. \tag{2.41}$$

[12] From Equation 2.37 and Equation 2.39, $t \propto \mathcal{D}^{-1}$

For a more precise and generalized derivation, see references [128, 136, 137].

Equation 2.41 gives the famous HLE relation between $\hat{\alpha}$ and $\hat{\beta}$ in the convention of $F_\nu \propto \nu^{-\hat{\beta}} t^{-\hat{\alpha}}$,

$$\hat{\alpha} = 2 + \hat{\beta} \tag{2.42}$$

When a characteristic frequency and its flux density are dominated by HLE and fixed in the comoving frame, they are observed to evolve in a certain way. Specifically, the peak frequency (ν_p) and the flux density at the peak frequency (F_{ν_p}) can be described as a function of time, and they are related[13],

$$\nu_p \propto t^{-1} \quad \text{and} \quad F_{\nu_p} \propto t^{-2}, \quad \rightarrow \quad F_{\nu_p} \propto \nu_p^2. \tag{2.43}$$

2.4.3 Progenitor and Central Engine

Early observational results of GRBs showed that GRBs are related to catastrophic, astrophysical events with γ-ray energy of $10^{49} - 10^{52}$ erg. In the late '90s, the association between long GRBs and Type Ic SNe was found, invoking deaths (collapses) of massive stars (§ 2.3.3) [27–29, 107]. Recently, GW-GRB 170817A confirmed that some short GRBs are attributed to mergers of two compact objects such as a neutron star (NS) and a NS, or a NS and black hole(BH) (§ 2.3.3) [42,43]. These observational results suggest, at least, two categories for the progenitor of GRBs.

After the end of the progenitor system, a central engine is formed to power a GRB relativistic jet (§ 2.4.1 and § 2.4.2). Regardless of the progenitor system,

[13] These relations can be derived by using Equation 2.39 and Equation 2.40.

the nature of the central engine is believed to be similar. The leading model for the central engine is a hyper-accreting BH [19,138,139], but a millisecond magnetar has also been proposed [140–142]. The central engine launches an outflow, which is accelerated relativistically by converting thermal energy to kinetic energy (the fireball model; § 2.4.4 and 2.4.5) or by converting magnetic energy to kinetic energy (the magnetic jet model; § 2.4.6) (Figure 2.19). Observations of X-ray flares indicate that the central engine can be re-active at a very late time [31,101,102,143,144].

2.4.4 Photosphere Model

The photosphere is defined as a outer shell from which photons can escape ($\tau_{\gamma\gamma} \approx 1$). Photospheric emission is naturally expected from the standard fireball picture [4,6,46,141,145]. A typical radius of the photosphere for GRBs is known to be $10^{10} - 10^{12}$ cm [128].

The photopheric emission is expected to be thermal, a blackbody (Planck

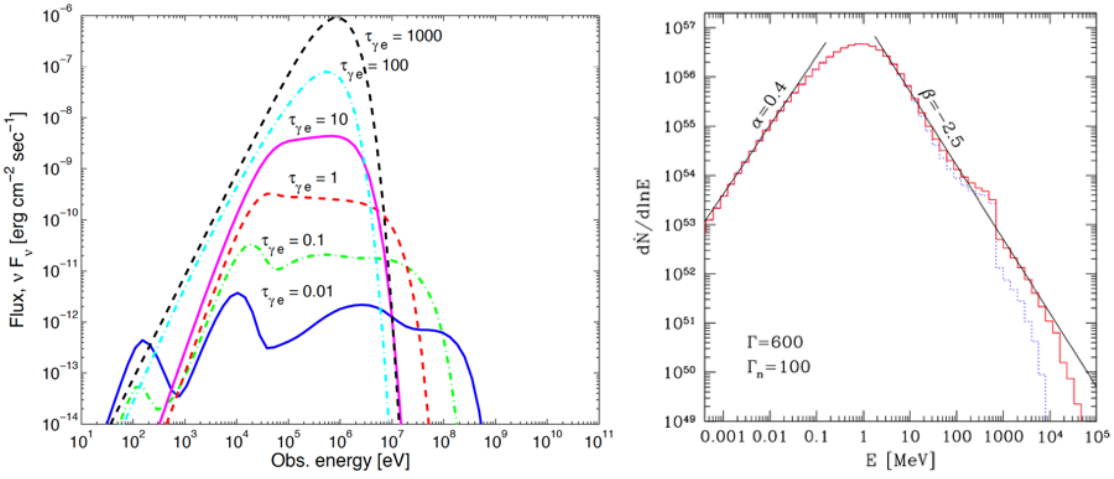

Figure 2.23: **GRB spectra expected from the photosphere.** *Left*: photon spectra obtained for different values of optical depth [146]. *Right*: quasi-thermal photon spectrum predicted in the dissipative photosphere model [147].

function) or a very hard spectrum ($F_\nu \propto \nu^{1.5-2.0}$ for the low-energy regime), if dissipation of thermal photons does not occur or occurs at a very large radius (left panel in Figure 2.23). It is possible that there are deviations in the spectrum due to various observational and geometrical effects such as the curvature effect [148, 148–152]. When significant dissipation occurs below the photosphere (Comptonization regime; $1 \lesssim \tau \lesssim 100$), the photon spectrum can be greatly altered, especially in the high-energy regime [141, 147, 153, 154]. Due to the Comptonization process, the high-energy spectrum becomes a power law in energy [146, 147] (right panel in Figure 2.23). For further details on the photospheric emission and models, see references [128, 155, 156].

2.4.5 Internal Shock Model

In an unsteady relativistic outflow, when slow outer shells are caught up by fast inner shells produced by later activities of the central engine, collisionless shocks (abrupt disturbance) occur, the so-called internal shocks [15]. The radius of the internal shocks (R_{IS}) can be estimated by considering the catch-up radius of two relativistic shells ($\Gamma_2 > \Gamma_1 \gg 1$) [53],

$$R_{\rm IS} = \beta_2 c \left(\frac{\beta_1 \Delta t}{\beta_2 - \beta_1} \right) \simeq \frac{c\Delta t}{\frac{1}{2\Gamma_1^2} - \frac{1}{2\Gamma_2^2}} \simeq 2\Gamma_1^2 c\Delta t \sim 10^{13} - 10^{14}\,{\rm cm} \tag{2.44}$$

where Δt is the launch time interval between the two shells.

This model easily explains the rapid variability observed in the GRB light curve (§ 2.3.1) [157]. The observer time, which is time when a photon (or pulse)

from an internal shock reaches the observer, can be written as,

$$t_{\rm obs} = t_{ej,1} + \frac{R_{IS}}{\beta_1 c} \simeq t_{ej,1} + \frac{R_{IS}}{2c\Gamma_1^2} \simeq t_{ej,1} + \Delta t \simeq t_{ej,2}, \tag{2.45}$$

where $t_{ej,1}$ ($t_{ej,2}$) is time when the outer (inner) shell is ejected. This implies that the observation time of each pulse is the same as each active time of the central engine; i.e., the observed light curve replicates the temporal activity of the central engine [157]. Also, the pulse width (or duration) is determined by the angular time scale defined in Equation 2.31, $\delta t = R_{\rm IS}/(2c\Gamma^2_{\rm bulk})$.

The leading radiation mechanism is synchrotron radiation (§ 2.2.2) from relativistic electrons accelerated in internal shocks (§ 2.2.1) [15]. Observed GRB spectra constrain the details of the internal shock model. First of all, only a small fraction of the fireball energy ($\eta \sim$ 1–5%) is converted to γ-rays [158–161]; i.e., internal shocks are inefficient in producing γ-rays, which is an important inherent issue in the internal shock model. The total efficiency is given by considering the dissipation efficiency[14] and the radiative efficiency[15]. Considering these two efficiencies, the total efficiency is very low compared to that of afterglow, and such low efficiency implies that the prompt emission should then be dominated by the early afterglow associated with an external shock, and the total energetics should be very high. These implications are not favored observationally and theoretically.

Another constraint of confronting this model is that a cooling frequency (ν_c) is

[14]The dissipation efficiency is conversion of kinetic energy of moving shells to internal energy of a shock, which is about 1–20% [157, 162, 163]

[15]The radiative efficiency is conversion of internal energy of a shock to observed γ-rays, which is proportional to $\epsilon_e \sim 0.1$ [164–166]

required to be very low in order to be match the observed E_p, so that a break usually seen in the GRB spectra should be regarded as the minimum injection frequency (ν_m). In this case, the asymptotic spectral index below (above) this break is expected to be $\hat{\beta} = 0.5$ ($\hat{\beta} = p/2$), which is softer than a typical GRB spectrum ($\hat{\beta} \sim 0$; § 2.3.1). Several internal shock models show that the internal shock spectrum is adjustable, and can be consistent with the observed GRB spectra [167–169]. For further details on the internal shock emission and models, see references [126–128].

2.4.6 Magnetic Jet Model

The internal shock model is based on the fireball framework, where the central engine releases energy in form of thermal energy. An alternative model for the prompt emission of GRBs is the magnetic jet model for which an outflow from the rapidly spinning central engine is dominated by the Poynting flux. The dynamic of the magnetic jet model is characterized by a magnetization parameter σ_0, which is defined as ratio between the initial Poynting flux luminosity, $L_{p,0}(t)$, and matter luminosity, $L_{m,0}(t)$,

$$\sigma_0 \equiv \frac{L_{p,0}(t)}{L_{m,0}(t)} = \frac{B'^2}{4\pi\rho' c^2} \gg 1, \tag{2.46}$$

where B' and ρ' are the magnetic field strength and the rest mass energy density, respectively, as measured in the comoving frame. In the early phase, the outflow is rapidly accelerated due to the non-zero magnetic pressure gradient, so that the bulk Lorentz factor reaches $\Gamma_{\rm bulk} \sim \sigma_0^{1/3}$ [170]. Above this point, the bulk Lorentz factor further increases as a function of radius ($\Gamma_{\rm bulk} \propto r^{1/3}$) due to magnetic dissipation

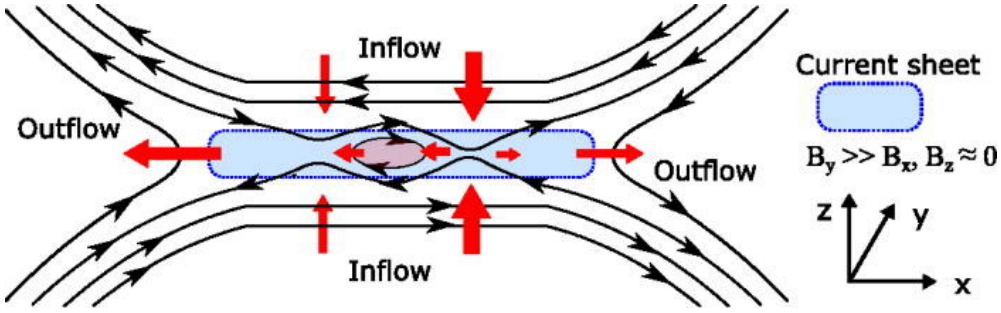

Figure 2.24: **A sketch for magnetic reconnection.** Black lines indicate a magnetic field. The pink region at the center indicates a magnetic island. The red arrows show the direction of the inflow and the outflow. Adopted from [173]

such as magnetic reconnection [171] or the magnetic pressure gradient within an expanding shell [172].

Magnetic reconnection is a reconnection of two magnetic field layers with opposite orientations approaching each other [175–178]. From this process, magnetic energy is efficiently converted to thermal or kinetic energy. Charged particles are accelerated by the electric field at the reconnection point (the so-called X-point) [179,180] or the first-order Fermi acceleration as particles are reflected back and forth between converging magnetic islands [181, 182] (Figure 2.24). Particle-in-cell (PIC) simulations show that the distribution of accelerated electrons is consistent with a non-thermal distribution [174, 182] (Figure 2.25), which can radiate by synchrotron radiation.

Many GRB models based on the magnetic dissipation are suggested [183–185]. One representative model is the Internal-Collision-induced MAgnetic Reconnection and Turbulence (ICMART) model [184]. This model describes the dynamics for a hybrid jet ($\sigma_0 \gtrsim 100$). According to this model, highly magnetized shells collide and dissipate magnetic energy in the outflow efficiently ($\eta \sim 35 - 50\%$). The emission

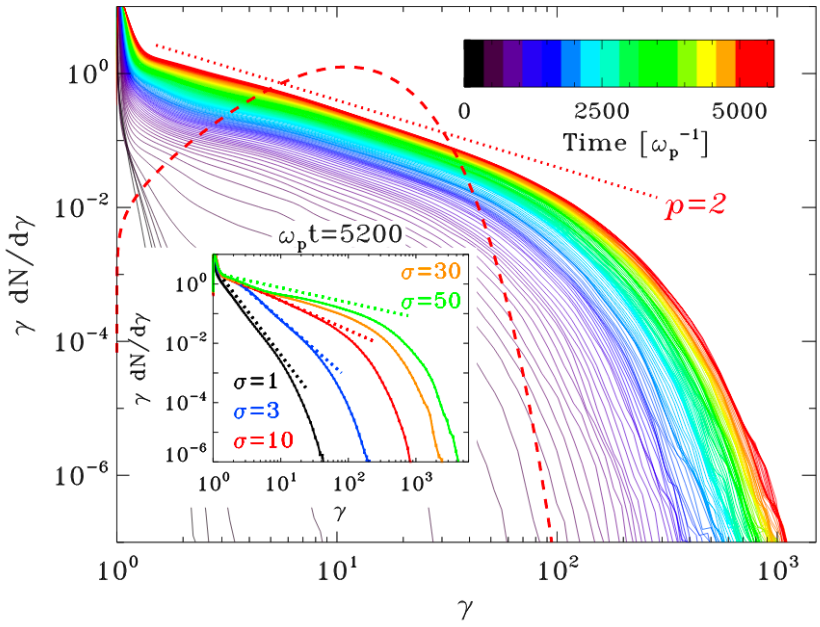

Figure 2.25: **Electron distribution accelerated by dissipation via magnetic reconnection.** Solid lines indicate temporal evolution of particle energy spectrum. A dotted red line shows the Maxwellian distribution. Adopted from [174]

radius for this model is $\sim 10^{15} - 10^{16}$ cm from the central engine, which is further away compared to the emission radius proposed by the most of the internal shock models ($R_{\rm IS} \sim 10^{13} - 10^{14}$ cm). This magnetic jet model alleviates several problems confronting the internal shock model such as low efficiency and inconsistency between the expected and observed spectral index (§ 2.4.5). For further details on the external shock emission and models, see references [128, 184].

2.4.7 External Shock Model

As a relativistic jet from the central engine sweeps up the ambient medium, the jet decelerates. In this collision, the shock environment is developed, the so-called external shock (Figure 2.26) [13]. When the mass collected from the ambient

medium is comparable to the initial mass of the GRB blastwave, the effect of the deceleration is important. The deceleration radius (R_{dec}), where the initial Lorentz factor decreases by a factor 2, is $R_{dec} \sim 10^{17}$ cm. The external shock model explains the normal decay phase of the GRB afterglow successfully (Figure 2.7) [31, 32, 186].

As shown in Figure 2.26, two shocks (forward and reverse shocks) are expected to develop. In general, the forward shock, which propagates into the circumburst medium, is responsible for the broadband afterglow (§ 2.3.2) [95, 96, 187], and the reverse shock, which propagates into the ejecta itself, is used for explaining early optical flashes [24, 188, 189]. The reverse shock is believed to fade away rapidly, but in some reverse shock models, the reverse shock is long-lived [190, 191]. Here, I focus on the forward shock model, because it is more relevant to my work.

The dynamics of the GRB blastwave can be described by a self-similar solution,

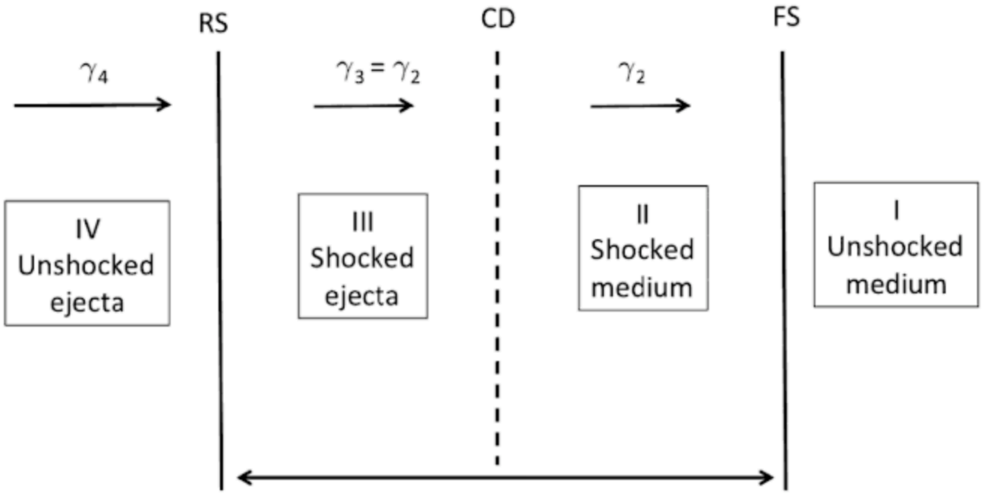

The surface between the shocked medium (III) and shocked ejecta (II) is called the contact discontinuity (CD). Adopted from [53]

Figure 2.26: **A sketch of the external shock system.** The FS and RS stand for the forward shock and the reverse shock, respectively. γ_i is the Lorentz factor of each ejecta, and p_i is the .

resulting in simple scalings [95, 96, 192]. The main radiation mechanism of the external forward shock model is synchrotron radiation (§ 2.2.2) [95, 96, 187]. In general, a medium density profile is described as a function of radius, $n(r,k) \propto r^{-k}$. In a simple model, this profile is assumed to be either uniform ($k = 0$), relevant to the interstellar medium (ISM), or a wind-like medium where density decays with the square of the radius ($k = 2$). Here I will consider these two k values for simplicity. For electrons accelerated in the shock, a minimum Lorentz factor is given by [95]

$$\gamma_m \simeq \epsilon_e \left(\frac{p-2}{p-1}\right) \frac{m_p}{m_e} \Gamma_{\rm bulk} \simeq 610 \epsilon_e \Gamma_{\rm bulk}, \quad \text{for } p > 2, \tag{2.47}$$

where ϵ_e is the fraction of internal energy that is given to electrons. The cooling frequency is given by Equation 2.10 with the magnetic field strength $B' = (32\pi m_p \epsilon_B n)^{1/2} \Gamma_{\rm bulk} c$, where ϵ_B[16] is the fraction of internal energy that goes to magnetic fields. In the adiabatic evolution of the forward shock, the energy of the blastwave (E) is constant [95, 128, 187],

$$E \sim n m_p c^2 r^3 \Gamma_{\rm bulk}^2 = \text{const} \rightarrow \begin{cases} \Gamma_{\rm bulk} \propto r^{-3/2} & \text{for ISM } (n = n_0), \\ \Gamma_{\rm bulk} \propto r^{-1/2} & \text{for wind } (n = n_0 r^{-2}), \end{cases} \tag{2.48}$$

where m_p is the mass of the proton[17]. Note that if there is a continuous energy injection into the blastwave[18], the scaling relations are changed [142, 193]. From

[16] By definition, $\epsilon_B + \epsilon_e + \epsilon_p = 1$, where ϵ_p is the fraction of internal energy that is partitioned to protons (ions).

[17] Since $m_p \gg m_e$, the total mass is approximated to the mass of protons.

[18] For example, $E \propto \int_0^t dt L(t) \propto \int_0^t dt\ t^{-q} \propto t^{1-q}$ where q is the energy injection coefficient, $q < 1$. Note that $q = 1$ refers no energy injection.

Equation 2.44,

$$t \sim \frac{r}{2\Gamma_{\rm bulk}^2 c} \propto \begin{cases} r^4 \propto \Gamma_{\rm bulk}^{-8/3} & \text{for ISM,} \\ r^2 \propto \Gamma_{\rm bulk}^4 & \text{for wind,} \end{cases} \tag{2.49}$$

Plugging Equation 2.48 and Equation 2.49 to the characteristic frequencies of synchrotron (ν_m and ν_c) gives [194]

$$\nu_m \propto \Gamma_{\rm bulk}\gamma_m^2 B' \propto t^{-3/2} \quad \text{and} \quad \nu_c \propto \Gamma_{\rm bulk}\gamma_c^2 B' \propto \begin{cases} t^{-1/2} & \text{for ISM,} \\ t^{1/2} & \text{for wind,} \end{cases} \tag{2.50}$$

where $B' \propto \Gamma_{\rm bulk}$, $\gamma_m \propto \Gamma_{\rm bulk}$, and $\gamma_c \propto \Gamma_{\rm bulk}^{-3} t^{-1}$. The specific flux at the peak of the spectrum can be written as

$$F_{\nu,\rm max} \propto P_{syn,\rm max}\, N_{\rm tot} \propto \begin{cases} \Gamma_{\rm bulk}^2 r^3 \propto t^0 & \text{for ISM,} \\ \Gamma_{\rm bulk}^2 r \propto t^{-1/2} & \text{for wind.} \end{cases} \tag{2.51}$$

The precise coefficients for each parameter can be found in a reference [194].

A light curve between or above two characteristic frequencies can be derived by combining Equation 2.15, Equation 2.50, and Equation 2.51. For example, in case of $\nu_m < \nu < \nu_c$ in wind, the specific flux ($F_\nu \propto \nu^{-\hat{\beta}} t^{-\hat{\alpha}}$) evolves

$$F_\nu \propto F_{\nu,\rm max} \left(\frac{\nu}{\nu_m}\right)^{-(p-1)/2} \propto t^{1/2} \nu^{-(p-1)/2} \nu_m^{(p-1)/2} \propto \nu^{-(p-1)/2} t^{-(3p-1)/2}. \tag{2.52}$$

Since both $\hat{\alpha}$ and $\hat{\beta}$ are a function of the electron spectral index (p), a relation

between $\hat{\alpha}$ and $\hat{\beta}$, the so-called closure relation (CR), can be specifically derived for each spectral regimes (see Table 2.3) [194]. The spectrum and corresponding light curve from the external forward shock are, therefore, described as a series of broken power laws [95], more accurately, smoothly-broken power laws [96, 195, 196] (Figure 2.28).

A large sample of observed afterglows allow to estimate micro-physical parameters such as ϵ_B, ϵ_e, and p, which are the key ingredients for determining flux and spectrum of the external forward shock at any given time (§ 2.4.7). Figure 2.27 shows the distribution of ϵ_e and ϵ_B. It is unclear that universal values exist in ϵ_e and ϵ_B. All the discussion above is valid for $p \geq 2$[19], which is the predicted range of p from both theoretical studies and numerical simulations; p has a universal value $\sim$ 2.2–2.4 [197–200]. In contrast, the observational studies found that p varies from one GRB to another, and the distribution of p forms a Gaussian function [201–204]; e.g., the p distribution of *Swift* GRB X-ray afterglows is well described by a Gaussian function centered at $p = 2.36$ and having the standard deviation of 0.59 [204]. For further details on the external shock emission and models, see references [31, 96, 194].

[19]The total energy of electrons is $\int_{E_{\rm min}}^{E_{\rm max}} EN(E)dE = (E_{\rm max}^{2-p} - E_{\rm min}^{2-p})/(2-p)$, which is divergent for $p < 2$. For $p < 2$, a cutoff in electron energy is required, which affects ν_m, and its evolution [194]

Table 2.3: **The subset of closure relations.** For the complete set, see [194]

	Condition			Closure Relation		
CR[a]	p[b]	Cooling regime	Environment	$\hat{\beta}(p)$[c]	$\hat{\alpha}(p)$[d]	$\hat{\alpha}(\hat{\beta})$
1	-	$\nu_c < \nu < \nu_m$	ISM/wind	$1/2$	$1/4$	-
2	$p > 2$	$\nu > \nu_m, \nu_c$	ISM/wind	$p/2$	$(3p-2)/4$	$(3\hat{\beta}-1)/2$
3	$p > 2$	$\nu_m < \nu < \nu_c$	ISM	$(p-1)/2$	$3(p-1)/4$	$3\hat{\beta}/2$
4	$p > 2$	$\nu_m < \nu < \nu_c$	wind	$(p-1)/2$	$(3p-1)/4$	$(3\hat{\beta}+1)/2$
5	$1 < p < 2$	$\nu > \nu_m, \nu_c$	ISM	$p/2$	$(3p+10)/16$	$(3\hat{\beta}+5)/8$
6	$1 < p < 2$	$\nu_m < \nu < \nu_c$	ISM	$(p-1)/2$	$3(p+2)/16$	$(6\hat{\beta}+9)/16$
7	$1 < p < 2$	$\nu > \nu_m, \nu_c$	wind	$p/2$	$(p+6)/8$	$(\hat{\beta}+3)/4$
8	$1 < p < 2$	$\nu_m < \nu < \nu_c$	wind	$(p-1)/2$	$(p+8)/8$	$(2\hat{\beta}+9)/8$

[a]Closure relation
[b]Electron spectral index
[c]Spectral index
[d]Temporal index

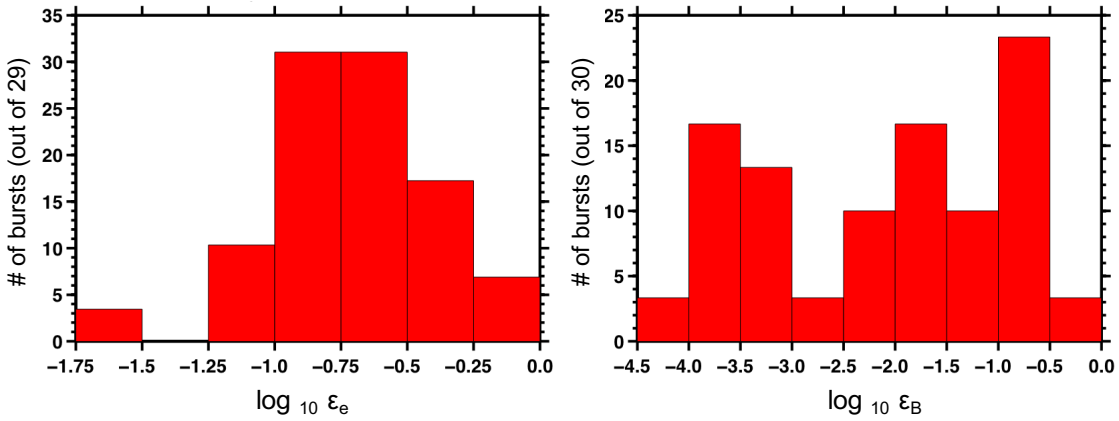

Figure 2.27: **Distribution of micro-physical parameters: ϵ_e and ϵ_B.** *Left*: the distribution of ϵ_e. The values of ϵ_e were drawn from the published literature. *Right*: the distribution of ϵ_B. The values were determined from the optical afterglow data with reasonable assumptions. Adopted from [205].

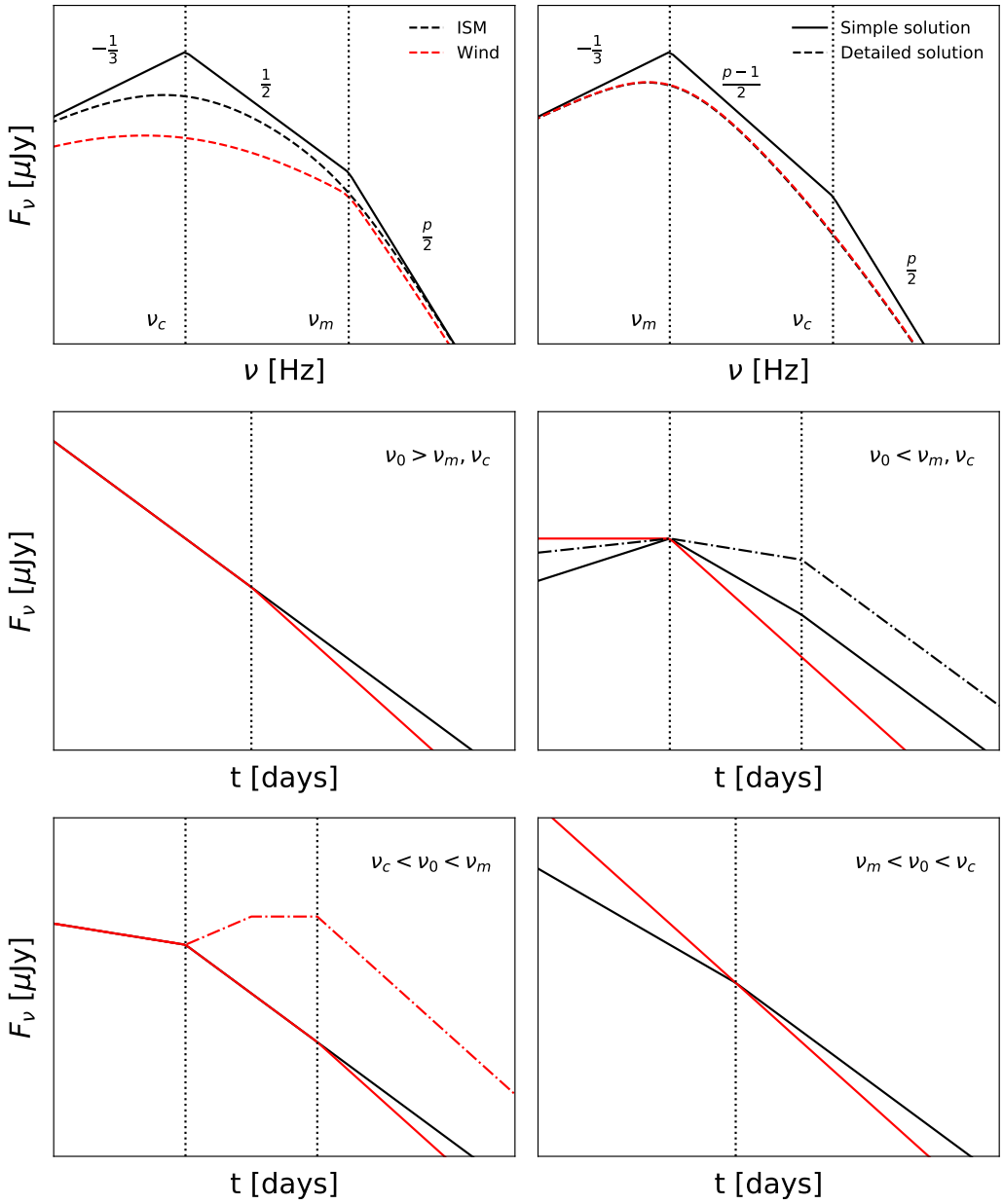

Figure 2.28: **Spectra and light curves for the external forward shock model.** *Top*: the energy spectra for the fast and slow cooling regimes. The solid (dashed) line is from the simple (detailed) analytic solutions [95, 187, 195]. The black and red indicate the ISM and wind solutions, respectively. *Middle* & *Bottom*: the light curves for different initial cooling regimes [95,187]. Since ν_m and ν_c evolve differently, there are more than one possibility even when it starts from the same cooling regime; e.g., ν_m passes a fixed frequency (ν_0) first, and then ν_c is followed. The solid (dashed) line is when ν_m (ν_c) passes first. The black and red indicate the ISM and wind solutions, respectively.

Chapter 3: The *Fermi* Gamma-ray Space Telescope

The *Fermi* Gamma-ray Space Telescope (*Fermi*) was launched on June 11, 2008 and opened a new era of the GRB research. Two scientific instruments on board *Fermi*, the Gamma-ray Burst Monitor (GBM) [34] and the Large Area Telescope (LAT) [35], cover eight orders of magnitude in energy from 8 keV to $>$ 300 GeV. Both instruments have a wide field of view (FoV); the GBM monitors the full sky unhindered by the Earth, and the LAT scans the full sky every 3 hours (2 orbits)[1]. In this chapter, I briefly describe the LAT and the GBM, and how they contribute to provide data used in a GRB analysis.

3.1 Large Area Telescope

The LAT is a pair-conversion telescope, which uses the pair conversion process[2] to measure the energy and direction of the photon through the electron and positron pair created in the detector. A pair-conversion telescope has three subsystems. A tracker converts the photon into the e^- and e^+ pair and tracks their trajectories. The trajectories are used for estimating the direction of the initial photon. A calorimeter

[1] On March 16, 2018, one of two solar arrays on the spacecraft, which power the *Fermi*, was stuck, resulting in the change of the observing strategy. See details in the Fermi Science Support Center (FSSC) webpage, `https://fermi.gsfc.nasa.gov/ssc/observations/types/post_anomaly/`.

[2] $p + \gamma \rightarrow p + e^+ + e^-$

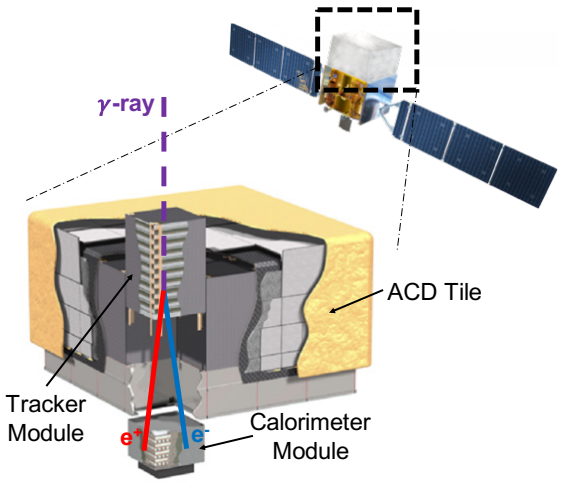

Figure 3.1: **The *Fermi* LAT and its subsystems.** An incoming γ-ray converts into an electron-positron pair in the Tracker, and, subsequently, the pair deposits their energy into the Calorimeter [35].

which measures the energy of the shower, typically with scintillators, provides a measure of the γ-ray energy. The anti-coincident detector consists of charged particle detectors, which covers the two subsystems, allowing incoming charged particles to be identified. The anti-coincident detector makes it possible to avoid being triggered by the overwhelming flux of cosmic rays.

The LAT consists of a 4 x 4 array of identical towers (Figure 3.1), and each tower comprises the two subsystems, the Tracker (TKR) [206] and the Calorimeter (CAL) [207]. The Anti-coincidence detector (ACD) covers the entire 4 x 4 array of towers. [208].

3.1.1 Tracker

The primary purpose of the TKR is to convert incoming γ-rays into electron-positron ($e^+ + e^-$) pairs and to track their paths, which are used for reconstructing

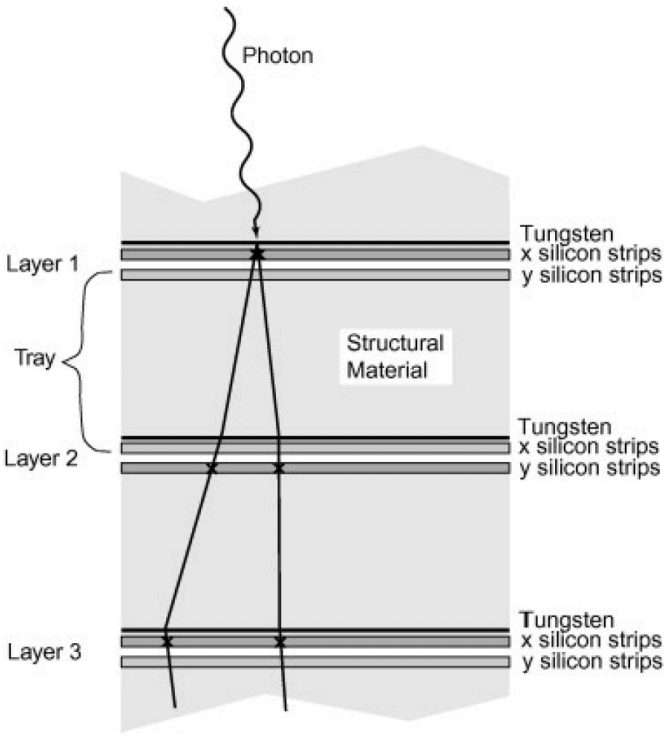

Figure 3.2: **A simplified diagram of the Tracker and its performance.** Each tungsten foil is followed with X-Y oriented SSDs, which are very close to each other. An incoming photon converts into a $e^+ + e^-$ pair, and the trajectories of the pair are detected by the successive SSDs [206].

the direction of the incoming γ-rays. The design of the TKR is intended to achieve a high conversion efficiency with a good directional resolution. Also, the TKR is designed to provide the primary trigger of the LAT instrument.

The TKR consists of 18 layers. Each of the top 16 layers has a plane of tungsten foil, which converts γ-rays into $e^+ + e^-$ pairs. This plane is immediately followed by a pair of X-Y oriented Silicon Strip Detectors (SSD), which read out the X and Y positions of the charged particles. For an ideal detector, the trajectories of the charged particles will be a straight line and the detector will measure their paths perfectly. However, in the real detector, the trajectories are deviated by the multiple Coulomb scattering in material in the detector, and charged particle positions are measured with finite accuracy. The gap between the tungsten foil and the pair of

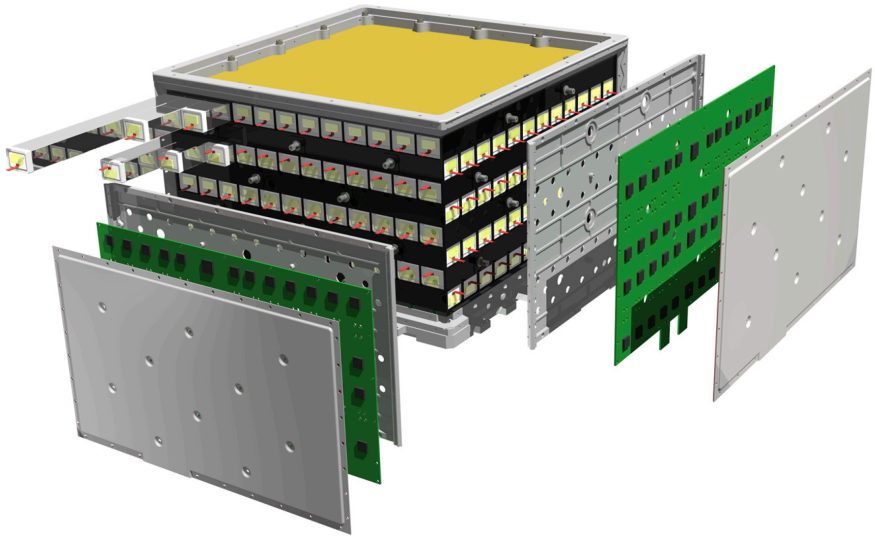

Figure 3.3: **Exploded view of a CAL module** [207].

X-Y SSDs is minimized in order to minimize the effect of multiple scattering in tungsten foil. The bottom two layers contain SSDs without tungsten foil, because the TKR trigger requires three successive hits.

Among the 16 layers of tungsten foils, the top 12 layers are made up of thin tungsten foil (0.03 X_0 for each). This design minimizes the effects of multiple scattering in the following layers of tungsten foil, and allows to get a good angular resolution for low-energy photons. For very high-energy photons, multiple scattering is unimportant, so that the last 4 layers are thick (0.18 X_0 for each) in order to increase the chance of interactions of high-energy γ-ray photons. As a result, about 63% of GeV photons at normal incidence are converted into $e^+ + e^-$ pairs.

3.1.2 Calorimeter

The primary purpose of the CAL is to measure the energy of incident γ-rays. The CAL module is positioned below the TKR module and is made up of 8 alternating orthogonal layers (Figure 3.3). Each layer has 12 thallium-activated cesium iodide, CsI(Tl), crystals; i.e., totally, 96 crystals for each module. As incident γ-rays and their secondary particles (e^+ and e^-) interact with the CsI(Tl) crystals, an electromagnetic shower is produced. Four photodiodes[3], two mounted on each side of each crystal, measure scintillation light from the crystals, which is proportional to the energy deposited in the crystal. The ratio between signals measured from two ends of a crystal can determine where the scintillation occurred along the crystal length; i.e., the three-dimensional positions of the shower are obtained. Combining all information, the CAL is able to image the electromagnetic shower profile with energy deposition and locations in individual crystals.

If energy of an incident γ-ray is fully absorbed by the CAL crystals without leakage, the true energy is given by summing up deposited energies from all crystals. However, such ideal energy measurement is not possible due to a limited size of the CAL, gaps between modules, and absorption in passive materials. Instead, the energies and locations measured by the CAL crystals are fitted with a electromagnetic shower profile, from which the γ-ray energy is estimated with a good energy resolution of $\Delta E/E < 10\%$ above 1 GeV. Since hadronic and electromagnetic shower profiles differ from each other, even for the same energy, the shower profile fit can

[3]Small and large photodiodes are for high and low energies, respectively.

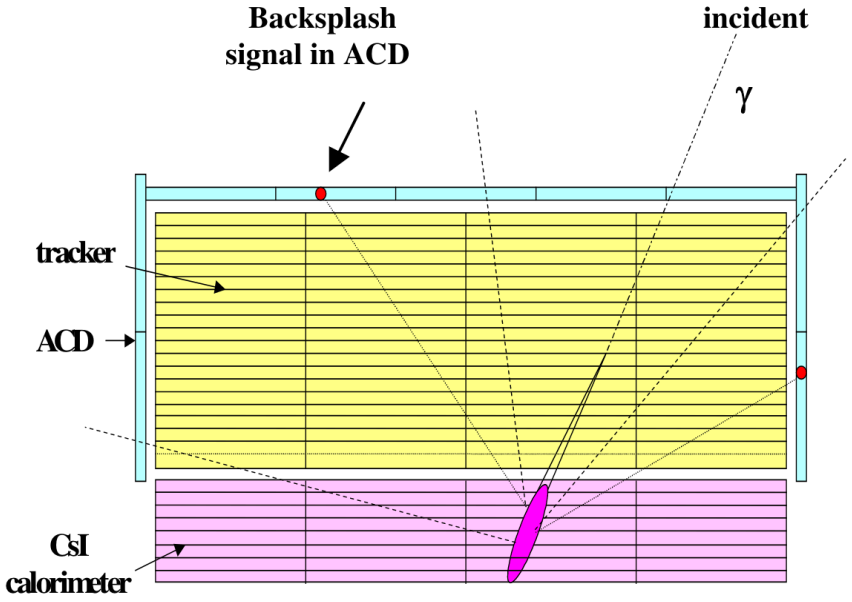

Figure 3.4: **Side view of the LAT subsystems with an example of a backsplash signal in ACD** [209].

help the background rejection.

3.1.3 Anti-coincidence Detector

The primary purpose of the ACD is to veto charged-particle backgrounds with a high efficiency. Since the flux of cosmic rays is a factor of 1000 higher than the total photon flux of all astrophysical sources, it is essential to reject triggers by cosmic rays.

The ACD covers the TKR and the CAL seamlessly with a set of 89 plastic scintillator tiles with 8 plastic scintillator ribbons to cover gaps between the tiles. The tiles and ribbons are connected to photomultiplier tubes (PMT) to detect scintillation light produced by incoming charged particles. Since γ-rays don't produce scintillation light, the ACD can distinguish γ-rays (signal) from cosmic rays (background).

For high energy events in the CAL, energy can propagate back upwards and be detected by the ACD, resulting in "false" veto (self-veto) signals. This is known as the backsplash effect (Figure 3.4), which reduces the efficiency of γ-ray detection, especially at the highest energies in the previous mission, EGRET on board *CGRO* [209]. The segmentation of the ACD alleviates this effect by ignoring veto signals from ACD segments far from the path of an incident photon.

The overall efficiency of ACD, the charged particle recognition efficiency, exceeds 99.97%[4], and the LAT can lower any residual background rate below 10% of the diffuse γ-ray background rate.

3.1.4 Event Reconstruction

All raw data measured by the LAT subsystems is processed to be converted to high level data (direction, energy, etc), which is called the event reconstruction [210]. The current version of the LAT event simulation and reconstruction software is "Pass8"[5].

When a photon enters the LAT subsystems, it converts into a sea of particles and photons, leaving signals in the LAT subsystems. Pass 8 [212] uses so-called tree-based tracking, where the conversion in the tracker is considered as the start of a shower, and the signals in the TKR and the CAL are modeled with the global approach (Figure 3.5 and Figure 3.6). The TKR hits are linked (left panel in Figure 3.5) and construct the tree-like structure (middle panel in Figure 3.5). The axis

[4]The false veto rates of the backsplash above 300 GeV and the electrical noise are $< 20\%$ and $< 1\%$, respectively.

[5]`https://fermi.gsfc.nasa.gov/ssc/data/analysis/documentation/Pass8_usage.html`

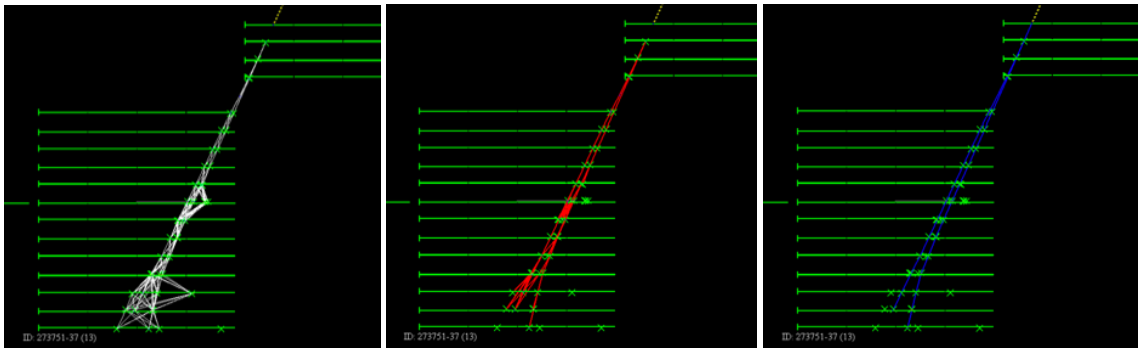

Figure 3.5: **The tree-based pattern recognition in the TKR**. *Left*: the construction of links. *Middle*: a tree is constructed attaching some of the links. *Right*: two tracks are identified inside the Tree. Adopted from [211].

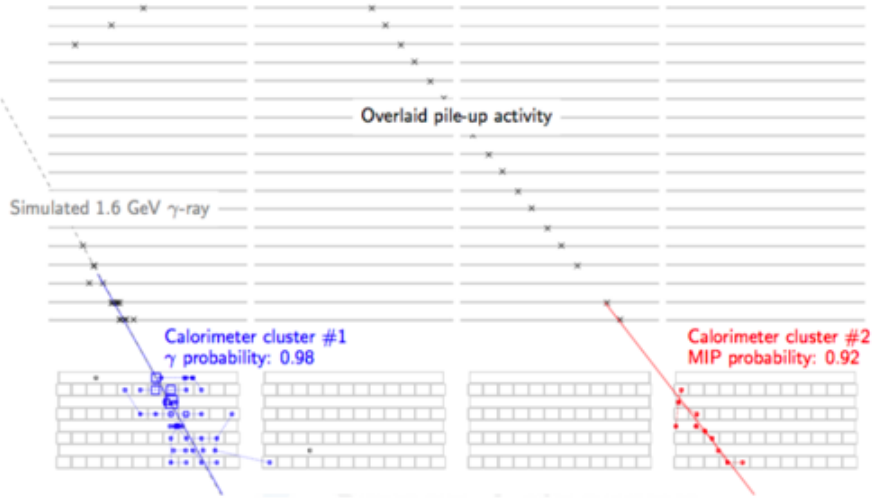

Figure 3.6: **The cluster identification in the CAL**. Adopted from [211].

of the resultant tree can be found by calculating the moments-of-inertia of the associated hits whose mass is determined as a function of the length and straightness of its branch. This axis is used for finding an associated cluster in the CAL (Figure 3.6), and the energy of this tree is estimated from this CAL cluster. Up to two tracks, longest and straightest, can be extracted and fitted with a Kalman Filter technique, which combines all the information of the tree and its branches (right panel in Figure 3.5). If more than one track is extracted, the vertex is also found,

where a pair conversion is expected to occur. The vertex, if present, generally yields the best information on the photon direction. The direction of the incoming photon is estimated by incorporating the best information about the tree, the tracks, and the vertex. The Pass 8 reconstruction estimates the energy of the photon by using a shower profile fit for the electromagnetic cascade within the CAL (§ 3.1.2). For low energies below about 1 GeV, the energy loss from the interaction in the TKR can not be ignored, and the CAL can catch the tail end of the shower initiating within the TKR. Therefore, the deposited energy in the CAL is corrected with information on the interaction in the TKR.

As a result, a large set of measurements from the TKR, the CAL, and the ACD reduces to a small set of parameters such as the direction, energy, time, and reconstruction quality. This high-level data is made available in the Flexible Image Transport System (FITS) format, provided by the Fermi Science Support Center (FSSC)[6]. Parameters and their definitions, frequently used for GRB analysis, are listed in Table 3.1 (see Figure 3.7 for the definition of angles).

3.1.5 Event Classification

Each photon is classified based on its probability of how sure the event is a photon as opposed to cosmic-ray background[7] [210,213]. The standard event classes are "`Transient`", "`Source`". "`Clean`", and "`Ultraclean`", in order of increasing probability[8]. The structure of the classification is similar to *Russian dolls* (stacking

[6] `https://fermi.gsfc.nasa.gov/cgi-bin/ssc/LAT/LATDataQuery.cgi`
[7] Note that this is not related to DATA_QUAL.
[8] For the detail of the selection criteria, see the references [210,213].

Table 3.1: **Frequently used parameters in publicly available LAT data**

Parameter	Definition	Unit
	Photon information	
ENERGY	Reconstructed energy of the event	MeV
RA	Reconstructed right ascension (J2000[a]) of the event	degree
DEC	Reconstructed declination (J2000) of the event	degree
THETA (θ)	Inclination angle of the event with respect to the LAT boresight	degree
PHI (ϕ)	Azimuthal angle of event with respect to the LAT boresight	degree
ZENITH_ANGLE(θ_z)	Angle between the reconstructed event direction and the zenith line	degree
TIME	Mission Elapsed Time (MET)[b] when the event was detected	second
	Spacecraft information	
LAT_MODE	Spacecraft mode[c]	
LAT_CONFIG	The configuration of the LAT[d]	
DATA_QUAL	The quality of the LAT data[e]	

[a]Equatorial coordinates in the 2000 frames.
[b]MET is defined as the total number of seconds since Jan. 1, 2001 (UTC)
[c]Three nominal modes: inertial point (3), maneuver (4), and survey (5). The other modes are not used for normal science.
[d]When LAT_CONFIG=1, it can be used for normal science.
[e]When DATA_QUAL=1, it can be used for normal science.

dolls); i.e., the `Transient` event class contains all events assigned to the more stringent event classes such as the `Source`. For the standard source analysis, the `Source` event class is recommended. For the analysis of transient events such as GRBs, the `Transient` event class can be used to benefit from increased photon statistics at the expense of a higher background fraction and broader Point Spread Function [9].

In addition, events in the same event class are subdivided into event types depending on the quality of the energy and direction reconstruction. There are three event type partitions[10]: where the pair conversion occurred in the TKR (thin layer or thick layer), the quality of energy dispersion (EDISP)[11], and the quality of the PSF. For the transient analysis, it is generally not necessary to select specific event types; i.e., all events assigned to the `Transient` event class are used.

[9]The probability distribution of the 2-dimensional direction.
[10]Later two event type partitions are newly introduced in Pass 8 [213].
[11]The probability distribution of the energy deviation between the reconstructed energy and the true energy of the event

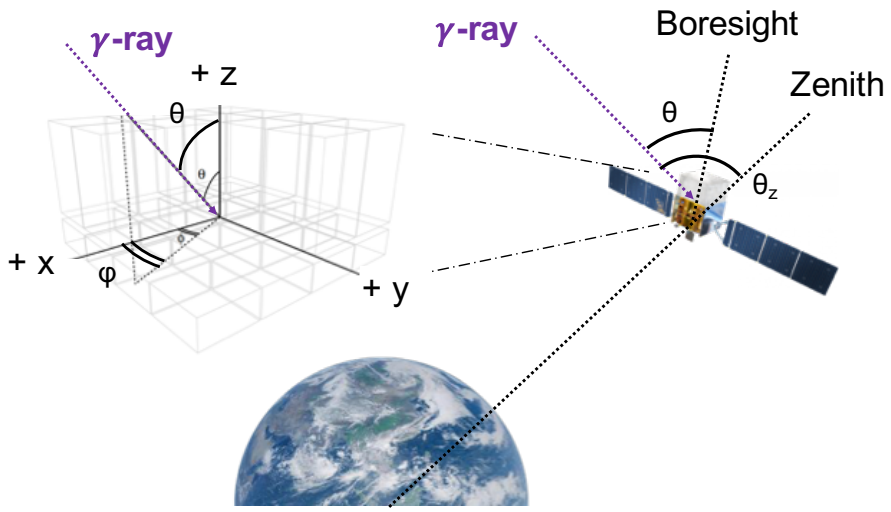

Figure 3.7: **Definition of the direction of the event with angles, θ, θ_z, and ϕ.**

The flux and spectrum of emission from a source can be correctly computed when the LAT response to detected events within a given event class is taken into account. From a dedicated Monte Carlo simulation[12], the response of the LAT to all possible energies and inclination angles are evaluated with good statistics. As a result, the incoming photon flux and the detected events are mapped with the so-called Instrument Response Function (IRF). The IRF is factored into three components: the efficiency in terms of the effective area, the PSF, and the EDISP. Each component of the IRF for a given event class is described as a function of the photon energy and incident angle.

In addition to the standard data selection, there is a very loose event selection, the so-called the LAT Low energy event selection (LLE; 30 MeV–100 MeV) [214][13]. This selection has the increased effective area by a factor of $\sim$ 50 (at 30 MeV) and

[12]The Monte Carlo simulation refers to a computational technique or algorithm which makes use of repeated random samplings and obtains numerical results for complicated problems with entangled parameters.

[13]`https://heasarc.gsfc.nasa.gov/W3Browse/fermi/fermille.html`

4.5 (at 100 MeV) at the expense of reliability in the direction of events. Since the energy resolution of the LLE is reasonable, the LLE can be regarded as the data from a rate detector like the GBM (§ 3.2). Due to high background, LLE data can be used only for short-duration, high-signal events such as GRBs and solar flares.

3.2 Gamma-ray Burst Monitor

The Gamma-ray Burst Monitor (GBM) is designed to measure temporal and spectral properties of the prompt emission of GRBs in the keV–MeV energy band. The GBM is a set of 14 scintillation detectors, which is dedicated to detecting and locating GRBs. Twelve thallium-activated sodium iodide (NaI; labeled as n0 to n9, na, and nb) detectors on each side of *Fermi* have an energy range of $\sim$ 8 keV to $\sim$ 1 MeV, oriented to different directions (Figure 3.8). Two bismuth germanate (BGO; labeled as b0 and b1) detectors measure the high-energy spectrum from $\sim$ 200 keV to 40 MeV, overlapping at low energy with the NaI detectors, and are positioned on opposites sides of *Fermi* (Figure 3.8). By comparing relative count rates in the NaI detectors, it is possible to estimate a source location with accuracy of $\sim$ 3 degrees [215, 216]. The energy bands of the GBM and the LLE are overlapped, allowing to perform cross-calibration and to observe the broadband energy spectrum without a gap.

The NaI crystal is a disk with a diameter of 12.7 cm (5") and a thickness of 1.27 cm (0.5"). Each NaI scintillator is attached to a single PMT, which measures the scintillation light and produces an electric signal. The BGO crystal has the

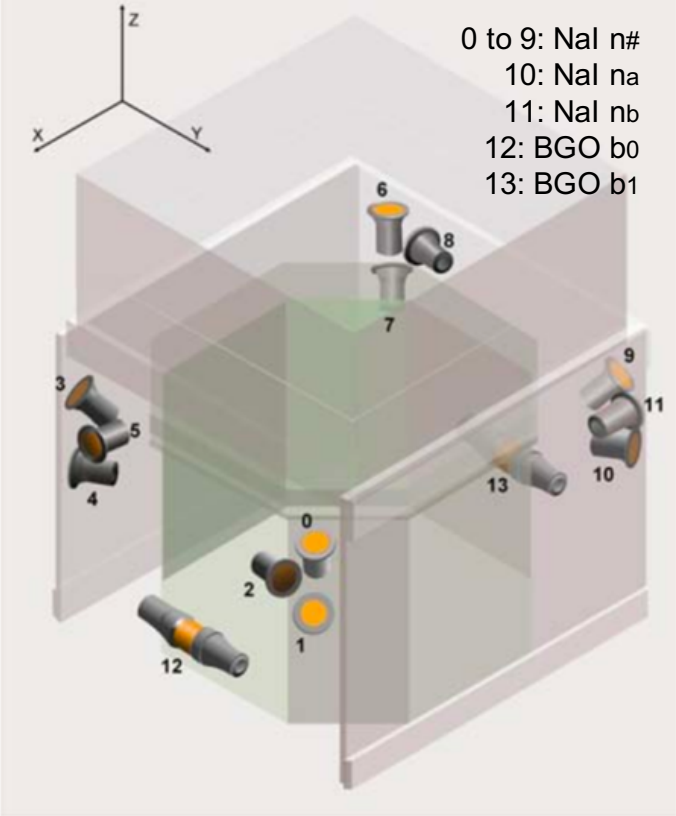

Figure 3.8: **The configuration of 14 GBM detectors.** The GBM consists of 12 NaI detectors (0 to 11) for low energies and 2 BGO detectors (12 and 13) for high energies [34]. Note that the low-numbered (high-numbered) NaI detectors are on the same side of the BGO b0 (b1) detector.

same diameter of 12.7 cm (5") and a larger thickness of 12.7 cm (5"). Two PMTs are mounted on both sides to each BGO crystal, resulting in better light collection. The peak heights of signals from the PMTs are buffered and converted into 128-channel energy resolution and 8-channel energy resolution, based on lookup tables. This process is called the "Pulse Height Analysis (PHA)". The distribution of the numbers of counts in each PHA channel is later used for the GRB spectral analysis (§ 5.1).

Similar to the LAT, the detector response of the GBM instrument was determined with the help of Monte Carlo simulations [217], and was simplified in form

Table 3.2: **Description of GBM data products**

Name	Description	Extension
CTIME	The counts accumulated every 0.064 s in 8 energy channels	pha
CSPEC	The counts accumulated every 1024 s in 128 energy channels	pha
TTE	Time-tagged event data precise to 2 microseconds in 128 energy channels	fits
DRM	The detector response matrix for the given time and location	rsp or rsp2[a]

[a]The response files have an extension either rsp (single matrices) and rsp2 (multiple matrices). The rsp2 file accounts for spacecraft slew during a long transient.

of the so-called Detector Response Matrix (DRM). Like the IRF of the LAT, the DRM is the mapping between the true energy of incoming photons and the apparent energy of measured events. The DRM depends on deposited energy, the direction to the source with respect to the spacecraft, and the orientation of the spacecraft with respect to the Earth.

When a rapid increase in the count rates is observed in two or more detectors satisfying the GBM trigger criteria[14], the GBM is triggered, and an alert is sent to the science community in near real time. The GBM team provides three types of data for each detector: CTIME, CSPEC, and TTE (Table 3.2)[15]. For a GRB triggering the GBM, the DRMs in the direction of the GRB for 14 detectors are also provided. One can also generate the DRMs for any given time and location with the tool "*gbmrsp*" provided by the GBM team[16].

[14]See the third GBM GRB catalog [61] for the recent trigger algorithms
[15]`https://heasarc.gsfc.nasa.gov/W3Browse/fermi/fermigbrst.html`
[16]`https://fermi.gsfc.nasa.gov/ssc/data/analysis/gbm/DOCUMENTATION.html`

Chapter 4: GRB Analysis Methods

In this chapter, I summarize the analysis methods generally used for characterizing temporal and spectral properties of GRBs. Note that the methods are applicable to the *Fermi* data.

4.1 Temporal Aspects

4.1.1 Light curve

Analyzing a GRB starts with building its light curve, the time-history of the GRB photon flux integrated over a specific energy band. The GRB light curve contains important information about a GRB such as the duration of the event and its variability, among others.

The T_{90} is typically used as a proxy for the GRB duration [10]. This is the time during which the cumulative GRB photon flux increases from 5% to 95% (right panel in Figure 4.1). However, the T_{90} has three limitations: (i) The duration of a burst depends on the energy band selection. In general, the duration of a GRB estimated in the low-energy band is longer than that in the high-energy band. The *Fermi* collaboration computes T_{90} in the 50–300 keV energy range [61, 219], which

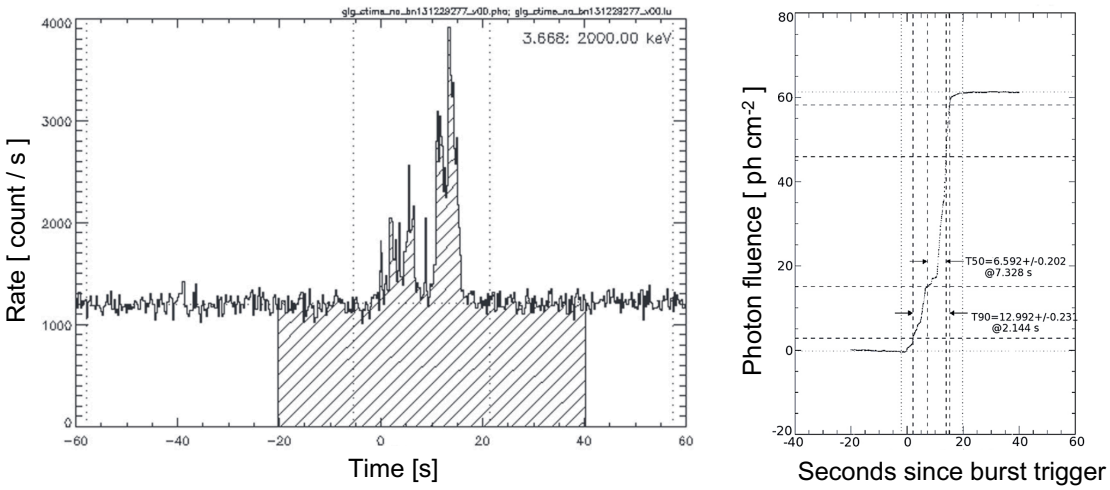

Figure 4.1: **Light curve and its duration of GRB 131219A.** *Left*: the light curve of GRB 131219A with the selection for calculating the duration of the GRB. *Right*: the duration plot of GRB 131219A, which is the integrated GRB fluence in the 50–300 keV energy range within the selected time interval. Adopted from [61]

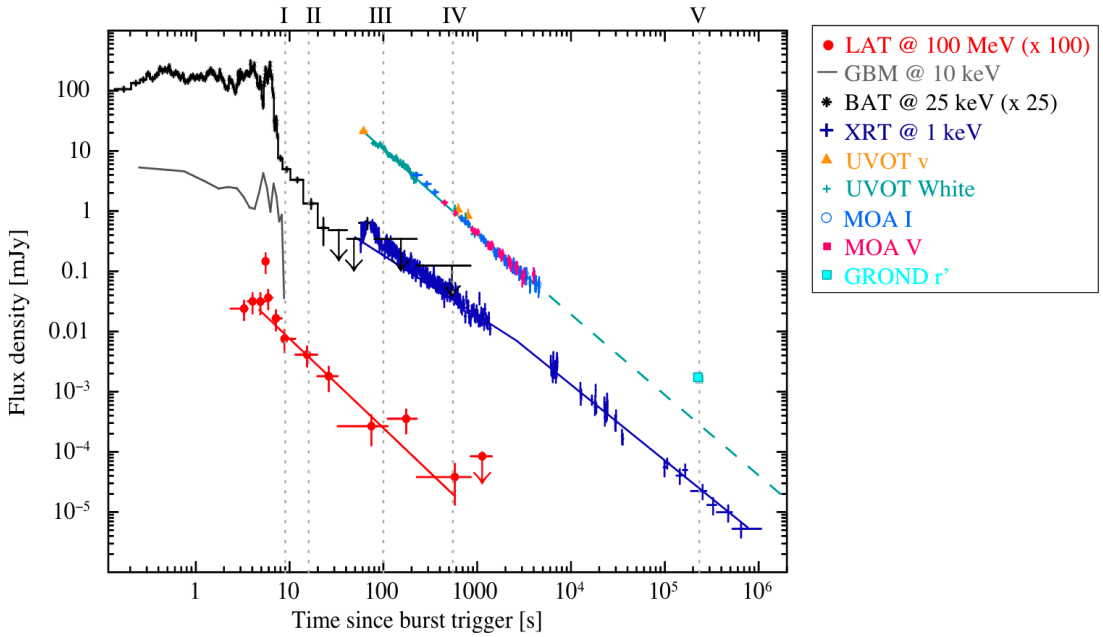

Figure 4.2: **Multi-wavelength afterglow light curve of GRB 110731A.** The flux density in different energies decays continuously in time. Adopted from [218]

was also used for BATSE GRBs [7]. (ii) The duration depends on the sensitivity of the detector. Instruments with a lower background rate can detect the fainter part of the burst emission resulting in longer duration measurements. (iii) When there is a bright precursor with a long quiescent period before the main emission of a GRB [73], the duration of the GRB can include the long quiescent period; i.e., the duration of the GRB does not represent the duration of emission.

One typically displays the count light curve and not the photon light curve for the GRB prompt phase (left panel in Figure 4.1). This corresponds to the number of events detected by the instrument minus the estimated background before accounting for the detector response functions. The count-rate curve can be a good approximation for showing the temporal characteristics of the prompt emission of GRBs, because, in most cases, the detected count rate is proportional to the true flux. On the other hand, the photon light curves are usually used for the GRB afterglow phase (Figure 4.2).

The prompt-emission light curves consist of one or more pulses. Pulses are typically asymmetrical and characterised with a Fast Rise and an Exponential Decay (FRED). The Norris function [65, 220] is a representative FRED profile[1],

$$I(t) = \frac{A\lambda}{\exp\left(\frac{\tau_1}{t} + \frac{t}{\tau_2}\right)} \quad \text{for } t > 0 \tag{4.1}$$

where $\lambda = \exp(2\mu)$ and $\mu = (\tau_1/\tau_2)^{1/2}$. This function describes adequately the overall shape of broad pulses but not always their detailed features [221].

[1]Here, I present the recent version of the Norris function (2005), which is simpler than the initial Norris function (1996)

While the γ-ray prompt emission shows a fast and intense variability as short as a few milliseconds, the afterglow emission slowly evolves on much longer time scales (Figure 4.2) [31, 32]. In contrast to the violent fluctuation in the prompt emission light curve, the afterglow light curve is relatively smooth (Figure 4.2) [31, 32].

The afterglow light curves are well described by a simple power law,

$$F(t) = F_0\, t^{-\hat{\alpha}}, \tag{4.2}$$

or a broken power law,

$$F(t) = \begin{cases} F_0\, t^{-\hat{\alpha}_1} & \text{if } t \leq t_b, \\ F_0\, t_b^{\hat{\alpha}_2 - \hat{\alpha}_1}\, t^{-\hat{\alpha}_2} & \text{if } t > t_b, \end{cases} \tag{4.3}$$

where t_b is a break time and $\hat{\alpha}_1$ ($\hat{\alpha}_2$) is a temporal index before (after) a temporal break. In many X-ray afterglows, flaring activities are seen, which can be also well described by a broken power law; alternatively, the Gaussian function or the Norris function can also be used for describing flares.

4.1.2 Variability

Figure 2.4 shows that the prompt emission is highly variable. As stated in § 2.4.5, such variability can reflect the temporal activity of the central engine, and it can be used for estimating several physical parameters such as the emission radius (Equation 2.44) and the bulk Lorentz factor (Equation 2.33). Here, I present two

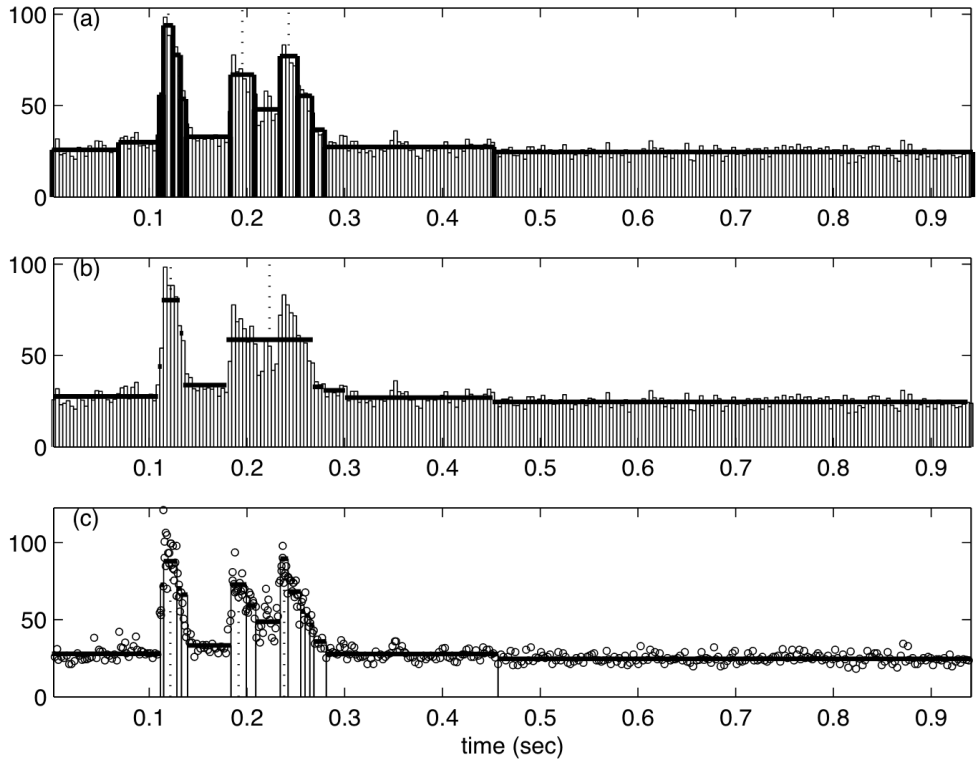

Figure 4.3: **Bayesian block algorithm applied to BATSE data for a burst (0551).** The Bayesian blocks are indicated with solid lines. The three panels show the Bayesian block results for different data types. Adopted from [222]

methods for identifying the variability of GRBs:

(i) The Bayesian block algorithm [222, 223] is widely used to find temporal structures in a GRB light curve [75, 83]. Basically, the Bayesian block algorithm divides the GRB light curve into several optimal segments (blocks), where each block has a constant count rate that is significantly different compared to those of the adjacent blocks (Figure 4.3).

This method is based on the Bayesian statistics (§ 4.2.5), where a prior probability in the number of blocks is introduced; this prior assigns smaller probability

to a large number of blocks [223],

$$P = P_0 {\gamma_p}^{N_{\text{blocks}}}. \tag{4.4}$$

In the Bayesian approach, the two models, M_i and M_j, can be compared by calculating the Bayes factor K (Equation 4.32),

$$K_{ij} = \frac{P(M_i \mid D)}{P(M_j \mid D)} = \frac{P(D \mid M_i)\, P(M_j)}{P(D \mid M_j)\, P(M_i)} = \frac{\mathcal{L}_i\, P(M_j)}{\mathcal{L}_j\, P(M_i)} = \frac{\mathcal{L}_i}{\mathcal{L}_j} {\gamma_p}^{-(N_i - N_j)}, \tag{4.5}$$

where D is observed data, $\mathcal{L}_i$ is the likelihood of the model M_i, and N_i is the number of blocks in the model M_i. Assuming that M_i has one more block compared to M_j, the ratio of two prior probabilities can be reduced to γ_p^{-1}. This parameter can be described as a function of the false-positive probability ${p_{f-p}}$[2] and the number of events N [223],

$$ncp\_prior \equiv -log(\gamma_p) = 4 - 73.53\, p_0\, N^{-0.478}, \tag{4.6}$$

where $p_0 \equiv (1 - p_{f-p})$. Note that this is not a unique method to estimate *ncp_prior*, and one can select an *ad hoc* value for *ncp_prior*, γ_p, or p_0. This *ncp_prior* works as a penalty for adding a new block, and this algorithm finds the optimal set of blocks, where each block has significance enough to compensate this penalty.

(ii) The wavelet transform, more specifically the Haar wavelet power spectrum

[2]Probability that indicates how often the algorithm falsely reports detection of a signal when no signal is present in reality. This is equal to the significance level.

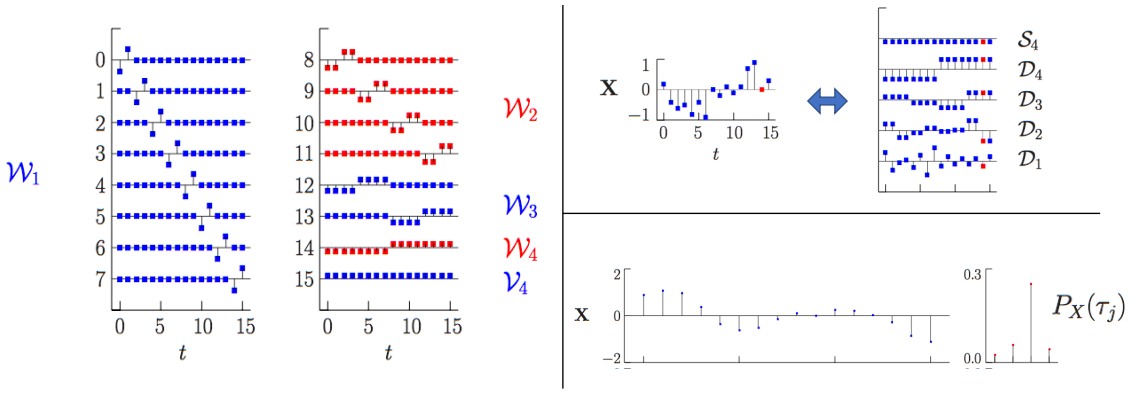

Figure 4.4: **A sketch for explaining the wavelet method.** *Left*: the Haar wavelets for level 4 ($\mathcal{W}_1$ to $\mathcal{W}_4$ and $\mathcal{V}_4$). *Top right*: the signal ($\mathbf{X}$) is decomposed to the wavelets ($\mathcal{D}_1$ to $\mathcal{D}_4$ and $\mathcal{S}_4$). *Bottom right*: the wavelet power spectrum. Adopted from [224]

(or the Haar wavelet scaleograms) [224], is generally adopted for estimating the minimum variability time of a GRB [225–228]. Similar to the Fourier transform, the wavelet transform decomposes a signal into its constituent wavelets. The Haar wavelet is the simplest wavelet, which is a step function taking values 1 and -1.

Figure 4.4 shows how the wavelet transform works. For example, let's consider the discrete Haar wavelet consisting of 16 elements, which can be grouped into five ($\mathcal{W}_1$ to $\mathcal{W}_4$ and $\mathcal{V}_4$). The $\mathcal{V}_4$ can represent a constant background, and the other groups are used for explaining fluctuations of different time scales δt_j, where $\delta t_j = 2^{j-1}\delta t_0$ and δt_0 is the finest binning of the data. Each wavelet has its own coefficient ($\mathbf{W}_1$ to $\mathbf{W}_4$ and $\mathbf{V}_4$), so that a light curve can be reproduced by

$$\mathbf{X} = \sum \mathcal{W}_i^T \mathbf{W}_i + \mathcal{V}_4^T \mathbf{V}_4 = \sum \mathcal{D}_i + \mathcal{S}_4, \tag{4.7}$$

where $\mathcal{D}_i$ and $\mathcal{S}_4$ are decomposed light curves corresponding to the elements, $\mathcal{W}_i$

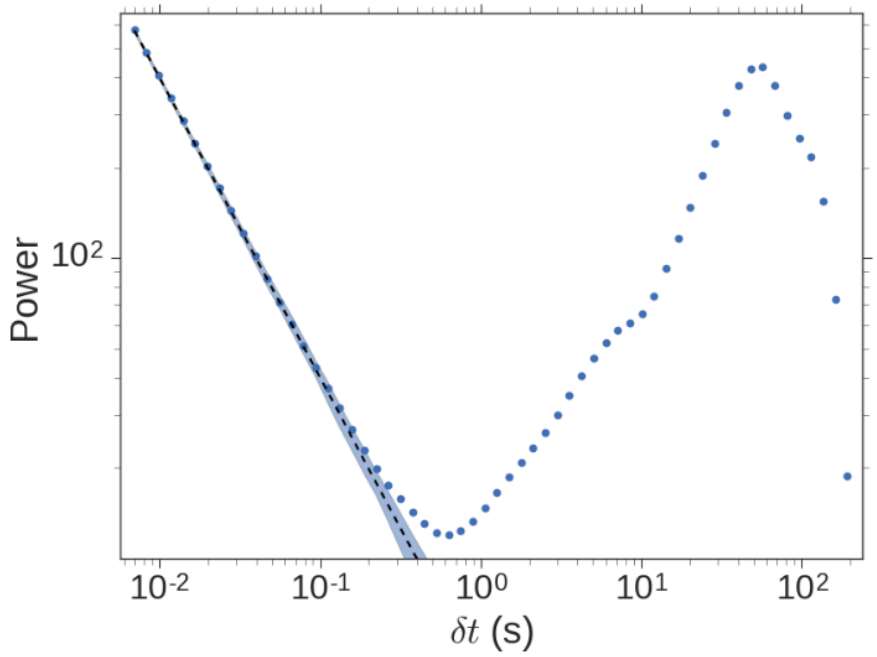

Figure 4.5: **Minimum variability estimated from the wavelet power spectrum for GRB 100724.** The blue points are the observed wavelet power spectrum (GRB 100724 + background). The black dashed line and the blue shaded region represent the background spectrum and its 99% containment interval, respectively. The minimum variability time for this GRB would be $\delta t_m \sim 0.3s$. Adopted from [228]

and $\mathcal{V}_4$. The power of each wavelet is defined as

$$P_{\mathbf{X}}(\tau_j) \equiv \frac{1}{N}||\mathbf{W}_j||^2. \tag{4.8}$$

Figure 4.5 shows an example of the GRB power spectrum, given by the continuous wavelet transformation[3]. The minimum variability is a time scale (δt) where the wavelet power spectrum of the observed signal deviates from the wavelet power spectrum from the Poisson fluctuation of the background [228].

[3]The concept of the continuous wavelet transformation is same to the discrete wavelet transformation, but this transform utilizes shifted and scaled (stretched or shrunk) copies of a basic wavelet.

4.1.3 Cross-correlation

The cross-correlation function (CCF) is commonly used for measuring time lags, named spectral lags, between the low- and high-energy of the γ-ray prompt emission (§ 2.3.1) [39, 229].

The spectral lag can be identified by calculating the strength of the correlation ($r_{\rm CCF}$) by progressively shifting one light curve with respect to the other by the lag τ,

$$r_{\rm CCF}(\tau) = \frac{\sum_{i=1}^{N}(x(t_i)-\bar{x})(y(t_i+\tau)-\bar{y})}{\left(\sqrt{\sum_{i=1}^{N}(x(t_i)-\bar{x})^2}\right)\left(\sqrt{\sum_{i=1}^{N}(y(t_i+\tau)-\bar{y})^2}\right)}, \tag{4.9}$$

where both light curve (flux or count rate) are composed of N data points whose means are $\bar{x}$ and $\bar{y}$, respectively. The two light curves are considered to be correlated (anti-correlated), when the coefficient at a given τ is close to +1 (-1). The spectral lag may exist if one can get the highest correlation coefficient when $\tau \neq 0$ with $r_{\rm CCF}(\tau) \sim 1$ (Figure 4.6). Note that for a given τ, this correlation coefficient ($r_{\rm CCF}$) is equivalent to the Pearson correlation coefficient r_p. If N is sufficiently large ($N \gtrsim 20$), r_p approximately follows a normal distribution with mean and standard deviation of 0 and $1/\sqrt{N}$, respectively.

If the data is not evenly sampled, the CCF method does not work. In this case, the Discrete Correlation function (DCF) can be alternatively employed [230]. In this method, each correlation coefficient for all measured pairs is separately computed

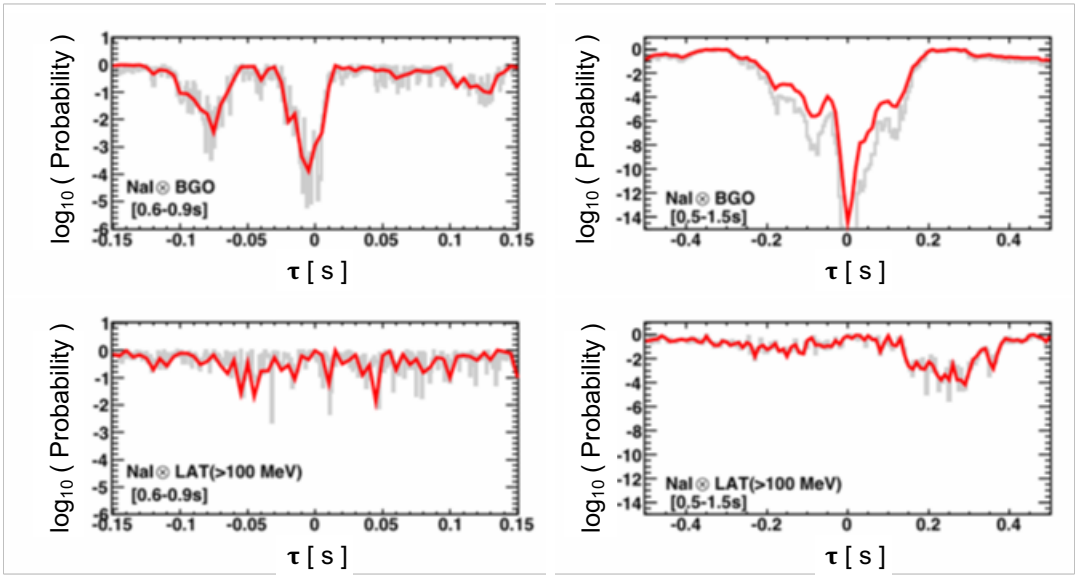

Figure 4.6: **Cross correlation function probability as a function of the lag τ observed in GRB 090510.** The red curves correspond to time bins of size 0.01 s, and the gray curves correspond to 0.005s. The upper two panels show a clear correlation between two energy bands, whereas the bottom two panels don't show a correlation. Adopted from [39]

(unbinned DCF),

$$r_{\mathrm{UDCF_{i,j}}} = \frac{(x(t_i) - \bar{x})(y(t_j) - \bar{y})}{\left(\sqrt{\sum_{i=1}^{N}(x(t_i) - \bar{x})^2}\right)\left(\sqrt{\sum_{j=1}^{N}(y(t_j) - \bar{y})^2}\right)}. \tag{4.10}$$

Each of $r_{\mathrm{UDCF_{i,j}}}$ is associated with the pairwise lag $\Delta t_{i,j} = t_j - t_i$. Then, they are binned based on their pairwise lag values; i.e., $\tau - \Delta\tau/2 \leq \Delta t_{i,j} < \tau + \Delta\tau/2$. Finally, the DCF for the time lag τ is defined as the average of r_{UDCF} contained in each bin,

$$r_{\mathrm{DCF}}(\tau) = \frac{\sum r_{\mathrm{UDCF_{i,j}}}}{M_\tau}, \tag{4.11}$$

where M_τ is the number of r_{UDCF} in each bin. Note that DCF(τ) is not defined for

a bin with no r_{UDCF}. The standard error of each DCF(τ) is

$$\sigma_{\mathrm{DCF}}(\tau) = \frac{\sqrt{\sum \left(r_{\mathrm{UDCF_{i,j}}} - r_{\mathrm{DCF}}(\tau)\right)^2}}{M_\tau - 1}. \tag{4.12}$$

Similar to CCF, DCF can be approximated to the Pearson correlation, and used for identifying the spectral lag.

4.2 Spectral Aspects

4.2.1 Forward Folding

We can naively think that the photon energy distribution (i.e., photon spectrum) of a source can be simply recovered by convolving the observed count spectrum with the instrument response function; however, a small dispersion on the energy measurement makes this approach impracticable as I will show using a toy model. Instead, the forward-folding method can efficiently recover the observed photon spectrum.

The response matrix of a γ-ray detector is generated using Monte Carlo simulations: the interactions of the photons from a source with the detector and the spacecraft are modeled with GEANT4[4]. The true energy of the incident photons are mapped to the measured energy of the detected photons. In the toy model, the measured energy of a photon whose true energy is E_0 follows a Gaussian distribution centered on E_0 with 10% uncertainties.

[4] `https://geant4.web.cern.ch/`

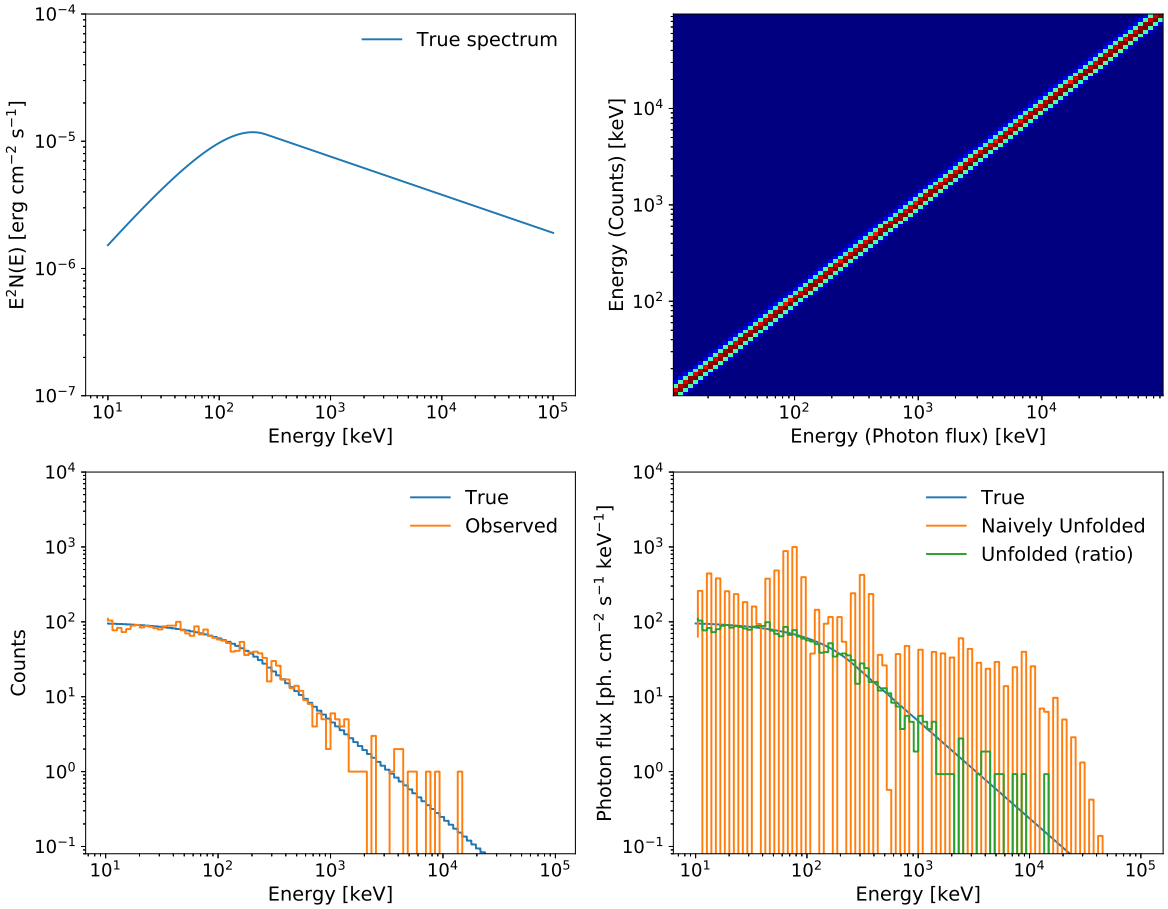

Figure 4.7: **A toy model for comparing the forward folding and unfolding by inverting the response matrix.** *Top left*: the true spectrum (the Band function). *Top right*: the response matrix. *Bottom left*: the true and observed counts in energy. *Bottom right*: the true and unfolded observed photon fluxes in energy. See the text for details.

Suppose T_j is the true number of photons from a source in a given energy bin j (i.e., true energy), and $R_{i,j}$ is an element of the response matrix that converts T_j to the number of photons observed in an energy bin i, S_i (i.e., reconstructed energy) [231][5],

$$S_i = \sum R_{i,j} T_j \quad \rightarrow \quad \boldsymbol{S} = R\,\boldsymbol{T}, \tag{4.13}$$

One may naively expect that the true photon spectrum can be recovered by con-

[5]Note that for simplicity, I ignore background.

volving the observed count spectrum (after background subtraction) with the inverse response matrix, ***T'***, [231],

$$\boldsymbol{T'} = R^{-1}(\boldsymbol{S}). \tag{4.14}$$

To test this method, I choose a Band function (Equation 4.17) with typical parameters (§ 2.3.1) as the true photon spectrum of the source (top–left panel in Figure 4.7). Next, I generate a response matrix in which the reconstructed photon energy follows a Gaussian distribution around the true photon energy, assuming that the energy resolution is $\delta E/E \sim 10\%$ (top–right panel in Figure 4.7).

The ideal observed count spectrum is obtained by convolving the true photon spectrum with the response matrix using Equation 4.13 (blue in the bottom-left panel in Figure 4.7). I generate a realistic observed synthetic spectrum for a photon-counting detector by applying Poisson fluctuations in each energy bin of the ideal observed spectrum (orange in the bottom-left panel in Figure 4.7). Using Equation 4.14, I should recover the true photon spectrum, which is definitely not the case as indicated by the dramatic difference between the orange histograms on the bottom left and right panels of Figure 4.7. This is due to the reconstructed energy dispersion in the instrument response matrix, which magnifies the Poisson fluctuations intrinsic to the counting-detectors.

One solution to recover/reconstruct the true photon spectrum of a GRB is to use the "forward folding" method. With this method, one must assume a photon spectral model for the source and a set of parameter values for the model. The model is folded through the instrument response using Equation 4.13. The resulting

photon spectrum should be similar to the observed photon spectrum if the model and its parameter values were those of the true photon spectrum. In scanning the whole parameter space, one finds the set of parameter values for which the photon spectrum best matches the observed photon spectrum. In this forward folding approach, the "unfolding" spectrum can be approximated by $T' = T \times (S_i - B_i)/M_i$, rather than imposing the inverted response matrix to the observed source counts (green in the bottom-left panel in figure 4.7).

4.2.2 Spectral Model

Generally, a GRB spectral model is usually displayed in the energy spectrum space, $E^2N(E)$ or νF_ν, in units of keV cm^{-2} s^{-1} or erg cm^{-2} s^{-1}, which is called a "Spectral Energy Distribution" (SED). The SED shows how the bolometric energy

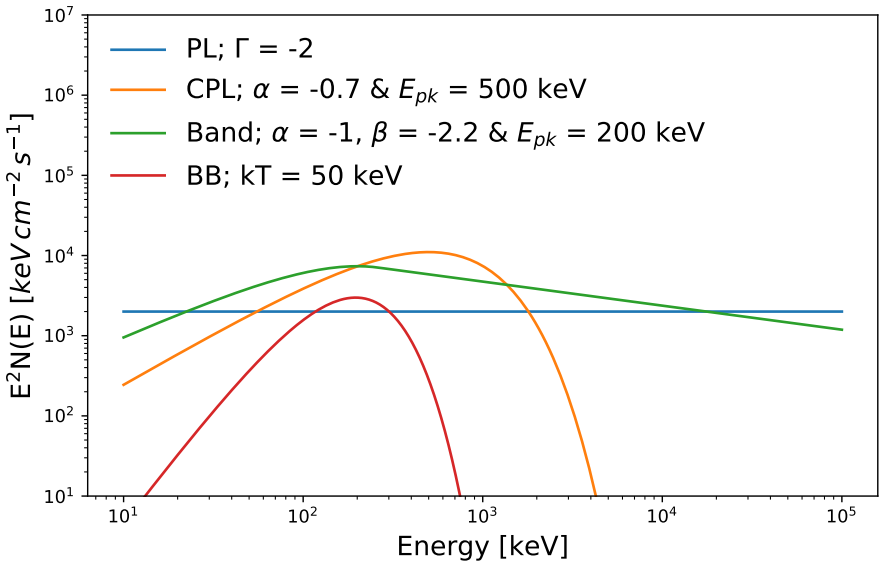

Figure 4.8: **Spectral energy distribution for GRB spectral models**: PL, CPL, Band, and BB.

of the source is distributed in energy. An analytical form of a GRB spectrum is, however, defined in the photon number space, $N(E)$, in units of photons cm^{-2} s^{-1} keV^{-1}, because the photon number spectrum is directly folded through the detector response (§ 4.2.1).

The following are four representative spectral models used to describe a GRB spectrum (Figure 4.8):

- Power law (PL),

$$N(E) = \frac{dN}{dE} = A\left(\frac{E}{100keV}\right)^{\Gamma}, \tag{4.15}$$

  where A is amplitude, and Γ is a photon index. This is the simplest model.

- Cutoff power law (CPL); a power law with an exponential cutoff,

$$N(E) = A\left(\frac{E}{100keV}\right)^{\alpha} \exp\left(-\frac{E(2+\alpha)}{E_{pk}}\right), \tag{4.16}$$

  where α is a photon index, and E_{pk} is the peak energy in the νF_{ν} spectrum. If $E_{pk} \to \infty$, the CPL becomes the PL; i.e., the PL is a subset of the CPL.

- Band function (Band) [8]; two smoothly connected power laws,

$$N(E) = \begin{cases} A\left(\frac{E}{100keV}\right)^{\alpha} \exp\left(-\frac{E(2+\alpha)}{E_{pk}}\right), & E < \frac{\alpha-\beta}{2+\alpha}E_{pk}, \\ A\left(\frac{E}{100keV}\right)^{\beta} \exp(\beta-\alpha)\left(\frac{\alpha-\beta}{2+\alpha}\frac{E_{pk}}{100keV}\right)^{\alpha-\beta}, & E \geq \frac{\alpha-\beta}{2+\alpha}E_{pk}, \end{cases} \tag{4.17}$$

  where α and β are low- and high-energy photon indices, respectively. When $\beta \to -\infty$, this function can be simplified to the CPL; i.e., the CPL is a subset

of the Band.

- Black body (BB); the Planck function in the photon number space

$$N(E) = A\frac{E^2}{(kT)^4}\left(\exp\left(\frac{E}{kT}\right) - 1\right)^{-1}, \tag{4.18}$$

where kT is temperature of the black body in unit of keV. At $E \ll kT$, this function is asymptotically as the PL with $\Gamma = +1$. For $E \gg kT$, this function is exponentially decay similar to the CPL.

4.2.3 Parameter Estimation - Maximum Likelihood Method

The best-fit parameters of a model are a set of parameters giving the minimum difference between unfolded model counts and observed counts. The process of finding a set of the best-fit parameters is called "parameter estimation". The "maximum likelihood" is the statistic widely used for parameter estimation. The idea is that the best-fit parameters are those maximizing the probability of the observed data given the model. The likelihood is defined as the total probability of observing the data (S) given the model (M) and current parameters (θ),

$$\mathcal{L}(\theta) = \prod_{i=1}^{N} \mathcal{L}_i(\theta) = \prod_{i=1}^{N} P(S_i|\theta, M). \tag{4.19}$$

In practice, twice the negative log likelihood is used, which is the so-called "fit statistic",

$$\text{fit statistic} = -2\log\mathcal{L} = -2\sum_{i=1}^{N}\log\left(P(S_i|\theta)\right). \tag{4.20}$$

In this definition, the goal is to find the values of parameters, which "minimizes" the fit statistics. This process is called the "minimization", and a tool for this process is called the "optimizer". One popular optimizer in the GRB field is `Minuit` [232].

Considering the probability distributions underlying observed data, one can choose a proper fit statistic. Most of observed data are drawn from one of two distributions: Poisson and Gaussian. The Poisson distribution is applied to photon count data from a photon-counting detector. The Gaussian distribution requires the standardized uncertainty, so that the uncertainty of data should be estimated beforehand. In a GRB analysis with the GBM, the background during a burst is estimated from a polynomial fit to time intervals before and after the burst. This fit gives median and uncertainty of the background, which can be used for the standardized uncertainty of the Gaussian probability distribution. Here, I introduce three fit statistics, which are continuously used for my work[6]:

- χ^2; Gaussian data,

$$P(s_i|\theta) = \frac{1}{\sigma_i\sqrt{2\pi}}\exp\left[\frac{-(s_i - m_i)}{2\sigma_i^2}\right], \quad \text{and} \quad \chi^2 = \sum_{i=1}^{N}\frac{s_i - m_i}{\sigma_i^2}, \tag{4.21}$$

  where s_i and σ_i are the observed data and its standard errors, respectively, and m_i is the predicted values based on the model with current parameters and instrumental response.

[6] `https://heasarc.gsfc.nasa.gov/xanadu/xspec/manual/XSappendixStatistics.html`

- C_{stat} (Cash statistic) [233]; Poisson data with Poisson background,

$$P(S_i|\theta) = \frac{t(m_i + f_i)^{S_i} e^{-t(m_i+f_i)}}{S_i!} \frac{(tf_i)^{B_i} e^{-(tf_i)}}{B_i!}, \tag{4.22}$$

and

$$C_{stat} = 2\sum_{i=1}^{N} t(m_i + f_i) - S_i log\left(t(m_i + f_i)\right) - S_i(1 - logS_i) + tf_i - B_i log(tf_i) - B_i(1 - logB_i), \tag{4.23}$$

where

$$f_i = \frac{S_i + B_i - 2tm_i + \sqrt{|S_i + B_i - 2tm_i|^2 + 8tm_iB_i}}{4t}, \tag{4.24}$$

t is the exposure time, S_i are the observed counts during t, B_i are the background counts, and m_i are the predicted count rates based on the current model and instrumental response. Note that Equation 4.24 is derived from the fact that the minimal $-2\log\mathcal{L}_i$ is given when $\partial(-2\log\mathcal{L}_i)/\partial f_i = 0$ is achieved. For large number of counts in each energy bin ($S_i \gtrsim 20$), the Poisson statistics can be approximated to the Gaussian statistics with $\sigma_i \sim \sqrt{S_i}$, so that C_{stat} is distributed as χ^2.

- PG_{stat}; Poisson data with Gaussian background,

$$P(S_i|\theta) = \frac{(M_i + tf_i)^{S_i} e^{-(M_i+tf_i)}}{S_i!} \frac{1}{\sigma_{B,i}\sqrt{2\pi}} \exp\left[\frac{-(B_i - tf_i)}{2\sigma_{B,i}^2}\right], \tag{4.25}$$

and

$$PG_{stat} = 2\sum_{i=1}^{N} t(m_i+f_i) - S_i log\left(t(m_i+f_i)\right) - S_i(1-logS_i) + \frac{(B_i - tf_i)}{2\sigma_{B,i}^2}, \quad (4.26)$$

where

$$f_i = \frac{-(\sigma_{B,i}^2 - B_i + tm_i) \pm \sqrt{(\sigma_{B,i}^2 - B_i + tm_i)^2 - 4(t\sigma_{B,i}^2 m_i - S_i\sigma_{B,i}^2 - tB_i m_i)}}{2t}, \quad (4.27)$$

B_i and $\sigma_{B,i}$ are mean and standard deviation of the background data, respectively.

The best fit corresponds to the set of parameter values which minimizes the fit statistic. Due to the multi-dimensionality of the minimization, it is possible that an optimizer returns a "local" minimum of the fit statistic and not its "global" minimum. To avoid this issue one runs the optimizer multiple times with different initial parameter values; If the optimizer returns the same minimum of the fit statistic as well as the same parameter values, it is likely that the fitting engine converged to the "global" minimum.

Identifying the best parameter values of a model doesn't mean that the model is a good fit to the data (i.e., goodness-of-fit). When the data set is eligible to be analyzed with χ^2 (e.g., the number of counts in each energy channel is large enough to be approximated to the Gaussian distribution), it is straightforward to estimate

the goodness-of-fit. Indeed, the goodness-of-fit is given by the reduced χ^2, χ^2_ν:

$$\chi^2_\nu = \chi^2_{\rm min}/{\rm dof}, \tag{4.28}$$

where $\chi^2_{\rm min}$ is the χ^2 value corresponding to the best fit, and dof is the degree of freedom, the number of data points minus the number of free parameters of the model. If $\chi^2_\nu \sim 1$, the model is a good fit to the observed data. If $\chi^2_\nu \gg 1$, it is unlikely that the observed data set is drawn from the model, so one may reject the model as the possible description of the observed data. If $\chi^2_\nu \ll 1$, the uncertainties of the data points may be over-estimated and prevent concluding if the model is good or not. In more complex cases (e.g., low count regime), the goodness-of-fit can be estimated using Monte Carlo simulations (see the appendix of the reference [70]).

If the model is a good fit to the data, we can determine the confidence interval for each parameter of the model. The confidence interval is the range of values within which the true value of the parameter lies at a certain confidence level (usually 68.3%); for a Gaussian distribution, 68.3% corresponds to an interval of 1σ around the distribution mean, $m \pm 1\,\sigma_m$. To determine the 68.3% confidence interval of a specific parameter, one varies the value of the parameter, in keeping all the others fixed at the values of the best fit, until the value of the fit statistic increases by one unit from its minimum.

4.2.4 Model Comparison - Likelihood Ratio

The nature of the GRB prompt emission is still debated within the community. Various models have been proposed for describing the shape of the γ-ray prompt emission spectra using one or multiple components; Comparing these models is crucial for a better understanding of the emission processes at play in the GRB jets.

In order to compare two models, M_0 and M_1, with n and m free parameters, respectively (n<m), one can use the likelihood ratio test. The likelihood ratio between M_0 (null hypothesis) and M_1 (alternative hypothesis) is defined as

$$\text{Ratio} = \frac{\mathcal{L}_0}{\mathcal{L}_1}, \tag{4.29}$$

where $\mathcal{L}_0$ and $\mathcal{L}_1$ are the likelihood values of M_0 and M_1, respectively. In the case of nested models[7], $\mathcal{L}_1 \geq \mathcal{L}_0$. In order to avoid numerical issues due to small values of $\mathcal{L}$, one preferably uses a so-called Test Statistic (TS),

$$\text{TS} = -2\log(\text{Ratio}) = -2\log\left(\frac{\mathcal{L}_0}{\mathcal{L}_1}\right) = 2\left(\log\mathcal{L}_1 - \log\mathcal{L}_0\right), \tag{4.30}$$

where higher the TS value, the more is M_1 is favored over M_0.

In the limit of large data sets ($N > 10$), Wilks' theorem [234] states that the TS values follow a $\chi^2(k)$ distribution with k = m - n. It is, therefore, straightforward to use the TS value for comparing models. For example, if M_0 and M_1 are nested with k

[7] Two models are nested when an alternative model contains all the terms of a null model with at least one additional term.

$= 1$, then the significance of M_1 over M_0 is given by $\sigma = 1 - F_{\chi^2(1)}(\mathrm{TS}) = \sqrt{\mathrm{TS}}$, where $\chi^2(1)$ is the χ^2 distribution with 1 dof and $F_{\chi^2(1)}(x)$ is its cumulative distribution function. In more complex cases where the TS distribution cannot be approximated with a χ^2 distribution, the TS distribution can be re-normalized using Monte Carlo simulations (see the appendix of the reference [70]).

4.2.5 Bayesian Model Comparison - Bayesian Information Criterion

The discussions in § 4.2.4 and § 4.2.3 are based on the "Frequentist" inference[8]. In the "Bayesian" approach, the probability of a model given the data (i.e., posterior probability) is defined by the Bayes' theorem,

$$P(M \mid S) = \frac{P(S \mid M)\, P(M)}{P(S)}, \tag{4.31}$$

where $P(S \mid M)$ is the probability (*likelihood*) of the observed data set (S) given the model (M). The probability $P(M)$ is the *prior* probability, which is the probability of the model. This probability can be estimated from other information such as previous observational results or physical intuition. The probability $P(S)$ is called the *marginal likelihood* of the data, which is independent of choosing models.

Similar to the likelihood ratio test, a model comparison is done by dividing the likelihoods of two models, which is called the Bayes factor K,

$$K = \frac{P(S \mid M_1)}{P(S \mid M_2)} = \frac{\int P(S \mid \theta_1, M_1)\pi(\theta_1 \mid M_1)d\theta_1}{\int P(S \mid \theta_2, M_2)\pi(\theta_2 \mid M_2)d\theta_2} = \frac{P(M_1 \mid S)\, P(M_2)}{P(M_2 \mid S)\, P(M_1)}, \tag{4.32}$$

[8]For the discussion on the Bayesian versus Frequentist inference, see the references [235]

where θ_i are a set of parameters in corresponding models M_i, $P(S \mid \theta_i, M_i)$ is the probability of observed data given θ_i ($\mathcal{L}_i(\theta_i)$ as defined in Equation 4.19), and $\pi(\theta_i \mid M_i)$ is the prior probability of parameters given M_i. Instead of integrating $P(S \mid \theta_i, M_i)$ over θ_i, one can take a certain set of parameters that maximizes $P(S \mid \theta_i, M_i)$, which is equivalent to the best parameter values of a model in § 4.2.3. In this case, the Bayes factor is equivalent to the likelihood ratio (Equation 4.29). Also, when two models are equally probable, $P(M_1) = P(M_2)$, the Bayes factor is equal to the ratio of the posterior probabilities of two models.

Another method to compare the two models is the Bayesian Information Criterion (BIC) [236]. The integration in Equation 4.32 can be approximated to the sum of $P(S \mid \theta_i, M_i)$ around its maximum [237],

$$\begin{aligned}\int P(S \mid \theta_i, M_i)\pi(\theta_i \mid M_i)d\theta_i \sim \left(\frac{2\pi}{N}\right)^{k_i/2} & P(S \mid \theta_{i,\max}, M_i)\pi(\theta_{i,\max} \mid M_i) \\ & \times \left|-\frac{1}{N}\frac{\partial^2 P(S \mid M_{i,\max})}{\partial \theta_i^2}\right|^{-1/2},\end{aligned} \tag{4.33}$$

and thus

$$-2\log\left(P(S \mid M_i)\right) = -2\log\left(P(S \mid \theta_{i,\max}, M_i)\right) + k_i \log(N) + \mathcal{O}(1), \tag{4.34}$$

where N is the number of observed data points, k_i is the number of parameters in M_i. Finally,

$$\text{BIC} = -2\log(\mathcal{L}_i) + k_i \log(N), \tag{4.35}$$

The term, $k_i \log(N)$, works as a penalty for the number of parameters in a model.

Table 4.1: **Evidence of the alternative model against the null model [237]**

ΔBIC	Evidence of H_1 against H_0
0 to 2	Not worth more than a bare mention
2 to 6	Positive
6 to 10	Strong
> 10	Very strong

The BIC value can be used for comparing two models with different number of parameters, where one model with lower BIC value is preferred over the other model with higher BIC value. Roughly speaking, if the BIC of an alternative model is at least 6 units lower than that of a null model, the alternative is strongly preferred over the null model (Table 4.1) [237].

Chapter 5: Dedicated Analysis on Individual GRBs

In this chapter, I present the dedicated analysis results on three bright GRBs, which are GRB 131108A, GRB 160709A, and GRB 190114C.

5.1 Data preparation

In this section, I summarize data preparation for a dedicated GRB analysis. The first step is to constitute a data set. Among 12 NaI detectors, I select 2–3 detectors that are triggered or show bright signals; increasing the number of detectors does not increase the significance of the fits. If any n0–n5 detectors are selected, b0 is also included in the data set. It is because the n0–n5 and b0 detectors are on the same side of GBM (§ 3.2). Likewise, if any n6–n9, na and nb detectors are selected, b1 is included. Among GBM data types (Table 3.2), I use `TTE` data, because `TTE` data has a high resolution in both energy (128 channels) and time (2 μs). Among 128 energy channels in each `TTE` data, a few low- and high-energy channels are ignored to avoid energy bins with electronic cut-off or overflows. In addition, for NaI data, energy channels close to the Iodine K-edge around 33.17 keV are excluded [217]. For LAT data, I use LAT `Transient020E` data and LLE data (§ 3.1.5). For the `Transient020E` data, I select the energy band from 100 MeV

to 10 GeV by using `gtselect` in the standard analysis tools (*Fermi Science Tools* version v11r5p3)[1], but if there are events above 10 GeV, I extend the energy limit such as 100 MeV–100 GeV. In addition to the energy cut, I apply two angular cuts, making use of `gtmktime`: a region of interest (ROI) cut centered on the best location of a burst and a maximum zenith angle (zmax) cut to prevent contamination from γ-rays from the Earth limb produced through interactions of cosmic rays with the Earth's atmosphere.

The next step is to determine time intervals of interest. This step is very important, especially in order to reveal the evolutionary feature of a burst. The simplest way is to divide the duration of the burst (T_{90}) into several equal time intervals. Alternatively, one can split up events into several bins satisfying the same signal-to-noise ratio (SNR) or test statistic (TS). The Bayesian block method (§ 4.1.2) is also a good option. However, this method, sometimes, does not reflect high-energy features, due to relatively low high-energy counts. I choose one of these methods, which best reveals the characteristics of a burst.

In order to produce a count spectrum (PHA file) containing both signals and backgrounds for a given time interval, `gtbin` is used for GBM, LLE, and LAT data. The background rate of each GBM detector is estimated by fitting background regions of the light curve before and after the burst with polynomial functions using "*RMfit*" (4.3.2)[2]. I create the background spectrum (bak file) for the time intervals of interest by using background fit obtained in *RMfit*. A similar approach is used to

[1] `http://fermi.gsfc.nasa.gov/ssc/`
[2] `https://fermi.gsfc.nasa.gov/ssc/data/analysis/rmfit`

generate the background spectrum of LLE data. The background spectrum of LAT is extracted by using `gtbkg`, which computes the predicted counts from cataloged point sources and diffuse emission components in the ROI. The cataloged pointed sources are drawn from the 3FGL catalog [238], and I use the publicly available[3] isotropic (`gll_iem_v06`) and galactic diffuse (`iso_P8R2_TRANSIENT020_V6_v06`) templates to model the diffuse emission components. The GBM and LLE instrument responses are provided publicly by the *Fermi* collaboration, and the LAT instrument response is generated by using `gtrspgen`.

The spectral fitting is mainly performed with the "*XSPEC* " software package (12.9.1)[4] [239], in which I use $PG_{\rm stat}$ (Equation 4.26) for the parameter estimation. I test models described in § 4.2.2 and their combinations. The best-fit model is selected by comparing the BIC value (Equation 4.35), where a model with the lowest BIC value is considered to be the best-fit model. Sometimes, the likelihood ratio test (LRT) is alternatively used (Equation 4.30). When I analyze LAT data alone, I use an unbinned likelihood analysis tool (`gtlike`) implemented in the *ScienceTools*, because this tool fits the source and background spectra simultaneously. Table 5.1 summarizes data selections that I used for the analysis on the three GRBs.

5.2 Bright γ-ray Flares Observed in GRB 131108A

In this section, I present the three bright γ-ray flares observed in GRB 131108A, which are $\sim 6 - 20$ times brighter than than an underlying light curve. I compare

[3] `http://fermi.gsfc.nasa.gov/ssc/data/access/lat/BackgroundModels.html`
[4] `https://heasarc.gsfc.nasa.gov/xanadu/xspec`

Table 5.1: **Summary of data preparation for three GRBs**

	GRB 131108A	GRB 160709A	GRB 190114C
NaI	n0, n3, n6, and n7	n3, n4, n6, and n7	n4 and n7
BGO	b0 and b1	b0 and b1	b0
NaI energy band	8 keV–30 keV and 40 keV–900 keV		
BGO energy band	260 keV–38 MeV		
LAT	Transient020E and LLE		
LAT energy band	100 MeV–10 GeV	100 MeV–10 GeV	100 MeV–100 GeV
LLE energy band	30 MeV–100 MeV	20 MeV–100 MeV	30 MeV–100 GeV
roi	15°	15°	12° / 10°
zmax	100°	100°	105° / 110°
Analysis tool	*Xspec* and *Fermi Science Tools*		
Fit statistic	$PG_{\rm stat}$		
Model Selection	BIC	LRT	BIC

spectral and temporal properties of three γ-ray flares and the X-ray flares. Also, I perform the broadband spectral analysis and the correlation test between the low- and high-energy bands.

5.2.1 Unusual LAT GRB Light Curve - γ-ray Flares

At 20:41:55.76 UTC on 2013 November 8 (T_0), LAT triggered on a bright high-energy emission from GRB 131108A [240], which is simultaneously observed by the GBM [241]. The duration of the burst T_{90}, is 18.2 seconds, but the high-energy emission lasts $\sim T_0 + 600$ seconds. With the observation of the bright afterglow of GRB 131104A by various instruments such as *Swift* [242, 243], *AGILE* [244], the accurate location and redshift of GRB 131108A were reported as (R.A., Dec.) = (156.50°, 9.66°) [243] and z $\sim$ 2.40 [245], respectively.

The LAT events of GRB 131108A are binned. For four sequential LAT events, we perform an unbinned likelihood analysis, and compute a test statistic (TS)[5] for the burst. If the resultant TS is lower than 9 (equivalent to 3 σ), we add the next

[5]the detection significance of the source above the background

event to the bin and compute the TS again. Once we have the bin with the TS ≥ 9, we collect the following four events, and repeat this procedure. As a result, each bin contains at least four LAT events, resulting in a TS ≥ 9. For each of these bins, I perform an unbinned maximum likelihood fit with χ^2 (Equation 4.21) on the energy spectrum with a PL model (Equation 4.15). Note that in this work, the power-law model is defined as $dN/dE = N_0 E^{-\Gamma}$.

The high-energy light curve of GRB 131108A contains three significant flares, which is unusual for LAT GRBs (Figure 5.1); rather, it resembles the canonical GRB afterglow light curve with three flares [31,32]. I find the best description of the LAT light curve by fitting several models and their parameters with the maximum likelihood method. The light curve is well-fitted with five components (χ^2 / dof = 20.8 / 34): a simple power law, a broken power law, and three Gaussian functions for the three bright pulses above an underlying emission. Note that single-component models such as a simple power law (χ^2 / dof = 130.8 / 47) or a broken power law (χ^2 / dof = 90.8 / 45) are not a good model for this light curve. The model of each pulse can be replaced with the Norris function [65] (χ^2 / dof = 20.5 / 31) , a broken power law (χ^2 / dof = 20.2 / 31), or a smoothly broken power law [246] (χ^2 / dof = 19.4 / 28). However, the Gaussian function is the best-fit model considering its statistics and the number of free parameters. The best-fit parameters for the three Gaussian functions are listed in Table 5.2. The fluence of each pulse is (2.0 ± 0.8), (1.6 ± 0.6), and $(1.7 \pm 0.7) \times 10^{-6}$ erg cm^{-2}, totally $(5.3 \pm 1.2) \times 10^{-6}$ erg cm^{-2}. The fluence of each pulse is comparable to that of emission during the early steep decay phase, $(1.7 \pm 0.4) \times 10^{-6}$ erg cm^{-2}. The decaying index of the later segment

Table 5.2: **The estimated physical properties of three flares in GRB 131108A**

	Peak flux[a] [$\times 10^{-6}$ erg cm^{-2} s^{-1}]	Peak time [s]	FWHM [b] [s]	Fluence[a] [$\times 10^{-6}$ erg cm^{-2}]
Flare 1	2.6 ± 1.3	3.5 ± 0.1	0.8 ± 0.2	2.0 ± 0.9
Flare 2	1.4 ± 0.6	6.0 ± 0.1	0.9 ± 0.2	1.6 ± 0.6
Flare 3	2.4 ± 1.0	8.5 ± 0.1	0.9 ± 0.2	1.6 ± 0.6

[a] in 100 MeV – 10 GeV
[b] Full width at half maximum

of the broken power law is $\hat{\alpha} = 1.6 \pm 0.2$, consistent with other LAT GRBs [37].

Considering the LAT light curve and its best-fit model, I define three time periods: the early steep decay period (time period 1; T_0+0.3 s – T_0+2 s), the three γ-ray unusual pulses with the underlying emission period (time period 2; T_0+2 s – T_0+10 s), and the long-lasting shallow decay period (time period 3; T_0+10 s – T_0+20 s). Note that the third time period can be extended until the end of the LAT emission, but I decide to limit the time interval to the end of the prompt emission for the joint-fit purpose. The evolution of the first and last periods is commonly seen in the LAT GRBs, but the phenomena of the second time period are noteworthy.

For the three time periods, I perform a broadband spectral analysis with GBM and LAT data in energy band from 10 keV to 10 GeV. In the first time period characterized by the short bright emission commonly observed in the broad energy band from 10 keV to 10 GeV, the best-fit model for this time period is the Band

function [8] with a high-energy cutoff,

$$\frac{dN}{dE} = \begin{cases} N_0 \left(\frac{E}{100\text{keV}}\right)^{\alpha} exp\left(-\frac{E(\alpha+2)}{E_p}\right) & \text{if } E \leq \frac{\alpha-\beta}{2+\alpha}E_p, \\ N_0 \left(\frac{E}{100\text{keV}}\right)^{\beta} \left(\frac{E_p}{100\text{keV}}\frac{\alpha-\beta}{2+\alpha}\right)^{\alpha-\beta} exp(\beta-\alpha) & \text{if } \frac{\alpha-\beta}{2+\alpha}E_p < E \leq E_c, \\ N_0 \left(\frac{E}{100\text{keV}}\right)^{\beta} \left(\frac{E_p}{100\text{keV}}\frac{\alpha-\beta}{2+\alpha}\right)^{\alpha-\beta} exp(\beta-\alpha) exp\left(\frac{E_c-E}{E_f}\right) & \text{if } E > E_c, \end{cases} \tag{5.1}$$

where α and β are the low- and high-energy photon indices, respectively, E_p is the peak energy of the Band function, E_c is the cutoff energy which is fixed to 50 MeV, and E_f is the e-folding energy for the high-energy cutoff (Table 5.3). The decrease in BIC as a result of adding the high-energy cutoff to the Band function is $\sim$ 17 units, implying that the high-energy cutoff is strongly required. One alternative model is a combination of two spectral components, Band (Equation 4.17) and CPL (Equation 4.16). This Band + CPL model describes the data slightly better (lower PG-stat), but the statistical improvement is not high enough to compensate the increase of a free parameter, making BIC higher than the best-fit model.

The second time interval where I found the unusual pulses shows a high count rate only in the low- (10 keV–1 MeV) and high-energy regimes (100 MeV–10 GeV) (upper panel in Figure 5.2). The observed data is best explained by a two-component model, CPL + CPL (orange in Figure 5.2), which is preferred over a single-component model such as Band (Table 5.3). The two CPLs have distinct peak energies, $E_{p,\text{low}} \sim 400$ keV and $E_{p,\text{high}} \sim 130$ MeV, respectively (Table 5.3). When any one of the CPL components is replaced with the Band function, β becomes very soft so that the high-energy segment of Band is indistinguishable from

the exponential cutoff. Therefore, the combination of Band and CPL is not necessary. The two-component scenario for GRB 131108A is also reported by [247], who analyzed the *AGILE* (350 keV–30 GeV) data and reached the conclusion that the extrapolation of the low-energy spectral component could not explain the high-energy emission, and an additional spectral component with a peak energy at few MeV is required. The CPL dominating in the low-energy band has $\alpha \simeq$ -0.5 consistent with that of the best-fit model in the first time period (Table 5.3), implying that the low-energy emission of the first and second time periods may be continuous. Given the best-fit model, the LAT emission is described by the high-energy CPL component. The fluence of this high-energy component during the second time period is $5.9^{+0.5}_{-0.8} \times 10^{-6}$ erg cm^{-2}, comparable to the sum of fluence from three γ-ray pulses, $(5.2 \pm 1.2) \times 10^{-6}$ erg cm^{-2} (Table 5.2). Most of the LAT emission during the second time period can be dominated by the three γ-ray pulses, and thus the high-energy CPL component may represent the spectral shape of the three γ-ray pulses.

During the third time period, short-soft pulses in the low-energy band ($<$ 500 keV) are observed. The best-fit model in this time period is the Band function (green in Figure 5.2). A CPL + CPL model does not give a better result, which requires the two more parameters but resulting in the similar statistics (Table 5.3). After T_0 + 20 s, the LAT spectrum is well-described by a power law with a photon index $\Gamma = 2.8 \pm 0.3$.

Figure 5.1 and the upper panel of Figure 5.2 show that the low- (keV to few MeV) and high-energy (100 MeV–10 GeV) light curves evolve differently, and the

broadband spectral analysis reveals the presence of the two spectral components. I check correlation between the low- and high-energy light curves with the DCF (Equation 4.12), which compares the variability of two light curves and estimates the time lag and the respective cross-correlation coefficient [248]. For this purpose, I performed a time-resolved spectral analysis for the time bin used for the LAT light curve (Figure 5.1) with the GBM data, and computed flux in the range of 10 keV–10 MeV with the best-fit model for each time interval (orange points in Figure 5.1). When the entire interval is considered, the correlation between the two light curves, 10 keV–10 MeV and 100 MeV–10 GeV, is evident (correlation coefficient peak = 0.8 $\pm$ 0.1). However, if only the light curves in the second time period is considered, the correlation analysis does not suggest any correlation between the two light curve (correlation coefficient peak $\sim$ 0.1).

Considering the temporal and spectral features, the γ-ray pulses invoke a distinct origin from the prompt emission of the low-energy band as well as the LAT extended emission. Therefore, from now on, the individual γ-ray pulse is called a "γ-ray flare".

5.2.2 Characteristics of γ-ray Flares

I compare and test the well-known properties of X-ray flares to the γ-ray flares in GRB 131108A.

A flux variation of the X-ray flares, $\delta F_\nu / F_\nu$, ranges from 6 [102] to higher than 100 [33]. The γ-ray flares are about 6 to 20 times brighter than the underlying

emission, which slowly changes in time, $F_\nu \sim 2.7 \times 10^{-7}$ erg cm^{-2} s^{-1} on average (see Figure 5.1), and thus the flux variation of the γ-ray flares is sub-normal, compared to X-ray flares [98]. The duration of the X-ray flares varies from few hours to a day [98, 249], and there is an empirical relation between the onset time and the duration of the X-ray flares, $\delta t/t \sim 0.1$ [98, 249, 250]. In case of the γ-ray flares, they last only few seconds (Table 5.2), much shorter than the X-ray flares [98]. Also, the γ-ray flares are observed in $< T_0 + 10$ s, which is rather earlier than any X-ray flares [98]. Combining these two unusual features, surprisingly, the temporal characteristics of the γ-ray flares are not in conflict with the empirical relation. A comparison between the flux variability and the temporal variability of the γ-ray flares ($\delta F_\nu/F_\nu$ vs. $\delta t/t$) shows that the γ-ray flares are consistent with X-ray flares [98]. This comparison implies that the γ-ray flares are not related to the fluctuations of the external shock as previously discussed for the X-ray flares [31,143].

The steep decay of the X-ray flares is regarded as a result of the curvature effect (§ 2.4.2.1), which is identified by testing the relation, $\hat{\alpha} = \hat{\beta} + 2$ (Equation 2.42) [98,104,105,246]. It is possible that the decay phase of the γ-ray flares can similarly show evidence of the curvature effect. Before testing the relation, I should remove the so-called T_0 effect [31, 251]. Each flare is attributed to the late-time activity of the central engine and thus has its own onset time (T_0). Since the shape of a light curve in the logarithmic space is very sensitive to the choice of T_0, the intrinsic light curve of the flare can only be provided if the light curve is shifted to the true T_0. Due to the underlying emission, however, the true onset of the γ-ray flares is ambiguous. Therefore, I choose the onset of each flare as the time when the flux of

the flare is 1/100 of its peak. Figure 5.3 shows the γ-ray flares after shifting them to the proper T_0 for each flare. For these light curves, I test the curvature effect relation. After selecting the data points corresponding to the decaying phase, I fit the measured photon indices (Γ) with a linear function, $\Gamma = f(t - T_0)$ (solid line in lower panel of Figure 5.3). Next, the photon index is converted to the spectral index, $\hat{\beta} = (\Gamma - 1)$. I then apply the HLE relation and get the temporal index as a function of time, $\hat{\alpha} = f(t - T_0) + 1$. Finally, the light curve expected by the curvature effect is described by a function of time, $F_\nu = F_{\nu,0}(t - T_0)^{f(t-T_0)+1}$ (solid line in upper panel of Figure 5.3). I fit this function with the observed, shifted flux points and conclude that the decay phases of all three γ-ray flares are consistent with the expectation by the curvature effect (Figure 5.3). Also, I find the spectral softening during the decay phase of the flares, which is the well-known phenomenon identified in the X-ray flares [98, 252].

The X-ray flares are likely attributed to internal shocks, where accelerated electrons at the shocks radiate via the synchrotron process. On the other hand, the γ-ray flares with $E_p \sim 130$ MeV may originate from the SSC process from same population of electrons that might have produced X-ray flares (§ 2.2.3.1). In principle, there could be two possible cases for the inverse Compton process: SSC from the internal emission region and the External Inverse Compton (EIC) from the external shock region [253, 254]. The observation of the high-latitude emission in the flares disfavors the EIC origin and supports the SSC origin. Assuming the typical electron Lorentz factor, $\gamma_e \gtrsim 10^3$, the peak energy of the seed photon should be $\lesssim 0.13$ keV (Equation 2.17), which is far below the GBM energy band. Another

possibility for the origin of the γ-ray flares is the residual collision in the internal dissipation process [255]. In this case, the γ-ray flares can be interpreted as the SSC counterpart of the optical emission produced by the residual collision at large radii. Note that there were no early X-ray and optical observations for this GRB, so that the seed synchrotron spectra of the γ-ray flares are unknown.

The very first steep decay emission in the first time period corresponds to the tail of the first bright broadband pulse. This decay emission is also consistent with the curvature effect (the first panel in Figure 5.3). The underlying emission in the second time period can be interpreted as the emission during the development of the forward shock [256], and the long-lasting decay emission (the third time period) can be the continuous emission from the fully developed forward shock (§ 2.4.7) when the total energy is not noticeably increased by the additional energy injection [24, 95]. The observation of GRB 131108A uncovers a new phenomenon in the high-energy GRB light curve. Even though the three γ-ray flares were observed in the prompt phase of the burst, they showed the temporal and spectral properties similar to those of the X-ray flares. Also, I found the evidence of the curvature effect in the GeV energy band for the first time.

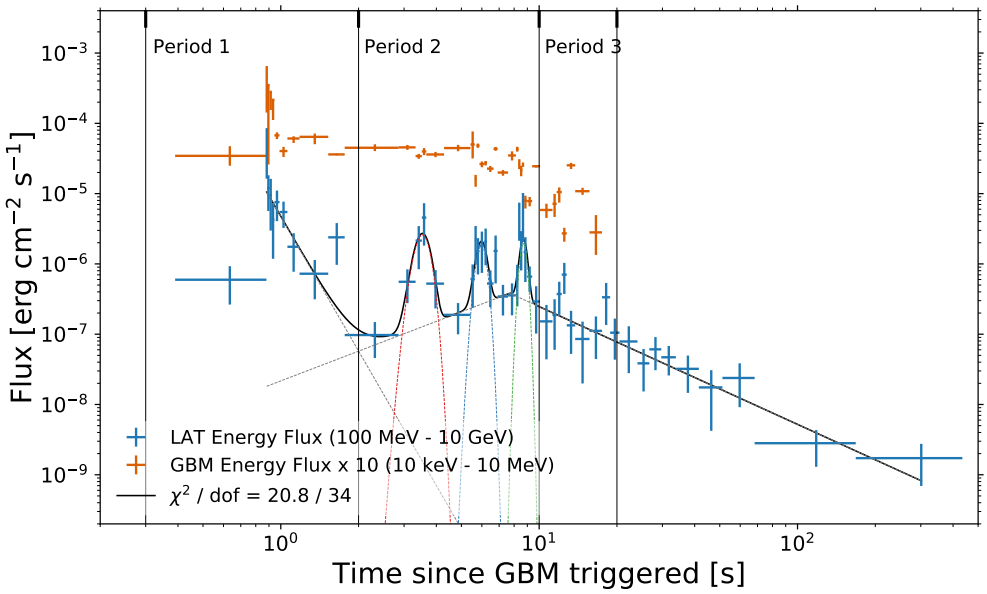

Figure 5.1: **GBM and LAT light curve of GRB 131108A.** The energy fluxes in the LAT energy band (100 MeV to 10 GeV) and in the GBM energy band (10 keV– 1 MeV) are plotted in blue and orange, respectively. They are calculated from the best-fit model for each time interval in the spectral analysis with each instrument. The solid black line shows the fit of the LAT light curve consisting of five components: a simple power law (dotted gray line), a broken power law (dotted gray line), and three Gaussian functions (dotted red, green, and blue lines). The lower panel shows the photon index of energy spectrum from 100 MeV to 10 GeV.

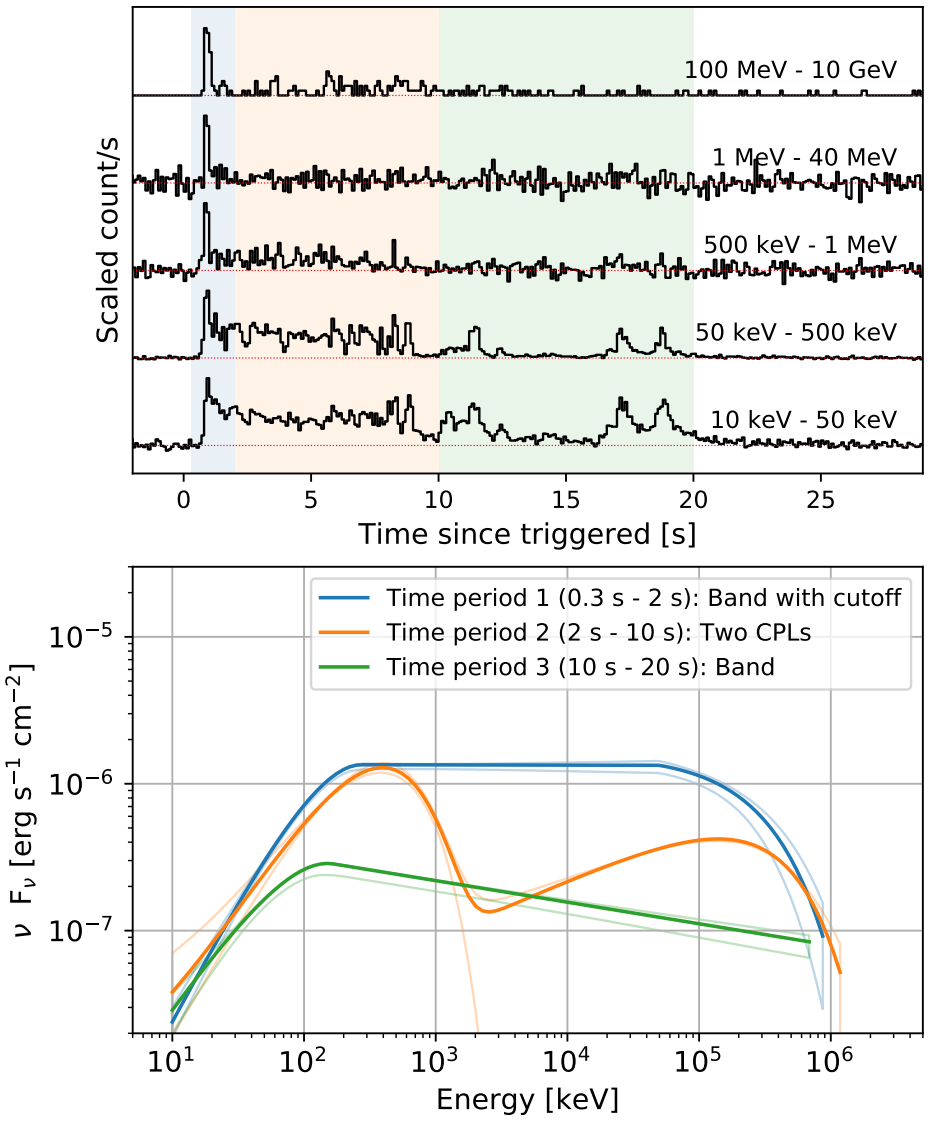

Figure 5.2: **Count-rate curves and spectral energy distributions for GRB 131108A**. The upper panel shows the scaled count-rate curves in different energy bands. The lower panel shows the joint-fit spectral energy distributions in energy band from 10 keV to 10 GeV for three time periods. The color coding of the shaded region in the upper panel and the spectrum in the lower panel indicates three time periods: blue (0.3 – 2 s), orange (2 – 10 s), and green (10 – 20 s). Each solid curve represents the best-fit spectral shape (thick) with 1 confidence level contour (thin) derived from the errors on the fit parameters.

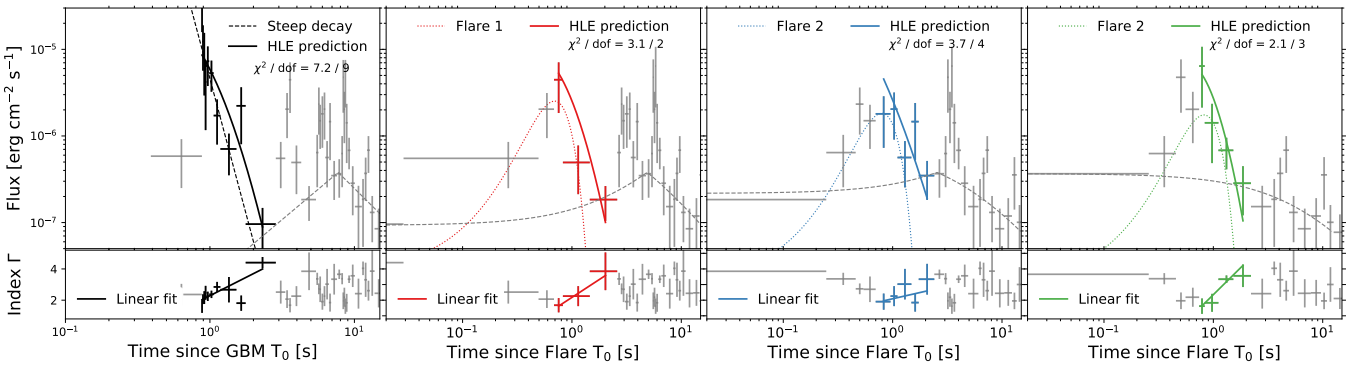

Figure 5.3: **Test of the curvature effect for early steep decay emission and three γ-ray flares.** The upper panels show the light curve of the early steep decay emission and the three γ-ray flares separately after removing the T_0 effect. The lower panel shows the evolution of the photon index. The data points corresponding to the decay phase of each flare are painted in red, blue, and green. The early steep decay phase is marked in black. The solid lines in the upper panels show the expected light curve derived from the relation of the curvature effect, $\hat{\alpha} = 2 + \hat{\beta}$. These theoretical light curves are computed from the linear fit of the photon indices of the decay phase (solid line in the lower panel).

Table 5.3: **The joint-fit spectral analysis result for GRB 131108A.**

time period	Model	α	β	Γ	$E_{p,\mathrm{low}}$ [keV]	$E_{p,\mathrm{high}}$ [MeV]	E_f [MeV]	PG-stat	dof	BIC
1	Band	$-0.50^{+0.06}_{-0.06}$	$-2.07^{+0.02}_{-0.02}$		$320.6^{+22.3}_{-20.1}$			745	695	771
(0.3 – 2 s)	Band with highcut[a]	$-0.48^{+0.07}_{-0.06}$	$-2.01^{+0.02}_{-0.02}$		$305.3^{+21.5}_{-19.8}$		$350.3^{+143.1}_{-87.6}$	722	694	754
2	Band	$-0.73^{+0.02}_{-0.02}$	$-2.24^{+0.01}_{-0.01}$		$389.7^{+14.2}_{-13.4}$			880	695	906
(2 – 10 s)	CPL + CPL	$-0.50^{+0.07}_{-0.07}$		$1.69^{+0.02}_{-0.03}$	$394.2^{+13.3}_{-12.4}$	$126.2^{+25.6}_{-19.5}$		821	693	860
3	Band	$-0.94^{+0.05}_{-0.05}$	$-2.15^{+0.02}_{-0.02}$		$168.0^{+12.5}_{-11.2}$			741	695	767
(10 – 20 s)	CPL + CPL	$-0.92^{+0.13}_{-0.09}$		$1.68^{+0.07}_{-0.11}$	$198.9^{+13.7}_{-12.0}$	$68.7^{+21.5}_{-15.5}$		742	693	781

[a] The cutoff energy E_c is fixed to 50 MeV

5.3 Multiple Components in the Broadband γ-ray Emission of the Short GRB 160709A

In this section, I present the analysis of the bright short GRB 160709A detected with both GBM and LAT. Even though the LAT has detected more than 120 GRBs, only 10% of them are short GRBs [37]. Due to the scarcity of short GRBs detected with LAT, the nature of their high-energy emission is not well established yet, and the bright short GRB 160709A will improve our understanding of the emission mechanisms powering short GRBs. This section is the summary of the published paper in the *Astrophysical Journal* (*ApJ*) [41].

5.3.1 Short GRB 160709A Detected by Both GBM and LAT

At 19:49:03.50 UT on 09 July 2016 (hereafter T_0), GRB 160709A triggered GBM with significance of 5.6 σ [257]. The ground analysis of *Swift*/BAT reported a 9 σ excess consistent with GRB 160709A at (R.A., Dec.) = (235.996°, -28.188°) within a 0.04° error radius [258]. GRB 160709A was also detected by LAT at $\sim$ 17 σ with the clean event type of the data beyond 100 MeV [259] as well as at 10 σ using LLE data beyond 10 MeV. The prompt emission of GRB 160709A was also detected by *Wind*/Konus [260], the *CALorimetric Electron Telescope (CALET)* [261], and *AstroSat* [262].

Figure 5.4 shows the light curves of GRB 160709A in various GBM and LAT energy bands. The GBM was triggered by a low-intensity pulse compared to the

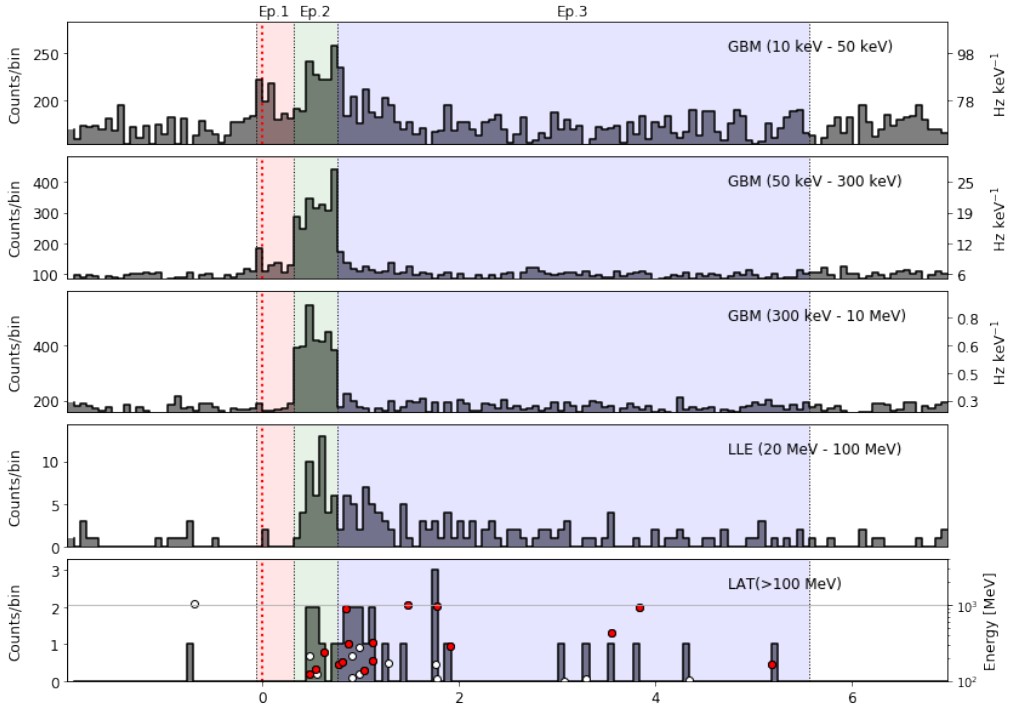

Figure 5.4: **Composite light curve of GRB 160709A in different energy ranges with the GBM, LLE, and LAT data.** The bin size is 0.064 seconds for all energy bands. The second panel shows the light curve in the energy range (50–300 keV) used for T_{90} calculation. In the bottom panel, the energies of the LAT events are displayed as circles where the highly associated events with GRB 160709A (with probability $> 90\%$) are filled in red. The red dotted vertical line represents GBM trigger time (T_0). The time interval of T_{90} is separated into three episodes by black dotted lines at T_0 + (-0.064, 0.320, 0.768, 5.568)s. The first and the last vertical lines represent T_{05} and T_{95}, respectively. The other two lines are chosen by the Bayesian-Block algorithm.

main emission episode observed about 0.3 seconds later. The main emission episode is followed by $\sim$ 4s–long tail. The T_{90} and T_{50} values of GRB 160709A computed between 50 and 300 keV [10] using GBM data are 5.63 $\pm$ 1.29 s and 0.58 $\pm$ 0.20 s, respectively. This GRB is considered as belonging to the short GRB category because its T_{50} value is a characteristic of a short GRB ($T_{50} \lesssim 1$), although the T_{90} value places GRB 160709A in the overlapped region of the T_{90} distribution of long and short GRBs [61]. This apparent inconsistency between T_{90} and T_{50} is explained

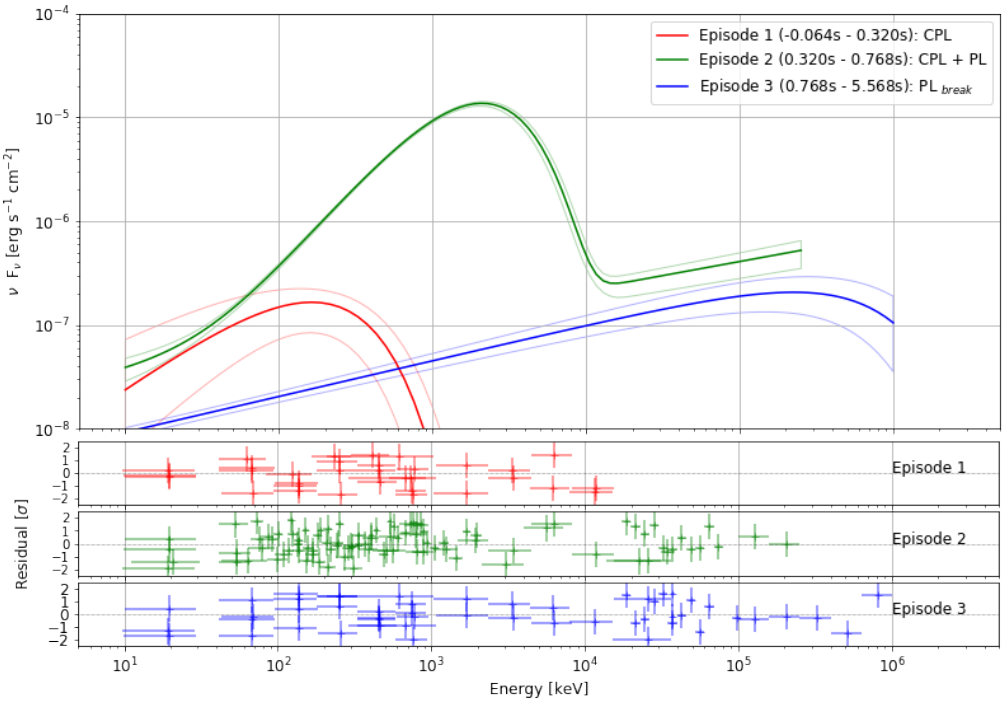

Figure 5.5: **GRB 160709A spectral energy distributions as measured by the *Fermi* GBM and LAT in different time intervals, using LAT Pass 8 data above 100 MeV and LAT–LLE data.** Each solid curve represents the best-fit spectral shape, within 1 σ confidence level contour derived from the errors on the fit parameters. Each episode is painted with distinct colors as Figure 5.4; red, green, and blue represent first, second, and third episode, respectively. The bottom panel shows the residuals of each best-fit model for the three episodes computed as (data-model)/error. Note that these residuals are not the same as the PG-stat contributions.

by the fact that the former is more sensitive to the low energy tail that follows the main emission episode. A similar result was also reported for the very bright short GRB 090510 detected with GBM [39]. The LAT detected more than 20 events above 100 MeV within $\sim$ 30 seconds. The highest energy photon is 991 MeV, detected at T_0 + 1.47 s.

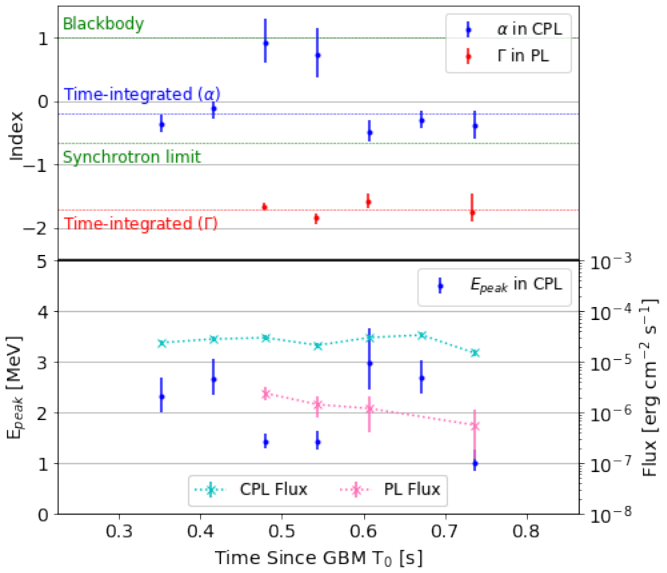

Figure 5.6: **Evolution of the CPL and PL parameters during the main emission episode.** The top panel shows the evolution of α (blue) and Γ (red). The horizontal lines show the time-integrated best-fit values of α and Γ, and blackbody radiation and synchrotron radiation limit (green, 1 and -2/3, respectively). Bottom panel shows the evolution of E_{peak} of CPL (Blue) and the fluxes of CPL and PL in 10 keV–40 MeV, which are cyan and pink respectively.

5.3.2 Multiple Spectral Components in GRB 160709A

I divide the time interval corresponding to T_{90} into three episodes (Figure 5.4). Both visual inspection of the composite light curve and the Bayesian-Block algorithm (§ 4.1.2) in different energy bands reach the same conclusion and result in the following cuts: [T_0-0.064 s, T_0 + 0.320 s], [T_0 + 0.320 s, T_0 + 0.768 s], and [T_0 + 0.768 s, T_0 + 5.536 s]. Table 5.4 shows the spectral fit results of the best-fit model and the alternative models.

The best-fit model for the first episode is CPL. The index of CPL agrees with the typical low-energy index of GRBs.

In the second episode, the Band model is not sufficient for describing the

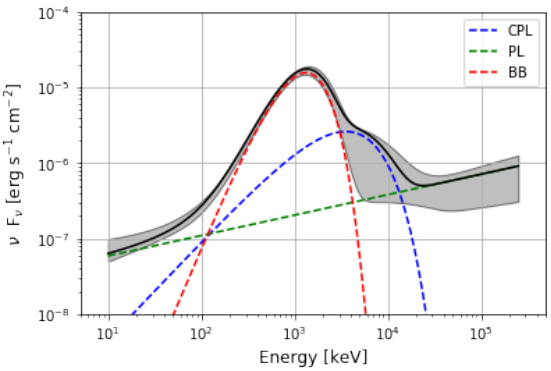

Figure 5.7: **Spectral energy distributions of GRB 160709A in the thermal dominant phase for the joint GBM + LLE + LAT analysis**. The time interval for the thermal dominant phase is from T_0+0.448 s to T_0+0.576 s. The solid black curve represents the CPL + PL + BB within 1 σ confidence level contour. The temperature of the BB component is about 340 keV.

prompt emission spectral shape of GRB 160709A. Instead, the CPL + PL model is a better description of data than the Band function alone. A three-component model (CPL + PL + BB) with fixed parameters (α = 0.7 and Γ = -1.5) [89] is an alternative model for this episode. I perform a time-resolved analysis for this episode with 64 ms time-binned intervals. Since the CPL + PL model is the best-fit model in this episode, I test the model in each time interval. Figure 5.6 shows the time evolution of PL and CPL parameters. Interestingly, the CPL parameters (blue and cyan) show significant evolution with time, contrast to that of the PL parameter (Γ; red). Especially in the third and fourth time intervals, [T_0 + 0.448 s, T_0 + 0.512 s] and [T_0 + 0.512 s, T_0 + 0.576 s], the slope of CPL (α) reaches $\sim$ +0.9 and $\sim$ +0.8, respectively. Such values are similar to a typical BB spectral index (Equation 4.18). I test the BB + PL model in these two time intervals. The model fits successfully the data with ΔPG-stat $\lesssim$ 2 with one more dof with respect to the CPL + PL model (Table 5.4). The temperatures of BB in the two sequential time

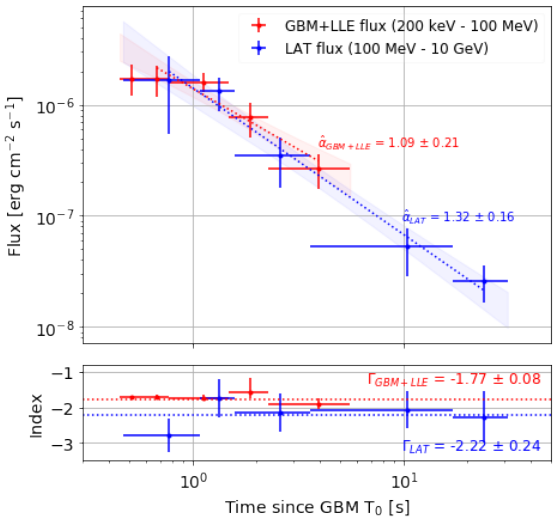

Figure 5.8: **Temporal evolution of the flux and the spectral index during the extended emission in GBM + LLE (Red, 200 keV–100 MeV) and LAT (Blue, 100 MeV–10 GeV) energy ranges.** The top panel shows the flux temporal evolution in dashed lines within 1 σ confidence level contour derived from the errors on the fit parameters. The indices of the temporal decay are displayed in this panel. The bottom panel shows the temporal evolution of power-law spectral indices.

intervals are 341^{+25}_{-23} keV and 334^{+30}_{-28} keV, respectively. A thermal dominant phase is defined based on this result, T_0 + 0.448 s to T_0 + 0.576 s, which is well described by the three-component model (Figure 5.7).

In the third time interval, the PL_{break} model is the best-fit model. The fit result shows a break at 219^{+134}_{-67} MeV with ΔPG-stat = 12 ($\sim 3.5\ \sigma$) with respect to a simple PL model. To track the temporal evolution of the energy spectrum below and above E_{break} independently, I perform spectral and temporal analyses in two different energy bands, GBM + LLE (200 keV to 100 MeV) and LAT (100 MeV to 10 GeV), with *Xspec* and *Fermi Science Tool*, respectively. For the GBM + LLE analysis, the time interval, [T_0 + 0.448 s, T_0 + 5.568 s], is considered. This time interval contains the part of the second episode and the third episode, assuming

that the additional PL component observed in the second episode and the PL_{break} component in the third episode originate from the same source. As for the LAT analysis, I use the time interval, [T_0 + 0.464 s, T_0 + 31 s] where they are the time of the first and last LAT events associated with GRB 160709A (with probability >90%). Figure 5.8 shows the evolution of the PL fluxes in the two energy bands. Both GBM + LLE and LAT show time-decaying features except the first point in the GBM + LLE energy range. I perform the maximum likelihood fit with the following power-law equation:

$$F(t) = F_0 \left(\frac{t}{1s} \right)^{-\hat{\alpha}} . \tag{5.2}$$

The flux in the two energy ranges decreases as a function of time with marginally different exponents of the temporal decays: the temporal indices $\hat{\alpha}$ of the GBM + LLE and LAT analyses are 1.09 $\pm$0.21 and 1.32 $\pm$ 0.16, respectively. During the time-decaying phase, the photon indices in the GBM + LLE and LAT energy bands are also different: 1.77 $\pm$ 0.08 and 2.22 $\pm$ 0.24, respectively (bottom panel in Figure 5.8). The photon index of GBM + LLE in the third episode is similar to that of the additional PL component observed in the second episode, $\Gamma_{\rm GBM+LLE} = -1.77$. These analogous features suggest that an emission process producing a power-law spectrum is continuous from the main episode to the tail end of the emission (at least in the energy band from 200 keV to 100 MeV). The photon index of LAT is slightly softer, $\Gamma_{\rm LAT} = -2.22$, implying a different emission process or condition.

Table 5.4: Spectral fitting to GBM + LLE + LAT data (8 keV–10 GeV) for various time intervals

T - T_0 [s]	Model	Band Model α	Band Model β	Band Model E_{peak} [keV]	Power Law with break Γ	Power Law with break E_{break} [MeV]	Blackbody kT [keV]	$PGstats$/dof	$\Delta PGstats$
Time-integrated analysis for each episode									
- 0.064 +0.320	PL				$-1.93^{+0.05}_{-0.06}$			710/709	
(Episode 1)	CPL	$-0.95^{+0.38}_{-0.31}$		163^{+82}_{-40}				683/708	- 29
+0.320 +0.768	CPL	$-0.40^{+0.05}_{-0.05}$		2329^{+149}_{-139}				882/708	
(Episode 2)	Band	$-0.34^{+0.06}_{-0.06}$	$-3.17^{+0.11}_{-0.12}$	2011^{+141}_{-127}				753/707	- 129
	CPL + PL	$-0.19^{+0.08}_{-0.07}$		2097^{+120}_{-114}	$-1.73^{+0.04}_{-0.04}$			735/706	- 147
	CPL + PL_{break}	$-0.18^{+0.08}_{-0.08}$		2081^{+120}_{-114}	$-1.61^{+0.07}_{-0.06}$	$58.6^{+46.0}_{-20.0}$		726/705	- 156
	CPL + BB	$-1.46^{+0.06}_{-0.06}$		14690^{+3608}_{-2619}			351^{+17}_{-16}	832/706	- 50
	3CM[a]	$-0.44^{+0.18}_{-0.17}$		2407^{+336}_{-258}	$-1.71^{+0.06}_{-0.05}$		358^{+60}_{-62}	733/704	- 149
	Fixed 3CM[b]	-0.70_{fixed}		2785^{+233}_{-234}	-1.50_{fixed}		376^{+36}_{-33}	738/706	- 144
+0.768 +5.568	PL				$-1.72^{+0.02}_{-0.02}$			857/709	
(Episode 3)	PL_{break}				$-1.66^{+0.03}_{-0.03}$	219^{+134}_{-67}		845/708	- 12
	$PL_{break+low\ roll-off}$[c]				$-1.75^{+0.05}_{-0.05}$	230^{+203}_{-82}		838/707	- 19
	$PL_{8\ keV–200\ keV}$				$-1.22^{+0.16}_{-0.15}$			321/230	
	$PL_{200\ keV–100\ MeV}$				$-1.77^{+0.08}_{-0.07}$			509/467	
	$PL_{100\ MeV–10\ GeV}$				$-2.22^{+0.24}_{-0.24}$				
	$PL_{200\ keV–10\ GeV}$	$-1.83^{+0.05}_{-0.04}$						521/477	
	Broken $PL_{200\ keV–10\ GeV}$	-1.77_{fixed}	-2.18_{fixed}			166^{+207}_{-95}		517/477	- 4
Time-resolved analysis for the second episode									
+0.448 +0.512	BB + PL				$-1.68^{+0.05}_{-0.06}$		341^{+25}_{-23}	667/707	
	CPL + PL	$0.91^{+0.38}_{-0.32}$		1423^{+148}_{-129}	$-1.67^{+0.06}_{-0.06}$			665/706	-2
+0.512 +0.576	BB + PL				$-1.85^{+0.07}_{-0.09}$		334^{+30}_{-28}	735/707	
	CPL + PL	$0.72^{+0.42}_{-0.35}$		1422^{+200}_{-156}	$-1.85^{+0.08}_{-0.09}$			734/706	-1
+0.448 +0.576	BB + PL				$-1.75^{+0.04}_{-0.04}$		338^{+19}_{-18}	751/707	
	CPL + PL	$0.85^{+0.28}_{-0.24}$		1419^{+115}_{-101}	$-1.74^{+0.04}_{-0.05}$			748/706	-3
	Fixed 3CM[d]	-0.70_{fixed}		3558^{+1883}_{-1390}	-1.73_{fixed}		338^{+23}_{-21}	746/706	-5

[a] Three-component model (CPL + PL + BB)

[b] Three-component model with fixed parameters suggested by [89](with α of CPL = -0.7, Γ of PL = -1.5, and BB)

[c] PL_{break} with low energy exponential roll-off, $E_{roll\text{-}off} = 25^{+16}_{-11}$ keV

[d] Γ in PL is fixed to Γ = -1.73 based on the time-integrated result.

5.3.3 Origin of the Thermal Emission Component

Given the steepness of the spectrum in the time-resolved analysis of the main episode, I interpret the spectrum as being dominated by thermal emission during ~ 0.12 s. As discussed in § 2.4.4, photospheric emission is naturally expected from the standard fireball model [46], and the photospheric model is suggested for the explanation of the spectrum with a very hard low-energy spectral index ($\alpha \gtrsim +0.7$; thermal emission) [145, 153, 167, 263, 264]. Since I found a very hard spectral index in GRB 160709A in the time interval [T_0 + 0.448 s, T_0 + 0.576 s], I test the photospheric model. This model constrains several important physical parameters such as the size of the central engine R_0, the photospheric radius $R_{\rm ph}$ and the bulk Lorentz factor $\Gamma_{\rm bulk}$ [148, 150, 151]. They are expressed as

$$R_0 \simeq \left[\frac{D_L \mathcal{R}}{2(1+z)^2}\left(\frac{F_{Th}}{F_{N-th}}\right)^{3/2}\right] \times \left[\frac{f_{N-th}}{\epsilon_T}\right]^{3/2}, \tag{5.3}$$

$$R_{ph} \simeq \left[\frac{\sigma_T}{16 m_p c^3}\frac{D_L^5 \mathcal{R}^3 F_{N-th}}{(1+z)^6}\right]^{1/4} \times [(1+\sigma_m) f_{N-th}]^{-1/4}, \tag{5.4}$$

and,

$$\Gamma_{\rm bulk} \simeq \left[\frac{\sigma_T}{m_p c^3}\frac{(1+z)^2 D_L F_{N-th}}{\mathcal{R}}\right]^{1/4} \times [(1+\sigma_m) f_{N-th}]^{-1/4}, \tag{5.5}$$

where z and D_L are redshift and luminosity distance. The luminosity distance D_L is calculated as

$$D_L = (1+z)\frac{c}{H_0}\int_0^z \frac{dz'}{\sqrt{\Omega_m (1+z')^3 + \Omega_\Lambda}} \tag{5.6}$$

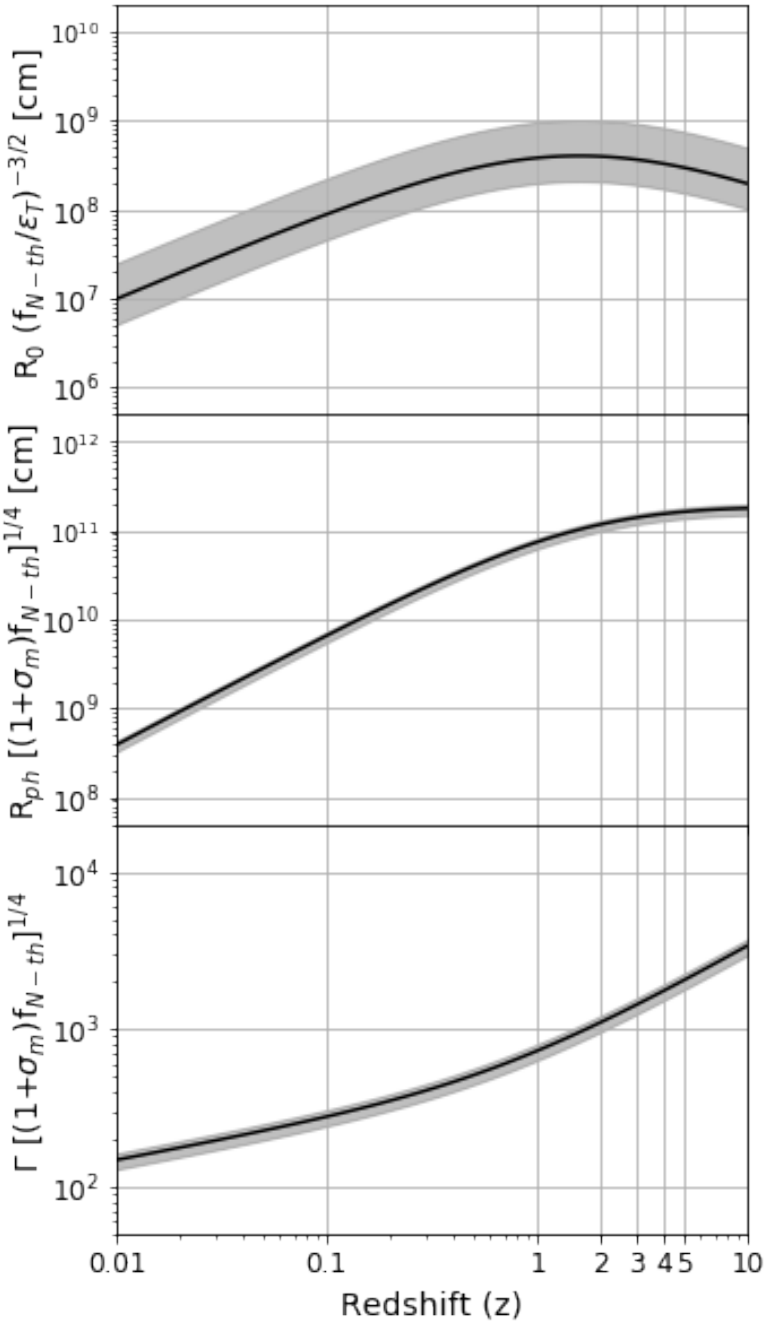

Figure 5.9: **Estimation of physical parameters as a function of redshift**: the initial fireball radius $R_0\,[f_{N-th}/\epsilon_T]^{-3/2}$, the photospheric radius $R_{\rm ph}\,[(1+\sigma_m)f_{N-th}]^{1/4}$ and the bulk Lorentz factor $\Gamma_{\rm bulk}\,[(1+\sigma_m)f_{N-th}]^{1/4}$. They were calculated by the photospheric model [148, 150, 151]. The solid-black line represents the most probable value at a given redshift within 1 σ confidence level contour. The three parameters increase with the redshift. For redshift z = 1, the size of the central engine is $R_0 = 3.8^{+5.9}_{-1.8} \times 10^8$ cm, the size of the photosphere is $R_{\rm ph} = 7.4^{+0.8}_{-1.2} \times 10^{10}$ cm, and the bulk Lorentz factor is $\Gamma_{\rm bulk} = 728^{+75}_{-93}$ assuming that the ratio f_{N-th}/ϵ_T and the product $(1+\sigma_m)f_{N-th}$ are equal to unity each.

with cosmological parameters from [265]. The fluxes F_{Th} and F_{N-th} are measured from the thermal component (BB) and non-thermal components (CPL and PL), respectively. The fluxes of the thermal and non-thermal components are $(2.1 \pm 0.3) \times 10^{-5}$ erg cm^{-2} s^{-1} and $(0.9 \pm 0.5) \times 10^{-5}$ erg cm^{-2} s^{-1}, respectively, which are computed in the energy band from 8 keV to 250 MeV. The parameter ϵ_T is the fraction of the initial energy released by the source in thermal form, σ_m is the magnetization of the relativistic outflow at the end of the acceleration process, and f_{N-Th} is the efficiency of non-thermal emission mechanism observed in the spectrum. The ratio between the measured BB flux and the expected BB flux $\mathcal{R}$ is given by Stefan–Boltzmann law;

$$\mathcal{R} = \left(\frac{F_{BB}}{\sigma T_{BB}^4} \right)^{1/2}. \tag{5.7}$$

As the redshift of GRB 160709A is unknown, therefore, I estimate R_0, $R_{\rm ph}$, and $\Gamma_{\rm bulk}$ as a function of redshift (Figure 5.9). The parameter R_0 ranges from 10^7–10^9 cm, $R_{\rm ph}$ from 10^8–10^{11} cm, and $\Gamma_{\rm bulk}$ from 10^2 to a few 10^3, assuming that the ratio f_{N-th}/ϵ_T and the product $(1+\sigma_m)f_{N-th}$ are of order unity, each, for $0.01 \lesssim z \lesssim 10$. This assumption is possible when f_{N-th} and ϵ_T have the same order. The f_{N-th} term should be $f_{N-th} \lesssim 0.1$ for an internal shock model (§ 2.4.5) [158] and can be higher than this limit for other models such as the magnetic reconnection model (§ 2.4.6). In terms of the fraction of the thermal energy of the source, the standard GRB scenario suggests $\epsilon_T \lesssim 0.1$ [40, 150, 151, 266]. The impact of σ_m on $R_{\rm ph}$ and $\Gamma_{\rm bulk}$ are negligible. A variation of σ_m of order 10^4 results in negligible changes of $R_{\rm ph}$ and $\Gamma_{\rm bulk}$, of order 10.

Since GRB 160709A is a short GRB, the expected size of R_0 is 10–100 times larger than the Schwarzschild radius of the central engine ($\sim 10^6$ cm) [267,268]. On the other hand, the size of photosphere $R_{\rm ph}$ is known to be 10^{11}–10^{13} cm (§ 2.4.4). The typical redshift of short GRBs is z $\sim$ 1 [125] (Table 2.2), and with a redshift of this order (or above) the values of R_0 and $R_{\rm ph}$ become plausible, $R_0 \sim 3.8 \times 10^8$ cm and $R_{\rm ph} \sim 7.4 \times 10^{10}$ cm. Note that they are still small, but can be explained by the unexpectedly high temperature of the BB component (kT $\sim$ 340 keV). The bulk Lorentz factor for $z \gtrsim 1$ is in harmony with a bulk Lorentz factor constrained from $\gamma\gamma$ opacity in other GRBs [38,125,269–273].

In conclusion, a thermal component in the time-resolved analyses can be interpreted as the photosphere emission of GRB 160709A. This burst clearly shows the thermal emission (BB) with very high temperature overwhelming non-thermal emission (CPL) in the 100 - 1000 keV energy band during the time interval [T_0 + 0.448 s, T_0 + 0.576 s]. Assuming the redshift of GRB1060709A, $z \gtrsim 1$, I derived the central engine radius $R_0 \simeq 10^8$ cm and the photospheric radius 10^{11} cm, which is surprisingly small compared to other previous reports.

5.3.4 Origin of the Additional Power-law Component

The additional spectral component emerges 0.448 s after T_0 during the main emission episode and persists up to the GeV domain until the end of the extended emission. The flux in two energy bands, the GBM + LLE (200 keV–100 MeV) and the LAT (100 MeV–10GeV), decreases with time as a PL function with two

different temporal exponents (Figure 5.8). This power-law decaying feature is well explained by the standard external forward shock model (§ 2.2.2 and § 2.4.7). I test the forward shock model with a set of closure relations derived in adiabatic hydrodynamic evolution (Table 2.3). Figure 5.10 shows the closure relations of different surrounding environment and cooling regime conditions. The two sets of spectral and temporal indices from the GBM + LLE and LAT analyses seem to be related with different closure relations; the set obtained from GBM + LLE analysis is positioned at a closure relation of the slow cooling condition ($\nu_m < \nu < \nu_c$) and ISM environment (red line in Figure 5.10), and the set from the LAT analysis is,

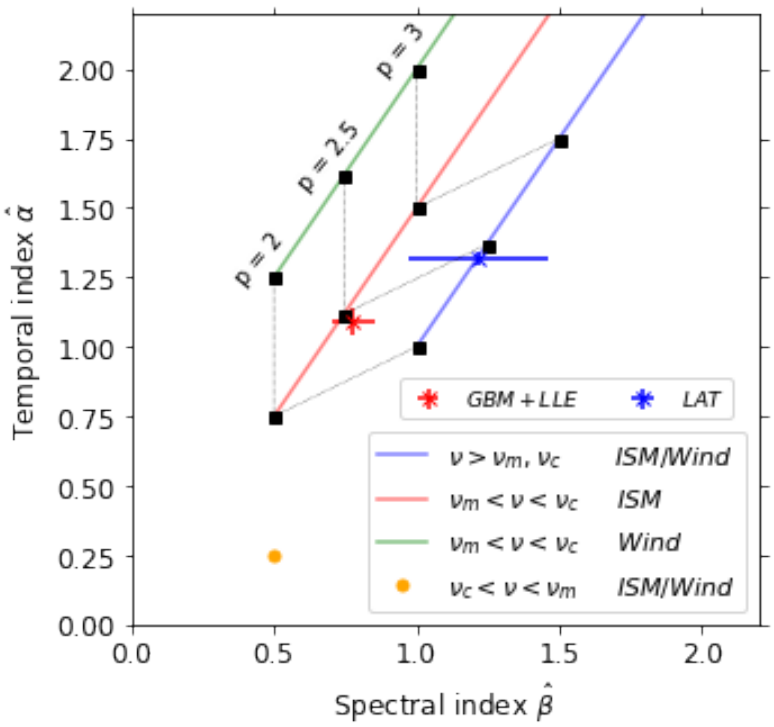

Figure 5.10: **Spectral and temporal indices observed in GRB 160709A and their best-matched closure relations.** The red and blue crosses correspond to the set indices obtained with the GBM + LLE and LAT analyses, respectively. The three colored lines (blue, red, and green) correspond to various closure relations. The gray lines connect the black points that have the same electron energy index (p = 2, 2.5, and 3) of three closure relations.

Table 5.5: **Closure relation test to GRB 160709A**

	Energy range	$\hat{\alpha}$	$\hat{\beta}$	$p_{\hat{\alpha}}$	$p_{\hat{\beta}}$	weighted average p
GBM + LLE	200 keV–100 MeV	1.09 ± 0.21	0.77 ± 0.08	2.46 ± 0.29	2.55 ± 0.16	2.49 ± 0.12
LAT	100 MeV–10 GeV	1.32 ± 0.16	1.22 ± 0.24	2.43 ± 0.21	2.44 ± 0.49	

on the other hand, at a closure relation corresponding to the fast cooling condition ($\nu > \nu_m$ and ν_c) with an undetermined surrounding environment condition (blue line in Figure 5.10).

This result implies that the surrounding medium of GRB 160709A is the ISM environment rather than the wind environment. This agrees with the theoretical expectation for the surrounding medium of short GRBs [5, 17, 274]. Also, this result suggests that ν_c is located in between the GBM + LLE energy band and the LAT energy band. The spectral break detected with 3.5 σ significance in the third episode ($E_{bk} \sim 166$ MeV) supports the hypothesis of the existence of ν_c at the high-energy band (> 100 MeV). I explore the plausibility of such high ν_c with a simple assumption. Assuming that the GRB isotropic energy $E_{\rm iso} = 10^{52}$ ergs and surrounding medium density n $= 10^{-3}$ cm^{-3} [275, 276], the electron cooling frequency ν_c in the ISM environment can be expressed as [95]

$$\nu_c \simeq 7.9 \times 10^{14} \epsilon_B^{-3/2} \left(\frac{E_{\rm iso}}{10^{52} ergs} \right)^{-1/2} \left(\frac{n}{10^{-3} cm^{-3}} \right)^{-1} \left(\frac{t}{1s} \right)^{-1/2} Hz \tag{5.8}$$

.

If ν_c is 166 MeV at 3 seconds, the middle of the third episode, the above equation gives the magnetic energy density fraction, $\epsilon_B \simeq 5.1 \times 10^{-4}$. This fraction is consistent with other observations [205] (Figure 2.27)

From the two $\hat{\beta}$[6] and $\hat{\alpha}$ sets and corresponding closure relations, I compute the value of the electron spectral index p of GRB 160709A (Table 5.5). The p values from the two different closure relations are consistent with each other. A weighed average of p_β is 2.49 ± 0.12, which is consistent with other observational studies [201–204].

In conclusion, the origin of the additional PL emission and the high-energy extended emission is regarded as the external forward shock. The spectral and temporal indices of the GBM + LLE (200 keV–100 MeV) and the LAT (100 MeV–10 GeV) analyses separately, have different closure relations, although the implications from the two closure relation do not conflict. I found that ν_c seems to be located between GBM + LLE and LAT energy bands. The surrounding environment is preferred to be the ISM environment rather than the wind environment. This analysis revealed the electron spectral index $p = 2.49 \pm 0.12$ for GRB 160709A. This is the first trial of testing GRB closure relations in the two distinct high energy bands, and the observational properties are well interpreted by the external forward shock model.

5.4 High-energy Observations of GRB 190114C by *Fermi* and *Swift*

In this section, I present the high-energy detection of GRB 190114C by *Fermi* and *Swift*, which was exceptionally bright in the observer frame. GRB 190114C was among the most luminous GRBs detected by GBM and LAT below $z < 1$ [37][7]. This burst shows the transitions from internal shock to external shock dominated emission

[6]Since the power law is defined as Equation 4.15, the spectral index $\hat{\beta}$ is equal to -(Γ+1).
[7]The brightest GRB is GRB 130427A

in both GBM and LAT. This burst is captivating due to its very high energy (VHE) emission above 100 GeV by MAGIC. Note that I led the GRB spectral analysis and contributed to the theoretical interpretation, and the overall work was coordinated by Daniel Kocevski [277].

5.4.1 Unusual High-energy Emission from GRB 190114C

On 2019 January 14 at 20:57:02.63 UT (T_0), GBM triggered and localized GRB 190114C. The burst occurred 68° from the LAT boresight and 90° from the Earth zenith at the time of the GBM trigger. The burst was particularly well detected by the GBM [278], producing over ∼30,000 counts per second above background in the most illuminated NaI detector. The LAT detected a gamma-ray counterpart located at R.A. (J2000), Dec.(J2000) = 54.57°, -26.99° with an error radius of 0.05° [278]. Such a high GBM count rate would normally trigger an Autonomous Repoint Request (ARR), in which the spacecraft slews to keep the burst within the LAT field of view (FOV). Unfortunately ARR maneuvers have been disabled since 2018 March 16 due to Sun pointing constraints as a result of an anomaly with one of the two Solar Drive Assemblies that articulate the pointing of the spacecraft's solar panels. As a result, the burst left in the LAT field of view (FOV) at T_0+150 sec and left the GBM FOV at T_0+260 sec when it was occulted by the Earth. The burst re-emerged from Earth occultation at T_0 + 2500 s, but remained outside the LAT field of view for an additional orbit, re-entering the LAT FoV at T_0 + 8600 s.

GRB 190114C triggered the *Swift* Burst Alert Telescope (BAT) at 20:57:03

UT, and the spacecraft immediately slewed to the on-board burst localization [279]. The X-ray Telescope (XRT) began observing the field at 20:58:07.1 UT, 64.63 sec after the GBM trigger, with settled observations beginning at T_0 + 68.27 sec. The UV Optical Telescope (UVOT) began observing the field at T_0+73.63 sec with a 150 sec finding chart exposure[8] using a White filter. The XRT and UVOT detected X-ray and optical counterparts, respectively, with a consistent location of R.A.(J2000), Dec.(J2000) = 54.505°, -26.946° with an uncertainty of 0.001° [281,282], which is also consistent with the LAT position. Both the XRT and UVOT continued observing the burst location for two weeks, with the last observation occurring 13.86 days post trigger.

A putative host galaxy was identified in Pan-STARRS archival imaging by [283]. The redshift of this burst was estimated with absorption lines in the afterglow spectrum, reported by the Nordic Optical Telescope (NOT), $z = 0.42$ [284]. Most notable the MAGIC Cherenkov telescopes [285] also detected the burst, which reported a significant detection of high-energy photons above 300 GeV. The MAGIC observations marks the first significant detection of a GRB by a ground based Cherenkov telescope.

Figure 5.11 shows the background subtracted BAT, GBM, and LAT light curves for GRB 190114C in several different energy ranges. The BAT and GBM light curve can be characterized by highly variable prompt emission episodes, separated by a quiescent period lasting roughly ∼7 seconds. The highest energy photon, with

[8]The finding chart data consists of a small subset of the pixels in an image, which helps ground-based observers localize GRBs [280].

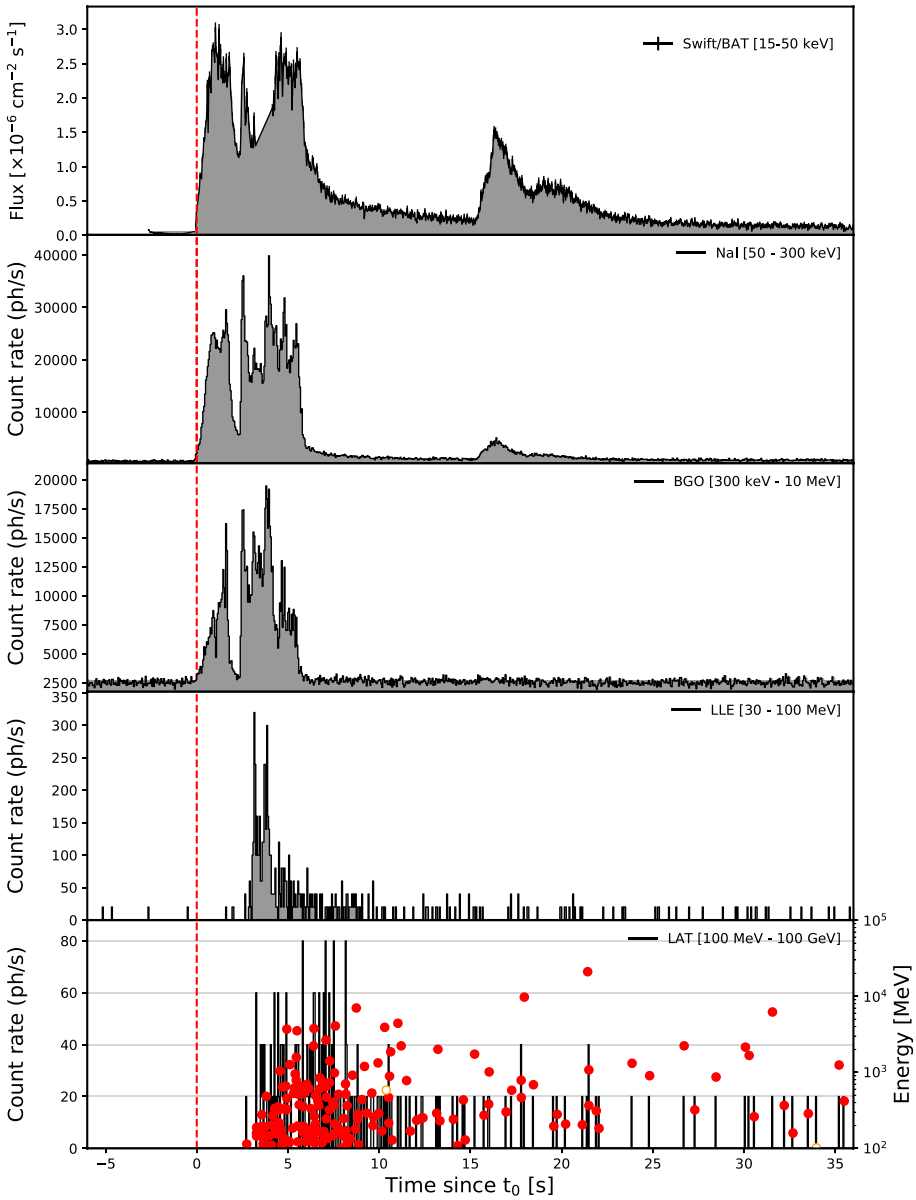

Figure 5.11: **Composite light curve for GRB 190114C**. The top three panels show the light curves for the most brightly illuminated NaI (4, 7) and BGO (0) detectors in the 8–20 keV, 20–200 keV, and 250–10 MeV energy ranges. The first panel displays the flux in the 15–50 keV energy range as measured from BAT. The bottom two panels show the LAT data for the LLE and `Transient 10` class events in the 30–100 MeV and >100 MeV energy ranges, respectively. The last panel shows the arrival times and energies of the individual LAT photons. Fill circles are the ones with probability p>0.9 to be associated with the GRB. The red vertical dashed line correspond to the GBM trigger time, and the dotted vertical lines are the intervals in which I perform time-resolved spectral analysis.

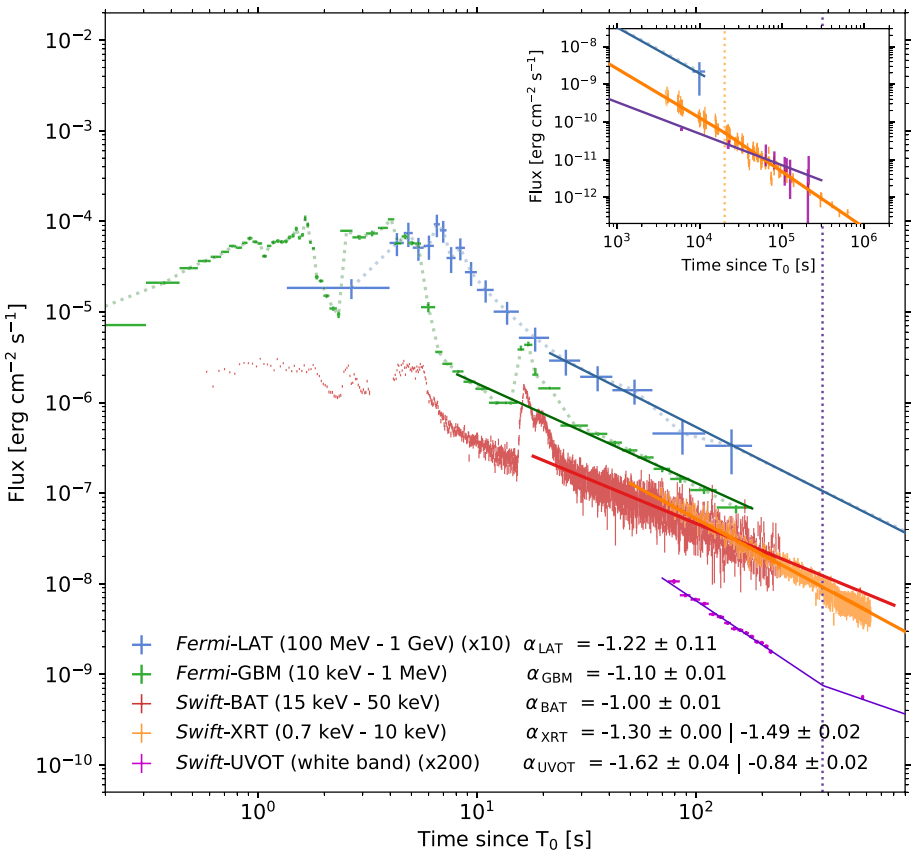

Figure 5.12: **Multi-wavelength afterglow light curves for GRB 190114C**: UVOT (purple), XRT (orange), BAT (red), GBM (green), and LAT (blue). The BAT, GBM, and LAT emission show a transition after $\sim$ T$_0$ + 10 s to an extended emission component decaying smoothly as a power-law in time (solid lines). Both XRT and UVOT light curves are well described by a broken power law, respectively (solid line), and their break times are 19.8 $\times$ 10^3 s ($\sim$ 5.5 hrs) and 377 s, respectively (dotted line). The inset shows the light curve of LAT, XRT and UVOT up to $\sim$ T$_0$ + 23 days.

an energy of 21.0 GeV, was detected at T_0+20.9 s, indicating a spectral hardening of the LAT detected component as the burst proceeds. The prompt emission appears superimposed on a smoothly varying emission component that is present during the quiescent period and extends beyond the cessation of the highly variable emission. The T_{90} and T_{50} durations (50–300 keV), which are 116.4±2.6 s and 6.9±0.3 s, respectively, reveal that significant GBM emission above background exists longer than the prompt emission seen within the first 25 seconds of the burst. The minimum

variability time (§ 4.1.2) is $t_{\rm min}$ = 5.41 ± 0.13 ms in the NaI detectors, 6.49 ± 0.38 ms in the BGO detectors and 30.00 ± 4.74 ms in the LLE band (20-200 MeV) of the LAT detector.

Figure 5.12 shows afterglow light curves of GRB 190114C for the XRT, BAT, GBM, and LAT data. The BAT, GBM, and LAT light curves show an obvious transition from the highly variable prompt emission to a smoothly decaying afterglow component. At later times, the three light curves commonly decay in time with consistent decay indices, $\alpha \sim$ -1, implying that they originate from the same emitting region. The XRT light curve is well described by a broken power law with temporal indices of -1.30 and -1.49 with the break occurring at approximately $t_{\rm break} \sim T_0$ + 19.8 × 10^3 s ($\sim$ 5.5 hrs) (see inset in Figure 5.12). The pre-break decay index of the XRT light curve differs from the indices measured for the BAT, GBM and LAT data, with $\alpha_{\rm XRT}$ = -1.3. On the other hand, the UVOT light curve exhibits decay slopes and a temporal break that are distinct from the XRT and BAT data. The temporal break occurs at $\sim$ 400 sec, with temporal indices before and after the break of -1.62 ± 0.04 and -0.84 ± 0.02 respectively. These decay indices are steeper than the decay observed in the XRT before the break in the UVOT data and shallower than the XRT decay afterwards. This implies that the UVOT is observing yet another distinct portion of the afterglow spectrum, although the break to a shallower decay index would indicate that the pre-break light curve contains additional emission contribution that does not affect the XRT flux.

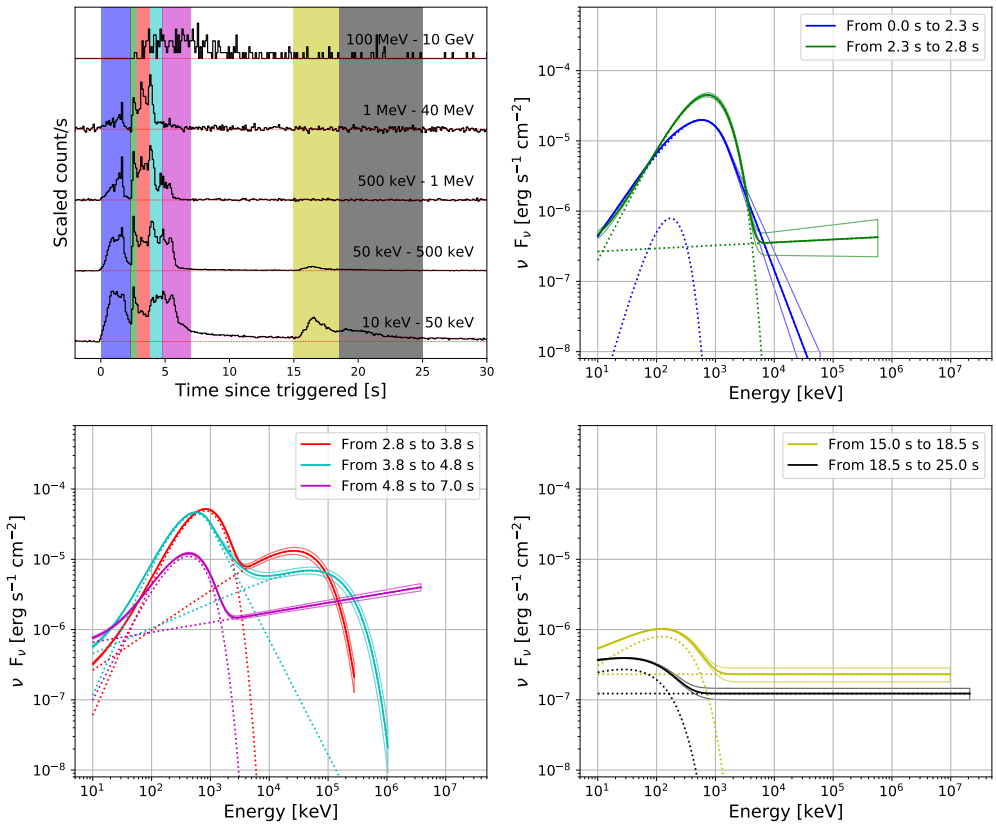

Figure 5.13: **Scaled light curves and spectra for GRB 190114C.** Each SED (and $\pm 1\sigma$ error contours) extends up to energy of the highest energy photon detected by LAT. The color coding used in the shading of time intervals in the top–left panel is carried over to the energy spectra in the other three panels. The best-fit model and its parameters are listed in Table 5.6.

5.4.2 Prompt Emission of GRB 190114C

I examine the underlying spectral characteristics of the prompt emission from GRB 190114C by performing joint time-resolved spectral analysis using the GBM and LAT data from T_0 to the start of the settled XRT observations at $T_0 + 68.27$ s.

The time interval from T_0 to $T_0 + 68.27$ seconds was subdivided into 7 intervals after considering the temporal characteristics shown in Figure 5.11. Figure 5.13 shows the best-fit model for each time interval. The spectrum of the first pulse

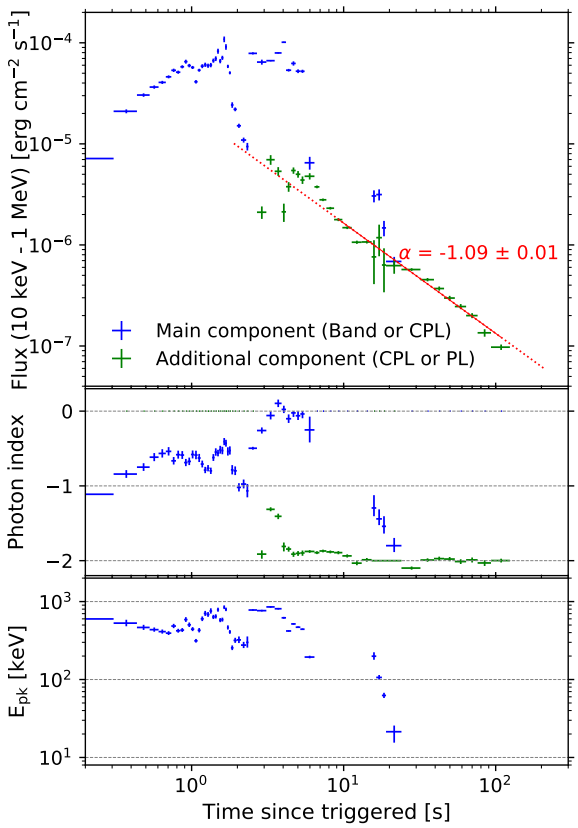

Figure 5.14: **Temporal and spectral evolution of each spectral component observed in GRB 190114C.** *Top*: flux, *Middle*: photon index, and *Bottom*: $E_{\rm pk}$.

phase (T_0 + 0 – 2.3 s) is best fitted with the Band + BB model. The addition of the BB component to the Band component is statistically preferred (ΔBIC $\sim$ 2). The peak energy ($E_{\rm pk}$) for the Band component is 586 $\pm$ 14 keV, and the temperature of the BB component is 44 $\pm$ 5 keV. The temperature of the BB component is consistent with similar components seen in other bright GRBs [40, 70, 79]

The main spectral component during the brightest emission episode observed from T_0 + 2.3 to 7.0 s is characterized by either CPL or Band. During this phase, the low-energy spectral index is very hard, ranging between -0.4 – 0.0 (see Table 5.6). The peak energy ($E_{\rm pk}$) reaches a maximum value of $E_{\rm pk} \sim$ 815 keV from T_0 +

2.8 to 3.8 s, before decreasing in time (see Table 5.6). This emission complex is characterized by many short and overlapping pulses, limiting our ability to characterize individual pulses, as they contain contributions from the spectral evolution of adjacent pulses.

An additional PL or CPL component begins to appear during the T_0 + 2.3 – 2.8 s time interval and lasts throughout the prompt emission phase. The arrival of the first LAT events above 100 MeV associated with the source begins at T_0 + ∼2.7 s, consistent with the emergence of this spectral component. In the third (T_0 + 2.8 – 3.8 s) and forth (T_0 + 3.8 – 4.8 s) time intervals, this additional component increases in brightness and exhibits a high-energy cutoff which increases in time, ranging from 26 – 52 MeV (see Table 5.6). The high-energy cutoff is strongly required in both time intervals compared to the models without the high-energy cutoff (ΔBIC $\gg$ 10). After $\sim$ 4.8 s, the high-energy cutoff in this additional component disappears, and the high-energy emission is well described by a PL with a photon index of $\Gamma = -1.86 \pm 0.01$ (or correspondingly a spectral index of $\hat{\beta} = 0.86 \pm 0.01$).

After the bright emission phase, the long-lived extended emission observed by both the GBM and the LAT is best described by a PL with an almost constant photon index of $\Gamma \sim -2$ (Figure 5.14). The energy flux of this extended emission phase (10 keV–1 MeV) shows a power-law decay in time with a temporal index of $\hat{\alpha}$ = -1.09 ± 0.02. The extrapolation of this extended emission back into the earlier bright emission phase reveals that the flux from the additional spectral component in the prompt emission evolves similarly to the extended emission. This implies that the emission from the additional component and the extended emission may

be due to the same emitting region. Since the power-law spectral and temporal characteristics of this broadband emission resemble the representative features of GRB afterglows, the end of the bright emission phase at about ~ 7 s represents the transition from the prompt to afterglow dominated emission.

In addition to the extended emission, a weaker, short-duration pulse, with soft emission primarily below $\lesssim 100$ keV, is observed from $T_0 + 15$ s to $T_0 + 25$ s. This weak pulse, along with the long-lasting extended emission, is well described with the CPL + PL model. We fix the photon index of the PL component to -2.0, assuming that the photon index of the energy spectrum of the extended emission is unchanged in time.

5.4.3 Afterglow of GRB 190114C

I continue the time-resolved spectral analysis from $T_0 + 68.27$ to $T_0 + 627.14$ seconds, but now include *Swift* data. For GBM, I now exclude channels below 50 keV for the n4 detector because of apparent attenuation due to partial blockage of the source by the spacecraft that is not accounted for in the GBM response. For LAT, I decrease the ROI size to 10° and increase the maximum zenith angle cut to 110°. Both changes are made in order to reduce the loss of exposure that occurs when the ROI exceeds the zenith angle cut and begins to overlap the Earths limb. This increase in exposure, though, comes at the expense of increased background during these intervals at which the burst position is approaching the Earth limb. The BAT and XRT data are provided by the *Swift* collaboration. The detail of the

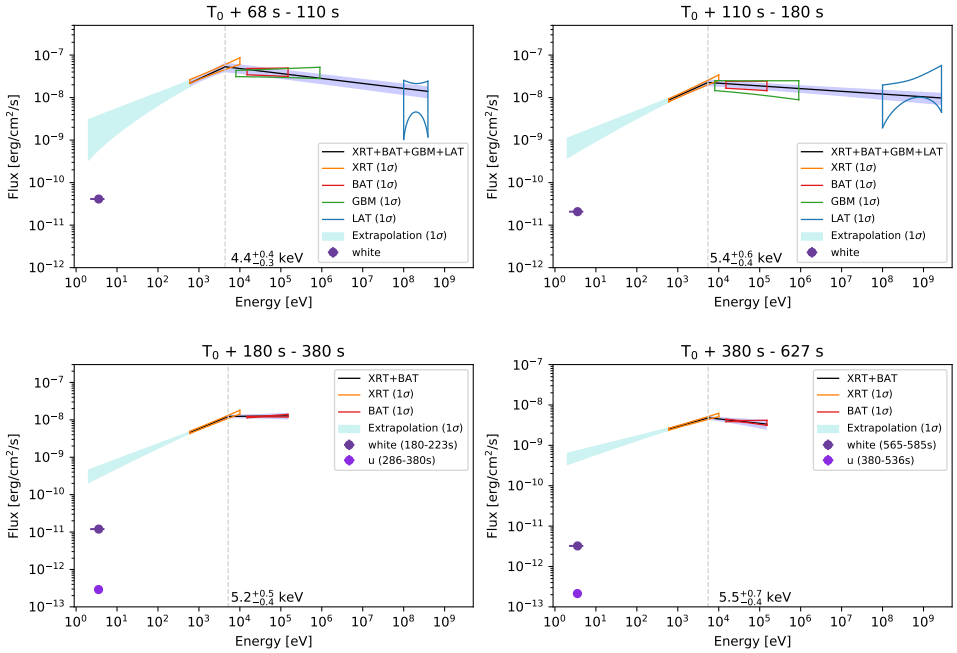

Figure 5.15: **Spectral energy distributions from the optical to gamma-ray energies for late time intervals of GRB 190114C**. The solid black lines represent the best-fitting broken power-law function. Each filled region corresponds to the 1-σ error contour of the power-law function best-fit to each individual instrument. The cyan regions are an extrapolation from the best-fitting broken power-law function. The dotted line denotes the best-fitted break energy $E_{\rm break}$. The simultaneous UVOT white and u band observations taken during the T_0 + 180 s to 380 s and T_0 + 380 s to 627 s intervals are also shown, but are not included in the joint spectral fit. Note that the UVOT observations are uncorrected for Galactic or host absorption and as such serve a lower-limits to the UV and optical flux.

data reduction can be found in the references [64, 286].

I test two models in the joint spectral fits, a PL and a broken power law (BKNPL). Each model is multiplied by two photoelectric absorption models, one for the Galactic absorption ("TBabs") and the other for the intrinsic host absorption absorption ("zTBabs")[9]. For the Galactic photoelectric absorption model, an equivalent hydrogen column density is fixed to 7.54×10^{19} atoms cm^{-2} [287]. I let an equivalent hydrogen column density for the intrinsic host absorption model free,

[9] `https://heasarc.gsfc.nasa.gov/xanadu/xspec/manual/node259.html`

but fix the redshift to $z = 0.4245$ [288].

I divided the extended emission phase, T_0 + 68.27–627.14 s, into four time intervals covering 68.27–110 s, 110–180 s, 180–380 s, and 380–627.18 s. For the first two time intervals, I fit XRT, BAT, GBM, and LAT data simultaneously by using different fit statistics to each data type: $C_{\rm Stat}$ for XRT, χ^2 for BAT data, and $PG_{\rm Stat}$ for GBM and LAT. Since the burst is outside the LAT FOV during the last two time intervals, I limit the joint fit during these intervals to XRT and BAT data. I fit the *Swift* data to both a PL and BKNPL models, using different fit statistics to each data type, χ^2 for BAT data and $C_{\rm Stat}$ for XRT. As shown in Table 5.7 and Figure 5.15, a BKNPL model is statistically preferred over the PL model in both time intervals. The low- and high-energy photon indices in the BKNPL model are consistent in both time intervals, yielding $\Gamma_{\rm low} \sim -1.6$ and $\Gamma_{\rm high} \sim -2.1$, respectively, with break energies of $\sim$ 4–6 keV. Note that the high-energy photon index is consistent with those observed in the additional component seen in the prompt phase. This result implies that BAT, GBM, and LAT are observing emission from the same side of the break in the energy spectrum from 10 keV to 100 GeV, which starts to appear during the prompt emission phase in the form of an additional spectral component, whereas XRT is measuring the energy spectrum below this break. The fit results for all four time intervals are listed in Table 5.7.

It has been argued that data near a spectral break may be better described by a smoothly broken power law (SBKNPL), as the energy spectrum near the break is not in the asymptotic regime [96]. The smoothness of the break is determined by the break energy, the electron spectral index (p), and the circumburst density profile,

and therefore can potentially provide additional constraints on the environment into which the afterglow is propagating. The SBKNPL is defined as

$$f(E) = A \left[\left(\frac{E}{E_{\rm break}} \right)^{-s\,\Gamma_{\rm low}} + \left(\frac{E}{E_{\rm break}} \right)^{-s\,\Gamma_{\rm high}} \right]^{-1/s}, \tag{5.9}$$

where $A_{\rm norm}$ is the normalization (in photons cm^{-2} s^{-1} keV^{-1}) and s describes the smoothness of the break; i.e., the lower the value of s, the smoother the break.

When the break energy corresponds to the synchrotron cooling frequency (ν_c), the low- and high-energy photon indices are given by $-(p+1)/2$ and $-(p+2)/2$, respectively. Also, the smoothness parameter can be described as a function of p depending on the circumburst density profile, $s = 1.15 - 0.06p$ for ISM and $s = 0.80 - 0.03p$ for wind. The smoothness parameter for the general density profiles is given by [195]. As a result, a SBKNPL becomes a function with three free parameters, $A_{\rm norm}$, $E_{\rm break}$, and p,

$$f(E) = A \left(\frac{E}{E_{\rm break}} \right)^{-(p+1)/2} \left[1 + \left(\frac{E}{E_{\rm break}} \right)^{s(p)/2} \right]^{-1/s(p)}. \tag{5.10}$$

Fits to the joint *Swift* and *Fermi* data to this SBKNPL reveal that the theoretical function is preferable to the simple PL model but less preferred than the BKNPL model, except for the first time interval.

Table 5.6: Spectral fitting to *Fermi* (GBM + LLE + LAT) data (10 keV–100 GeV) for various time intervals

			Main component				Additional component					
From [s]	To [s]	Model[a]	Norm.[b]	$\Gamma_{\rm low}$	$\Gamma_{\rm high}$	E_{pk} [keV]	Norm.[b]	$\Gamma_{\rm PL}$	E_{pk} [MeV]	kT [keV]	$PG_{\rm stat}/dof$	BIC
0.0	2.3	Band	$0.518^{+0.005}_{-0.005}$	$-0.73^{+0.01}_{-0.01}$	$-4.00^{+0.27}_{-0.42}$	$548.6^{+7.7}_{-7.6}$					518/353	542
		Band+BB	$0.481^{+0.011}_{-0.011}$	$-0.77^{+0.01}_{-0.01}$	$-4.20^{+0.31}_{-0.46}$	$585.4^{+14.2}_{-13.6}$	$11.54^{+5.46}_{-4.30}$			$44.2^{+4.9}_{-4.7}$	505/351	540
2.3	2.8	CPL+PL	$0.555^{+0.009}_{-0.009}$	$-0.36^{+0.03}_{-0.03}$		$730.0^{+16.2}_{-15.5}$	$0.018^{+0.004}_{-0.003}$	$-1.96^{+0.05}_{-0.06}$			425/352	454
2.8	3.8	CPL+PL	$0.374^{+0.006}_{-0.006}$	$-0.09^{+0.03}_{-0.03}$		$840.8^{+13.1}_{-12.9}$	$0.040^{+0.002}_{-0.002}$	$-1.68^{+0.01}_{-0.01}$			769/352	799
		CPL+CPL	$0.355^{+0.007}_{-0.007}$	$-0.04^{+0.03}_{-0.03}$		$814.9^{+13.4}_{-13.0}$	$0.061^{+0.004}_{-0.004}$	$-1.43^{+0.02}_{-0.02}$	$26.1^{+2.6}_{-2.3}$		477/351	512
3.8	4.8	Band+PL	$0.706^{+0.011}_{-0.011}$	$-0.05^{+0.03}_{-0.03}$	$-3.60^{+0.19}_{-0.28}$	$562.8^{+9.6}_{-9.2}$	$0.050^{+0.003}_{-0.003}$	$-1.64^{+0.02}_{-0.02}$			577/351	612
		Band+CPL	$0.675^{+0.010}_{-0.010}$	$-0.05^{+0.03}_{-0.03}$	$-3.63^{+0.21}_{-0.26}$	$563.1^{+8.8}_{-9.6}$	$0.065^{+0.004}_{-0.004}$	$-1.64^{+0.02}_{-0.02}$	$51.5^{+9.8}_{-7.4}$		519/350	560
4.8	7.0	CPL+PL	$0.322^{+0.006}_{-0.006}$	$-0.30^{+0.04}_{-0.04}$		$425.4^{+7.7}_{-7.4}$	$0.057^{+0.002}_{-0.002}$	$-1.86^{+0.01}_{-0.01}$			467/352	494
15	18.5	CPL+PL	$0.080^{+0.005}_{-0.005}$	$-1.41^{+0.08}_{-0.06}$		$122.9^{+7.5}_{-6.7}$	$0.014^{+0.003}_{-0.003}$	-2.00 fixed			407/353	430
18.5	25	CPL+PL	$0.030^{+0.005}_{-0.004}$	$-1.74^{+0.09}_{-0.08}$		$27.7^{+3.3}_{-4.1}$	$0.008^{+0.001}_{-0.001}$	-2.00 fixed			454/353	478

[a] For the PL, CPL, and Band models, the pivot energy is fixed to 100 keV
[b] photons $\rm cm^{-2}\ s^{-1}\ keV^{-1}$

Table 5.7: Spectral fitting to *Fermi* and *Swift* data (1 keV–100 GeV) for various time intervals

From [s]	To [s]	Model[a]	$\Gamma_{\rm ph,low}$	$\Gamma_{\rm ph,high}$	$E_{\rm break}$ [keV]	p	nH [10^{22} atoms cm^{-2}]	$PG_{\rm Stat}$	$C_{\rm Stat}$	χ^2	dof[b]	BIC
68.27	110	PL	$-2.09^{+0.01}_{-0.01}$				$10.55^{+0.27}_{-0.26}$	522	659	53	1104	1262
		BKNPL	$-1.55^{+0.13}_{-0.12}$	$-2.12^{+0.02}_{-0.02}$	$4.36^{+0.35}_{-0.30}$		$8.18^{+0.55}_{-0.54}$	524	630	57	1102	1253
		SBKNPL$_{\rm ISM}$	$-(p+1)/2$	$-(p+2)/2$	$0.24^{+0.91}_{-0.23}$	$2.28^{+0.09}_{-0.07}$	$10.18^{+0.27}_{-0.26}$	524	653	55	1103	1268
		SBKNPL$_{\rm wind}$	$-(p+1)/2$	$-(p+2)/2$	$0.10^{+2.59}_{-0.09}$	$2.30^{+0.14}_{-0.08}$	$10.24^{+0.27}_{-0.26}$	524	654	55	1103	1268
110	180	PL	$-2.01^{+0.03}_{-0.03}$				$10.43^{+0.23}_{-0.23}$	652	672	50	1105	1402
		BKNPL	$-1.57^{+0.08}_{-0.08}$	$-2.06^{+0.02}_{-0.02}$	$5.44^{+0.62}_{-0.40}$		$8.30^{+0.40}_{-0.39}$	653	629	52	1103	1374
		SBKNPL$_{\rm ISM}$	$-(p+1)/2$	$-(p+2)/2$	$1.68^{+3.01}_{-1.04}$	$2.22^{+0.10}_{-0.07}$	$9.80^{+0.23}_{-0.23}$	657	656	50	1104	1398
		SBKNPL$_{\rm wind}$	$-(p+1)/2$	$-(p+2)/2$	$1.04^{+3.01}_{-0.87}$	$2.25^{+0.10}_{-0.10}$	$9.94^{+0.23}_{-0.23}$	657	659	50	1104	1401
180	380	PL	$-1.90^{+0.01}_{-0.01}$				$9.57^{+0.17}_{-0.15}$		774	66	810	866
		BKNPL	$-1.54^{+0.06}_{-0.06}$	$-1.99^{+0.05}_{-0.05}$	$5.18^{+0.46}_{-0.36}$		$7.93^{+0.29}_{-0.28}$		727	63	808	830
		SBKNPL$_{\rm ISM}$	$-(p+1)/2$	$-(p+2)/2$	$5.60^{+0.145}_{-1.512}$	$2.20^{+0.10}_{-0.02}$	$9.07^{+0.15}_{-0.14}$		756	64	809	854
		SBKNPL$_{\rm wind}$	$-(p+1)/2$	$-(p+2)/2$	$6.88^{+0.35}_{-0.44}$	$2.25^{+0.16}_{-0.02}$	$9.21^{+0.16}_{-0.15}$		761	64	809	858
380	627.14	PL	$-1.86^{+0.01}_{-0.01}$				$9.09^{+0.13}_{-0.14}$		700	47	839	775
		BKNPL	$-1.71^{+0.05}_{-0.05}$	$-2.11^{+0.08}_{-0.09}$	$5.52^{+0.72}_{-0.38}$		$8.43^{+0.24}_{-0.23}$		686	42	837	768
		SBKNPL$_{\rm ISM}$	$-(p+1)/2$	$-(p+2)/2$	$8.67^{+37.30}_{-6.78}$	$2.18^{+0.20}_{-0.16}$	$8.67^{+0.20}_{-0.11}$		694	44	838	772
		SBKNPL$_{\rm wind}$	$-(p+1)/2$	$-(p+2)/2$	$9.16^{+36.96}_{-4.91}$	$2.20^{+0.19}_{-0.10}$	$8.77^{+0.18}_{-0.09}$		695	45	838	774

[a]Since the XRT data is included, a model is multiplied by the photoelectric absorption models, TBabs with fixed hydrogen column density of 7.54×10^{19} and zTBabs with fixed redshift of 0.4245.

[b]Total degree of freedom

5.4.4 Attenuation in the Additional Power-law Component

GRB 190114C was extremely well detected by both *Fermi* and *Swift* and serves as an exquisite example of the overall interpretation of previous GBM and LAT observations of GRBs. In this section and the following section, I focus on the characteristics of the additional PL component, which is interpreted as the afterglow component. The rest of the interpretation of this burst can be found in the paper published by the *Fermi* and *Swift* collaborations [277].

The spectral analysis of the prompt emission phase of GRB 190114C shows that there are at least two spectral components: Band+BB or Band (or CPL) + PL. The PL component is initially attenuated at energies greater than ~ 100 MeV, which can be interpreted as due to opacity to electron-positron pair production within the source (§ 2.2.4) [289]. The cutoff energy associated with this turnover is observed to increase with time before disappearing entirely at later times. Similar behaviour has been observed in other LAT detected bursts [60] and has been attributed to the expansion of the emitting region, as the pair production opacity is expected to scale as $\tau_{\gamma\gamma} \propto R^{-1}$ (Equation 2.33). This cutoff energy can be used to obtain a direct estimate of the bulk Lorentz factor of the emission region. Assuming that the critical energy where the opacity is equal to 1, $\tau_{\gamma\gamma}(E_c) = 1$, is the cutoff energy of the PL component (the peak energy of the CPL), the bulk Lorentz factor is [60]

$$\Gamma_{\rm bulk} \simeq \left[\sigma_{\rm T}\left(\frac{D}{c\delta t}\right)^2 E_{\rm piv}\, A\, C(\Gamma)\,(1+z)^{-2(\Gamma+1)}\left(\frac{E_c E_{\rm piv}}{m_e^2 c^4}\right)^{-\Gamma-1}\right]^{\frac{1}{2(1-\Gamma)}}, \qquad (5.11)$$

where $C(\Gamma)$ is a numerical constant, $C(\Gamma) \approx 0.597(-\Gamma)^{-2.30}$ for $1.0 \leq -\Gamma \leq 2.9$, and $E_{\rm piv}$ is 100 keV. For the definitions of other parameters, see Equation 2.33 and Equation 4.16. The spectral cutoff at $E_c \sim 143\,{\rm MeV}$[10] in a time period from $T_0 + 3.8$ s to 4.8 s with the variability timescale of $t_v \sim 6$ ms, the bulk Lorentz factor is $\Gamma_{\rm bulk} \sim 214$, which is consistent with other LAT GRBs, $\Gamma_{\rm bulk} > 100$ [38, 125, 272]

5.4.5 Spectral Break Observed in the Afterglow Phase

The broadband fits to the simultaneous *Fermi* and *Swift* data show evidence for a spectral break in the hard X-ray band (5–10 keV). In the context of the forward shock model, this spectral break could belong to either the minimum electron frequency (ν_m) or the cooling frequency (ν_c) (§ 2.4.7). Considering the expected spectral indices below and above the break (Table 2.3), both hypotheses, $\nu_{\rm obs,bk} = \nu_m$ and $\nu_{\rm obs,bk} = \nu_c$ are consistent with the observation (Figure 2.28), assuming the electron spectral index p is about 2.1. Therefore, the spectral information alone cannot distinguish these two hypotheses.

When observed temporal features are considered, one of the hypotheses is challenged. If the observed break is ν_m, the temporal index below ν_m is expected to be $\hat{\alpha} = 1/4$ for either ISM or wind circumburst environments (Table 2.3), which is inconsistent with the XRT decay index of $\hat{\alpha}_{\rm XRT} = 1.32$. Therefore, this hypothesis is disfavored.

On the other hand, if the spectral break is ν_c with $p \sim 2.1$, the observed broadband data are consistent with the expectation. The expected temporal index

[10] $E_c = E_{\rm pk}/(2-\Gamma)$.

below and above ν_c for wind (ISM) is 1.3 (0.8) and 1.1 (1.1), respectively (Table 2.3). As shown in Figure 5.12, the temporal index for BAT, GBM, and LAT, which are measured above the break energy, are about 1.0–1.2, consistent with the expectation. Furthermore, the temporal index of XRT pins down the circumburst environment of GRB 190114C. The observed $\hat{\alpha}_{\rm XRT}$ matches $\hat{\alpha}_{\rm wind}$, but does not match $\hat{\alpha}_{\rm ISM}$. Also, if we are indeed observing an afterglow spectrum in which the XRT data are below ν_c, the estimated density profile index k, $n(r) \propto r^{-k}$, is given by [195]

$$k = \frac{8\hat{\alpha} - 12\hat{\beta}}{2\hat{\alpha} - 3\hat{\beta} + 1} = 1.92, \tag{5.12}$$

which also supports a wind profile ($k = 2$) scenario. Therefore, the break is more likely to be the cooling break developed in a wind-like circumburst environment.

One challenge of this hypothesis is that the observed peak energy does not increase in time as much as expected. According to the external forward shock model, the expected evolution of the cooling break is $\nu_{\rm c} \propto t^{+1/2}$ in a wind-like environment (Equation 2.50). Despite an initial increase in the break energy between the first two intervals, the break energy is consistent with remaining constant after $T_0 > 180$ s. This implies that GRB 190114C may occur in a stratified environment; i.e., the wind density profile may not extend up to the radius where the outflow swept up at $T_0 \gtrsim 180$ s.

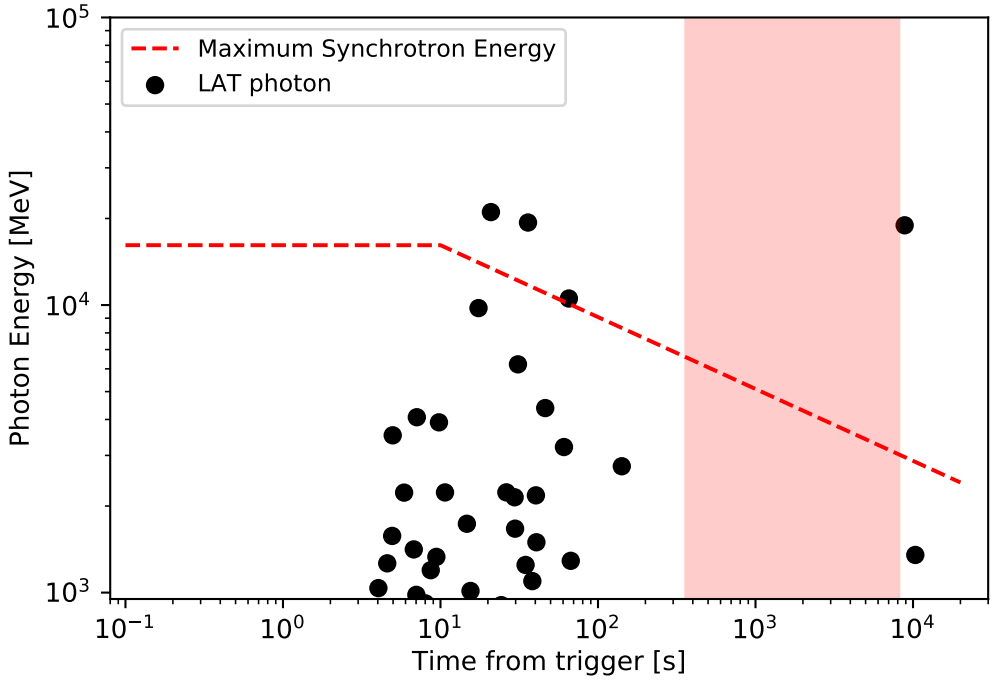

Figure 5.16: **Time versus detected photon energies from GRB 190114C.** The black dots denote events above 1 GeV with >90%-probability association with GRB190114C. The dashed line represents the maximum synchrotron limit for the adiabatic jet with the wind case. The red shaded region represents a non-observable period for GRB 190114C due to Earth avoidance.

5.4.6 Possible SSC Contribution to the High-energy Emission

All discussion above is derived without taking into account the effect of possible SSC emission; i.e., the LAT emission is interpreted as the synchrotron emission from accelerated electrons in the external forward shock (§ 2.4.7). The existence of late-time high-energy photons detected by the LAT poses a direct challenge to this interpretation (Figure 5.16).

According to the external forward shock model, the outflow begins to transfer its internal energy to the circumstellar medium, and $\Gamma_{\rm bulk}$ of the forward shock decreases with distance from the central engine as $\Gamma \propto R^{-(3-k)/2}$ (Equation 2.49).

As a result, the maximum synchrotron energy decreases with time as the afterglow expands. Plugging in $\Gamma_{\rm bulk} = 214$ (§ 5.4.4) and $z = 0.4245$ to Equation 2.13[11] gives the initial maximum synchrotron energy of $\nu_{\rm max,0} \simeq 16$ GeV. Figure 5.16 shows the expected maximum synchrotron energy as a function of time along with the observed LAT photons above 1 GeV. There exist several high-energy photons that exceed the expected maximum synchrotron energy at the time of their arrival, including a 18.9 GeV photon arriving roughly 8900 sec after T_0, almost an order of magnitude higher in energy than our estimate for $\nu_{\rm max}$ at this time. It is clear that these high-energy events either necessitate an additional emission mechanism at higher energies, or a revision of the fundamental assumptions used to calculate $\nu_{\rm max}$.

The SSC mechanism (§ 2.2.3) could produce significant emission above $\nu_{\rm max}$. The emergence of the SSC component in the LAT energy band should result in a hardening of the LAT spectrum and/or be apparent as deviations in the observed light curve, neither of which was observed in this burst at least up to 1 GeV. One possible solution would require an SSC component to remain sub-dominant to the forward shock synchrotron emission throughout the evolution of the LAT observed emission. Such a scenario could occur when the local energy density of the synchrotron photons is lower than the energy density of the local magnetic field; i.e., $Y \lesssim 1$ (Equation 2.20). Furthermore, a detailed numerical simulation of the SSC emission considering the evolution of the external-shock emission showed that the expected SSC emission could remain weaker than the primary synchrotron emission

[11] In this work, the maximum synchrotron energy is assumed to be $\sim$ 106 MeV at the rest frame [36].

even if $Y > 1$ [290]. This effect could prevent a significant SSC contribution to the LAT light curve and spectra, while still producing high-energy photons that exceed the maximum synchrotron limit.

A strong Klein-Nishina (KN) effect could significantly constrain SSC emission at high energies (§ 2.2.3), which suppresses the production of very high-energy (VHE; 100 GeV to 100 TeV) photons yielding a cutoff in the SSC spectrum. If the observed synchrotron spectrum is unaffected by significant SSC losses due to the KN effect ($Y \ll 1$), γ_c needs to be well above the critical Lorentz factor $\hat{\gamma_c}$ [58],

$$\hat{\gamma_c} \equiv \frac{\Gamma_{\rm bulk} m_e c^2}{h\nu_{\rm syn,c}}, \quad \text{and,} \quad Y(\gamma_c) \propto \left(\frac{\hat{\gamma_c}}{\gamma_c}\right)^2. \tag{5.13}$$

For $\Gamma_{\rm bulk} \sim 100$ and $h\nu_{\rm syn,c} \sim 4$keV at $T_0 + 90$ s, γ_c should be higher than 10^4. When $\gamma_m < \gamma_c$ and $\hat{\gamma_c} < \gamma_c$, high-energy SSC photons are not expected to be strongly damped until $> \Gamma_{\rm bulk}\gamma_c m_e c^2 \sim 0.5$ TeV (Equation 2.18). Therefore, the LAT detected photons are not expected to be significantly effected by the KN suppression, although the VHE spectrum observed by MAGIC could exhibit curvature due to this effect (MAGIC and many collaborations 2019, submitted).

In summary, in the LAT energy range, there exist high-energy photons that are in tension with the theoretical maximum photon energy that can be achieved through shock accelerated synchrotron emission. The detection of the VHE emission above 300 GeV by MAGIC concurrent with the LAT observation further compounds this issue, which may be resolved by introducing the SSC emission above $\nu_{\rm max}$.

Chapter 6: Systematic Studies of a Large Sample of GRBs

In this chapter, I present two systematic studies. One is to search for evidence of HLE (§ 2.4.2.1) in the *Fermi* GBM GRBs. The other is to test the standard forward shock model (§ 2.4.7; Table 2.3) in the *Fermi* LAT GRBs.

6.1 Search for Evidence of High Latitude Emission in Gamma-ray Burst Broad Pulses

In this section, I present a systematic study of the prompt emission of GBM GRBs. Several studies have been performed to search for the evidence of HLE in the prompt emission of GRBs. However, it is not straightforward to uncover the HLE evidence in the prompt phase because the observed temporal and spectral shapes of the prompt emission vary from one another. Also, overlaps of multiple pulses [65, 291] and multiple spectral components in energy spectrum [38–41, 60, 89] make it hard to find the HLE evidence during the prompt phase of GRBs. I test the HLE relation ($F_{\nu,E_p} \propto E_p^2$; Equation 2.43) and search for the evidence of HLE in the decaying phase of broad pulses.

6.1.1 Search for Broad-Pulse GBM GRBs

An initial sample consists of 2157 GRBs listed in the GBM catalog observed in 2008–2017 [61, 76, 219, 292]. In order to test the HLE relation, I need to perform a time-resolved analysis on a sufficient number of bins. Since the time-resolved spectral analysis requires bright GRBs, I select GRBs with energy fluence and peak flux in the energy band from 10 keV to 1 MeV higher than 2.5×10^{-5} erg cm^{-2} and 1.8×10^{-6} erg cm^{-2} s^{-1}, respectively. For each GRB, I take the energy fluence and peak flux values from the GBM online catalog [120], and 175 GRBs (~ 8.1 %) survive after these cuts.

For each GRB, I configure a data set adopting the set of detectors listed in the GBM online catalog [120]. For the data set, I gather events of 50–300 keV and apply the Bayesian block algorithm (§ 4.1.2) [223]. At the same time, I estimate a background rate by extrapolating a polynomial function fitted for time intervals before and after the burst. Finally, I construct a background subtracted count rate curve with the Bayesian-block bins. I define a pulse as a series of bins where the count rates are $3\,\sigma$ above the background level. Among pulses in a GRB, I choose the brightest pulse that has the highest count rate bin. For the brightest broad pulse, I impose four criteria to filter out pulses with serious contamination by background and/or overlapping pulses. These criteria are not based on any physical models or functional pulse profiles. For each criterion, I also prescribe a yellow flag (warning) or red (rule out) flag, if a pulse does not satisfy a criterion.

1. The pulse should contain 90% of the GRB fluence;

- Yellow flag: 70% $\leq$ pulse fluence $<$ 90%,
- Red flag: pulse fluence $<$ 70%.

This criterion is directly related to the fluence and peak flux cuts. This criterion checks whether the pulse is bright enough for a time-resolved analysis. With this criterion, a bright GRB composed of multiple low-fluence pulses will be removed.

2. The decaying phase time interval (T_{decay}) should be longer than the rising phase time interval (T_{rise});

   - Yellow flag: $1/2 \leq T_{rise}/T_{decay} < 1$,
   - Red flag: $T_{rise}/T_{decay} < 1/2$.

   A parameter T_{rise} is defined as duration from the start of the first bin of a broad pulse to the peak of the broad pulse, and T_{decay} is from the end of T_{rise} to the end of the last bin of the broad pulse. This is related to a pulse shape. There isn't a standard broad pulse shape, but a single pulse is believed to be asymmetric [65, 293, 294]. This criterion is intended to exclude a broad pulse composed by superposition of many pulses.

3. During the decay phase of a broad pulse, any bump should not exist. However, if a single bump exists, I impose a criterion on the duration of the bump (T_{bump}). The duration should be shorter than 1/4 of the decaying phase time;

   - Yellow flag: $T_{bump}/T_{decay} < 1/4$,

- Red flag: $T_{bump}/T_{decay} \geq 1/4$, or $N_{bump} \geq 2$

During the decaying phase, the count rate of bins should decrease with time. If a bin has a higher count rate than the previous bin, a series of the irregular bins is called a bump. The bump ends when a following count rate becomes lower than the bin before the start of the bump. This criterion is to minimize the interplay of coexistent pulses. Any sub-dominant pulses on top of the broad pulse make it difficult to extract temporal and spectral features of the broad pulse.

4. The pulse should not overlap any nearby pulses.

   - Yellow flag: a distinct pulse within 10 seconds
   - Red flag: a distinct pulse within 5 seconds

   To test this criterion, I check the count rates of three nearby bins within 5 s and 10 s before and after the bright pulse. If any nearby pulse has a count rate $3\,\sigma$ above the background level, I prescribe a yellow or red flag depending on the proximity of the pulse overlapping the broad pulse.

If a broad pulse receives at least one red flag or at least two yellow flags, the pulse is removed from our sample. After the selection procedure, our final sample consists of 32 bright broad pulses within 32 GRBs.

6.1.2 Test of the HLE Relation and Results

I test three representative models for each time interval, a simple power law (PL; Equation 4.15), a power law with exponential cutoff (CPL; Equation 4.16), and the Band function (Band; Equation 4.17). For the parameter estimation, see § 5.1. I use PG_{Stat} (Equation 4.26) to estimate parameters and their errors. The best-fit model for each time interval is determined by comparing PG_{Stat} from each model. The best-fit model is determined by the likelihood ratio (Equation 4.30); Band when ΔPG_{Stat}(CPL - Band) > 11.83 units, CPL when ΔPG_{Stat}(PL - CPL) > 8.58 units or PL otherwise, similar to the criteria employed by the GBM catalog [61, 76, 219, 292].

The value of F_{ν,E_p} in CPL or Band and its corresponding errors cannot be directly computed from the parameter estimation procedure, so I compute them with the Monte Carlo simulation. I synthesize 10^5 spectra with best-fit parameters and corresponding covariance matrix given by the best-fit model, and compute F_{ν,E_p} for each synthesized spectrum. From the F_{ν,E_p} distribution constructed by 10^5 synthesized F_{ν,E_p} values, I get mean and asymmetric errors of F_{ν,E_p}. Since this work is to test the scaling relation between E_p and F_{ν,E_p}, I ignore time intervals of which the best-fit model is PL.

With the spectral analysis results, I test the HLE relation,

$$F_{\nu,E_p} \propto E_p^{\delta}, \quad \text{where } \delta = 2 \text{ for HLE.} \tag{6.1}$$

I determine the existence of the HLE signature by a χ^2 goodness-of-fit test (§ 4.2.3).

First, I fit the HLE relation with $\delta = 2$ to all possible sets of temporally connected points. I use at least four points because it is possible that two or three points may be aligned in a specific slope by chance, while the plausibility of four points lining up at the specific value is relatively unlikely. For a set that agrees with the HLE relation ($\chi^2_\nu \equiv \chi^2/\mathrm{dof} < 2$), I fit the same relation again but leaving δ free. If any sets of points show δ close to the HLE index ($|\delta - 2| < \sigma_\delta$) with $\sigma_\delta < 1.5$, I classify the broad pulse as a "clear" case. The final value of δ is the one obtained from the fit using the largest number of points. For a broad pulse that don't have any series of points consistent with the HLE relation, I assign the pulse to a "weak" or "N/A" case through visual inspection. A weak case shows either an agreement with the HLE prediction except for few outliers or points lining up at a specific slope different from the HLE index. The weak cases are ambiguous so that one may classify these cases into N/A rather than weak.

In addition to the E_p–F_{ν,E_p} relation, the test of two other scaling relations, t–E_p and t–F_{ν,E_p}, would confirm whether or not the agreement of the E_p–F_{ν,E_p} relation is artificial (Equation 2.43),

$$\begin{aligned} E_p &\propto {t_{\mathrm{obs}}}^{-1}, \\ F_{\nu,E_p} &\propto {t_{\mathrm{obs}}}^{-2}, \end{aligned} \tag{6.2}$$

where t_{obs} is observer time measured from the beginning of a broad pulse. Since the beginning of observed broad pulses is not usually the same as the GBM trigger time, I need to reset this observer time at the beginning of the broad pulse [31]. To eliminate the t_0 effect, I define and calculate the pulse start time (t_0^{obs}) where the background subtracted count rate starts to rise $3\,\sigma$ above the background level.

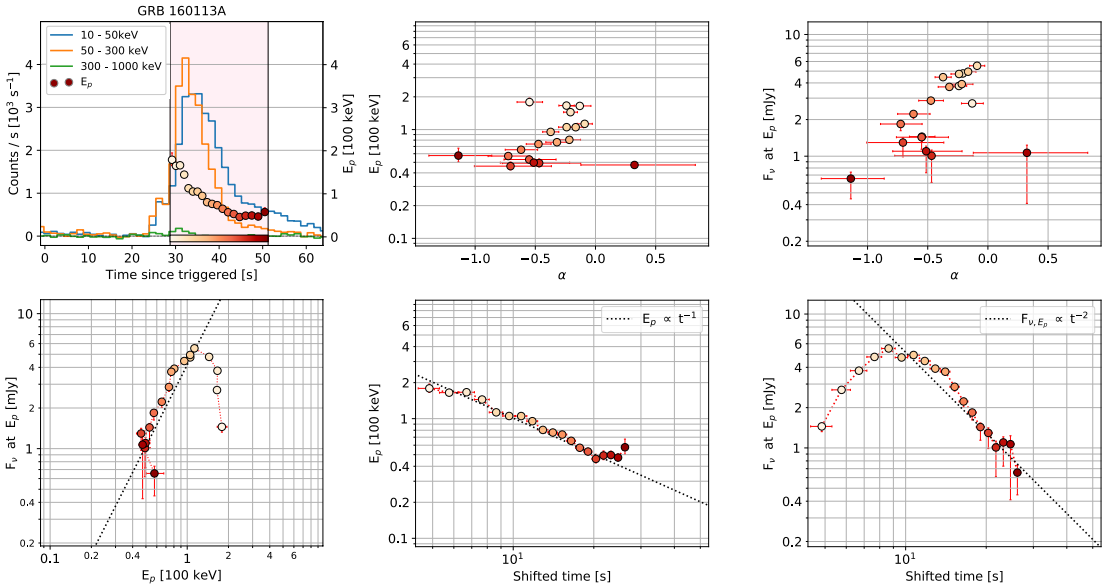

Figure 6.1: **Spectral analysis on a broad pulse in GRB 160113A.** The top left panel shows a count rate curve with the evolution of E_p. The pink shaded region indicates a time interval where either the CPL or Band is the best-fit model. The color gradation used in E_p^2 represents the lapse of time, and the color coding is used in the other panels. The others two top panels (upper center and upper right) show α vs E_p and α vs. F_{ν,E_p}, respectively. The bottom panels show the agreement between data and the HLE relations: E_p–F_{ν,E_p}, t–E_p and t–F_{ν,E_p} from left to right. The dotted lines in the bottom panels indicate the lines predicted by the HLE theory.

Figure 6.1 shows the analysis result of GRB 160113A as an example. The upper–left panel show a count rate curve in three different energy bands; 10–50 keV, 50–300 keV, and 300–1000 keV. This shows the existence of spectral lags as well as pulse shapes in different energy bands. Also, I plot the temporal evolution of E_p on top of the count rate curve to see the correlation between E_p and the count rate. In most cases, two patterns, "hard to soft" or "flux tracking", are seen, which is consistent with other observational studies (§ 2.3.1) [65, 84, 292, 295–297]. A low-energy photon index (α) versus E_p (upper–center) and α versus F_{ν,E_p} (upper–right) are plotted in order to see the evolution of α versus E_p and F_{ν,E_p}. The tests of the

Table 6.1: Spectral analysis parameters for selected GRBs.

GRB name	Pulse start [s]	Analysis start [s]	Analysis end [s]	# of bins	HLE evidence	Power-law index	χ^2_ν
GRB 081009A	-0.194	1.630	7.130	19	N/A	-	-
GRB 081221A	16.922	18.290	35.290	19	Clear	1.8 ± 0.6	0.2
GRB 081224A	-0.260	0.500	28.000	14	Clear	2.0 ± 0.4	1.5
GRB 090717A	-0.360	3.400	16.400	13	Weak	-	-
GRB 090719A	-0.136	3.480	14.480	14	Weak	-	-
GRB 090820A	29.494	32.830	39.830	21	Clear	2.0 ± 0.9	0.1
GRB 100324B	-0.066	1.130	11.630	21	Clear	2.1 ± 0.4	0.5
GRB 101023A	60.842	60.630	95.130	15	Clear	1.8 ± 0.3	0.5
GRB 110301A	-0.086	1.750	10.250	19	Clear	1.9 ± 0.3	0.4
GRB 110721A	-0.132	0.500	22.500	14	Clear	2.0 ± 1.4	0.2
GRB 110920A	-0.076	5.000	185.500	29	Clear	2.1 ± 1.0	0.1
GRB 120204A	19.636	29.080	62.580	19	N/A	-	-
GRB 120624B	1.950	10.750	37.750	14	Weak	-	-
GRB 121122A	-0.062	0.170	11.170	14	N/A	-	-
GRB 130219A	72.754	77.830	112.330	14	N/A	-	-
GRB 130305A	0.498	1.830	14.830	9	N/A	-	-
GRB 131028A	2.482	5.250	31.750	17	Weak	-	-
GRB 131214A	56.154	60.250	81.750	13	Clear	1.7 ± 0.5	2.0
GRB 140206B	5.202	5.830	27.330	22	Clear	2.3 ± 0.9	2.2
GRB 140329A	19.400	22.500	28.500	14	Clear	2.2 ± 0.8	2.0
GRB 141028A	6.118	7.630	39.130	17	Clear	2.4 ± 1.1	0.7
GRB 150213B	-0.062	2.170	5.170	14	Clear	1.9 ± 0.4	1.3
GRB 150306A	-0.562	2.750	12.750	9	Clear	2.0 ± 0.4	0.4
GRB 150403A	-0.818	3.250	29.750	23	N/A	-	-
GRB 150902A	-0.032	8.500	14.500	19	Weak	-	-
GRB 151107B	-0.050	7.250	42.750	12	Clear	2.2 ± 0.5	0.2
GRB 160113A	24.334	28.750	51.250	19	Clear	2.1 ± 0.2	1.1
GRB 160509A	-0.626	8.170	36.670	16	Clear	2.1 ± 0.6	0.4
GRB 160530B	-0.536	3.880	15.880	19	Clear	2.1 ± 0.2	2.0
GRB 160910A	-0.078	6.330	31.830	19	Weak	-	-
GRB 170921B	-0.152	0.440	37.440	19	N/A	-	-
GRB 171210A	-0.588	1.500	108.000	24	Weak	-	-

HLE relations are presented in the lower panels.

From the χ^2 goodness of fit test, I find that clear HLE evidence is observed in 18 out of 32 broad pulses ($\sim 56\%$). The fit results of the HLE relation are shown in Table 6.1 and Figure 6.2.

As shown in Table 6.1, the clear sample has $\delta \sim 2$. Since the distribution of δ resembles a Gaussian function (Figure 6.2), I estimate median and width of the distribution with the Monte Carlo simulation. I generate 10^5 synthesized distributions based on 18 measured δ and σ_δ. From the simulation, I get the median and the width of the true δ distribution, $\delta = 1.99^{+0.14}_{-0.14}$ and $\sigma_\delta = 0.34\ ^{+0.21}_{-0.13}$, respectively.

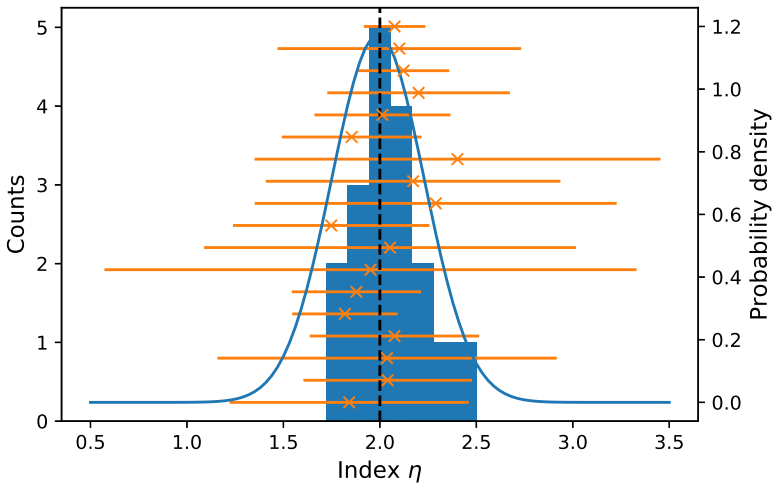

Figure 6.2: **Distribution of δ in $F_{\nu,E_p} \propto E_p^{\delta}$.** The blue bar is the distribution of δ, and the blue line shows a normal probability function given by the Monte Carlo simulation with 18 broad pulses. The median and width of the distribution is 1.99 and 0.34, respectively. The orange error bars indicate the fit results of 18 GRBs with the HLE signature. The black dotted line represents the HLE expectation, $\delta = 2$, and the data and corresponding distribution agree with the HLE theory.

6.1.3 Implication of the observation of HLE in the Prompt Emission

The observed data of the clear sample satisfy not only the HLE relation between E_p and F_{ν,E_p}, but also, in most cases, the other HLE relations related to $t_{\rm obs}$, $t_{\rm obs}$–E_p and $t_{\rm obs}$–F_{ν,E_p}. In few cases, the observed data are aligned but show a slope steeper than the HLE expected. One explanation for these exceptions is an inaccurate definition of the $t_0^{\rm obs}$. The actual t_0 cannot be exactly measured due to the background fluctuation, the detector sensitivity, or overlaps of pulses. The combination of these effects hides the beginning of a broad pulse, and $t_0^{\rm obs}$ is set later than $t_0^{\rm true}$. This observational effect results in the change of the slopes in $t_{\rm obs}$–E_p and $t_{\rm obs}$–F_{ν,E_p} spaces. Considering this observational limit, the true slope can be shallower than the observed slope, resulting in satisfying the HLE relations. The

effect arising from the bulk acceleration can provide another explanation for the steeper slopes [85, 104, 137].

In an effort to minimize the effects of pulse overlaps, I chose relatively clean broad pulses by imposing four criteria (Section 6.1.1). For the energy spectrum, I assume that each time-resolved energy spectrum is dominated by a single spectral component, which is PL, CPL or the Band function. I acknowledge that the best-fit for each time interval may be a combination of two or more spectral components, instead of one of the tested models (§ 2.3.1). However, it is still possible to observe the HLE evidence with testing of a single spectral component, if one component overwhelms the other components so that a single component model can adequately describe the dominant component. The clearly observed scaling relation supports that the analysis with a single component can be valid because it is difficult to explain the specific evolution of E_p and F_{ν,E_p} in the presence of equally bright multi-components. With a multi-component spectral analysis, I expect to find more broad pulses showing the HLE signature, which might be hidden in a single component spectral analysis. In analyzing the broad pulses with multiple spectral components, it is not easy to take a systematic approach.

This study identifies the observational evidence of HLE for the first time. The observation of the HLE evidence in relatively long GRBs ($T_{90} \gtrsim 10$) implies that the emission radius for those GRBs is $r \sim 10^{16}$ cm (Equation 2.31),

$$r \sim 2\Gamma_{\rm bulk}^2 c\delta t = 1.6 \times 10^{16} {\rm cm} \left(\frac{\Gamma_{\rm bulk}}{300}\right) \left(\frac{\delta t_{\rm obs}}{3s}\right). \tag{6.3}$$

This large emission radius of the gamma-ray emitting region strongly disfavors some prompt emission models such as a photosphere model (§ 2.4.4; $R_{\rm ph} \sim 10^{10}$–10^{12} cm) or a internal shock model (§ 2.4.5; $R_{\rm IS} \sim 10^{13}$–10^{14} cm) but favors a magnetic dissipation model such as the ICMART model (§ 2.4.6; $R_{\rm ICMART} \sim 10^{15}$–$10^{16}$ cm) [184].

In conclusion, this study agrees with the prediction of the HLE theory and successfully identifies the observational evidence of HLE for the first time.

6.2 Closure Relations of γ-ray Bursts in High-Energy Emission

I perform a systematic study with high-energy emission of 186 GRBs observed by *Fermi* LAT from August 2008 to August 2018. Out of the 186 GRBs in the Second Fermi-LAT Gamma-ray Burst Catalog (2FLGC) [37], 59 GRBs fulfill our selection criteria and are used as described in § 6.2.1. I test the external forward shock model (§ 2.4.7) assuming adiabatic hydrodynamic evolution by comparing the properties of the selected GRBs with a set of the standard closure relations (Table 2.3). Two density profiles, ISM and wind, are tested. In addition to the circumburst condition, three cooling regimes are considered; $\nu > \nu_m$ and ν_c, $\nu_m < \nu < \nu_c$, and $\nu_c < \nu < \nu_m$. Since the synchrotron self-absorption process is relevant to emission well below infrared [45], I neglect the closure relations related to the self-absorption regime. Evolution after the jet break is considered not to be relevant to this work, because the jet break is usually observed ~ 3 day later. I find the best-matched closure relation for each GRB, and discuss implications of the physical

conditions of GRBs deduced from the best-matched closure relation.

6.2.1 Procedure for Finding the Best-match Closure Relation

I define the LAT extended emission as emission after the GBM T_{90} measured in the energy range from 50 keV to 300 keV. The light curve and energy spectrum of the LAT extended emission are analyzed in the 2FLGC, and I adopt the values of temporal and spectral indices from the 2FLGC.

In the 2FLGC, a light curve of the LAT extended emission is fitted with a simple power law (Equation 4.2) and a broken power law (Equation 4.3). Since a broken power law is never significantly better than a simple power law, I adopt a temporal index from the simple power law. I impose a criterion on the error size of the temporal index to remove a GRB with a large error, resulting in a meaningless classification. The error size of the temporal index is required to be less than 1/2, because two typical closure relations, $\hat{\alpha} = (3\hat{\beta}$ - 1)/2 and $\hat{\alpha} = 3\hat{\beta}/2$, are differentiated by the value of 1/2 when its spectral index is the same.

The energy spectrum of the GRB extended emission is fitted with a simple power law in the energy range from 100 MeV to 100 GeV. Similarly to the error-size cut of the temporal index, I also require the error on the spectral index to be less than 1/3. The difference in the error-size criteria results from the consideration of the maximum slope of a closure relation ($\hat{\alpha} \sim 3\hat{\beta}/2$). After these procedures, 59 out of 186 GRBs are selected (58 long and 1 short GRBs).

I test the standard closure relations as shown in Table 2.3, eight in total. For

the set of $\hat{\beta}$ and $\hat{\alpha}$ pairs satisfying our selection criteria, I perform a statistical analysis to find which closure relation best fits each pair.

According to Bayes' Theorem, the probability of a closure relation (CR) given observed $\hat{\beta}$ and $\hat{\alpha}$ is (Equation 4.31)

$$P(CR \mid \hat{\alpha}, \hat{\beta}) = \frac{P(\hat{\alpha}, \hat{\beta} \mid CR)\, P(CR)}{P(\hat{\alpha}, \hat{\beta})}. \tag{6.4}$$

For any choice of two closure relations, the Bayes factor K can be computed for comparing which model better describes the observed data (Equation 4.32),

$$K_{ij} = \frac{P(\hat{\alpha}, \hat{\beta} \mid CR_i)}{P(\hat{\alpha}, \hat{\beta} \mid CR_j)} = \frac{\int P(\hat{\alpha}, \hat{\beta}, \mid \theta_i, CR_i)\pi(\theta_i \mid CR_i)d\theta_i}{\int P(\hat{\alpha}, \hat{\beta}, \mid \theta_j, CR_j)\pi(\theta_j \mid CR_j)d\theta_j}. \tag{6.5}$$

According to the external forward shock model, the spectral and temporal indices are a function of the electron spectral index p, except for CR1 (see Table 2.3). Because both $\hat{\beta}$ and $\hat{\alpha}$ are a function of p, I can convert $\hat{\beta}$ and $\hat{\alpha}$ to $p_{\hat{\beta}}$ and $p_{\hat{\alpha}}$, respectively. The likelihood $P(\hat{\alpha}, \hat{\beta} \mid CR_i)$ can be therefore estimated by requiring that both $p_{\hat{\beta}}$ and $p_{\hat{\alpha}}$ satisfy the constraint of the closure relation and that $p_{\hat{\beta}}$ and $p_{\hat{\alpha}}$ are identical. Under the assumption that the uncertainties on $p_{\hat{\beta}}$ and $p_{\hat{\alpha}}$ are normally distributed and considering these two requirements, the quantity $P(\hat{\alpha}, \hat{\beta} \mid CR_i)$ can be described as

$$\begin{aligned} P(\hat{\alpha}, \hat{\beta} \mid CR_i) &= \int P(\hat{\alpha}, \hat{\beta}, \mid \theta_i, CR_i)\pi(\theta_i \mid CR_i)d\theta_i \\ &\simeq P(p_{\hat{\alpha},i} = p_{\hat{\beta},i} \mid CR_i) \prod_{j=\hat{\alpha},\hat{\beta}} P(p_{j,i} \subset p_c \mid CR_i), \end{aligned} \tag{6.6}$$

where p_c refers to the p constraint of the corresponding closure relation. The likelihood $P(p_{\hat{\alpha}} = p_{\hat{\beta}} \mid \mathrm{CR}_i)$ is

$$P(p_{\hat{\alpha},i} = p_{\hat{\beta},i} \mid CR_i) = \frac{1}{\sqrt{2\pi(\sigma^2_{p_{\hat{\alpha},i}} + \sigma^2_{p_{\hat{\beta},i}})}} \exp\left[-\frac{(p_{\hat{\beta},i} - p_{\hat{\alpha},i})^2}{2(\sigma^2_{p_{\hat{\alpha},i}} + \sigma^2_{p_{\hat{\beta},i}})}\right], \tag{6.7}$$

where $\sigma_{p_{\hat{\alpha},i}}$ and $\sigma_{p_{\hat{\beta},i}}$ are the 1-sigma error of $p_{\hat{\alpha},i}$ and $p_{\hat{\beta},i}$, respectively. The probability $P(p_j \subset p_c \mid \mathrm{CR}_i)$ can be calculated by

$$P(p_j \subset p_c \mid CR_i) = \begin{cases} 1 & \text{if } p_j \subset p_c, \\ 2 \times \int\limits_{p \text{ in } p_c} \frac{1}{\sigma_{p_j}\sqrt{2\pi}} \exp\left[-\frac{(p-p_j)^2}{2\sigma^2_{p_j}}\right] dp & \text{otherwise,} \end{cases} \tag{6.8}$$

which is a two-sided probability of the region satisfying the p constraint.

In case of CR1, $\hat{\beta}$ and $\hat{\alpha}$ are not a function of p, and they are independent. Instead, I calculate the likelihood for the data with

$$P(\hat{\alpha}, \hat{\beta} \mid CR_1) = \frac{1}{2\pi\sigma_{\hat{\alpha}}\sigma_{\hat{\beta}}} \exp\left[-\frac{(\hat{\alpha} - 1/4)^2}{2\sigma^2_{\hat{\alpha}}} - \frac{(\hat{\beta} - 1/2)^2}{2\sigma^2_{\hat{\beta}}}\right]. \tag{6.9}$$

The best-matched closure relation is determined by comparing the quantity of $P(\hat{\alpha}, \hat{\beta} \mid \mathrm{CR}_i)$. A model with the highest $P(\hat{\alpha}, \hat{\beta} \mid \mathrm{CR}_i)$ is a possible best-matched model. However, if the possible best-matched model gives

$$\chi^2 = \frac{(p_{\hat{\beta},\mathrm{best}} - p_{\hat{\alpha},\mathrm{best}})^2}{\sigma^2_{p_{\hat{\alpha},\mathrm{best}}} + \sigma^2_{p_{\hat{\beta},\mathrm{best}}}} > 1.65, \tag{6.10}$$

then the best-matched closure relation is not assigned; i.e., such GRBs are called

Table 6.2: **The number of classified GRBs for each closure relation.**

Class	$\nu_c < \nu < \nu_m$	$\nu > \nu_m, \nu_c$		$\nu_m < \nu < \nu_c$		UC[a]	Total
	I/W[b] CR1	I/W CR2	ISM CR5[c]	ISM CR3	wind CR4		
Long	1	20	3	19	4	11	58
Short	-	-	-	1	-	-	1
Total	1	20	3	20	4	11	59

[a] unclassified
[b] ISM/wind
[c] $1 < p < 2$

"unclassified (UC)". When the best-matched closure relation is assigned, the Bayes factor against the other closure relations is computed. The smallest Bayes factor, which is given by the best-matched closure relation against the most competitive alternative, can be used for estimating the strength of how much the best-matched closure relation is supported by the data against the others. A Bayes factor smaller than 3 means that the best-matched closure relation is not significantly better than the other closure relations [298].

6.2.2 Closure Relation Classification Results

The classification results are summarized in Figure 6.3 and Table 6.2. In total, 48 out of 59 GRBs are classified into one of the standard closure relations, and the others are unclassified. Only 5 of the 8 closure relations, CR1–CR5, are preferred for the classified GRBs. In Figure 6.3, the set of closure relations, and 59 GRBs are plotted. Depending on the value of the Bayes factor compared to the most competing model, the degree of transparency is determined; i.e., the less ambiguity

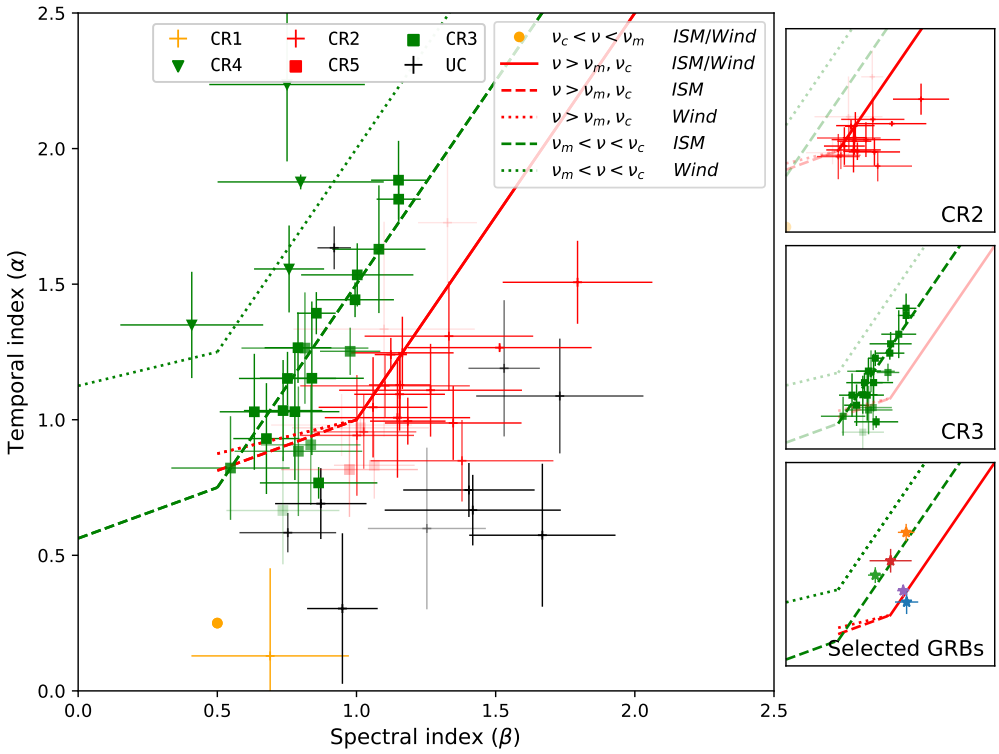

.

Figure 6.3: **The result of classifying LAT GRBs to a set of closure relations.** The color of data points and lines differentiates a cooling regime; red is used for the fast cooling ($\nu > \nu_m$ and ν_c), green for the slow cooling ($\nu_m < \nu < \nu_c$), orange for $\nu_c < \nu < \nu_m$. Note that for $\nu_c < \nu < \nu_m$, the spectral and temporal indices are specifically determined: $\hat{\beta} = 0.5$ and $\hat{\alpha} = 0.25$. Each set of $\hat{\alpha}$ and $\hat{\beta}$ is depicted by color corresponding to the best-matched closure relation, but an unclassified GRB is displayed in black. The closure relation line style is related to the surrounding environment property; a solid line is used for an undetermined environment, a dashed line for ISM, and a dotted line for wind. Two sub-panels (top and middle) show classified events for the two most frequently used closure relations, separately. Also, a bottom sub-panel shows some selected GRBs, which are broadly studied with multi-wavelength observations: GRB 080916C (blue), GRB 090510A (orange), GRB 090926A (green), GRB 110731A (red), and GRB 130427A (purple)

of the classification, the higher the visibility. Note that there are some green points on top of red dotted and dashed lines. This is because for those closure relations (CR5 and CR6), the error size of $p_{\hat{\alpha}}$, $\sigma_{p_{\hat{\alpha}}}$, is four times larger than one given by other closure relations (CR2, CR3, and CR4), so that the value of $P(\hat{\alpha}, \hat{\beta} \mid CR_i)$ decreases significantly. Most of the classified events have spectral and temporal indices from 0.5 to 1.5, but the unclassified GRBs tend to have either a soft spectrum ($\hat{\beta} \sim 1.5$) or a shallow decay ($\hat{\alpha} < 0.5$). Table 6.2 shows how many GRBs are sorted into each closure relation. The most frequent classified class is CR3 derived from a cooling condition of $\nu_m < \nu < \nu_c$ with a uniform density profile (ISM). Also, many GRBs are classified into CR2 for which ν is higher than both ν_m and ν_c with undetermined circumburst environment.

I compute $p_{\hat{\alpha}}$ and $p_{\hat{\beta}}$ from $\hat{\alpha}$ and $\hat{\beta}$, respectively, by applying the conversions of the best-matched closure relation. Figure 6.4 shows a scatter plot of $p_{\hat{\beta}}$ versus $p_{\hat{\alpha}}$ and the distribution of the weighted average of $p_{\hat{\beta}}$ and $p_{\hat{\alpha}}$. The red (CR 2 and 5) and green points (CR 3 and 4) are related to the different cooling regime, the fast cooling ($\nu > \nu_c$ and ν_m) and the slow cooling ($\nu_m < \nu < \nu_c$), respectively. In the upper panel of Figure 6.4, the red and green points are clustered in different areas. Such deviation is also evident in the weighted p distribution of the fast cooling and the slow cooling (see the lower panel of Figure 6.4).

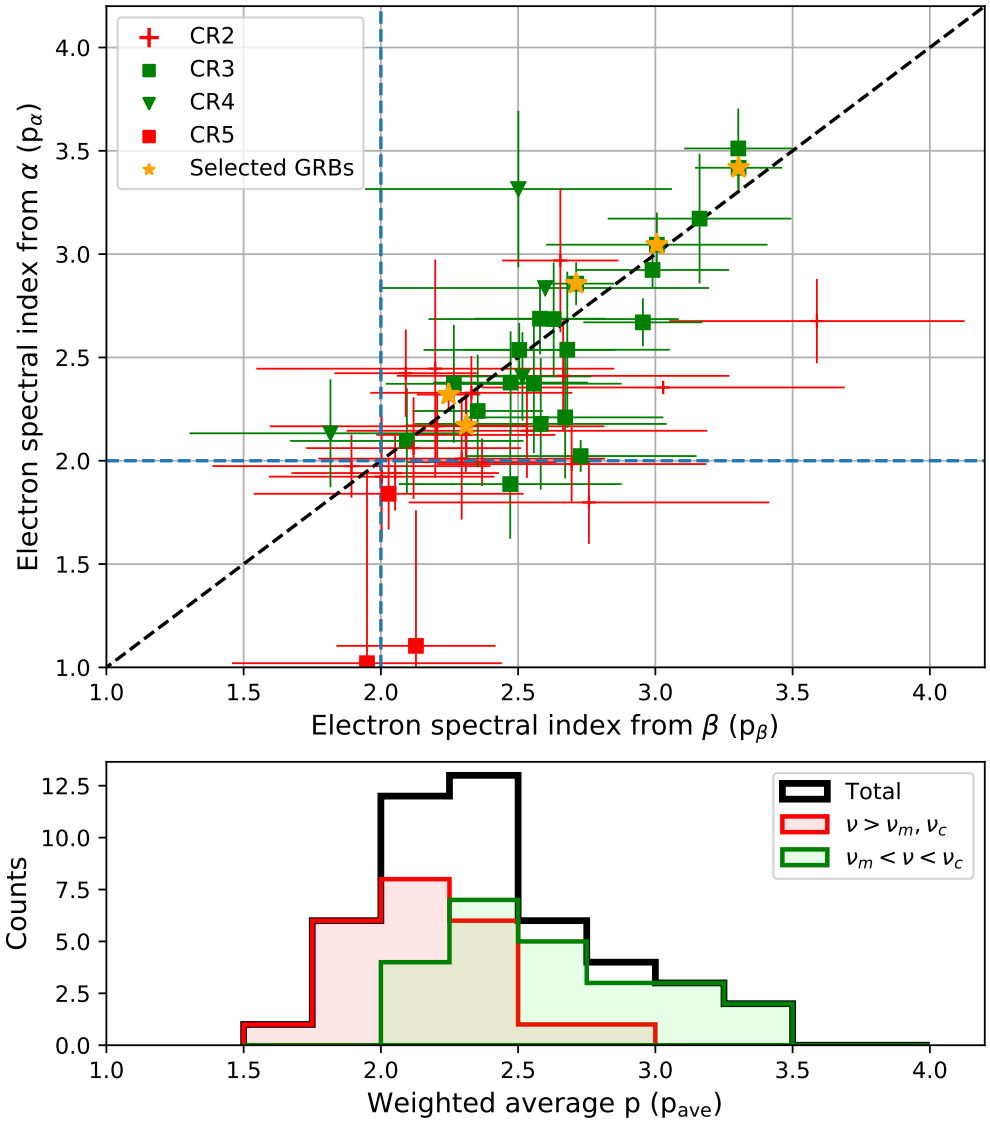

Figure 6.4: **Distribution of the electron spectral index** p. Upper panel: scatter plot of $p_{\hat{\beta}}$ versus $p_{\hat{\alpha}}$ for 48 classified GRBs. Each data point is displayed in red (fast cooling; $\nu > \nu_m$, ν_c) or green (slow cooling; $\nu_m < \nu < \nu_c$) depending on the cooling regime of the best-matched closure relation. The Black dashed line indicates the identity line. The selected GRBs, GRB 080916C, GRB 090510A, GRB 090926A, GRB 110731A, and GRB 130427A, are marked with an additional yellow star point. Bottom panel: the distribution of the weighted average of $p_{\hat{\beta}}$ and $p_{\hat{\alpha}}$.

6.2.3 Micro-physical Parameters for the LAT Extended Emission

In this section, I discuss several micro-physical parameters inferred from the test of closure relations to the LAT extended emission: surrounding circumburst environment, ϵ_B, and p.

As described in § 2.4.3, a long GRB is attributed to the core-collapse of a massive star [19,299,300], and stellar winds from the massive star form the circumburst density profile as a function of radius [301]. As the radius from the central engine increases, the density profile is no longer purely described by the stellar winds, but is influenced by the interstellar medium. A short GRB originates from the merger of two compact objects, and thus a uniform density profile with a lower density environment is expected [5,17,42,274].

Among 58 long GRBs, I identified the environment of 26 GRBs, and most of them (22 out of 26) are related to the ISM. Other observational studies reach similar conclusions [121,302]. It was found that all of their long GRB sample fits best with a constant density medium from 0.1 to 30 cm^{-3} [302]. Also, the majority of the long GRBs detected by *Swift* were compatible with a uniform density profile rather than a wind profile [121]. These results are in tension with the expectation that the progenitors of long GRBs are massive stars whose external density decreases with radius in proportional to radius squared. This implies that a wind profile may not be extended at the radii of the forward external shock [121]. Another possible explanation for such conflicted results is that our assumption of the wind density profile is too simple; i.e., the wind profile can deviate from the simple description

[303]. In our sample, there is one short GRB, GRB 090510, which is related to the ISM consistent with the theoretical expectation.

On the other hand, I found that 24 GRBs are classified into the slow-cooling condition, $\nu_m < \nu < \nu_c$ (Table 6.2). This result implies that for those GRBs ν_c is required to be higher than the LAT extended emission energy band ($\nu_{\rm LAT}$) in order to satisfy this cooling condition. Since the spectral and temporal indices are computed from the energy band, 100 MeV–10 GeV, ν_c should be at least higher than a frequency equivalent to 100 MeV.

According to the external forward shock model, the cooling frequency ν_c is described as a function of four parameters: the fraction of the total energy behind the shock in the magnetic field ϵ_B, the isotropic energy $E_{\rm iso}$, the circumburst density profile n, and the observed time $t_{\rm obs}$. Among the four parameters, the distributions of the isotropic energy and the observed time do not show any dependence on the cooling condition (2FLGC). I take the average value of $E_{\rm iso}$ and $t_{\rm obs}$ from 2FLGC, $E_{\rm iso} \sim 10^{53}$ ergs and $t_{\rm obs} \sim 10^3$ s. Since most GRBs favor the ISM circumburst condition, the density profile is assumed to be ISM, $n = 1$ cm^{-3}. Under these reasonable assumptions, ϵ_B has an upper limit [57],

$$\epsilon_B \lesssim 4.8 \times 10^{-7}\ (1+z)^{-1/3}\ {\nu_{c,\ 100\ MeV}}^{-2/3}\ {E_{53}}^{-1/3}\ {n_1}^{-2/3}\ {t_3}^{-1/3}\ (1+Y)^{-4/3}, \tag{6.11}$$

where $\nu_{c,\ 100\ MeV} = h\nu_c$ / 100 MeV, $E_{53} = E_{\rm iso}$ / 10^{53} ergs, $n_1 = n$ / 1 cm^{-3}, and t_3 = $t_{\rm obs}$ / 10^3 s. Even with $Y \ll 1$ (Equation 2.20), the GRBs classified into the slow-cooling condition require a very small value of ϵ_B ($\lesssim 10^{-7}$). Such a small value of

ϵ_B, however, does not conflict with other observational studies in the X-ray, optical, and radio bands (Figure 2.27) [186, 205, 304–308]

For GRBs with a very small ϵ_B, the contribution from the SSC emission to the GeV emission cannot be ignored [57, 58, 309], and it is possible that the emerging SSC emission can lead spectral and temporal indices deviated from those expected from the synchrotron process. Several studies show that the SSC contribution to the LAT energy band from 100 MeV to few GeV is small due to the Klein-Nishina effect [304, 310]. I have not found strong evidence of SSC-induced deviation from the standard closure relation at present. To assess the specific contribution of SSC emission, the detailed spectrum and its evolution of the electron distribution should be studied by multi-wavelength modeling [307], which is unknown in a systematic way. Instead, the relative change in the spectral and temporal indices due to the contribution of SSC can be explored. Several studies found that the standard closure relation can deviate due to emerging SSC emission, and such deviation directs to the area between the slow cooling line and the fast cooling line [290, 311], suggesting that for GRBs with a set of $\hat{\beta}$ and $\hat{\alpha}$ scattered around such region, the SSC contribution may be important in understanding their evolution of spectrum and light curve, and the standard closure relations may not work properly.

Both theoretical studies and numerical simulations on an electron spectrum developed in a relativistic shock show that an electron spectral index p has a universal value $\sim 2.2 - 2.4$ [197–200]. In contrast, the observational studies found that p varies from one GRB to another, and the distribution of p forms a Gaussian function [201–204]. In accordance with other observational studies, Figure 6.4 shows

that the weighted averages of p obtained from the classified GRBs are distributed in the range from 1.5 to 3.5, rather than having a universal p. To get median and 1 σ of the p distribution, I perform a Monte Carlo simulation study. For each $p_{\rm ave}$ value, I assume that mean and error of $p_{\rm ave}$ follow a normal distribution, and randomly generate a p value with a probability given by the normal distribution. I gather the simulated p values and make a distribution. The simulated distribution is fitted with a Gaussian function by the maximum likelihood method. I repeat this procedure 10^5 times. From the 10^5 set of median and 1 σ value, I estimate median and 1 σ of the true p distribution, which are $p = 2.40 \pm 0.03$ and $\sigma_p = 0.44 \pm 0.03$. This result is consistent with other observational results [204], where the distribution of p measured from *Swift* GRB X-ray afterglows is well described by a Gaussian function centered at $p = 2.36$ and having the standard deviation of 0.59.

Next, I test dependence of p on the electron cooling condition. The $p_{\rm ave}$ distribution of CR2 (fast cooling) and the combined $p_{\rm ave}$ distribution of CR3 and CR4 (slow cooling) are compared. The simulation for these two sets yields that the $p_{\rm ave}$ distribution of the fast cooling has median and 1 σ of 2.22 ± 0.04 and 0.30 ± 0.04, respectively, and in the case of the slow cooling, median and 1 σ are 2.61 ± 0.04 and $0.43\ ^{+0.04}_{-0.03}$, respectively. Since the two distributions are not aligned (see lower panel in Figure 6.4), I perform the Kolmogorov–Smirnov (KS) test on them. As a result, the null hypothesis that the two distributions are drawn from the same reference distribution is rejected at 3.2 σ (two-sided p-value = 1.2×10^{-3}). This implies that the slope of the electron spectral distribution is possibly related to the cooling regime.

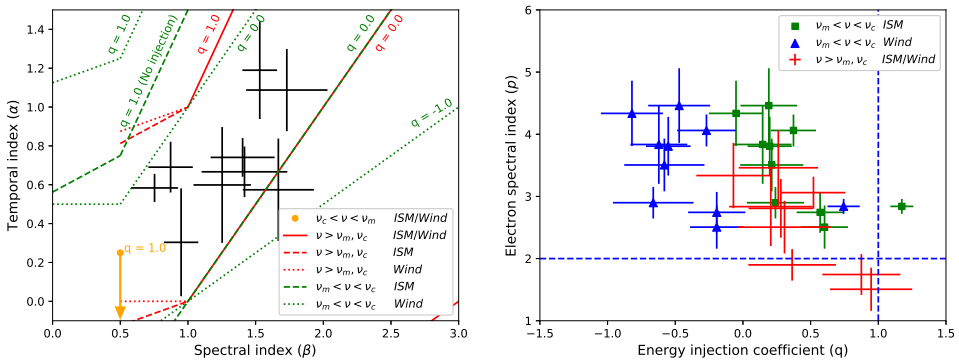

Figure 6.5: **Test of unclassified GRBs with the refreshed shock model.** *Left*: closure relation lines for several energy injection coefficients, $q = 1$, 0 and -1, are plotted with the unclassified GRBs. Note that $q = 1$ is no energy injection. *Right*: the estimated values of q and p for unclassified GRBs are plotted. The red points are when all unclassified GRBs satisfy a closure relation of the fast cooling. The green and blue points are for the slow cooling with ISM and wind, respectively.

In addition, I explore the dependence of p on the surrounding environment. I compare CR3 (ISM) and CR4 (wind). In case of ISM, the median and standard deviation are 2.62 ± 0.04 and 0.43 ± 0.04, respectively. For wind, the median and standard deviation are 2.60 ± 0.11 and $0.40\ ^{+0.13}_{-0.11}$, respectively. Since the two results agree within 1 σ, the dependence of p on surrounding environment is unclear.

In conclusion, the derived physical conditions such as the electron spectral index, the upper limit of ϵ_B, and the surrounding environment do not conflict with those from the X-ray and optical bands.

6.2.4 Possible explanation for unclassified GRBs

For unclassified GRBs, I consider modifications to the standard external shock model. First of all, I test an external forward shock model with a continuous energy injection from the central engine during the afterglow phase, the so-called "refreshed shock model" [31, 193]. According to this model, the isotropic energy evolves as

$E_{iso} \propto t^{1-q}$, where q is the energy injection coefficient. For values of $q < 1$, there is continuous energy injection from the central engine whereas $q = 1$ is identical to an instantaneous energy injection. The energy injection from a spinning-down newly-born magnetar gives $q = 0$ [142, 193]. There is no general consensus for the energy injection mechanism and the value of q. As the forward external shock is supported by energy injected from the central engine, the temporal index is smaller than in models without energy injections is described as a function of q [31],

$$\hat{\alpha}(p, q) = \begin{cases} \frac{3q-2}{4} & \text{CR1}, \\ \frac{(2p-4)+(p+2)q}{4} & \text{CR2}, \\ \frac{(2p-6)+(p+3)q}{4} & \text{CR3}, \\ \frac{(2p-2)+(p+1)q}{4} & \text{CR4}, \end{cases} \tag{6.12}$$

whereas the spectral index $\hat{\beta}$ is independent to the energy injection coefficient. As the coefficient q decreases (more energy is injected), the temporal index becomes smaller (slower flux decreases).

Since the true value of q for each GRB is unknown, any closure relation (CR2, CR3, and CR4) can be the best-matched closure relation for an unclassified GRB if an appropriate q value is chosen. I can calculate a proper value of q and corresponding p for each closure relation, assuming that the relation is the best-matched closure relation (Equation 6.12). As shown in Figure 6.5, the required q value varies, and a universal value for q is not determined. Rather, I estimate the maximum energy

injection coefficient in order to satisfy any one of the closure relations. I find that unclassified GRBs can be explained with values larger than $q \sim 0.45$ on average. The values of p are distributed in the range of $2.5 \lesssim p \lesssim 5$, which are slightly higher than those of the classified events. Assuming that all unclassified GRBs meet the same closure relation and choosing an appropriate q value for each GRB, there may be anti-correlation between q and p (see Figure 6.5 right panel), which implies that a larger energy injection results in a softer electron spectrum. I stress that this anti-correlation is only valid under this strong assumption.

In addition, I consider a model describing an external forward shock in the presence of a reverse shock [24, 312–314]. New closure relations can be derived from that model [315], which have the same form as the closure relations of the refreshed shock model for $q = 0$. In Figure 6.5 (left panel), a few of the unclassified GRBs are consistent with a value of $q = 0$ lines. For those GRBs, this model can explain their evolution of spectrum and light curve.

There are other external shock models for the jet geometry, the structured outflow and the non-uniform surrounding medium [126, 263, 316, 317]. To test these models for the unclassified GRBs, the detailed characteristics of each GRB should be investigated, which is beyond the scope of this study.

To sum up, the spectrum and temporal evolution of the LAT high energy extended emission are well explained by the standard external forward shock model, except for few GRBs. For few GRBs, several external shock models can be suggested.

Chapter 7: Conclusion and Future Prospect

Throughout this thesis, I have discussed the temporal and spectral evolution of γ-ray bursts. Such evolutionary features of GRBs are studied with both dedicated analyses on individual GRBs and systematic analyses on a large sample of GBM and LAT GRBs. The following is the summary of my work.

I found that a bright short GRB, GRB 160709A, showed the thermal emission on top of the non-thermal emission (§ 5.3.2). This thermal emission was clearly identified only in the time-resolved spectral analysis, and this emission faded in time (§ 5.3.3). This time-resolved spectral analysis suggests that this short GRB requires at least three spectral components, consistent with what has been reported in long GRBs [89].

Similar to some bright LAT GRBs such as GRB 090510 [39] and GRB 090926A [60], GRB 160709A and GRB 190114C showed an additional PL component extended from keV to GeV (§ 5.3.4 and § 5.4.5). Tracking the temporal and spectral features of the broadband PL component found that this component is consistent with emission from the external forward shock. Furthermore, I showed that most of the LAT extended emission is consistent with the external forward shock model with the systematic approach of a large sample of the LAT GRBs (§ 6.2). These

results constrained several micro-physical parameters, which allows to broaden our understanding of the detail of the emission process and the surrounding environment.

On the other hand, observations of GRB 131108A suggested new phenomena in the high-energy emission (§ 5.2.1). In the broadband analysis on GRB 131108A, I found the three GeV flares on top of the underlying power-law decay emission. Furthermore, the temporal and spectral analyses suggested that the flares are thought to originate from a distinct emission source. One possible explanation is the SSC process, where sub-keV photons were up-scattered by interaction with high-energy electrons (§ 5.2.2). The observation of the high-energy photons in GRB 190114C also suggested that the LAT emission may be attributed to both synchrotron and SSC emission processes (§ 5.4.6). The simultaneous MAGIC observation of GRB 190114C in the TeV energy band supports the consideration of the SSC contribution to GRBs, which help us reveal the detail of GRB physics such as the properties of the emitting region and the total energetics of GRBs.

Since the relativistic jet expands with an angle of a few degrees, the geometry of the outgoing shell plays an important role in evolution of temporal and spectral characteristics of GRBs. One of the geometrical effects is HLE, which has been identified in afterglow of GRBs. From the systematic study of GBM GRBs, I found the evidence of HLE in the prompt phase of GRBs for the first time (§ 6.1). Also, in the dedicated analysis in GRB 131108A, I showed that the decaying phase of the GeV flares are consistent with HLE, which is again the first identification of HLE in the GeV energy range (§ 5.2.2). These results support that the geometrical effect

in GRBs is universal in all energy bands, regardless of the emission region/phase.

These studies shed light on the physics of GRBs and how the relativistic jet evolves in time, especially for the high-energy emission. However, many open questions are remained unsolved. One troublesome problem is the origin of the prompt emission, especially non-thermal emission. Generally, the prompt emission is believed to originate from internal shocks or magnetic dissipation. The radiation mechanism for both models is the synchrotron process. This constrains a GRB spectrum to be similar to the synchrotron spectrum, resulting in certain slope and width around the peak energy (§ 2.2.2). In many cases, when observed data are fitted with empirical models such as Band and CPL, the resultant spectra have the low-energy photon index higher than the asymptotic limit of synchrotron emission ($\alpha \geq -2/3$). This fact challenges any model invoking the synchrotron process as the main emission mechanism of the observed prompt emission spectrum.

Recently, it was argued that the Band function with $\alpha \geq -2/3$ can be adequately fitted with the synchrotron spectrum [318]; when the two spectra are forward-folded through the GBM instrument response, the resulting count spectra are not different from each other. In addition, several groups successfully fit the observed data directly with the proper synchrotron spectrum, not with the empirical models such as Band or CPL [318–320]. These studies may alleviate the tension from disagreement between the observed spectra and the expected synchrotron spectrum. In addition, the universality of the multi-component spectrum has been suggested, where the GRB prompt spectrum consists of three spectral components [321]. The validity of this argument cannot be clearly tested with current missions due to

low sensitivity. Such ambiguities in the prompt emission spectrum can be resolved with more sensitive future missions such as the All-sky Medium Energy Gamma-ray Observatory (AMEGO) [322]. I performed a simulation study that showed that AMEGO would be able to detect many more low-luminous short GRBs than *Fermi* by a factor of $\sim$ 2–3.

The recent MAGIC detection of the VHE emission from GRB 190114C suggest that it is possible that we may miss VHE emission from many bright GRBs. Even though the MAGIC detection was made in the afterglow phase, the possibility of the VHE emission during the prompt emission cannot be ruled out. Like *Fermi*, the High-Altitude Water Cherenkov Observatory (HAWC) has a large field of view, providing an excellent chance to observe the prompt emission in the VHE regime from 100 GeV to 100 TeV [323, 324]. If the VHE prompt emission is observed by HAWC, it will provide the information on the energetics of GRBs that will be crucial to understand the origin of the prompt emission.

Bibliography

[1] Ray W. Klebesadel, Ian B. Strong, and Roy A. Olson. Observations of Gamma-Ray Bursts of Cosmic Origin. ApJ, 182:L85, Jun 1973.

[2] E. P. Mazets, S. V. Golenetskii, V. N. Ilinskii, V. N. Panov, R. L. Aptekar, Iu. A. Gurian, M. P. Proskura, I. A. Sokolov, Z. Ia. Sokolova, and T. V. Kharitonova. Catalog of cosmic gamma-ray bursts from the KONUS experiment data. Ap &SS, 80(1):3–83, Nov 1981.

[3] M. Ruderman. Theories of gamma -ray bursts. In P. G. Bergman, E. J. Fenyves, and L. Motz, editors, Seventh Texas Symposium on Relativistic Astrophysics, volume 262, pages 164–180, Oct 1975.

[4] G. Cavallo and M. J. Rees. A qualitative study of cosmic fireballs and gamma-ray bursts. MNRAS, 183:359–365, May 1978.

[5] B. Paczynski. Gamma-ray bursters at cosmological distances. ApJ, 308:L43–L46, Sep 1986.

[6] J. Goodman. Are gamma-ray bursts optically thick? ApJ, 308:L47, Sep 1986.

[7] William S. Paciesas, Charles A. Meegan, Geoffrey N. Pendleton, Michael S. Briggs, Chryssa Kouveliotou, Thomas M. Koshut, John Patrick Lestrade, Michael L. McCollough, Jerome J. Brainerd, and Jon Hakkila. The Fourth BATSE Gamma-Ray Burst Catalog (Revised). ApJS, 122(2):465–495, Jun 1999.

[8] D. Band, J. Matteson, L. Ford, B. Schaefer, D. Palmer, B. Teegarden, T. Cline, M. Briggs, W. Paciesas, and G. Pendleton. BATSE Observations of Gamma-Ray Burst Spectra. I. Spectral Diversity. ApJ, 413:281, Aug 1993.

[9] M. S. Briggs, D. L. Band, R. M. Kippen, R. D. Preece, C. Kouveliotou, J. van Paradijs, G. H. Share, R. J. Murphy, S. M. Matz, and A. Connors. Observations of GRB 990123 by the Compton Gamma Ray Observatory. ApJ, 524(1):82–91, Oct 1999.

[10] Chryssa Kouveliotou, Charles A. Meegan, Gerald J. Fishman, Narayana P. Bhat, Michael S. Briggs, Thomas M. Koshut, William S. Paciesas, and Geoffrey N. Pendleton. Identification of Two Classes of Gamma-Ray Bursts. ApJ, 413:L101, Aug 1993.

[11] Michael S. Briggs, William S. Paciesas, Geoffrey N. Pendleton, Charles A. Meegan, Gerald J. Fishman, John M. Horack, Martin N. Brock, Chryssa Kouveliotou, Dieter H. Hartmann, and Jon Hakkila. BATSE Observations of the Large-Scale Isotropy of Gamma-Ray Bursts. ApJ, 459:40, Mar 1996.

[12] C. A. Meegan, G. J. Fishman, R. B. Wilson, W. S. Paciesas, G. N. Pendleton, J. M. Horack, M. N. Brock, and C. Kouveliotou. Spatial distribution of γ-ray bursts observed by BATSE. Nature, 355(6356):143–145, Jan 1992.

[13] M. J. Rees and P. Mészáros. Relativistic fireballs - Energy conversion and time-scales. MNRAS, 258:41, Sep 1992.

[14] P. Mészáros and M. J. Rees. Relativistic Fireballs and Their Impact on External Matter: Models for Cosmological Gamma-Ray Bursts. ApJ, 405:278, Mar 1993.

[15] M. J. Rees and P. Mészáros. Unsteady Outflow Models for Cosmological Gamma-Ray Bursts. ApJ, 430:L93, Aug 1994.

[16] David Eichler, Mario Livio, Tsvi Piran, and David N. Schramm. Nucleosynthesis, neutrino bursts and γ-rays from coalescing neutron stars. Nature, 340(6229):126–128, Jul 1989.

[17] Bohdan Paczynski. Cosmological gamma-ray bursts. ACTAA, 41:257–267, Jan 1991.

[18] R. Narayan, B. Paczynski, and T. Piran. Gamma-ray bursts as the death throes of massive binary stars. ApJL, 395:L83–L86, August 1992.

[19] S. E. Woosley. Gamma-Ray Bursts from Stellar Mass Accretion Disks around Black Holes. ApJ, 405:273, Mar 1993.

[20] E. Costa, F. Frontera, J. Heise, M. Feroci, J. in't Zand, F. Fiore, M. N. Cinti, D. Dal Fiume, L. Nicastro, and M. Orlandini. Discovery of an X-ray afterglow associated with the γ-ray burst of 28 February 1997. Nature, 387(6635):783–785, Jun 1997.

[21] J. vanParadijs, P. J. Groot, T. Galama, C. Kouveliotou, R. G. Strom, J. Telting, R. G. M. Rutten, G. J. Fishman, C. A. Meegan, and M. Pettini. Transient optical emission from the error box of the γ-ray burst of 28 February 1997. Nature, 386(6626):686–689, Apr 1997.

[22] D. A. Frail, S. R. Kulkarni, L. Nicastro, M. Feroci, and G. B. Taylor. The radio afterglow from the γ-ray burst of 8 May 1997. Nature, 389(6648):261–263, Sep 1997.

[23] M. R. Metzger, S. G. Djorgovski, S. R. Kulkarni, C. C. Steidel, K. L. Adelberger, D. A. Frail, E. Costa, and F. Frontera. Spectral constraints on the redshift of the optical counterpart to the γ-ray burst of 8 May 1997. Nature, 387(6636):878–880, Jun 1997.

[24] P. Mészáros and M. J. Rees. Optical and Long-Wavelength Afterglow from Gamma-Ray Bursts. ApJ, 476(1):232–237, Feb 1997.

[25] Ralph A. M. J. Wijers, Martin J. Rees, and Peter Mészáros. Shocked by GRB 970228: the afterglow of a cosmological fireball. MNRAS, 288(4):L51–L56, Jul 1997.

[26] Mario Vietri. The Afterglow of Gamma-Ray Bursts: The Cases of GRB 970228 and GRB 970508. ApJ, 488(2):L105–L108, Oct 1997.

[27] T. J. Galama, P. M. Vreeswijk, J. van Paradijs, C. Kouveliotou, T. Augusteijn, H. Böhnhardt, J. P. Brewer, V. Doublier, J. F. Gonzalez, and B. Leibundgut. An unusual supernova in the error box of the γ-ray burst of 25 April 1998. Nature, 395(6703):670–672, Oct 1998.

[28] S. R. Kulkarni, D. A. Frail, M. H. Wieringa, R. D. Ekers, E. M. Sadler, R. M. Wark, J. L. Higdon, E. S. Phinney, and J. S. Bloom. Radio emission from the unusual supernova 1998bw and its association with the γ-ray burst of 25 April 1998. Nature, 395(6703):663–669, Oct 1998.

[29] T. J. Galama, N. Tanvir, P. M. Vreeswijk, R. A. M. J. Wijers, P. J. Groot, E. Rol, J. van Paradijs, C. Kouveliotou, A. S. Fruchter, and N. Masetti. Evidence for a Supernova in Reanalyzed Optical and Near-Infrared Images of GRB 970228. ApJ, 536(1):185–194, Jun 2000.

[30] N. Gehrels, G. Chincarini, P. Giommi, K. O. Mason, J. A. Nousek, A. A. Wells, N. E. White, S. D. Barthelmy, D. N. Burrows, and L. R. Cominsky. The Swift Gamma-Ray Burst Mission. ApJ, 611(2):1005–1020, Aug 2004.

[31] Bing Zhang, Y. Z. Fan, Jaroslaw Dyks, Shiho Kobayashi, Peter Mészáros, David N. Burrows, John A. Nousek, and Neil Gehrels. Physical Processes Shaping Gamma-Ray Burst X-Ray Afterglow Light Curves: Theoretical Implications from the Swift X-Ray Telescope Observations. ApJ, 642(1):354–370, May 2006.

[32] J. A. Nousek, C. Kouveliotou, D. Grupe, K. L. Page, J. Granot, E. Ramirez-Ruiz, S. K. Patel, D. N. Burrows, V. Mangano, and S. Barthelmy. Evidence for a Canonical Gamma-Ray Burst Afterglow Light Curve in the Swift XRT Data. ApJ, 642(1):389–400, May 2006.

[33] D. N. Burrows, P. Romano, A. Falcone, S. Kobayashi, B. Zhang, A. Moretti, P. T. O'Brien, M. R. Goad, S. Campana, and K. L. Page. Bright X-ray Flares in Gamma-Ray Burst Afterglows. Science, 309(5742):1833–1835, Sep 2005.

[34] Charles Meegan, Giselher Lichti, P. N. Bhat, Elisabetta Bissaldi, Michael S. Briggs, Valerie Connaughton, Roland Diehl, Gerald Fishman, Jochen Greiner, and Andrew S. Hoover. The Fermi Gamma-ray Burst Monitor. ApJ, 702(1):791–804, Sep 2009.

[35] W. B. Atwood, A. A. Abdo, M. Ackermann, W. Althouse, B. Anderson, M. Axelsson, L. Baldini, J. Ballet, D. L. Band, and G. Barbiellini. The Large Area Telescope on the Fermi Gamma-Ray Space Telescope Mission. ApJ, 697(2):1071–1102, Jun 2009.

[36] M. Ackermann, M. Ajello, K. Asano, M. Axelsson, L. Baldini, J. Ballet, G. Barbiellini, D. Bastieri, K. Bechtol, and R. Bellazzini. The First Fermi-LAT Gamma-Ray Burst Catalog. ApJS, 209(1):11, Nov 2013.

[37] M. Ajello, M. Arimoto, M. Axelsson, L. Baldini, G. Barbiellini, D. Bastieri, R. Bellazzini, P. N. Bhat, E. Bissaldi, and R. D. Blandford. A Decade of Gamma-Ray Bursts Observed by Fermi-LAT: The Second GRB Catalog. ApJ, 878(1):52, Jun 2019.

[38] A. A. Abdo, M. Ackermann, M. Ajello, K. Asano, W. B. Atwood, M. Axelsson, L. Baldini, J. Ballet, G. Barbiellini, and M. G. Baring. Fermi Observations of GRB 090902B: A Distinct Spectral Component in the Prompt and Delayed Emission. ApJ, 706(1):L138–L144, Nov 2009.

[39] M. Ackermann, K. Asano, W. B. Atwood, M. Axelsson, L. Baldini, J. Ballet, G. Barbiellini, M. G. Baring, D. Bastieri, and K. Bechtol. Fermi Observations of GRB 090510: A Short-Hard Gamma-ray Burst with an Additional, Hard Power-law Component from 10 keV TO GeV Energies. ApJ, 716(2):1178–1190, Jun 2010.

[40] Sylvain Guiriec, Valerie Connaughton, Michael S. Briggs, Michael Burgess, Felix Ryde, Frédéric Daigne, Peter Mészáros, Adam Goldstein, Julie McEnery, and Nicola Omodei. Detection of a Thermal Spectral Component in the Prompt Emission of GRB 100724B. ApJ, 727(2):L33, Feb 2011.

[41] Donggeun Tak, Sylvain Guiriec, Z. Lucas Uhm, Manal Yassine, Nicola Omodei, and Julie McEnery. Multiple Components in the Broadband γ-Ray Emission of the Short GRB 160709A. ApJ, 876(1):76, May 2019.

[42] B. P. Abbott, R. Abbott, T. D. Abbott, F. Acernese, K. Ackley, C. Adams, T. Adams, P. Addesso, R. X. Adhikari, and V. B. Adya. GW170817: Observation of Gravitational Waves from a Binary Neutron Star Inspiral. PRL, 119(16):161101, Oct 2017.

[43] B. P. Abbott, R. Abbott, T. D. Abbott, F. Acernese, K. Ackley, C. Adams, T. Adams, P. Addesso, R. X. Adhikari, and V. B. Adya. Gravitational Waves and Gamma-Rays from a Binary Neutron Star Merger: GW170817 and GRB 170817A. ApJ, 848(2):L13, Oct 2017.

[44] P. Mészáros, P. Laguna, and M. J. Rees. Gasdynamics of relativistically expanding gamma-ray burst sources - Kinematics, energetics, magnetic fields, and efficiency. ApJ, 415:181–190, September 1993.

[45] J. I. Katz. Low-Frequency Spectra of Gamma-Ray Bursts. ApJ, 432:L107, Sep 1994.

[46] T. Piran. Gamma-ray bursts and the fireball model. Phys Reports, 314(6):575–667, Jun 1999.

[47] P. Mészáros and M. J. Rees. Delayed GEV Emission from Cosmological Gamma-Ray Bursts - Impact of a Relativistic Wind on External Matter. MNRAS, 269:L41, Jul 1994.

[48] Enrico Fermi. On the Origin of the Cosmic Radiation. Physical Review, 75(8):1169–1174, Apr 1949.

[49] G. F. Krymskii. A regular mechanism for the acceleration of charged particles on the front of a shock wave. Akademiia Nauk SSSR Doklady, 234:1306–1308, Jun 1977.

[50] A. R. Bell. The acceleration of cosmic rays in shock fronts - I. MNRAS, 182:147–156, Jan 1978.

[51] R. D. Blandford and J. P. Ostriker. Particle acceleration by astrophysical shocks. ApJ, 221:L29–L32, Apr 1978.

[52] G. B. Rybicki and A. P. Lightman. Radiative processes in astrophysics. New York, Wiley-Interscience, 1979. 393 p., 1979.

[53] Bing Zhang. The Physics of Gamma-Ray Bursts. Cambridge University Press, 2018.

[54] P. Kumar, R. A. Hernández, Ž. Bošnjak, and R. Barniol Duran. Maximum synchrotron frequency for shock-accelerated particles. MNRAS, 427(1):L40–L44, Nov 2012.

[55] O. C. deJager, A. K. Harding, P. F. Michelson, H. I. Nel, P. L. Nolan, P. Sreekumar, and D. J. Thompson. Gamma-Ray Observations of the Crab Nebula: A Study of the Synchro-Compton Spectrum. ApJ, 457:253, January 1996.

[56] He Gao, Wei-Hua Lei, Xue-Feng Wu, and Bing Zhang. Compton scattering of self-absorbed synchrotron emission. MNRAS, 435(3):2520–2531, Nov 2013.

[57] Re'em Sari and Ann A. Esin. On the Synchrotron Self-Compton Emission from Relativistic Shocks and Its Implications for Gamma-Ray Burst Afterglows. ApJ, 548(2):787–799, Feb 2001.

[58] E. Nakar, S. Ando, and R. Sari. Klein-Nishina Effects on Optically Thin Synchrotron and Synchrotron Self-Compton Spectrum. ApJ, 703:675–691, September 2009.

[59] T. Piran and A. Shemi. Fireballs in the Galactic halo and gamma-ray bursts. ApJL, 403:L67–L69, February 1993.

[60] M. Ackermann, M. Ajello, K. Asano, M. Axelsson, L. Baldini, J. Ballet, G. Barbiellini, M. G. Baring, D. Bastieri, K. Bechtol, R. Bellazzini, B. Berenji, P. N. Bhat, E. Bissaldi, R. D. Blandford, E. Bonamente, A. W. Borgland, A. Bouvier, J. Bregeon, A. Brez, M. S. Briggs, M. Brigida, P. Bruel, R. Buehler, S. Buson, G. A. Caliandro, R. A. Cameron, P. A. Caraveo, S. Carrigan, J. M. Casandjian, C. Cecchi, Ö. Çelik, V. Chaplin, E. Charles, A. Chekhtman, J. Chiang, S. Ciprini, R. Claus, J. Cohen-Tanugi, V. Connaughton, J. Conrad, S. Cutini, C. D. Dermer, A. de Angelis, F. de Palma, B. L. Dingus, E. d. C. e. Silva, P. S. Drell, R. Dubois, C. Favuzzi, S. J. Fegan, E. C. Ferrara, W. B. Focke, M. Frailis, Y. Fukazawa, S. Funk, P. Fusco, F. Gargano, D. Gasparrini, N. Gehrels, S. Germani, N. Giglietto, F. Giordano, M. Giroletti, T. Glanzman, G. Godfrey, A. Goldstein, J. Granot, J. Greiner, I. A. Grenier, J. E. Grove, S. Guiriec, D. Hadasch, Y. Hanabata, A. K. Harding, K. Hayashi, M. Hayashida, E. Hays, D. Horan, R. E. Hughes, R. Itoh, G. Jóhannesson, A. S. Johnson, W. N. Johnson, T. Kamae, H. Katagiri, J. Kataoka, R. M. Kippen, J. Knödlseder, D. Kocevski, C. Kouveliotou, M. Kuss, J. Lande, L. Latronico, S.-H. Lee, M. Llena Garde, F. Longo, F. Loparco, M. N. Lovellette, P. Lubrano, A. Makeev, M. N. Mazziotta, S. McBreen, J. E. McEnery, S. McGlynn, C. Meegan, J. Mehault, P. Mészáros, P. F. Michelson, T. Mizuno, C. Monte, M. E. Monzani, E. Moretti, A. Morselli, I. V. Moskalenko, S. Murgia, H. Nakajima, T. Nakamori, M. Naumann-Godo, S. Nishino, P. L. Nolan, J. P. Norris, E. Nuss, M. Ohno, T. Ohsugi, A. Okumura, N. Omodei, E. Orlando, J. F. Ormes, M. Ozaki, W. S. Paciesas, D. Paneque, J. H. Panetta, D. Parent, V. Pelassa, M. Pepe, M. Pesce-Rollins, V. Petrosian, F. Piron, T. A. Porter, R. Preece, J. L. Racusin, S. Rainò, R. Rando, A. Rau, M. Razzano, S. Razzaque, A. Reimer, O. Reimer, T. Reposeur, L. C. Reyes, J. Ripken, S. Ritz, M. Roth, F. Ryde, H. F.-W. Sadrozinski, A. Sander, J. D. Scargle, T. L. Schalk, C. Sgrò, E. J. Siskind, P. D. Smith, G. Spandre, P. Spinelli, M. Stamatikos, F. W. Stecker, M. S. Strickman, D. J. Suson, H. Tajima, H. Takahashi, T. Tanaka, Y. Tanaka, J. B. Thayer, J. G. Thayer, L. Tibaldo, D. Tierney, K. Toma, D. F. Torres, G. Tosti, A. Tramacere, Y. Uchiyama, T. Uehara, T. L. Usher, J. Vandenbroucke, A. J. van der Horst, V. Vasileiou, N. Vilchez, V. Vitale, A. von Kienlin, A. P. Waite, P. Wang, C. Wilson-Hodge, B. L. Winer, K. S. Wood, X. F. Wu, R. Yamazaki,

Z. Yang, T. Ylinen, and M. Ziegler. Detection of a Spectral Break in the Extra Hard Component of GRB 090926A. ApJ, 729:114, March 2011.

[61] P. Narayana Bhat, Charles A. Meegan, Andreas von Kienlin, William S. Paciesas, Michael S. Briggs, J. Michael Burgess, Eric Burns, Vandiver Chaplin, William H. Cleveland, and Andrew C. Collazzi. The Third Fermi GBM Gamma-Ray Burst Catalog: The First Six Years. ApJS, 223(2):28, Apr 2016.

[62] A. A. Abdo, M. Ackermann, M. Arimoto, K. Asano, W. B. Atwood, M. Axelsson, L. Baldini, J. Ballet, D. L. Band, and G. Barbiellini. Fermi Observations of High-Energy Gamma-Ray Emission from GRB 080916C. Science, 323(5922):1688, Mar 2009.

[63] P. Veres, Z. Bagoly, I. Horváth, A. Mészáros, and L. G. Balázs. A Distinct Peak-flux Distribution of the Third Class of Gamma-ray Bursts: A Possible Signature of X-ray Flashes? ApJ, 725(2):1955–1964, Dec 2010.

[64] Amy Lien, Takanori Sakamoto, Scott D. Barthelmy, Wayne H. Baumgartner, John K. Cannizzo, Kevin Chen, Nicholas R. Collins, Jay R. Cummings, Neil Gehrels, Hans A. Krimm, Craig. B. Markwardt, David M. Palmer, Michael Stamatikos, Eleonora Troja, and T. N. Ukwatta. The Third Swift Burst Alert Telescope Gamma-Ray Burst Catalog. ApJ, 829(1):7, Sep 2016.

[65] J. P. Norris, R. J. Nemiroff, J. T. Bonnell, J. D. Scargle, C. Kouveliotou, W. S. Paciesas, C. A. Meegan, and G. J. Fishman. Attributes of Pulses in Long Bright Gamma-Ray Bursts. ApJ, 459:393, Mar 1996.

[66] J. P. Norris, G. F. Marani, and J. T. Bonnell. Connection between Energy-dependent Lags and Peak Luminosity in Gamma-Ray Bursts. ApJ, 534(1):248–257, May 2000.

[67] Kunihito Ioka and Takashi Nakamura. Peak Luminosity-Spectral Lag Relation Caused by the Viewing Angle of the Collimated Gamma-Ray Bursts. ApJL, 554(2):L163–L167, Jun 2001.

[68] Z. Lucas Uhm and Bing Zhang. Toward an Understanding of GRB Prompt Emission Mechanism. I. The Origin of Spectral Lags. ApJ, 825(2):97, Jul 2016.

[69] S. Guiriec, M. S. Briggs, V. Connaugthon, E. Kara, F. Daigne, C. Kouveliotou, A. J. van der Horst, W. Paciesas, C. A. Meegan, P. N. Bhat, S. Foley, E. Bissaldi, M. Burgess, V. Chaplin, R. Diehl, G. Fishman, M. Gibby, M. M. Giles, A. Goldstein, J. Greiner, D. Gruber, A. von Kienlin, M. Kippen, S. McBreen, R. Preece, A. Rau, D. Tierney, and C. Wilson-Hodge. Time-resolved Spectroscopy of the Three Brightest and Hardest Short Gamma-ray Bursts Observed with the Fermi Gamma-ray Burst Monitor. ApJ, 725:225–241, December 2010.

[70] S. Guiriec, F. Daigne, R. Hascoët, G. Vianello, F. Ryde, R. Mochkovitch, C. Kouveliotou, S. Xiong, P. N. Bhat, and S. Foley. Evidence for a Photospheric Component in the Prompt Emission of the Short GRB 120323A and Its Effects on the GRB Hardness-Luminosity Relation. ApJ, 770(1):32, Jun 2013.

[71] D. Burlon, G. Ghirlanda, G. Ghisellini, D. Lazzati, L. Nava, M. Nardini, and A. Celotti. Precursors in Swift Gamma Ray Bursts with Redshift. ApJL, 685(1):L19, Sep 2008.

[72] E. Troja, S. Rosswog, and N. Gehrels. Precursors of Short Gamma-ray Bursts. ApJ, 723(2):1711–1717, Nov 2010.

[73] Sylvia Zhu. Precursors in Gamma-ray Bursts Observed by Fermi. PhD thesis, University of Maryland, College park, 01 2015.

[74] Davide Lazzati. Precursor activity in bright, long BATSE gamma-ray bursts. MNRAS, 357(2):722–731, Feb 2005.

[75] You-Dong Hu, En-Wei Liang, Shao-Qiang Xi, Fang-Kun Peng, Rui-Jing Lu, Lian-Zhong Lü, and Bing Zhang. Internal Energy Dissipation of Gamma-Ray Bursts Observed with Swift: Precursors, Prompt Gamma-Rays, Extended Emission, and Late X-Ray Flares. ApJ, 789(2):145, Jul 2014.

[76] David Gruber, Adam Goldstein, Victoria Weller von Ahlefeld, P. Narayana Bhat, Elisabetta Bissaldi, Michael S. Briggs, Dave Byrne, William H. Cleveland, Valerie Connaughton, and Roland Diehl. The Fermi GBM Gamma-Ray Burst Spectral Catalog: Four Years of Data. ApJS, 211(1):12, Mar 2014.

[77] R. D. Preece, M. S. Briggs, R. S. Mallozzi, G. N. Pendleton, W. S. Paciesas, and D. L. Band. The Synchrotron Shock Model Confronts a "Line of Death" in the BATSE Gamma-Ray Burst Data. ApJL, 506:L23–L26, October 1998.

[78] F. Ryde, M. Axelsson, B. B. Zhang, S. McGlynn, A. Pe'er, C. Lundman, S. Larsson, M. Battelino, B. Zhang, and E. Bissaldi. Identification and Properties of the Photospheric Emission in GRB090902B. ApJ, 709(2):L172–L177, Feb 2010.

[79] M. Axelsson, L. Baldini, G. Barbiellini, M. G. Baring, R. Bellazzini, J. Bregeon, M. Brigida, P. Bruel, R. Buehler, G. A. Caliandro, R. A. Cameron, P. A. Caraveo, C. Cecchi, R. C. G. Chaves, A. Chekhtman, J. Chiang, R. Claus, J. Conrad, S. Cutini, F. D'Ammando, F. de Palma, C. D. Dermer, E. d. C. e. Silva, P. S. Drell, C. Favuzzi, S. J. Fegan, E. C. Ferrara, W. B. Focke, Y. Fukazawa, P. Fusco, F. Gargano, D. Gasparrini, N. Gehrels, S. Germani, N. Giglietto, M. Giroletti, G. Godfrey, S. Guiriec, D. Hadasch, Y. Hanabata, M. Hayashida, X. Hou, S. Iyyani, M. S. Jackson, D. Kocevski, M. Kuss, J. Larsson, S. Larsson, F. Longo, F. Loparco, C. Lundman, M. N. Mazziotta, J. E. McEnery, T. Mizuno, M. E. Monzani, E. Moretti, A. Morselli,

S. Murgia, E. Nuss, T. Nymark, M. Ohno, N. Omodei, M. Pesce-Rollins, F. Piron, G. Pivato, J. L. Racusin, S. Rainò, M. Razzano, S. Razzaque, A. Reimer, M. Roth, F. Ryde, D. A. Sanchez, C. Sgrò, E. J. Siskind, G. Spandre, P. Spinelli, M. Stamatikos, L. Tibaldo, M. Tinivella, T. L. Usher, J. Vandenbroucke, V. Vasileiou, G. Vianello, V. Vitale, A. P. Waite, B. L. Winer, K. S. Wood, J. M. Burgess, P. N. Bhat, E. Bissaldi, M. S. Briggs, V. Connaughton, G. Fishman, G. Fitzpatrick, S. Foley, D. Gruber, R. M. Kippen, C. Kouveliotou, P. Jenke, S. McBreen, S. McGlynn, C. Meegan, W. S. Paciesas, V. Pelassa, R. Preece, D. Tierney, A. von Kienlin, C. Wilson-Hodge, S. Xiong, and A. Pe'er. GRB110721A: An Extreme Peak Energy and Signatures of the Photosphere. ApJL, 757:L31, October 2012.

[80] A. Goldstein, P. Veres, E. Burns, M. S. Briggs, R. Hamburg, D. Kocevski, C. A. Wilson-Hodge, R. D. Preece, S. Poolakkil, O. J. Roberts, C. M. Hui, V. Connaughton, J. Racusin, A. von Kienlin, T. Dal Canton, N. Christensen, T. Littenberg, K. Siellez, L. Blackburn, J. Broida, E. Bissaldi, W. H. Cleveland, M. H. Gibby, M. M. Giles, R. M. Kippen, S. McBreen, J. McEnery, C. A. Meegan, W. S. Paciesas, and M. Stanbro. An Ordinary Short Gamma-Ray Burst with Extraordinary Implications: Fermi-GBM Detection of GRB 170817A. ApJL, 848(2):L14, Oct 2017.

[81] Ore Gottlieb, Ehud Nakar, Tsvi Piran, and Kenta Hotokezaka. A cocoon shock breakout as the origin of the γ-ray emission in GW170817. MNRAS, 479(1):588–600, Sep 2018.

[82] E. Burns, P. Veres, V. Connaughton, J. Racusin, M. S. Briggs, N. Christensen, A. Goldstein, R. Hamburg, D. Kocevski, J. McEnery, E. Bissaldi, T. Dal Canton, W. H. Cleveland, M. H. Gibby, C. M. Hui, A. von Kienlin, B. Mailyan, W. S. Paciesas, O. J. Roberts, K. Siellez, M. Stanbro, and C. A. Wilson-Hodge. Fermi GBM Observations of GRB 150101B: A Second Nearby Event with a Short Hard Spike and a Soft Tail. ApJL, 863(2):L34, Aug 2018.

[83] A. vonKienlin, P. Veres, O. J. Roberts, R. Hamburg, E. Bissaldi, M. S. Briggs, E. Burns, A. Goldstein, D. Kocevski, R. D. Preece, C. A. Wilson-Hodge, C. M. Hui, B. Mailyan, and C. Malacaria. Fermi-GBM GRBs with Characteristics Similar to GRB 170817A. ApJ, 876(1):89, May 2019.

[84] Rui-Jing Lu, Jun-Jie Wei, En-Wei Liang, Bin-Bin Zhang, Hou-Jun Lü, Lian-Zhong Lü, Wei-Hua Lei, and Bing Zhang. A Comprehensive Analysis of Fermi Gamma-Ray Burst Data. II. E $_p$ Evolution Patterns and Implications for the Observed Spectrum-Luminosity Relations. ApJ, 756(2):112, Sep 2012.

[85] Z. Lucas Uhm, Bing Zhang, and Judith Racusin. Toward an Understanding of GRB Prompt Emission Mechanism. II. Patterns of Peak Energy Evolution and Their Connection to Spectral Lags. ApJ, 869(2):100, Dec 2018.

[86] Lorenzo Amati. The $E_{p,i}$-E_{iso} correlation in gamma-ray bursts: updated observational status, re-analysis and main implications. MNRAS, 372(1):233–245, Oct 2006.

[87] D. Yonetoku, T. Murakami, T. Nakamura, R. Yamazaki, A. K. Inoue, and K. Ioka. Gamma-Ray Burst Formation Rate Inferred from the Spectral Peak Energy-Peak Luminosity Relation. ApJ, 609(2):935–951, Jul 2004.

[88] Giancarlo Ghirlanda, Gabriele Ghisellini, and Davide Lazzati. The Collimation-corrected Gamma-Ray Burst Energies Correlate with the Peak Energy of Their νF_ν Spectrum. ApJ, 616(1):331–338, Nov 2004.

[89] S. Guiriec, C. Kouveliotou, F. Daigne, B. Zhang, R. Hascoët, R. S. Nemmen, D. J. Thompson, P. N. Bhat, N. Gehrels, M. M. Gonzalez, Y. Kaneko, J. McEnery, R. Mochkovitch, J. L. Racusin, F. Ryde, J. R. Sacahui, and A. M. Ünsal. Toward a Better Understanding of the GRB Phenomenon: a New Model for GRB Prompt Emission and its Effects on the New ${L_i}^{NT}$-${E_{peak,i}}^{rest,NT}$ Relation. ApJ, 807(2):148, Jul 2015.

[90] David L. Band and Robert D. Preece. Testing the Gamma-Ray Burst Energy Relationships. ApJ, 627(1):319–323, Jul 2005.

[91] Daniel Kocevski. On the Origin of High-energy Correlations in Gamma-Ray Bursts. ApJ, 747(2):146, Mar 2012.

[92] E. W. Liang, Z. G. Dai, and X. F. Wu. The Luminosity-E_p Relation within Gamma-Ray Bursts and the Implications for Fireball Models. ApJL, 606(1):L29–L32, May 2004.

[93] G. Ghirlanda, L. Nava, and G. Ghisellini. Spectral-luminosity relation within individual Fermi gamma rays bursts. A&A, 511:A43, Feb 2010.

[94] D. A. Perley, S. B. Cenko, A. Corsi, N. R. Tanvir, A. J. Levan, D. A. Kann, E. Sonbas, K. Wiersema, W. Zheng, X. H. Zhao, J. M. Bai, M. Bremer, A. J. Castro-Tirado, L. Chang, K. I. Clubb, D. Frail, A. Fruchter, E. Göğüş, J. Greiner, T. Güver, A. Horesh, A. V. Filippenko, S. Klose, J. Mao, A. N. Morgan, A. S. Pozanenko, S. Schmidl, B. Stecklum, M. Tanga, A. A. Volnova, A. E. Volvach, J. G. Wang, J. M. Winters, and Y. X. Xin. The Afterglow of GRB 130427A from 1 to 10^{16} GHz. ApJ, 781(1):37, Jan 2014.

[95] Re'em Sari, Tsvi Piran, and Ramesh Narayan. Spectra and Light Curves of Gamma-Ray Burst Afterglows. ApJ, 497(1):L17–L20, Apr 1998.

[96] Jonathan Granot and Re'em Sari. The Shape of Spectral Breaks in Gamma-Ray Burst Afterglows. ApJ, 568(2):820–829, Apr 2002.

[97] G. Ghirlanda, G. Ghisellini, and L. Nava. The onset of the GeV afterglow of GRB 090510. A&A, 510:L7, February 2010.

[98] G. Chincarini, A. Moretti, P. Romano, A. D. Falcone, D. Morris, J. Racusin, S. Campana, S. Covino, C. Guidorzi, G. Tagliaferri, D. N. Burrows, C. Pagani, M. Stroh, D. Grupe, M. Capalbi, G. Cusumano, N. Gehrels, P. Giommi, V. La Parola, V. Mangano, T. Mineo, J. A. Nousek, P. T. O'Brien, K. L. Page, M. Perri, E. Troja, R. Willingale, and B. Zhang. The First Survey of X-Ray Flares from Gamma-Ray Bursts Observed by Swift: Temporal Properties and Morphology. ApJ, 671(2):1903–1920, Dec 2007.

[99] S. R. Kulkarni, D. A. Frail, R. Sari, G. H. Moriarty-Schieven, D. S. Shepherd, P. Udomprasert, A. C. S. Readhead, J. S. Bloom, M. Feroci, and E. Costa. Discovery of a Radio Flare from GRB 990123. ApJL, 522(2):L97–L100, Sep 1999.

[100] E. Berger, A. M. Soderberg, D. A. Frail, and S. R. Kulkarni. A Radio Flare from GRB 020405: Evidence for a Uniform Medium around a Massive Stellar Progenitor. ApJL, 587(1):L5–L8, Apr 2003.

[101] P. W. A. Roming, D. Vanden Berk, V. Pal'shin, C. Pagani, J. Norris, P. Kumar, H. Krimm, S. T. Holland, C. Gronwall, A. J. Blustin, B. Zhang, P. Schady, T. Sakamoto, J. P. Osborne, J. A. Nousek, F. E. Marshall, P. Mészáros, S. V. Golenetskii, N. Gehrels, D. D. Frederiks, S. Campana, D. N. Burrows, P. T. Boyd, S. Barthelmy, and R. L. Aptekar. GRB 060313: A New Paradigm for Short-Hard Bursts? ApJ, 651:985–993, November 2006.

[102] P. Romano, A. Moretti, P. L. Banat, D. N. Burrows, S. Campana, G. Chincarini, S. Covino, D. Malesani, G. Tagliaferri, S. Kobayashi, B. Zhang, A. D. Falcone, L. Angelini, S. Barthelmy, A. P. Beardmore, M. Capalbi, G. Cusumano, P. Giommi, M. R. Goad, O. Godet, D. Grupe, J. E. Hill, J. A. Kennea, V. La Parola, V. Mangano, P. Mészáros, D. C. Morris, J. A. Nousek, P. T. O'Brien, J. P. Osborne, A. Parsons, M. Perri, C. Pagani, K. L. Page, A. A. Wells, and N. Gehrels. X-ray flare in XRF 050406: evidence for prolonged engine activity. A&A, 450:59–68, April 2006.

[103] E. W. Liang, B. Zhang, P. T. O'Brien, R. Willingale, L. Angelini, D. N. Burrows, S. Campana, G. Chincarini, A. Falcone, N. Gehrels, M. R. Goad, D. Grupe, S. Kobayashi, P. Mészáros, J. A. Nousek, J. P. Osborne, K. L. Page, and G. Tagliaferri. Testing the Curvature Effect and Internal Origin of Gamma-Ray Burst Prompt Emissions and X-Ray Flares with Swift Data. ApJ, 646:351–357, July 2006.

[104] Z. L. Uhm and B. Zhang. Evidence of Bulk Acceleration of the GRB X-Ray Flare Emission Region. ApJL, 824:L16, June 2016.

[105] L.-W. Jia, Z. L. Uhm, and B. Zhang. A Statistical Study of GRB X-Ray Flares: Evidence of Ubiquitous Bulk Acceleration in the Emission Region. ApJS, 225:17, July 2016.

[106] J. S. Bloom, S. R. Kulkarni, S. G. Djorgovski, A. C. Eichelberger, P. Côté, J. P. Blakeslee, S. C. Odewahn, F. A. Harrison, D. A. Frail, A. V. Filippenko, D. C. Leonard, A. G. Riess, H. Spinrad, D. Stern, A. Bunker, A. Dey, B. Grossan, S. Perlmutter, R. A. Knop, I. M. Hook, and M. Feroci. The unusual afterglow of the γ-ray burst of 26 March 1998 as evidence for a supernova connection. Nature, 401(6752):453–456, Sep 1999.

[107] Jens Hjorth, Jesper Sollerman, Palle Møller, Johan P. U. Fynbo, Stan E. Woosley, Chryssa Kouveliotou, Nial R. Tanvir, Jochen Greiner, Michael I. Andersen, Alberto J. Castro-Tirado, José María Castro Cerón, Andrew S. Fruchter, Javier Gorosabel, Páll Jakobsson, Lex Kaper, Sylvio Klose, Nicola Masetti, Holger Pedersen, Kristian Pedersen, Elena Pian, Eliana Palazzi, James E. Rhoads, Evert Rol, Edward P. J. van den Heuvel, Paul M. Vreeswijk, Darach Watson, and Ralph A. M. J. Wijers. A very energetic supernova associated with the γ-ray burst of 29 March 2003. Nature, 423(6942):847–850, Jun 2003.

[108] Alexei V. Filippenko. Optical Spectra of Supernovae. ARAA, 35:309–355, Jan 1997.

[109] K. Iwamoto, P. A. Mazzali, K. Nomoto, H. Umeda, T. Nakamura, F. Patat, I. J. Danziger, T. R. Young, T. Suzuki, T. Shigeyama, T. Augusteijn, V. Doublier, J. F. Gonzalez, H. Boehnhardt, J. Brewer, O. R. Hainaut, C. Lidman, B. Leibundgut, E. Cappellaro, M. Turatto, T. J. Galama, P. M. Vreeswijk, C. Kouveliotou, J. van Paradijs, E. Pian, E. Palazzi, and F. Frontera. A hypernova model for the supernova associated with the γ-ray burst of 25 April 1998. Nature, 395(6703):672–674, Oct 1998.

[110] K. Z. Stanek, T. Matheson, P. M. Garnavich, P. Martini, P. Berlind, N. Caldwell, P. Challis, W. R. Brown, R. Schild, K. Krisciunas, M. L. Calkins, J. C. Lee, N. Hathi, R. A. Jansen, R. Windhorst, L. Echevarria, D. J. Eisenstein, B. Pindor, E. W. Olszewski, P. Harding, S. T. Holland , and D. Bersier. Spectroscopic Discovery of the Supernova 2003dh Associated with GRB 030329. ApJL, 591(1):L17–L20, Jul 2003.

[111] D. Malesani, G. Tagliaferri, G. Chincarini, S. Covino, M. Della Valle, D. Fugazza, P. A. Mazzali, F. M. Zerbi, P. D'Avanzo, S. Kalogerakos, A. Simoncelli, L. A. Antonelli, L. Burderi, S. Campana, A. Cucchiara, F. Fiore, G. Ghirlanda, P. Goldoni, D. Götz, S. Mereghetti, I. F. Mirabel, P. Romano, L. Stella, T. Minezaki, Y. Yoshii, and K. Nomoto. SN 2003lw and GRB 031203: A Bright Supernova for a Faint Gamma-Ray Burst. ApJL, 609(1):L5–L8, Jul 2004.

[112] E. Pian, P. A. Mazzali, N. Masetti, P. Ferrero, S. Klose, E. Palazzi, E. Ramirez-Ruiz, S. E. Woosley, C. Kouveliotou, J. Deng, A. V. Filippenko, R. J. Foley, J. P. U. Fynbo, D. A. Kann, W. Li, J. Hjorth, K. Nomoto, F. Patat, D. N. Sauer, J. Sollerman, P. M. Vreeswijk, E. W. Guenther, A. Levan, P. O'Brien,

N. R. Tanvir, R. A. M. J. Wijers, C. Dumas, O. Hainaut, D. S. Wong, D. Baade, L. Wang, L. Amati, E. Cappellaro, A. J. Castro-Tirado, S. Ellison, F. Frontera, A. S. Fruchter, J. Greiner, K. Kawabata, C. Ledoux, K. Maeda, P. Møller, L. Nicastro, E. Rol, and R. Starling. An optical supernova associated with the X-ray flash XRF 060218. Nature, 442(7106):1011–1013, Aug 2006.

[113] B. P. Abbott, R. Abbott, T. D. Abbott, M. R. Abernathy, F. Acernese, K. Ackley, C. Adams, T. Adams, P. Addesso, R. X. Adhikari, and et al. Observation of Gravitational Waves from a Binary Black Hole Merger. PRL, 116(6):061102, Feb 2016.

[114] J. H. Taylor and J. M. Weisberg. A new test of general relativity - Gravitational radiation and the binary pulsar PSR 1913+16. ApJ, 253:908–920, Feb 1982.

[115] D. A. Coulter, R. J. Foley, C. D. Kilpatrick, M. R. Drout, A. L. Piro, B. J. Shappee, M. R. Siebert, J. D. Simon, N. Ulloa, D. Kasen, B. F. Madore, A. Murguia-Berthier, Y. C. Pan, J. X. Prochaska, E. Ramirez-Ruiz, A. Rest, and C. Rojas-Bravo. Swope Supernova Survey 2017a (SSS17a), the optical counterpart to a gravitational wave source. Science, 358(6370):1556–1558, Dec 2017.

[116] Li-Xin Li and Bohdan Paczyński. Transient Events from Neutron Star Mergers. ApJL, 507(1):L59–L62, Nov 1998.

[117] C. Freiburghaus, S. Rosswog, and F. K. Thielemann. R-Process in Neutron Star Mergers. ApJL, 525(2):L121–L124, Nov 1999.

[118] M. G. Aartsen, K. Abraham, M. Ackermann, J. Adams, J. A. Aguilar, M. Ahlers, M. Ahrens, D. Altmann, T. Anderson, I. Ansseau, and et al. An All-sky Search for Three Flavors of Neutrinos from Gamma-ray Bursts with the IceCube Neutrino Observatory. ApJ, 824(2):115, Jun 2016.

[119] M. G. Aartsen, M. Ackermann, J. Adams, J. A. Aguilar, M. Ahlers, M. Ahrens, D. Altmann, T. Anderson, C. Arguelles, T. C. Arlen, and et al. Search for Prompt Neutrino Emission from Gamma-Ray Bursts with IceCube. ApJL, 805(1):L5, May 2015.

[120] *Fermi*/GBM collaboration. *Fermi* GBM Burst Online Catalog. `https://heasarc.gsfc.nasa.gov/W3Browse/fermi/fermigbrst.html`.

[121] S. Schulze, S. Klose, G. Björnsson, P. Jakobsson, D. A. Kann, A. Rossi, T. Krühler, J. Greiner, and P. Ferrero. The circumburst density profile around GRB progenitors: a statistical study. A&A, 526:A23, February 2011.

[122] N. Gehrels, C. L. Sarazin, P. T. O'Brien, B. Zhang, L. Barbier, S. D. Barthelmy, A. Blustin, D. N. Burrows, J. Cannizzo, J. R. Cummings, M. Goad,

S. T. Holland, C. P. Hurkett, J. A. Kennea, A. Levan, C. B. Markwardt, K. O. Mason, P. Meszaros, M. Page, D. M. Palmer, E. Rol, T. Sakamoto, R. Willingale, L. Angelini, A. Beardmore, P. T. Boyd, A. Breeveld, S. Campana, M. M. Chester, G. Chincarini, L. R. Cominsky, G. Cusumano, M. de Pasquale, E. E. Fenimore, P. Giommi, C. Gronwall, D. Grupe, J. E. Hill, D. Hinshaw, J. Hjorth, D. Hullinger, K. C. Hurley, S. Klose, S. Kobayashi, C. Kouveliotou, H. A. Krimm, V. Mangano, F. E. Marshall, K. McGowan, A. Moretti, R. F. Mushotzky, K. Nakazawa, J. P. Norris, J. A. Nousek, J. P. Osborne, K. Page, A. M. Parsons, S. Patel, M. Perri, T. Poole, P. Romano, P. W. A. Roming, S. Rosen, G. Sato, P. Schady, A. P. Smale, J. Sollerman, R. Starling, M. Still, M. Suzuki, G. Tagliaferri, T. Takahashi, M. Tashiro, J. Tueller, A. A. Wells, N. E. White, and R. A. M. J. Wijers. A short γ-ray burst apparently associated with an elliptical galaxy at redshift z = 0.225. Nature, 437(7060):851–854, Oct 2005.

[123] A. S. Fruchter, A. J. Levan, L. Strolger, P. M. Vreeswijk, S. E. Thorsett, D. Bersier, I. Burud, J. M. Castro Cerón, A. J. Castro-Tirado, C. Conselice, T. Dahlen, H. C. Ferguson, J. P. U. Fynbo, P. M. Garnavich, R. A. Gibbons, J. Gorosabel, T. R. Gull, J. Hjorth, S. T. Holland , C. Kouveliotou, Z. Levay, M. Livio, M. R. Metzger, P. E. Nugent, L. Petro, E. Pian, J. E. Rhoads, A. G. Riess, K. C. Sahu, A. Smette, N. R. Tanvir, R. A. M. J. Wijers, and S. E. Woosley. Long γ-ray bursts and core-collapse supernovae have different environments. Nature, 441(7092):463–468, May 2006.

[124] W. Fong and E. Berger. The Locations of Short Gamma-Ray Bursts as Evidence for Compact Object Binary Progenitors. ApJ, 776(1):18, Oct 2013.

[125] J. L. Racusin, S. R. Oates, P. Schady, D. N. Burrows, M. de Pasquale, D. Donato, N. Gehrels, S. Koch, J. McEnery, T. Piran, P. Roming, T. Sakamoto, C. Swenson, E. Troja, V. Vasileiou, F. Virgili, D. Wanderman, and B. Zhang. Fermi and Swift Gamma-ray Burst Afterglow Population Studies. ApJ, 738(2):138, Sep 2011.

[126] T. Piran. The physics of gamma-ray bursts. Reviews of Modern Physics, 76:1143–1210, October 2004.

[127] P. Mészáros. Gamma-ray bursts. Reports on Progress in Physics, 69(8):2259–2321, Aug 2006.

[128] Pawan Kumar and Bing Zhang. The physics of gamma-ray bursts & relativistic jets. Phys Reports, 561:1–109, Feb 2015.

[129] Jonathan Granot and Enrico Ramirez-Ruiz. Jets and Gamma-Ray Burst Unification Schemes. arXiv e-prints, page arXiv:1012.5101, Dec 2010.

[130] James E. Rhoads. How to Tell a Jet from a Balloon: A Proposed Test for Beaming in Gamma-Ray Bursts. ApJL, 487(1):L1–L4, Sep 1997.

[131] J. E. Rhoads. The Dynamics and Light Curves of Beamed Gamma-Ray Burst Afterglows. ApJ, 525:737–749, November 1999.

[132] J. L. Racusin, E. W. Liang, D. N. Burrows, A. Falcone, T. Sakamoto, B. B. Zhang, B. Zhang, P. Evans, and J. Osborne. Jet Breaks and Energetics of Swift Gamma-Ray Burst X-Ray Afterglows. ApJ, 698:43–74, June 2009.

[133] S. R. Kulkarni, S. G. Djorgovski, S. C. Odewahn, J. S. Bloom, R. R. Gal, C. D. Koresko, F. A. Harrison, L. M. Lubin, L. Armus, and R. Sari. The afterglow, redshift and extreme energetics of the γ-ray burst of 23 January 1999. Nature, 398(6726):389–394, Apr 1999.

[134] P. Mészáros, M. J. Rees, and R. A. M. J. Wijers. Energetics and beaming of gamma ray burst triggers. New Astronomy, 4(4):303–312, Jul 1999.

[135] P. Mészáros and M. J. Rees. GRB 990123: reverse and internal shock flashes and late afterglow behaviour. MNRAS, 306(3):L39–L43, Jul 1999.

[136] Pawan Kumar and Alin Panaitescu. Afterglow Emission from Naked Gamma-Ray Bursts. ApJ, 541(2):L51–L54, Oct 2000.

[137] Z. Lucas Uhm and Bing Zhang. On the Curvature Effect of a Relativistic Spherical Shell. ApJ, 808(1):33, Jul 2015.

[138] Robert Popham, S. E. Woosley, and Chris Fryer. Hyperaccreting Black Holes and Gamma-Ray Bursts. ApJ, 518(1):356–374, Jun 1999.

[139] Ramesh Narayan, Tsvi Piran, and Pawan Kumar. Accretion Models of Gamma-Ray Bursts. ApJ, 557(2):949–957, Aug 2001.

[140] V. V. Usov. Millisecond pulsars with extremely strong magnetic fields as a cosmological source of γ-ray bursts. Nature, 357(6378):472–474, Jun 1992.

[141] C. Thompson. A model of gamma-ray bursts. MNRAS, 270:480–498, Oct 1994.

[142] Z. G. Dai and T. Lu. Gamma-ray burst afterglows and evolution of post-burst fireballs with energy injection from strongly magnetic millisecond pulsars. A &A, 333:L87–L90, May 1998.

[143] Kunihito Ioka, Shiho Kobayashi, and Bing Zhang. Variabilities of Gamma-Ray Burst Afterglows: Long-acting Engine, Anisotropic Jet, or Many Fluctuating Regions? ApJ, 631(1):429–434, Sep 2005.

[144] A. D. Falcone, D. N. Burrows, D. Lazzati, S. Campana, S. Kobayashi, B. Zhang, P. Mészáros, K. L. Page, J. A. Kennea, and P. Romano. The Giant X-Ray Flare of GRB 050502B: Evidence for Late-Time Internal Engine Activity. ApJ, 641(2):1010–1017, Apr 2006.

[145] P. Mészáros and M. J. Rees. Steep Slopes and Preferred Breaks in Gamma-Ray Burst Spectra: The Role of Photospheres and Comptonization. ApJ, 530(1):292–298, Feb 2000.

[146] Asaf Peer, Peter Mészáros, and Martin J. Rees. The Observable Effects of a Photospheric Component on GRB and XRF Prompt Emission Spectrum. ApJ, 642(2):995–1003, May 2006.

[147] Andrei M. Beloborodov. Collisional mechanism for gamma-ray burst emission. MNRAS, 407(2):1033–1047, Sep 2010.

[148] Asaf Peer, Felix Ryde, Ralph A. M. J. Wijers, Peter Mészáros, and Martin J. Rees. A New Method of Determining the Initial Size and Lorentz Factor of Gamma-Ray Burst Fireballs Using a Thermal Emission Component. ApJ, 664(1):L1–L4, Jul 2007.

[149] Asaf Peer. Temporal Evolution of Thermal Emission from Relativistically Expanding Plasma. ApJ, 682(1):463–473, Jul 2008.

[150] F. Daigne and R. Mochkovitch. The expected thermal precursors of gamma-ray bursts in the internal shock model. MNRAS, 336:1271–1280, November 2002.

[151] R. Hascoët, F. Daigne, and R. Mochkovitch. Prompt thermal emission in gamma-ray bursts. A &A, 551:A124, March 2013.

[152] Wei Deng and Bing Zhang. Low Energy Spectral Index and E_p Evolution of Quasi-thermal Photosphere Emission of Gamma-Ray Bursts. ApJ, 785(2):112, Apr 2014.

[153] M. J. Rees and P. Mészáros. Dissipative Photosphere Models of Gamma-Ray Bursts and X-Ray Flashes. ApJ, 628(2):847–852, Aug 2005.

[154] Andrei M. Beloborodov. Regulation of the Spectral Peak in Gamma-Ray Bursts. ApJ, 764(2):157, Feb 2013.

[155] Asaf Peer and Felix Ryde. Photospheric emission in gamma-ray bursts. International Journal of Modern Physics D, 26(10):1730018–296, Jan 2017.

[156] A. M. Beloborodov and P. Mészáros. Photospheric Emission of Gamma-Ray Bursts. Space Science Reviews, 207(1-4):87–110, Jul 2017.

[157] Shiho Kobayashi, Tsvi Piran, and Re'em Sari. Can Internal Shocks Produce the Variability in Gamma-Ray Bursts? ApJ, 490:92, Nov 1997.

[158] F. Daigne and R. Mochkovitch. Gamma-ray bursts from internal shocks in a relativistic wind: temporal and spectral properties. MNRAS, 296(2):275–286, May 1998.

[159] Pawan Kumar. Gamma-Ray Burst Energetics. ApJ, 523(2):L113–L116, Oct 1999.

[160] M. Spada, A. Panaitescu, and P. Mészáros. Analysis of Temporal Features of Gamma-Ray Bursts in the Internal Shock Model. ApJ, 537(2):824–832, Jul 2000.

[161] D. Guetta, M. Spada, and E. Waxman. Efficiency and Spectrum of Internal Gamma-Ray Burst Shocks. ApJ, 557(1):399–407, Aug 2001.

[162] Re'em Sari and Tsvi Piran. Cosmological gamma-ray bursts: internal versus external shocks. MNRAS, 287(1):110–116, May 1997.

[163] R. Mochkovitch, V. Maitia, and R. Marques. Internal Shocks in a Relativistic Wind as a Source for Gamma-Ray Bursts? Ap &SS, 231(1-2):441–444, Sep 1995.

[164] A. Panaitescu, M. Spada, and P. Mészáros. Power Density Spectra of Gamma-Ray Bursts in the Internal Shock Model. ApJ, 522(2):L105–L108, Sep 1999.

[165] Shiho Kobayashi and Re'em Sari. Ultraefficient Internal Shocks. ApJ, 551(2):934–939, Apr 2001.

[166] Bing Zhang, Enwei Liang, Kim L. Page, Dirk Grupe, Bin-Bin Zhang, Scott D. Barthelmy, David N. Burrows, Sergio Campana, Guido Chincarini, and Neil Gehrels. GRB Radiative Efficiencies Derived from the Swift Data: GRBs versus XRFs, Long versus Short. ApJ, 655(2):989–1001, Feb 2007.

[167] A. Peer and B. Zhang. Synchrotron Emission in Small-Scale Magnetic Fields as a Possible Explanation for Prompt Emission Spectra of Gamma-Ray Bursts. ApJ, 653:454–461, December 2006.

[168] K. Asano and T. Terasawa. Slow Heating Model of Gamma-ray Burst: Photon Spectrum and Delayed Emission. ApJ, 705:1714–1720, November 2009.

[169] Z. L. Uhm and B. Zhang. Fast-cooling synchrotron radiation in a decaying magnetic field and γ-ray burst emission mechanism. Nature Physics, 10:351–356, May 2014.

[170] Peter Goldreich and William H. Julian. Stellar Winds. ApJ, 160:971, Jun 1970.

[171] G. Drenkhahn. Acceleration of GRB outflows by Poynting flux dissipation. A &A, 387:714–724, May 2002.

[172] Jonathan Granot, Serguei S. Komissarov, and Anatoly Spitkovsky. Impulsive acceleration of strongly magnetized relativistic flows. MNRAS, 411(2):1323–1353, Feb 2011.

[173] Shuji Kamio, Qinghong Cao, Keita Abe, Morio Sakumura, Naoto Suzuki, Takenori G. Watanabe, Koji Ishiguchi, Ryota Imazawa, Takuma Yamada, and Michiaki Inomoto. Multipoint Spectroscopy Measurement of Spherical Tokamak Heating by Magnetic Reconnection in UTST. Plasma and Fusion Research, 6:2402033–2402033, Jan 2011.

[174] Lorenzo Sironi and Anatoly Spitkovsky. Relativistic Reconnection: An Efficient Source of Non-thermal Particles. ApJL, 783(1):L21, Mar 2014.

[175] P. A. Sweet. The Neutral Point Theory of Solar Flares. In B. Lehnert, editor, Electromagnetic Phenomena in Cosmical Physics, volume 6 of IAU Symposium, page 123, Jan 1958.

[176] E. N. Parker. Sweet's Mechanism for Merging Magnetic Fields in Conducting Fluids. JGR, 62(4):509–520, Dec 1957.

[177] H. E. Petschek. Magnetic Field Annihilation. In The Physics of Solar Flares, Proceedings of the AAS-NASA Symposium held 28-30 October, 1963 at the Goddard Space Flight Center, Greenbelt, MD., volume 50, page 425, 1964.

[178] A. Lazarian and Ethan T. Vishniac. Reconnection in a Weakly Stochastic Field. ApJ, 517(2):700–718, Jun 1999.

[179] S. Zenitani and M. Hoshino. The Generation of Nonthermal Particles in the Relativistic Magnetic Reconnection of Pair Plasmas. ApJL, 562(1):L63–L66, Nov 2001.

[180] C. H. Jaroschek, R. A. Treumann, H. Lesch, and M. Scholer. Fast reconnection in relativistic pair plasmas: Analysis of particle acceleration in self-consistent full particle simulations. Physics of Plasmas, 11(3):1151–1163, Mar 2004.

[181] J. F. Drake, M. Swisdak, H. Che, and M. A. Shay. Electron acceleration from contracting magnetic islands during reconnection. Nature, 443(7111):553–556, Oct 2006.

[182] Fan Guo, Yi-Hsin Liu, William Daughton, and Hui Li. Particle Acceleration and Plasma Dynamics during Magnetic Reconnection in the Magnetically Dominated Regime. ApJ, 806(2):167, Jun 2015.

[183] Maxim Lyutikov and Roger Blandford. Gamma Ray Bursts as Electromagnetic Outflows. arXiv e-prints, pages astro–ph/0312347, Dec 2003.

[184] Bing Zhang and Huirong Yan. The Internal-collision-induced Magnetic Reconnection and Turbulence (ICMART) Model of Gamma-ray Bursts. ApJ, 726(2):90, Jan 2011.

[185] Jonathan C. McKinney and Dmitri A. Uzdensky. A reconnection switch to trigger gamma-ray burst jet dissipation. MNRAS, 419(1):573–607, Jan 2012.

[186] X.-G. Wang, B. Zhang, E.-W. Liang, H. Gao, L. Li, C.-M. Deng, S.-M. Qin, Q.-W. Tang, D. A. Kann, F. Ryde, and P. Kumar. How Bad or Good Are the External Forward Shock Afterglow Models of Gamma-Ray Bursts? ApJS, 219:9, July 2015.

[187] R. A. Chevalier and Z.-Y. Li. Wind Interaction Models for Gamma-Ray Burst Afterglows: The Case for Two Types of Progenitors. ApJ, 536:195–212, June 2000.

[188] Shiho Kobayashi and Bing Zhang. GRB 021004: Reverse Shock Emission. ApJL, 582(2):L75–L78, Jan 2003.

[189] Bing Zhang, Shiho Kobayashi, and Peter Mészáros. Gamma-Ray Burst Early Optical Afterglows: Implications for the Initial Lorentz Factor and the Central Engine. ApJ, 595(2):950–954, Oct 2003.

[190] Z. Lucas Uhm and Andrei M. Beloborodov. On the Mechanism of Gamma-Ray Burst Afterglows. ApJL, 665(2):L93–L96, Aug 2007.

[191] F. Genet, F. Daigne, and R. Mochkovitch. The rise of the afterglow in GRB 050820a. A &A, 471(1):1–5, Aug 2007.

[192] R. D. Blandford and C. F. McKee. Fluid dynamics of relativistic blast waves. Physics of Fluids, 19:1130–1138, Aug 1976.

[193] B. Zhang and P. Mészáros. Gamma-Ray Burst Afterglow with Continuous Energy Injection: Signature of a Highly Magnetized Millisecond Pulsar. ApJL, 552:L35–L38, May 2001.

[194] He Gao, Wei-Hua Lei, Yuan-Chuan Zou, Xue-Feng Wu, and Bing Zhang. A complete reference of the analytical synchrotron external shock models of gamma-ray bursts. NewAR, 57(6):141–190, Dec 2013.

[195] H. J. van Eerten and R. A. M. J. Wijers. Gamma-ray burst afterglow scaling coefficients for general density profiles. MNRAS, 394(4):2164–2174, Apr 2009.

[196] Z. Lucas Uhm and Bing Zhang. On the Non-existence of a Sharp Cooling Break in Gamma-Ray Burst Afterglow Spectra. ApJ, 780(1):82, Jan 2014.

[197] P. Mészáros, M. J. Rees, and R. A. M. J. Wijers. Viewing Angle and Environment Effects in Gamma-Ray Bursts: Sources of Afterglow Diversity. ApJ, 499:301–308, May 1998.

[198] J. G. Kirk, A. W. Guthmann, Y. A. Gallant, and A. Achterberg. Particle Acceleration at Ultrarelativistic Shocks: An Eigenfunction Method. ApJ, 542:235–242, October 2000.

[199] A. Achterberg, Y. A. Gallant, J. G. Kirk, and A. W. Guthmann. Particle acceleration by ultrarelativistic shocks: theory and simulations. MNRAS, 328:393–408, December 2001.

[200] Anatoly Spitkovsky. Particle Acceleration in Relativistic Collisionless Shocks: Fermi Process at Last? ApJ, 682(1):L5, Jul 2008.

[201] R. Shen, P. Kumar, and E. L. Robinson. No universality for the electron power-law index (p) in gamma-ray bursts and other relativistic sources. MNRAS, 371:1441–1447, September 2006.

[202] R. L. C. Starling, A. J. van der Horst, E. Rol, R. A. M. J. Wijers, C. Kouveliotou, K. Wiersema, P. A. Curran, and P. Weltevrede. Gamma-Ray Burst Afterglows as Probes of Environment and Blast Wave Physics. II. The Distribution of p and Structure of the Circumburst Medium. ApJ, 672:433–442, January 2008.

[203] P. A. Curran, R. L. C. Starling, A. J. van der Horst, and R. A. M. J. Wijers. Testing the blast wave model with Swift GRBs. MNRAS, 395:580–592, May 2009.

[204] P. A. Curran, P. A. Evans, M. de Pasquale, M. J. Page, and A. J. van der Horst. On the Electron Energy Distribution Index of Swift Gamma-ray Burst Afterglows. ApJL, 716:L135–L139, June 2010.

[205] Rodolfo Santana, Rodolfo Barniol Duran, and Pawan Kumar. Magnetic Fields in Relativistic Collisionless Shocks. ApJ, 785(1):29, Apr 2014.

[206] W. B. Atwood, R. Bagagli, L. Baldini, R. Bellazzini, G. Barbiellini, F. Belli, T. Borden, A. Brez, M. Brigida, and G. A. Caliandro. Design and initial tests of the Tracker-converter of the Gamma-ray Large Area Space Telescope. Astroparticle Physics, 28(4-5):422–434, Dec 2007.

[207] J. Eric Grove and W. Neil Johnson. The calorimeter of the Fermi Large Area Telescope. In Society of Photo-Optical Instrumentation Engineers (SPIE), volume 7732, page 77320J, Jul 2010.

[208] A. A. Moiseev, R. C. Hartman, J. F. Ormes, D. J. Thompson, M. J. Amato, T. E. Johnson, K. N. Segal, and D. A. Sheppard. The anti-coincidence detector for the GLAST large area telescope. Astroparticle Physics, 27(5):339–358, Jun 2007.

[209] A.A. Moiseev, J.F. Ormes, R.C. Hartman, T.E. Johnson, J.W. Mitchell, and D.J. Thompson. Observation and simulations of the backsplash effects in high-energy -ray telescopes containing a massive calorimeter. Astroparticle Physics, 22(3):275 – 283, 2004.

[210] M. Ackermann, M. Ajello, A. Albert, A. Allafort, W. B. Atwood, M. Axelsson, L. Baldini, J. Ballet, G. Barbiellini, and D. Bastieri. The Fermi Large Area Telescope on Orbit: Event Classification, Instrument Response Functions, and Calibration. ApJS, 203(1):4, Nov 2012.

[211] Marco Tinivella. A review of Cosmic-ray electrons and fermi-LAT. arXiv e-prints, page arXiv:1610.03672, Oct 2016.

[212] W. Atwood, A. Albert, L. Baldini, M. Tinivella, J. Bregeon, M. Pesce-Rollins, C. Sgrò, P. Bruel, E. Charles, A. Drlica-Wagner, A. Franckowiak, T. Jogler, L. Rochester, T. Usher, M. Wood, J. Cohen-Tanugi, and S. Zimmer for the Fermi-LAT Collaboration. Pass 8: Toward the Full Realization of the Fermi-LAT Scientific Potential. arXiv e-prints, page arXiv:1303.3514, Mar 2013.

[213] P. Bruel, T. H. Burnett, S. W. Digel, G. Johannesson, N. Omodei, and M. Wood. Fermi-LAT improved Pass~8 event selection. arXiv e-prints, page arXiv:1810.11394, Oct 2018.

[214] V. Pelassa, R. Preece, F. Piron, N. Omodei, S. Guiriec, Fermi LAT Collaboration, and Fermi GBM Collaboration. The LAT Low-Energy technique for Fermi Gamma-Ray Bursts spectral analysis. In The 2009 Fermi Symposium, page arXiv:1002.2617, Feb 2010.

[215] V. Connaughton, M. S. Briggs, A. Goldstein, C. A. Meegan, W. S. Paciesas, R. D. Preece, C. A. Wilson-Hodge, M. H. Gibby, J. Greiner, and D. Gruber. Localization of Gamma-Ray Bursts Using the Fermi Gamma-Ray Burst Monitor. ApJS, 216(2):32, Feb 2015.

[216] F. Berlato, J. Greiner, and J. Michael Burgess. Improved Fermi-GBM GRB Localizations Using BALROG. ApJ, 873(1):60, Mar 2019.

[217] E. Bissaldi, A. von Kienlin, G. Lichti, H. Steinle, P. N. Bhat, M. S. Briggs, G. J. Fishman, A. S. Hoover, R. M. Kippen, and M. Krumrey. Ground-based calibration and characterization of the Fermi gamma-ray burst monitor detectors. Experimental Astronomy, 24(1-3):47–88, May 2009.

[218] M. Ackermann, M. Ajello, K. Asano, L. Baldini, G. Barbiellini, M. G. Baring, D. Bastieri, R. Bellazzini, R. D. Blandford, and E. Bonamente. Multiwavelength Observations of GRB 110731A: GeV Emission from Onset to Afterglow. ApJ, 763(2):71, Feb 2013.

[219] Andreas von Kienlin, Charles A. Meegan, William S. Paciesas, P. N. Bhat, Elisabetta Bissaldi, Michael S. Briggs, J. Michael Burgess, David Byrne, Vandiver Chaplin, and William Cleveland. The Second Fermi GBM Gamma-Ray Burst Catalog: The First Four Years. ApJS, 211(1):13, Mar 2014.

[220] J. P. Norris, J. T. Bonnell, D. Kazanas, J. D. Scargle, J. Hakkila, and T. W. Giblin. Long-Lag, Wide-Pulse Gamma-Ray Bursts. ApJ, 627(1):324–345, Jul 2005.

[221] Jon Hakkila and Robert D. Preece. Gamma-Ray Burst Pulse Shapes: Evidence for Embedded Shock Signatures? ApJ, 783(2):88, Mar 2014.

[222] Jeffrey D. Scargle. Studies in Astronomical Time Series Analysis. V. Bayesian Blocks, a New Method to Analyze Structure in Photon Counting Data. ApJ, 504(1):405–418, Sep 1998.

[223] Jeffrey D. Scargle, Jay P. Norris, Brad Jackson, and James Chiang. Studies in Astronomical Time Series Analysis. VI. Bayesian Block Representations. ApJ, 764(2):167, Feb 2013.

[224] Donald B. Percival and Andrew T. Walden. Wavelet Methods for Time Series Analysis. Cambridge Series in Statistical and Probabilistic Mathematics. Cambridge University Press, 2000.

[225] Katharine C. Walker, Bradley E. Schaefer, and E. E. Fenimore. Gamma-Ray Bursts Have Millisecond Variability. ApJ, 537(1):264–269, Jul 2000.

[226] G. A. MacLachlan, A. Shenoy, E. Sonbas, K. S. Dhuga, B. E. Cobb, T. N. Ukwatta, D. C. Morris, A. Eskandarian, L. C. Maximon, and W. C. Parke. Minimum variability time-scales of long and short GRBs. MNRAS, 432(2):857–865, Jun 2013.

[227] Vahid Z. Golkhou and Nathaniel R. Butler. Uncovering the Intrinsic Variability of Gamma-Ray Bursts. ApJ, 787(1):90, May 2014.

[228] G. Vianello, R. Gill, J. Granot, N. Omodei, J. Cohen-Tanugi, and F. Longo. The Bright and the Slow—GRBs 100724B and 160509A with High-energy Cutoffs at $\lesssim$100 MeV. ApJ, 864(2):163, Sep 2018.

[229] En-Wei Liang, Bin-Bin Zhang, Mike Stamatikos, Bing Zhang, Jay Norris, Neil Gehrels, Jin Zhang, and Z. G. Dai. Temporal Profiles and Spectral Lags of XRF 060218. ApJL, 653(2):L81–L84, Dec 2006.

[230] R. A. Edelson and J. H. Krolik. The Discrete Correlation Function: A New Method for Analyzing Unevenly Sampled Variability Data. ApJ, 333:646, Oct 1988.

[231] Glen Cowan. Statistical data analysis. Oxford Science Publications, 1997.

[232] F. James and M. Roos. Minuit - a system for function minimization and analysis of the parameter errors and correlations. Computer Physics Communications, 10(6):343–367, Dec 1975.

[233] W. Cash. Parameter estimation in astronomy through application of the likelihood ratio. ApJ, 228:939–947, Mar 1979.

[234] S. S. Wilks. The large-sample distribution of the likelihood ratio for testing composite hypotheses. Ann. Math. Statist., 9(1):60–62, 03 1938.

[235] Louis Lyons. Bayes and Frequentism: a particle physicist's perspective. Contemporary Physics, 54(1):1–16, Feb 2013.

[236] Gideon Schwarz. Estimating the Dimension of a Model. Annals of Statistics, 6(2):461–464, Jul 1978.

[237] Robert E. Kass and Adrian E. Raftery. Bayes factors. Journal of the American Statistical Association, 90(430):773–795, 1995.

[238] F. Acero, M. Ackermann, M. Ajello, A. Albert, W. B. Atwood, M. Axelsson, L. Baldini, J. Ballet, G. Barbiellini, D. Bastieri, A. Belfiore, R. Bellazzini, E. Bissaldi, R. D. Blandford, E. D. Bloom, J. R. Bogart, R. Bonino, E. Bottacini, J. Bregeon, R. J. Britto, P. Bruel, R. Buehler, T. H. Burnett, S. Buson, G. A. Caliandro, R. A. Cameron, R. Caputo, M. Caragiulo, P. A. Caraveo, J. M. Casandjian, E. Cavazzuti, E. Charles, R. C. G. Chaves, A. Chekhtman, C. C. Cheung, J. Chiang, G. Chiaro, S. Ciprini, R. Claus, J. Cohen-Tanugi, L. R. Cominsky, J. Conrad, S. Cutini, F. D'Ammando, A. de Angelis, M. DeKlotz, F. de Palma, R. Desiante, S. W. Digel, L. Di Venere, P. S. Drell, R. Dubois, D. Dumora, C. Favuzzi, S. J. Fegan, E. C. Ferrara, J. Finke, A. Franckowiak, Y. Fukazawa, S. Funk, P. Fusco, F. Gargano, D. Gasparrini, B. Giebels, N. Giglietto, P. Giommi, F. Giordano, M. Giroletti, T. Glanzman, G. Godfrey, I. A. Grenier, M.-H. Grondin, J. E. Grove, L. Guillemot, S. Guiriec, D. Hadasch, A. K. Harding, E. Hays, J. W. Hewitt, A. B. Hill, D. Horan, G. Iafrate, T. Jogler, G. Jóhannesson, R. P. Johnson, A. S. Johnson, T. J. Johnson, W. N. Johnson, T. Kamae, J. Kataoka, J. Katsuta, M. Kuss, G. La Mura, D. Landriu, S. Larsson, L. Latronico, M. Lemoine-Goumard, J. Li, L. Li, F. Longo, F. Loparco, B. Lott, M. N. Lovellette, P. Lubrano, G. M. Madejski, F. Massaro, M. Mayer, M. N. Mazziotta, J. E. McEnery, P. F. Michelson, N. Mirabal, T. Mizuno, A. A. Moiseev, M. Mongelli, M. E. Monzani, A. Morselli, I. V. Moskalenko, S. Murgia, E. Nuss, M. Ohno, T. Ohsugi, N. Omodei, M. Orienti, E. Orlando, J. F. Ormes, D. Paneque, J. H. Panetta, J. S. Perkins, M. Pesce-Rollins, F. Piron, G. Pivato, T. A. Porter, J. L. Racusin, R. Rando, M. Razzano, S. Razzaque, A. Reimer, O. Reimer, T. Reposeur, L. S. Rochester, R. W. Romani, D. Salvetti, M. Sánchez-Conde, P. M. Saz Parkinson, A. Schulz, E. J. Siskind, D. A. Smith, F. Spada, G. Spandre, P. Spinelli, T. E. Stephens, A. W. Strong, D. J. Suson, H. Takahashi, T. Takahashi, Y. Tanaka, J. G. Thayer, J. B. Thayer, D. J. Thompson, L. Tibaldo, O. Tibolla, D. F. Torres, E. Torresi, G. Tosti, E. Troja, B. Van Klaveren, G. Vianello, B. L. Winer, K. S. Wood, M. Wood, S. Zimmer, and Fermi-LAT Collaboration. Fermi Large Area Telescope Third Source Catalog. ApJS, 218:23, June 2015.

[239] K. A. Arnaud. XSPEC: The First Ten Years. In G. H. Jacoby and J. Barnes, editors, Astronomical Data Analysis Software and Systems V, volume 101 of Astronomical Society of the Pacific Conference Series, page 17, 1996.

[240] J. L. Racusin, S. Zhu, D. Kocevski, M. Ohno, N. Omodei, E. Troja, and G. Vianello. GRB 131108A: Fermi-LAT onboard detection of a burst. GRB Coordinates Network, Circular Service, No. 15464, #1 (2013), 15464, 2013.

[241] G. Younes. GRB 131108A: Fermi GBM observation. GRB Coordinates Network, Circular Service, No. 15477, #1 (2013), 15477, 2013.

[242] M. M. Chester and M. C. Stroh. GRB 131108A: Swift/UVOT detection. GRB Coordinates Network, Circular Service, No. 15476, #1 (2013), 15476, 2013.

[243] M. C. Stroh and J. A. Kennea. GRB 131108A: Swift-XRT observations. GRB Coordinates Network, Circular Service, No. 15474, #1 (2013), 15474, 2013.

[244] A. Giuliani, F. Longo, F. Verrecchia, C. Pittori, M. Marisaldi, F. Fuschino, F. Lucarelli, M. E. Del, F. Lazzarotto, I. Donnarumma, Y. Evangelista, M. Feroci, L. Pacciani, P. Soffitta, E. Costa, I. Lapshov, M. Rapisarda, G. Barbiellini, A. Bulgarelli, F. Gianotti, M. Trifoglio, G. Di Cocco, C. Labanti, V. Fioretti, M. Galli, A. Chen, S. Mereghetti, F. Perotti, P. Caraveo, M. Cardillo, E. Striani, M. Tavani, A. Argan, G. Piano, S. Sabatini, V. Vittorini, G. Pucella, A. Pellizzoni, A. Trois, M. Pilia, S. Vercellone, P. W. Cattaneo, A. Rappoldi, A. Morselli, P. Picozza, M. Prest, E. Vallazza, P. Lipari, D. Zanello, P. Giommi, and G. Valentini. GRB 131108A: AGILE/GRID observation. GRB Coordinates Network, Circular Service, No. 15479, #1 (2013), 15479, 2013.

[245] A. de Ugarte Postigo, C. C. Thoene, J. Gorosabel, R. Sanchez-Ramirez, J. P. U. Fynbo, N. R. Tanvir, A. Cabrera-Lavers, and A. Garcia. GRB 131108A: redshift from 10.4m GTC. GRB Coordinates Network, 15470:1, Jan 2013.

[246] E. W. Liang, B. Zhang, P. T. O'Brien, R. Willingale, L. Angelini, D. N. Burrows, S. Campana, G. Chincarini, A. Falcone, N. Gehrels, M. R. Goad, D. Grupe, S. Kobayashi, P. Mészáros, J. A. Nousek, J. P. Osborne, K. L. Page, and G. Tagliaferri. Testing the Curvature Effect and Internal Origin of Gamma-Ray Burst Prompt Emissions and X-Ray Flares with Swift Data. ApJ, 646:351–357, July 2006.

[247] A. Giuliani, S. Mereghetti, M. Marisaldi, F. Longo, E. Del Monte, C. Pittori, F. Verrecchia, M. Tavani, P. Cattaneo, L. Pacciani, S. Vercellone, and A. Rappoldi. A prompt extra component in the high energy spectrum of GRB 131108A. arXiv e-prints, July 2014.

[248] B. Rani, P. J. Wiita, and A. C. Gupta. Nearly Periodic Fluctuations in the Long-term X-Ray Light Curves of the Blazars AO 0235+164 and 1ES 2321+419. ApJ, 696:2170–2178, May 2009.

[249] C. A. Swenson and P. W. A. Roming. Gamma-Ray Burst Flares: X-Ray Flaring. II. ApJ, 788:30, June 2014.

[250] G. Chincarini, J. Mao, R. Margutti, M. G. Bernardini, C. Guidorzi, F. Pasotti, D. Giannios, M. Della Valle, A. Moretti, P. Romano, P. D'Avanzo,

G. Cusumano, and P. Giommi. Unveiling the origin of X-ray flares in gamma-ray bursts. MNRAS, 406:2113–2148, August 2010.

[251] S. Kobayashi and B. Zhang. The Onset of Gamma-Ray Burst Afterglow. ApJ, 655:973–979, February 2007.

[252] A. D. Falcone, D. Morris, J. Racusin, G. Chincarini, A. Moretti, P. Romano, D. N. Burrows, C. Pagani, M. Stroh, D. Grupe, S. Campana, S. Covino, G. Tagliaferri, R. Willingale, and N. Gehrels. The First Survey of X-Ray Flares from Gamma-Ray Bursts Observed by Swift: Spectral Properties and Energetics. ApJ, 671:1921–1938, December 2007.

[253] X.-Y. Wang, Z. Li, and P. Mészáros. GeV-TeV and X-Ray Flares from Gamma-Ray Bursts. ApJL, 641:L89–L92, April 2006.

[254] Y.-Z. Fan, T. Piran, R. Narayan, and D.-M. Wei. High-energy afterglow emission from gamma-ray bursts. MNRAS, 384:1483–1501, March 2008.

[255] Zhuo Li and Eli Waxman. Prompt Optical Emission from Residual Collisions in Gamma-Ray Burst Outflows. ApJ, 674(2):L65, Feb 2008.

[256] A. Maxham, B.-B. Zhang, and B. Zhang. Is GeV emission from Gamma-Ray Bursts of external shock origin? MNRAS, 415:77–82, July 2011.

[257] P. Jenke. GRB 160709A: Fermi GBM Observations. GRB Coordinates Network, 19676, 2016.

[258] T. Sakamoto, S. D. Barthelmy, J. R. Cummings, N. Gehrels, H. A. Krimm, A. Y. Lien, C. B. Markwardt, D. M. Palmer, J. P. Norris, M. Stamatikos, and T. N. Ukwatta. GRB 160709A, Swift-BAT detection and localization. GRB Coordinates Network, 19681, 2016.

[259] S. Guiriec, G. Vianello, and J. Racusin. GRB 160709A: Fermi-LAT detection. GRB Coordinates Network, 19675, 2016.

[260] D. Frederiks, S. Golenetskii, R. Aptekar, P. Oleynik, M. Ulanov, D. Svinkin, A. Tsvetkova, A. Lysenko, A. Kozlova, and T. Cline. Konus-Wind observation of GRB 160709A (short/hard). GRB Coordinates Network, 19677, 2016.

[261] Y. Asaoka, A. Yoshida, T. Sakamoto, Y. Kawakubo, M. Moriyama, Y. Yamada, K. Yamaoka, S. Nakahira, I. Takahashi, S. Ozawa, S. Torii, Y. Shimizu, T. Tamura, W. Ishizaki, M. L. Cherry, S. Ricciarini, and P. S. Marrocchesi. GRB 160709A CALET Gamma-Ray Burst Monitor detection. GRB Coordinates Network, 19701, 2016.

[262] V. Bhalerao, V. Kumar, D. Bhattacharya, A. R. Rao, and S. Vadawale. GRB160709A: Astrosat CZTI detection of short GRB. GRB Coordinates Network, 19740, 2016.

[263] P. Mészáros, E. Ramirez-Ruiz, M. J. Rees, and B. Zhang. X-Ray-rich Gamma-Ray Bursts, Photospheres, and Variability. ApJ, 578:812–817, October 2002.

[264] K. Asano and P. Mészáros. Photon and neutrino spectra of time-dependent photospheric models of gamma-ray bursts. JCAP, 9:008, September 2013.

[265] Planck Collaboration, P. A. R. Ade, N. Aghanim, M. Arnaud, M. Ashdown, J. Aumont, C. Baccigalupi, A. J. Banday, R. B. Barreiro, J. G. Bartlett, and et al. Planck 2015 results. XIII. Cosmological parameters. A&A, 594:A13, September 2016.

[266] B. Zhang and A. Pe'er. Evidence of an Initially Magnetically Dominated Outflow in GRB 080916C. ApJL, 700:L65–L68, August 2009.

[267] F. Ryde and A. Pe'er. Quasi-blackbody Component and Radiative Efficiency of the Prompt Emission of Gamma-ray Bursts. ApJ, 702:1211–1229, September 2009.

[268] A. Pe'er, H. Barlow, S. O'Mahony, R. Margutti, F. Ryde, J. Larsson, D. Lazzati, and M. Livio. Hydrodynamic Properties of Gamma-Ray Burst Outflows Deduced from the Thermal Component. ApJ, 813:127, November 2015.

[269] Y. Lithwick and R. Sari. Lower Limits on Lorentz Factors in Gamma-Ray Bursts. ApJ, 555:540–545, July 2001.

[270] E. E. Fenimore, R. I. Epstein, and C. Ho. The escape of 100 MeV photons from cosmological gamma-ray bursts. A&AS, 97:59–62, January 1993.

[271] M. G. Baring and A. K. Harding. The Escape of High-Energy Photons from Gamma-Ray Bursts. ApJ, 491:663–686, December 1997.

[272] A. A. Abdo, M. Ackermann, M. Ajello, K. Asano, W. B. Atwood, M. Axelsson, L. Baldini, J. Ballet, G. Barbiellini, M. G. Baring, and et al. A limit on the variation of the speed of light arising from quantum gravity effects. Nature, 462:331–334, November 2009.

[273] X.-H. Zhao, Z. Li, and J.-M. Bai. The Bulk Lorentz Factors of Fermi-LAT Gamma Ray Bursts. ApJ, 726:89, January 2011.

[274] S. Rosswog, M. Liebendörfer, F.-K. Thielemann, M. B. Davies, W. Benz, and T. Piran. Mass ejection in neutron star mergers. A&A, 341:499–526, January 1999.

[275] M. G. Bernardini, C. L. Bianco, L. Caito, M. G. Dainotti, R. Guida, and R. Ruffini. GRB 970228 and a class of GRBs with an initial spikelike emission. A&A, 474:L13–L16, October 2007.

[276] L. Caito, M. G. Bernardini, C. L. Bianco, M. G. Dainotti, R. Guida, and R. Ruffini. GRB060614: a "fake" short GRB from a merging binary system. A&A, 498:501–507, May 2009.

[277] M. Ajello, M. Arimoto, M. Axelsson, L. Baldini, G. Barbiellini, D. Bastieri, R. Bellazzini, A. Berretta, E. Bissaldi, R. D. Blandford, R. Bonino, E. Bottacini, J. Bregeon, P. Bruel, R. Buehler, E. Burns, S. Buson, R. A. Cameron, R. Caputo, P. A. Caraveo, E. Cavazzuti, S. Chen, G. Chiaro, S. Ciprini, J. Cohen-Tanugi, D. Costantin, S. Cutini, F. D'Ammando, M. DeKlotz, P. de la Torre Luque, F. de Palma, A. Desai, N. Di Lalla, L. Di Venere, F. Fana Dirirsa, S. J. Fegan, A. Franckowiak, Y. Fukazawa, S. Funk, P. Fusco, F. Gargano, D. Gasparrini, N. Giglietto, R. Gill, F. Giordano, M. Giroletti, J. Granot, D. Green, I. A. Grenier, M. H. Grondin, S. Guiriec, E. Hays, D. Horan, G. Jóhannesson, D. Kocevski, M. Kovac'evic', M. Kuss, S. Larsson, L. Latronico, M. Lemoine-Goumard, J. Li, I. Liodakis, F. Longo, F. Loparco, M. N. Lovellette, P. Lubrano, S. Maldera, D. Malyshev, A. Manfreda, G. Martí-Devesa, M. N. Mazziotta, J. E. McEnery, I. Mereu, M. Meyer, P. F. Michelson, W. Mitthumsiri, T. Mizuno, M. E. Monzani, E. Moretti, A. Morselli, I. V. Moskalenko, M. Negro, E. Nuss, N. Omodei, M. Orienti, E. Orlando, M. Palatiello, V. S. Paliya, D. Paneque, Z. Pei, M. Persic, M. Pesce-Rollins, V. Petrosian, F. Piron, H. Poon, T. A. Porter, G. Principe, J. L. Racusin, S. Rainò, R. Rando, B. Rani, M. Razzano, S. Razzaque, A. Reimer, O. Reimer, F. Ryde, P. M. Saz Parkinson, D. Serini, C. Sgrò, E. J. Siskind, G. Spandre, P. Spinelli, H. Tajima, K. Takagi, M. N. Takahashi, D. Tak, J. B. Thayer, D. J. Thompson, D. F. Torres, E. Troja, J. Valverde, B. Van Klaveren, K. Wood, M. Yassine, G. Zaharijas, P. N. Bhat, M. S. Briggs, W. Cleveland , M. Giles, A. Goldstein, M. Hui, C. Malacaria, R. Preece, O. Roberts, P. Veres, A. von Kienlin, S. B. Cenko, P. O'Brien, A. P. Beardmore, A. Lien, J. P. Osborne, A. Tohuvavohu, V. D'Elia, A. D'A, M. Perri, J. Gropp, N. Klingler, M. Capalbi, G. Tagliaferri, and M. Stamatikos. Fermi and Swift Observations of GRB 190114C: Tracing the Evolution of High-Energy Emission from Prompt to Afterglow. arXiv e-prints, page arXiv:1909.10605, Sep 2019.

[278] R. Hamburg, P. Veres, C. Meegan, E. Burns, V. Connaughton, A. Goldstein, D. Kocevski, and O. J. Roberts. GRB 190114C: Fermi GBM detection. GRB Coordinates Network, Circular Service, No. 23707, #1 (2019), 23707, 2019.

[279] J. D. Gropp, J. A. Kennea, N. J. Klingler, H. A. Krimm, S. J. Laporte, A. Y. Lien, M. J. Moss, D. M. Palmer, B. Sbarufatti, and M. H. Siegel. GRB 190114C: Swift detection of a very bright burst with a bright optical counterpart. GRB Coordinates Network, Circular Service, No. 23688, #1 (2019), 23688, 2019.

[280] Peter W. A. Roming, Thomas E. Kennedy, Keith O. Mason, John A. Nousek, Lindy Ahr, Richard E. Bingham, Patrick S. Broos, Mary J. Carter, Barry K. Hancock, Howard E. Huckle, S. D. Hunsberger, Hajime Kawakami, Ronnie Killough, T. Scott Koch, Michael K. McLelland, Kelly Smith, Philip J. Smith, Juan Carlos Soto, Patricia T. Boyd, Alice A. Breeveld, Stephen T. Holland, Mariya Ivanushkina, Michael S. Pryzby, Martin D. Still, and Joseph

Stock. The Swift Ultra-Violet/Optical Telescope. Space Science Reviews, 120(3-4):95–142, Oct 2005.

[281] J. P. Osborne, A. P. Beardmore, P. A. Evans, and M. R. Goad. GRB 190114C: Enhanced Swift-XRT position. GRB Coordinates Network, Circular Service, No. 23704, #1 (2019), 23704, 2019.

[282] M. H. Siegel and J. D. Gropp. GRB 190114C: Swift/UVOT Detection. GRB Coordinates Network, Circular Service, No. 23725, #1 (2019), 23725, 2019.

[283] A. de Ugarte Postigo, D. A. Kann, C. C. Thoene, and L. Izzo. GRB 190114C: Possible host galaxy in Pan-STARRS. GRB Coordinates Network, Circular Service, No. 23692, #1 (2019), 23692, 2019.

[284] J. Selsing, J. P. U. Fynbo, K. E. Heintz, and D. Watson. GRB 190114C: NOT optical counterpart and redshift. GRB Coordinates Network, Circular Service, No. 23695, #1 (2019), 23695, 2019.

[285] R. Mirzoyan, K. Noda, E. Moretti, A. Berti, C. Nigro, J. Hoang, S. Micanovic, M. Takahashi, Y. Chai, A. Moralejo, and MAGIC Collaboration. MAGIC detects the GRB 190114C in the TeV energy domain. GRB Coordinates Network, Circular Service, No. 23701, #1 (2019), 23701, 2019.

[286] P. A. Evans, A. P. Beardmore, K. L. Page, J. P. Osborne, P. T. O'Brien, R. Willingale, R. L. C. Starling, D. N. Burrows, O. Godet, L. Vetere, J. Racusin, M. R. Goad, K. Wiersema, L. Angelini, M. Capalbi, G. Chincarini, N. Gehrels, J. A. Kennea, R. Margutti, D. C. Morris, C. J. Mountford, C. Pagani, M. Perri, P. Romano, and N. Tanvir. Methods and results of an automatic analysis of a complete sample of Swift-XRT observations of GRBs. MNRAS, 397:1177–1201, August 2009.

[287] R. Willingale, R. L. C. Starling, A. P. Beardmore, N. R. Tanvir, and P. T. O'Brien. Calibration of X-ray absorption in our Galaxy. MNRAS, 431:394–404, May 2013.

[288] A. J. Castro-Tirado, Y. Hu, E. Fernandez-Garcia, A. Valeev, V. Sokolov, S. Guziy, S. Oates, S. Jeong, S. B. Pandey, I. Carrasco, and D. Reverte-Paya. GRB 190114C: refined redshift by the 10.4m GTC. GRB Coordinates Network, 23708:1, Jan 2019.

[289] J. Granot, J. Cohen-Tanugi, and E. d. C. e. Silva. Opacity Buildup in Impulsive Relativistic Sources. ApJ, 677:92–126, April 2008.

[290] T. Fukushima, S. To, K. Asano, and Y. Fujita. Temporal Evolution of the Gamma-ray Burst Afterglow Spectrum for an Observer: GeV-TeV Synchrotron Self-Compton Light Curve. ApJ, 844:92, August 2017.

[291] J. Hakkila and R. D. Preece. Unification of Pulses in Long and Short Gamma-Ray Bursts: Evidence from Pulse Properties and Their Correlations. ApJ, 740:104, October 2011.

[292] H.-F. Yu, R. D. Preece, J. Greiner, P. Narayana Bhat, E. Bissaldi, M. S. Briggs, W. H. Cleveland, V. Connaughton, A. Goldstein, A. von Kienlin, C. Kouveliotou, B. Mailyan, C. A. Meegan, W. S. Paciesas, A. Rau, O. J. Roberts, P. Veres, C. Wilson-Hodge, B.-B. Zhang, and H. J. van Eerten. The Fermi GBM gamma-ray burst time-resolved spectral catalog: brightest bursts in the first four years. A &A, 588:A135, April 2016.

[293] F. Ryde and R. Svensson. On the Variety of the Spectral and Temporal Behavior of Long Gamma-Ray Burst Pulses. ApJ, 566:210–228, February 2002.

[294] D. Kocevski, F. Ryde, and E. Liang. Search for Relativistic Curvature Effects in Gamma-Ray Burst Pulses. ApJ, 596:389–400, October 2003.

[295] L. A. Ford, D. L. Band, J. L. Matteson, M. S. Briggs, G. N. Pendleton, R. D. Preece, W. S. Paciesas, B. J. Teegarden, D. M. Palmer, B. E. Schaefer, T. L. Cline, G. J. Fishman, C. Kouveliotou, C. A. Meegan, R. B. Wilson, and J. P. Lestrade. BATSE observations of gamma-ray burst spectra. 2: Peak energy evolution in bright, long bursts. ApJ, 439:307–321, January 1995.

[296] E. Liang and V. Kargatis. Dependence of the spectral evolution of γ-ray bursts on their photon fluence. Nature, 381:49–51, May 1996.

[297] R.-J. Lu, Y.-F. Liang, D.-B. Lin, J. Lv, X.-G. Wang, H.-J. Lv, H.-B. Liu, E.-W. Liang, and B. Zhang. A comprehensive analysis of Fermi Gamma-Ray Burst Data: IV. Spectral lag and Its Relation to Ep Evolution. ArXiv e-prints, August 2018.

[298] Robert E. Kass and Adrian E. Raftery. Bayes factors. Journal of the American Statistical Association, 90(430):773–795, 1995.

[299] A. I. MacFadyen and S. E. Woosley. Collapsars: Gamma-Ray Bursts and Explosions in "Failed Supernovae". ApJ, 524:262–289, October 1999.

[300] S. E. Woosley and J. S. Bloom. The Supernova Gamma-Ray Burst Connection. ARAA, 44:507–556, September 2006.

[301] R. A. Chevalier and Z.-Y. Li. Gamma-Ray Burst Environments and Progenitors. ApJL, 520:L29–L32, July 1999.

[302] S. A. Yost, F. A. Harrison, R. Sari, and D. A. Frail. A Study of the Afterglows of Four Gamma-Ray Bursts: Constraining the Explosion and Fireball Model. ApJ, 597:459–473, November 2003.

[303] J. J. Eldridge, F. Genet, F. Daigne, and R. Mochkovitch. The circumstellar environment of Wolf-Rayet stars and gamma-ray burst afterglows. MNRAS, 367:186–200, March 2006.

[304] P. Kumar and R. Barniol Duran. On the generation of high-energy photons detected by the Fermi Satellite from gamma-ray bursts. MNRAS, 400:L75–L79, November 2009.

[305] P. Kumar and R. Barniol Duran. External forward shock origin of high-energy emission for three gamma-ray bursts detected by Fermi. MNRAS, 409:226–236, November 2010.

[306] R. Barniol Duran. Constraining the magnetic field in GRB relativistic collisionless shocks using radio data. Monthly Notices of the Royal Astronomical Society, 442(4):3147–3154, 06 2014.

[307] Paz Beniamini, Lara Nava, Rodolfo Barniol Duran, and Tsvi Piran. Energies of GRB blast waves and prompt efficiencies as implied by modelling of X-ray and GeV afterglows. MNRAS, 454(1):1073–1085, Nov 2015.

[308] Bin-Bin Zhang, Hendrik van Eerten, David N. Burrows, Geoffrey Scott Ryan, Philip A. Evans, Judith L. Racusin, Eleonora Troja, and Andrew MacFadyen. An analysis of *Chandra* deep follow-up gamma-ray bursts: Implications for off-axis jets. ApJ, 806(1):15, jun 2015.

[309] A. Panaitescu and P. Mészáros. Gamma-Ray Bursts from Upscattered Self-absorbed Synchrotron Emission. ApJL, 544:L17–L21, November 2000.

[310] Xiang-Yu Wang, Hao-Ning He, Zhuo Li, Xue-Feng Wu, and Zi-Gao Dai. Klein-nishina effects on the high-energy afterglow emission of gamma-ray bursts. ApJ, 712(2):1232–1240, mar 2010.

[311] M. Lemoine. The synchrotron self-Compton spectrum of relativistic blast waves at large Y. MNRAS, 453:3772–3784, November 2015.

[312] P. Mészáros and M. J. Rees. Gamma-Ray Bursts: Multiwaveband Spectral Predictions for Blast Wave Models. ApJL, 418:L59, December 1993.

[313] P. Mészáros and M. J. Rees. GRB 990123: reverse and internal shock flashes and late afterglow behaviour. MNRAS, 306:L39–L43, July 1999.

[314] R. Sari and T. Piran. Predictions for the Very Early Afterglow and the Optical Flash. ApJ, 520:641–649, August 1999.

[315] S. Kobayashi. Light Curves of Gamma-Ray Burst Optical Flashes. ApJ, 545:807–812, December 2000.

[316] B. Zhang and P. Mészáros. Gamma-Ray Bursts: progress, problems and prospects. International Journal of Modern Physics A, 19:2385–2472, 2004.

[317] H. Gao, W.-H. Lei, Y.-C. Zou, X.-F. Wu, and B. Zhang. A complete reference of the analytical synchrotron external shock models of gamma-ray bursts. NewAR, 57:141–190, December 2013.

[318] J. Michael Burgess, Damien Bégué, Ana Bacelj, Dimitrios Giannios, Francesco Berlato, and Jochen Greiner. Gamma-ray bursts as cool synchrotron sources. arXiv e-prints, page arXiv:1810.06965, Oct 2018.

[319] J. M. Burgess, R. D. Preece, V. Connaughton, M. S. Briggs, A. Goldstein, P. N. Bhat, J. Greiner, D. Gruber, A. Kienlin, C. Kouveliotou, S. McGlynn, C. A. Meegan, W. S. Paciesas, A. Rau, S. Xiong, M. Axelsson, M. G. Baring, C. D. Dermer, S. Iyyani, D. Kocevski, N. Omodei, F. Ryde, and G. Vianello. Time-resolved Analysis of Fermi Gamma-Ray Bursts with Fast- and Slow-cooled Synchrotron Photon Models. ApJ, 784(1):17, Mar 2014.

[320] Bin-Bin Zhang, Z. Lucas Uhm, Valerie Connaughton, Michael S. Briggs, and Bing Zhang. Synchrotron Origin of the Typical GRB Band Function - A Case Study of GRB 130606B. ApJ, 816(2):72, Jan 2016.

[321] S. Guiriec, C. Kouveliotou, D. H. Hartmann, J. Granot, K. Asano, P. Mészáros, R. Gill, N. Gehrels, and J. McEnery. A Unified Model for GRB Prompt Emission from Optical to γ-Rays: Exploring GRBs as Standard Candles. ApJL, 831(1):L8, Nov 2016.

[322] Julie McEnery, Juan Abel Barrio, Ivan Agudo, Marco Ajello, José-Manuel Álvarez, Stefano Ansoldi, Sonia Anton, Natalia Auricchio, John B. Stephen, Luca Baldini, Cosimo Bambi, Matthew Baring, Ulisses Barres, Denis Bastieri, John Beacom, Volker Beckmann, Wlodek Bednarek, Denis Bernard, Elisabetta Bissaldi, Peter Bloser, Harsha Blumer, Markus Boettcher, Steven Boggs, Aleksey Bolotnikov, Eugenio Bottacini, Vladimir Bozhilov, Enrico Bozzo, Michael Briggs, Jim Buckley, Sara Buson, Riccardo Campana, Regina Caputo, Martina Cardillo, Ezio Caroli, Daniel Castro, S. Brad Cenko, Eric Charles, Wenlei Chen, Teddy Cheung, Stefano Ciprini, Paolo Coppi, Rui Curado da Silva, Sara Cutini, Filippo D'Ammand o, Alessandro De Angelis, Michaël De Becker, Georgia De Nolfo, Stefano Del Sordo, Mattia Di Mauro, Leonardo Di Venere, Stefano Dietrich, Seth Digel, Alberto Dominguez, Michele Doro, Elizabeth Ferrara, Brian Fields, Justin Finke, Luca Foffano, Chris Fryer, Yasushi Fukazawa, Stefan Funk, Dario Gasparrini, Joseph Gelfand, Markos Georganopoulos, Francesco Giordano, Andrea Giuliani, Christian Gouiffes, Brian Grefenstette, Isabelle Grenier, Sean Griffin, Eric Grove, Sylvain Guiriec, Alice Harding, Pat Harding, Dieter Hartmann, Elizabeth Hays, Margarita Hernanz, Jack Hewitt, Jamie Holder, Michelle Hui, Andrew Inglis, Robert Johnson, Sam Jones, Gottfried Kanbach, Oleg Kargaltsev, Sarah Kaufmann, Matthew Kerr, Carolyn Kierans, Fabian Kislat, Alexei V. Klimenko, Jurgen Knodlseder, Daniel Kocveski, Joachim Kopp, Henric Krawczynsiki, John Krizmanic, Hidetoshi Kubo, Naoko Kurahashi Neilson, Philippe Laurent, Jean-Philippe Lenain, Hui Li, Amy Lien, Tim Linden, Jan Lommler, Francesco

Longo, Michael Lovellette, Marcos López, Antonios Manousakis, Lea Marcotulli, Alexand re Marcowith, Manel Martinez, Marc McConnell, Jessica Metcalfe, Eileen Meyer, Manuel Meyer, Roberto Mignani, John Mitchell, Tsunefumi Mizuno, Alexander Moiseev, Daniel Morcuende, Igor Moskalenko, Michael Moss, Kazuhiro Nakazawa, M. Nicola Mazziotta, Uwe Oberlack, Masanori Ohno, Foteini Oikonomou, Roopesh Ojha, Nicola Omodei, Elena Orlando, Nepomuk Otte, Vaidehi S Paliya, Lucas Parker, Barbara Patricelli, Jeremy Perkins, Maria Petropoulou, Carlotta Pittori, Martin Pohl, Troy Porter, Elisa Prandini, Chanda Prescod-Weinstein, Judith Racusin, Riccardo Rand o, Bindu Rani, Marc Ribó, James Rodi, Miguel A. Sanchez-Conde, Pablo Saz Parkinson, Richard Schirato, Peter Shawhan, Chris Shrader, Jacob Smith, Karl Smith, Antonio Stamerra, Lukasz Stawarz, Andy Strong, Inga Stumke, Hiro Tajima, Hiromitsu Takahashi, Yasuyuki Tanaka, Vincent Tatischeff, Lih-Sin The, David Thompson, Luigi Tibaldo, John Tomsick, Lucas Uhm, Tonia Venters, Tom Vestrand, Giacomo Vianello, Zorawar Wadiasingh, Roland Walter, Xilu Wang, David Williams, Colleen Wilson-Hodge, Matthew Wood, Richard Woolf, Eric Wulf, George Younes, Luca Zampieri, Silvia Zane, Bing Zhang, Haocheng Zhang, Stephan Zimmer, Andreas Zoglauer, and Alexander van der Horst. All-sky Medium Energy Gamma-ray Observatory: Exploring the Extreme Multimessenger Universe. arXiv e-prints, page arXiv:1907.07558, Jul 2019.

[323] A. U. Abeysekara, J. A. Aguilar, S. Aguilar, R. Alfaro, E. Almaraz, C. Álvarez, J. de D. Álvarez-Romero, M. Álvarez, R. Arceo, J. C. Arteaga-Velázquez, C. Badillo, A. Barber, B. M. Baughman, N. Bautista-Elivar, E. Belmont, E. Benítez, S. Y. BenZvi, D. Berley, A. Bernal, E. Bonamente, J. Braun, R. Caballero-Lopez, I. Cabrera, A. Carramiñana, L. Carrasco, M. Castillo, L. Chambers, R. Conde, P. Condreay, U. Cotti, J. Cotzomi, J. C. D'Olivo, E. de la Fuente, C. De León, S. Delay, D. Delepine, T. DeYoung, L. Diaz, L. Diaz-Cruz, B. L. Dingus, M. A. Duvernois, D. Edmunds, R. W. Ellsworth, B. Fick, D. W. Fiorino, A. Fland es, N. I. Fraija, A. Galindo, J. L. García-Luna, G. García-Torales, F. Garfias, L. X. González, M. M. González, J. A. Goodman, V. Grabski, M. Gussert, C. Guzmán-Ceron, Z. Hampel-Arias, T. Harris, E. Hays, L. Hernandez-Cervantes, P. H. Hüntemeyer, A. Imran, A. Iriarte, J. J. Jimenez, P. Karn, N. Kelley-Hoskins, D. Kieda, R. Langarica, A. Lara, R. Lauer, W. H. Lee, E. C. Linares, J. T. Linnemann, M. Longo, R. Luna-García, H. Martínez, J. Martínez, L. A. Martínez, O. Martínez, J. Martínez-Castro, M. Martos, J. Matthews, J. E. McEnery, G. Medina-Tanco, J. E. Mendoza-Torres, P. A. Miranda-Romagnoli, T. Montaruli, E. Moreno, M. Mostafa, M. Napsuciale, J. Nava, L. Nellen, M. Newbold, R. Noriega-Papaqui, T. Oceguera-Becerra, A. Olmos Tapia, V. Orozco, V. Pérez, E. G. Pérez-Pérez, J. S. Perkins, J. Pretz, C. Ramirez, I. Ramírez, D. Rebello, A. Rentería, J. Reyes, D. Rosa-González, A. Rosado, J. M. Ryan, J. R. Sacahui, H. Salazar, F. Salesa, A. Sandoval, E. Santos, M. Schneider, A. Shoup, S. Silich, G. Sinnis, A. J. Smith, K. Sparks, W. Springer,

F. Suárez, N. Suarez, I. Taboada, A. F. Tellez, G. Tenorio-Tagle, A. Tepe, P. A. Toale, K. Tollefson, I. Torres, T. N. Ukwatta, J. Valdes-Galicia, P. Vanegas, V. Vasileiou, O. Vázquez, X. Vázquez, L. Villaseñor, W. Wall, J. S. Walters, D. Warner, S. Westerhoff, I. G. Wisher, J. Wood, G. B. Yodh, D. Zaborov, and A. Zepeda. On the sensitivity of the HAWC observatory to gamma-ray bursts. Astroparticle Physics, 35(10):641–650, May 2012.

[324] Ignacio Taboada and Rudy C. Gilmore. Prospects for the detection of GRBs with HAWC. Nuclear Instruments and Methods in Physics Research A, 742:276–277, Apr 2014.